

**University of Miami  
Scholarly Repository**

---

Open Access Dissertations

Electronic Theses and Dissertations

---

2012-11-14

# Development and Evaluation of New Algorithms for the Retrieval of Wind and Internal Wave Parameters from Shipborne Marine Radar Data

Björn Lund  
*University of Miami*, blund@gmx.com

Follow this and additional works at: [http://scholarlyrepository.miami.edu/oa\\_dissertations](http://scholarlyrepository.miami.edu/oa_dissertations)

---

## Recommended Citation

Lund, Björn, "Development and Evaluation of New Algorithms for the Retrieval of Wind and Internal Wave Parameters from Shipborne Marine Radar Data" (2012). *Open Access Dissertations*. Paper 894.

---

This Open access is brought to you for free and open access by the Electronic Theses and Dissertations at Scholarly Repository. It has been accepted for inclusion in Open Access Dissertations by an authorized administrator of Scholarly Repository. For more information, please contact [jrenaud@miami.edu](mailto:jrenaud@miami.edu).

<b>Report Documentation Page</b>			Form Approved OMB No. 0704-0188					
<p>Public reporting burden for the collection of information is estimated to average 1 hour per response, including the time for reviewing instructions, searching existing data sources, gathering and maintaining the data needed, and completing and reviewing the collection of information. Send comments regarding this burden estimate or any other aspect of this collection of information, including suggestions for reducing this burden, to Washington Headquarters Services, Directorate for Information Operations and Reports, 1215 Jefferson Davis Highway, Suite 1204, Arlington VA 22202-4302. Respondents should be aware that notwithstanding any other provision of law, no person shall be subject to a penalty for failing to comply with a collection of information if it does not display a currently valid OMB control number.</p>								
1. REPORT DATE <b>DEC 2012</b>	2. REPORT TYPE	3. DATES COVERED <b>00-00-2012 to 00-00-2012</b>						
<b>4. TITLE AND SUBTITLE</b> <b>Development and Evaluation of New Algorithms for the Retrieval of Wind and Internal Wave Parameters from Shipborne Marine Radar Data</b>			5a. CONTRACT NUMBER					
			5b. GRANT NUMBER					
			5c. PROGRAM ELEMENT NUMBER					
<b>6. AUTHOR(S)</b>			5d. PROJECT NUMBER					
			5e. TASK NUMBER					
			5f. WORK UNIT NUMBER					
<b>7. PERFORMING ORGANIZATION NAME(S) AND ADDRESS(ES)</b> <b>University of Miami, Coral Gables, FL, 33124</b>			8. PERFORMING ORGANIZATION REPORT NUMBER					
<b>9. SPONSORING/MONITORING AGENCY NAME(S) AND ADDRESS(ES)</b>			10. SPONSOR/MONITOR'S ACRONYM(S)					
			11. SPONSOR/MONITOR'S REPORT NUMBER(S)					
<b>12. DISTRIBUTION/AVAILABILITY STATEMENT</b> <b>Approved for public release; distribution unlimited</b>								
<b>13. SUPPLEMENTARY NOTES</b>								
<b>14. ABSTRACT</b> <p>The goal of this work is to develop and evaluate techniques for the retrieval of wind and internal wave (IW) information from marine X-band radar data. While ocean wind measurements are crucial for the transfer of energy and momentum across the air-sea interface, IWs play an important role in tidal energy transport. Marine radars work by transmitting microwave energy from a rotating antenna that also measures the backscatter. The radar backscatter from the sea surface is controlled by the wind-generated small ripple waves through the Bragg-scattering mechanism. Surface winds are thus the dominant factor for generating the radar backscatter. The varying surface current fields associated with IWs interact with the ripples, generating rough convergent and smooth divergent zones. Radars are capable of imaging such IW-induced surface signatures as bands of enhanced and weakened backscatter.</p>								
<b>15. SUBJECT TERMS</b>								
<b>16. SECURITY CLASSIFICATION OF:</b> <table border="1" style="width: 100%; border-collapse: collapse;"> <tr> <td style="width: 33.33%; padding: 2px;">a. REPORT <b>unclassified</b></td> <td style="width: 33.33%; padding: 2px;">b. ABSTRACT <b>unclassified</b></td> <td style="width: 33.33%; padding: 2px;">c. THIS PAGE <b>unclassified</b></td> </tr> </table>			a. REPORT <b>unclassified</b>	b. ABSTRACT <b>unclassified</b>	c. THIS PAGE <b>unclassified</b>	<b>17. LIMITATION OF ABSTRACT</b> <b>Same as Report (SAR)</b>	<b>18. NUMBER OF PAGES</b> <b>244</b>	<b>19a. NAME OF RESPONSIBLE PERSON</b>
a. REPORT <b>unclassified</b>	b. ABSTRACT <b>unclassified</b>	c. THIS PAGE <b>unclassified</b>						

UNIVERSITY OF MIAMI

DEVELOPMENT AND EVALUATION OF NEW ALGORITHMS FOR THE  
RETRIEVAL OF WIND AND INTERNAL WAVE PARAMETERS FROM  
SHIPBORNE MARINE RADAR DATA

By

Björn Lund

A DISSERTATION

Submitted to the Faculty  
of the University of Miami  
in partial fulfillment of the requirements for  
the degree of Doctor of Philosophy

Coral Gables, Florida

December 2012

©2012  
Björn Lund  
All Rights Reserved

UNIVERSITY OF MIAMI

A dissertation submitted in partial fulfillment of  
the requirements for the degree of  
Doctor of Philosophy

DEVELOPMENT AND EVALUATION OF NEW ALGORITHMS FOR THE  
RETRIEVAL OF WIND AND INTERNAL WAVE PARAMETERS FROM  
SHIPBORNE MARINE RADAR DATA

Björn Lund

Approved:

---

Hans C. Gruber, Sc.D.  
Professor of Applied Marine Physics

---

M. Brian Blake, Ph.D.  
Dean of the Graduate School

---

Adrianus J. Reniers, Ph.D.  
Associate Professor of  
Applied Marine Physics

---

Roland Romeiser, Ph.D.  
Associate Professor of  
Applied Marine Physics

---

Jochen Horstmann, Ph.D.  
Scientist  
Centre for Maritime Research and  
Experimentation, La Spezia, Italy

---

Eric Terrill, Ph.D.  
Director, Coastal Observing  
Research and Development  
Center  
Scripps Institution of  
Oceanography, University of  
California, San Diego

LUND, BJÖRN

(Ph.D., Applied Marine Physics)

Development and Evaluation of New Algorithms  
for the Retrieval of Wind and Internal Wave Parameters  
from Shipborne Marine Radar Data

(December 2012)

Abstract of a dissertation at the University of Miami.

Dissertation supervised by Professor Hans C. Graber.

No. of pages in text. (214)

The goal of this work is to develop and evaluate techniques for the retrieval of wind and internal wave (IW) information from marine X-band radar data. While ocean wind measurements are crucial for the transfer of energy and momentum across the air-sea interface, IWs play an important role in tidal energy transport. Marine radars work by transmitting microwave energy from a rotating antenna that also measures the backscatter. The radar backscatter from the sea surface is controlled by the wind-generated small ripple waves through the Bragg-scattering mechanism. Surface winds are thus the dominant factor for generating the radar backscatter. The varying surface current fields associated with IWs interact with the ripples, generating rough convergent and smooth divergent zones. Radars are capable of imaging such IW-induced surface signatures as bands of enhanced and weakened backscatter.

The advantage of radar-based wind information is that it is obtained from a large area around the instrument. Marine radar wind data are therefore much less likely to be affected by platform-induced air flow distortions than in-situ measurements. Previous investigators have already demonstrated marine radar's suitability as a wind sensor [31, 30], however, these works have been limited to fixed-platform data. Here, the focus lies

on shipborne marine radar data. Such data present the challenge that the existing wind streak-based approach for retrieving wind directions cannot be directly applied. This is because the wind streak signal may become obscured by the horizontal ship motion, since wind streaks become visible only after averaging over a sequence of radar images. In addition, moving platforms face a greater variability of conditions, which may further complicate a radar-based wind retrieval.

Grazing incidence HH-polarized (horizontal transmit and receive) X-band radar data exhibit a single intensity peak in upwind direction. To retrieve the wind direction, this work proposes a least-squares fit technique that identifies the upwind peak in the range-averaged backscatter dependency on the antenna look direction. This technique requires no motion correction and is therefore well-suited for shipborne data. In addition, it functions well even if sections of the radar field of view are masked. An empirical model function is derived to retrieve the wind speed from the mean radar backscatter intensity. Data from the U.S. Office of Naval Research (ONR) Impact of Typhoons on the Ocean in the Pacific (ITOP) experiment are used for a comparison between radar-based wind estimates and anemometer measurements. The two data sets show good agreement.

In addition, this work proposes a technique that uses geolocated marine radar data to extract wind streak information through a localized Radon transform. To compare streak- and upwind peak-based wind direction retrieval techniques, fixed and moving platform marine radar data from the ONR-sponsored High Resolution Air-Sea Interaction (Hi-Res) experiment are used. Wind directions obtained using the upwind peak method show a better agreement with the reference data than those obtained from the wind streaks. The difference between fixed and moving platform for the wind streak approach

indicates that the image geolocation affects the wind retrieval negatively. Standard deviations as low as  $6.0^\circ$  and 0.42 m/s for the comparison between radar-based and reference wind data show that marine radars can yield highly reliable wind estimates.

Regarding IWs, a new fully automated tool to retrieve IW signatures from marine radar image sequences is developed and applied to data collected during ONR's Non-Linear Internal Wave Initiative / Shallow Water '06 experiment (NLIWI/SW06). Marine radars have the advantage over satellite systems that their high temporal resolution enables the study of the IW evolution. The proposed technique employs our knowledge about the wind dependency of the radar backscatter to correct for the image ramp, i.e. the return signal's dependency on range and antenna look direction. The ramp-corrected radar images are then geolocated and averaged, which greatly enhances the IW signal. By determining the IW group velocity and correcting for it before the radar images are averaged, the IW signal is further enhanced. Such pre-processing enables a reliable retrieval of IW surface signatures by clustering local peaks and troughs, and tracking those clusters through time.

This work also includes a detailed analysis of data collected during the tracking of a particularly energetic IW. The radar-derived time series of IW speed, direction, and soliton maps yield unique information about the IW's spatio-temporal evolution, including evidence of wave-wave interactions. In addition, it is demonstrated that marine radar data can be used to retrieve information about the interior ocean dynamics associated with the IW. The IW-induced backscatter modulation is correlated with the measured surface current gradients and IW amplitudes. Alternatively, results are shown where IW amplitudes were derived from the distances between positive and negative

radar backscatter peaks. This approach was first introduced by Xue et al. [132] and is based on an extended Korteweg-de-Vries (eKdV) equation. This approach has the advantage that it is much less dependent on the prevailing wind conditions.

To summarize, the marine radar backscatter dependency on wind is analyzed, and new wind retrieval techniques from shipborne radar data are proposed. The gained knowledge on the backscatter's wind dependency is then applied to marine radar data containing IW surface signatures. This work proposes a new methodology for retrieving these signatures and uses the resulting IW soliton maps to derive information about the IW-associated interior ocean dynamics.

## Acknowledgment

This work was made possible thanks to the financial support by the Center for Southeastern Tropical Advanced Remote Sensing (CSTARS) of the University of Miami and by the U.S. Office of Naval Research (ONR) under Grants N00014-05-1-0758, N00014-07-1-0650, N00014-08-1-0793, and N00014-09-1-0392.

Marine radar and anemometer data from the ONR High Resolution Air-Sea Interaction (Hi-Res) experiment were kindly made available by Eric Terrill, who also provided the marine radar scanner and antenna for the ONR Impact of Typhoons on the Ocean in the Pacific (ITOP) program. Jim Moum and Emily Shroyer kindly shared their in-situ data from ONR's Non-Linear Internal Wave Initiative / Shallow Water '06 experiment (NLIWI/SW06), and provided valuable information on internal waves (IWs) in the Mid-Atlantic Bight.

Chapters 3 and 4 on marine radar wind retrieval, as well as chapter 5 and appendix C on IWs have already been published or submitted for publication. I would like to acknowledge my co-authors Hans Graber, Roland Romeiser, Jingshuang Xue, Jochen Horstmann, and Eric Terrill for their helpful contributions to these papers. For chapter 6, Jingshuang Xue kindly provided radar-based IW amplitude estimates using a higher-order Korteweg-de-Vries equation.

I would like to thank Jochen Horstmann, Ad Reniers, Roland Romeiser, and Eric Terrill for their comments and suggestions during my dissertation and for being part of my dissertation committee. Especially, I would like to thank my advisor Hans Graber for his advice, guidance, and support throughout the years I have worked towards this thesis.

During the summer of 2011, I spent three months at the NATO Undersea Research Centre (today Centre for Maritime Research and Experimentation). Many thanks to Jochen Horstmann and Hans Graber for making this possible. The scientific exchange with Jochen

Horstmann's group, in particular Ruben Carrasco and Cristina Lido, made this a rewarding experience.

I would also like to acknowledge Sophia Brumer, Tripp Collins, William Drennan, Zhixuan Feng, Katrin Hessner, Wolfgang Hüneburg, Frances May, Henry Potter, Rafael Ramos, Mike Rebozo, Konstanze Reichert, Astrid Werkmeister, and Neil Williams for their help, guidance, and friendship. I am grateful to the AMP division's faculty, staff, and students for creating an excellent work environment. Finally, I wish to thank my friends, especially Oana Ioncel, who made living in Miami a great experience, and my family for their continuous support.

# Contents

<b>List of Figures</b>	<b>ix</b>
<b>1 Introduction</b>	<b>1</b>
1.1 Background and Motivation . . . . .	1
1.2 Research Objectives and Overview . . . . .	4
<b>2 Marine X-Band Radar Background</b>	<b>8</b>
2.1 History of Marine Radar as Oceanographic Instrument . . . . .	8
2.2 Marine Radar Technical Specifications . . . . .	11
2.3 Imaging Mechanism . . . . .	14
2.4 Discussion and Recent Developments . . . . .	18
<b>3 Wind Retrieval from Shipborne Marine Radar Data</b>	<b>23</b>
3.1 Introductory Remarks . . . . .	24
3.2 Data Overview . . . . .	27
3.3 Rain Recognition . . . . .	29
3.4 Wind Retrieval . . . . .	31
3.4.1 Measurement Principle . . . . .	33
3.4.2 Comparison Between Reference Sensors . . . . .	34
3.4.3 Derivation of the Empirical Model Functions . . . . .	38
3.4.3.1 Shadowing of the Radar Field of View . . . . .	39

3.4.3.2	Radar Backscatter Dependency on Range and Antenna Look Direction . . . . .	39
3.4.3.3	Wind Direction . . . . .	41
3.4.3.4	Wind Speed . . . . .	43
3.4.4	Test of the Empirical Model Functions . . . . .	48
3.4.4.1	Wind Direction . . . . .	48
3.4.4.2	Wind Speed . . . . .	50
3.4.5	Sensitivity Study . . . . .	50
3.5	Discussion . . . . .	53
<b>4</b>	<b>Ocean Surface Wind Retrieval from Stationary and Moving Platform Marine Radar Data</b>	<b>56</b>
4.1	Introductory Remarks . . . . .	57
4.2	Data Overview . . . . .	58
4.3	Wind Direction Retrieval . . . . .	60
4.3.1	Wind Streaks . . . . .	60
4.3.2	Upwind Peak . . . . .	63
4.4	Wind Speed Retrieval . . . . .	64
4.5	Discussion . . . . .	66
<b>5</b>	<b>Analysis of Internal Wave Signatures in Marine Radar Data</b>	<b>68</b>
5.1	Introductory Remarks . . . . .	69
5.2	Data Overview . . . . .	71
5.3	Methodology . . . . .	73
5.3.1	Data Pre-processing . . . . .	73
5.3.1.1	Azimuthal Position of Radar Pulses . . . . .	73
5.3.1.2	Radar Interference Spikes . . . . .	77
5.3.1.3	Radar Backscatter Ramp Correction and Normalization .	78

5.3.1.4	Georeferencing . . . . .	84
5.3.1.5	Bright Target Detection . . . . .	85
5.3.2	Retrieval of IW Packet Parameters . . . . .	88
5.3.2.1	Radon Transform . . . . .	88
5.3.2.2	IW Packet Direction . . . . .	89
5.3.2.3	IW Packet Speed . . . . .	94
5.3.3	IW-enhanced Radar Images . . . . .	95
5.3.3.1	IW Motion Correction . . . . .	100
5.3.3.2	Gaussian Smoothing . . . . .	100
5.3.4	IW Signature Retrieval . . . . .	102
5.3.4.1	Clusterization of Radar Return Peaks . . . . .	102
5.3.4.2	Cluster Filtering . . . . .	103
5.3.4.3	Cluster Sequencing . . . . .	105
5.4	Results . . . . .	108
5.5	Discussion . . . . .	111
<b>6</b>	<b>Study of Internal Wave Evolution by Marine Radar</b>	<b>115</b>
6.1	Introductory Remarks . . . . .	116
6.2	Marine Radar Data Availability and Environmental Conditions . . . . .	117
6.3	Marine Radar Imaging Mechanism of IWs . . . . .	119
6.3.1	Current Measurements as a Tool to Determine Dominant IW Imaging Mechanism . . . . .	120
6.3.2	ASIS Response to IW as Observed by Marine Radar from <i>R/V Knorr</i> 123	
6.4	IW Propagation Direction . . . . .	126
6.5	IW Propagation Speed . . . . .	129
6.6	Correction for Background Current . . . . .	138
6.7	Evolution of IW Surface Signatures . . . . .	142
6.8	IW Characteristics from Radar Backscatter Intensity . . . . .	144

6.9	IW Amplitudes from Peak-to-Peak Distances via Extended Korteweg-de-Vries Equation . . . . .	156
6.10	Discussion . . . . .	160
<b>7</b>	<b>Conclusions and Outlook</b>	<b>163</b>
7.1	Summary of Conclusions . . . . .	163
7.2	Future Work . . . . .	167
<b>Bibliography</b>		<b>174</b>
<b>A</b>	<b>Marine Radar Backscatter Ramp Definition</b>	<b>188</b>
<b>B</b>	<b>SW '06 WaMoS Data Correction</b>	<b>192</b>
B.1	Introductory Remarks . . . . .	192
B.2	Image Acquisition Time . . . . .	192
B.3	Bearing Control . . . . .	194
B.4	Ship Heading and Location . . . . .	198
B.5	Pre- vs Post-correction . . . . .	201
B.6	WaMoS Radar Image Acquisition from <i>Oceanus</i> : An Overview . . . . .	204
<b>C</b>	<b>Retrieval of Internal Wave Signatures from Marine Radar Data</b>	<b>206</b>
C.1	Introductory Remarks . . . . .	206
C.2	Data Overview . . . . .	208
C.3	Methodology . . . . .	209
C.4	Discussion . . . . .	212

# List of Figures

2.1	WaMoS hardware components. . . . .	10
2.2	Illustration of radar antenna horizontal and vertical beam width (a, b) and WaMoS resolution cell size (c). . . . .	15
3.1	Pictures of <i>R/V Roger Revelle</i> in Kaohsiung harbor, taken on June 16, 2010, and of the ship's main mast with the X-band radar antennas for wind retrieval (bottom) and navigation (top) [photo credit: Wolfgang Hüneburg, OceanWaveS GmbH]. . . . .	27
3.2	Map of the track of <i>R/V Roger Revelle</i> during the storms from August 6, 00:00 UTC to August 9, 23:59 UTC and from September 12, 15:53 UTC to September 17, 15:56 UTC, 2010. The corresponding significant wave height estimates by WaMoS are color coded. . . . .	29
3.3	Radar images collected in absence of rain on August 8, 2010, 06:40 UTC (top left) and during rain on August 8, 2010, 06:50 UTC (top right). Histograms of the radar backscatter intensities are shown below. The numbers with arrows indicate the lengths of the first bars, including pixels with zero intensity, which exceed the range of the y-axis. . . . .	30

3.4	Time series showing percentage of image pixels with zero backscatter intensity for radar images collected from August 6, 00:00 UTC to August 9, 23:59 UTC (top) and September 12, 15:53 UTC to September 17, 15:56 UTC, 2010 (bottom). . . . .	32
3.5	Time series of wind speed and direction measurements from ship anemometers 1 and 2 from August 6, 00:00 UTC to August 9, 23:59 UTC and September 12, 15:53 UTC to September 17, 15:56 UTC, 2010. . . . .	35
3.6	Scatter plots and statistical parameters of wind speed (top) and wind direction (bottom) measurements by ship anemometers 1 and 2 during the August and September storms. . . . .	37
3.7	Standard deviation (marked by diamonds) and bias (crosses) for wind speed (red curves) and direction (blue curves) measurements acquired by the ship anemometers as a function of the angle between the ship's heading and the wind direction measured by Anemometer-1. A histogram showing the number of data points per $10^\circ$ bin is plotted in the background. . . . .	38
3.8	Image of the average radar backscatter intensity measured from 03:00 to 03:30 UTC on August 09, 2010, with the ship heading upwind. The image was composed out of 1270 individual radar images. The slices of the image where the radar field of view is obstructed are framed in red. . . . .	40
3.9	Radar backscatter intensity image collected on August 9, 2010, 18:23:41 UTC. . . . .	41
3.10	Average radar backscatter intensity as a function of range (top) and antenna look direction (bottom) for image collected on August 9, 2010, 18:23:41 UTC. The backscatter dependency on range does not include the shadowed antenna look directions that are shown in gray for the backscatter dependency on antenna look direction. The corresponding best-fit curves are shown in blue. . . . .	42

3.11 Time series of wind direction estimates obtained from the upwind peak in the radar data (red) and measurements made by Anemometer-1 (blue) during the storm from August 6, 00:00 UTC to August 9, 23:59 UTC, 2010. Radar measurements made during rain and at times when the wind data from the two ship anemometers strongly disagreed, i.e. discarded data points, are shown in gray. . . . .	43
3.12 Scatter plot and statistical parameters of wind direction measurements acquired by Anemometer-1 and estimates derived from the upwind peak in the radar data for the August storm. Again, discarded data points are shown in gray. . . . .	44
3.13 Scatter plot showing the wind speed from Anemometer-1, corresponding radar backscatter intensity, and the best-fit curve based on a third-degree polynomial function for data acquired during the August storm. Discarded data points are shown in gray. . . . .	46
3.14 Time series of wind speed obtained from the radar data through the proposed model function (red) and Anemometer-1 (blue) during the storm from August 6, 00:00 UTC to August 9, 23:59 UTC, 2010. Discarded radar data points are shown in gray. . . . .	47
3.15 Scatter plot and statistical parameters of wind speed measurements acquired by Anemometer-1 and estimates obtained from the radar backscatter intensities for the August storm. Discarded data points are shown in gray. . . . .	47
3.16 Time series of wind direction estimates obtained from the upwind peak in the radar data (red) and measurements made by Anemometer-1 (blue) during the storm from September 12, 15:53 UTC to September 17, 15:56 UTC, 2010. Discarded radar data points are shown in gray. . . . .	49

3.17 Scatter plot and statistical parameters of wind direction measurements acquired by Anemometer-1 and estimates derived from the upwind peak in the radar data for the September storm. Discarded data points are shown in gray. . . . .	49
3.18 Time series of wind speed obtained from the radar data through the proposed model function (red) and Anemometer-1 (blue) during the storm from September 12, 15:53 UTC to September 17, 15:56 UTC, 2010. Discarded radar data points are shown in gray. . . . .	51
3.19 Scatter plot and statistical parameters of wind speed measurements acquired by Anemometer-1 and estimates obtained from the radar backscatter intensities for the September storm. Discarded data points are shown in gray. . . . .	51
3.20 Standard deviation (marked by diamonds) and bias (crosses) for wind speed (red curves) and direction (blue curves) measurements acquired by Anemometer-1 and estimates from the radar data as a function of the wind speed. A histogram showing the number of data points per 1 m/s bin is plotted in the background. . . . .	52
3.21 Standard deviation (marked by diamonds) and bias (crosses) for wind speed (red curves) and direction (blue curves) measurements acquired by Anemometer-1 and estimates from the radar data as a function of the angle between the ship's heading and the wind direction. A histogram showing the number of data points per 10° bin is plotted in the background. . . . .	53
4.1 Map of Hi-Res experiment (a) and pictures of <i>Flip</i> (b) and <i>Sproul</i> (c). Photo sources: <a href="http://www.mpl.ucsd.edu/resources/flip.intro.html">http://www.mpl.ucsd.edu/resources/flip.intro.html</a> and <a href="http://shipsked.ucsd.edu/Ships/Robert_Gordon_Sproul/photos.php">http://shipsked.ucsd.edu/Ships/Robert_Gordon_Sproul/photos.php</a> . . . . .	59
4.2 Average of 32 radar images collected from <i>Flip</i> starting June 11, 2006, 00:00:28 UTC. . . . .	61

4.3	Example of average backscatter intensity for a given transform box in Cartesian (a) and Radon (b) space. The standard deviation as a function of Radon projection angle is given on the right (c). . . . .	62
4.4	Radar backscatter intensity as a function of antenna look direction (relative to north) for <i>Flip</i> image collected on June 11, 2006, 00:00 UTC. The corresponding best-fit curve is shown in blue. . . . .	64
4.5	Scatter plot of radar backscatter intensity and reference wind speed for <i>Flip</i> . The empirical model function is shown in red. . . . .	65
4.6	Time series of wind measurements from reference sensors (blue) and radars (wind speed and upwind peak direction in red, wind streak direction in magenta) for <i>Sprout</i> and <i>Flip</i> . . . . .	67
5.1	Overview map of NLIWI study area with mooring locations marked by crosses (left). Map detailing local bathymetry and <i>R/V Oceanus</i> track as it was following an IW packet on August 14, 2006, from 04:00 to 23:00 UTC. The ship track is shown in red, with each full hour marked by a black dot. Mooring locations are marked by white crosses (right). . . . .	72
5.2	Average of ship-heading-oriented radar backscatter images collected from <i>Oceanus</i> on August 18, 2006, from 13:40 to 13:50 UTC, with masked area framed in red and saturation area marked by white circle (top). The corresponding mean backscatter intensities as functions of antenna look direction (left) and range (right) are shown at the bottom with masked or saturated data, respectively, marked in gray. . . . .	74
5.3	Marine radar data pre-processing scheme. . . . .	75
5.4	Mean number of radar pulses per degree clockwise from north obtained from <i>Oceanus</i> over a 1-hour period starting August 15, 2006, 12:00 UTC (left). Corresponding pulse position error if a constant antenna repetition time is assumed (right). Vertical bars mark the up- and downwind directions.	76

5.5	Histogram of ship heading changes within antenna repetition time (2.5 s) for August 14, 2006, from 04:00 to 23:00 UTC. . . . .	78
5.6	Zoom into raw polar marine radar image with radar interference spikes (left) and after correction (right). The data were collected on August 14, 2006, 00:01 UTC. . . . .	79
5.7	Mean radar backscatter intensity as function of range computed from 1-min-long sequence of marine radar images collected on August 14, 2006, 06:12 UTC (a). Corresponding mean radar backscatter intensity as function of antenna look direction (clockwise from north) (b). Zoom into data of first image (c). Amplitude of directional radar backscatter intensity variations computed for a range-shrunked version of same 1-min data set (d). In all four plots, the radar measurements are shown in red and the least-squares-fit curves in blue. Measurements from masked antenna look directions are displayed in gray. . . . .	81
5.8	Marine radar image in polar coordinates from August 14, 2006, 06:12 UTC (a). Corresponding ramp image obtained from empirical model function (b). Resulting ramp-subtracted image (c). . . . .	82
5.9	Standard deviation as function of range for 1-min sequence of marine radar images from August 14, 2006, 06:12 UTC (a). Ramp-subtracted and normalized image from same sequence (b). . . . .	83
5.10	Image of standard deviation for 1-min sequence of marine radar images from August 14, 2006, 06:12 UTC. . . . .	84

5.11 Normalized and georeferenced marine radar data averaged over a 1-min interval in Cartesian coordinates (left). The image origin corresponds to the ship position on August 14, 2006, 06:12:02 UTC. The sequence's last image was acquired at 06:12:58 UTC. Image locations at which radar data are available from less than 50% of the total number of radar images have been treated as if no data are available. The image on the right illustrates the data availability. For the white area, data from the full sequence (23 images) are available. . . . .	86
5.12 1-min average of marine radar data collected starting August 14, 2006, 06:00 UTC with (top left) and without backscatter signal from moorings (top right). Zoom into images from top (bottom left and right, respectively) and corresponding image to illustrate mooring detection (bottom center). In the latter, pixel clusters with normalized backscatter intensities greater or equal 3 are marked in red. Neighboring pixels with intensities below the threshold but still well above the background are assumed to belong to the bright targets and marked in black. Finally, the green frames around each individual cluster mark pixels that are considered as replacement values. . .	87
5.13 Flow chart detailing retrieval of IW packet speed and direction from pre-processed marine radar data. . . . .	88
5.14 Pre-processed marine radar data averaged over a 1-min interval starting August 14, 2006, 06:00 UTC (a). Overlapping Radon transform boxes (b). .	90
5.15 Radar backscatter intensity within select Radon transform box in Cartesian coordinates (a). Corresponding image in Radon space (b). Standard deviation of Radon transform intensities as function of projection direction. The dominant direction, associated with the maximum standard deviation, is marked by a dashed line (c). . . . .	92

5.16 Histogram of dominant directions from all 63 Radon transform boxes. The dashed line marks the first rough estimate for the IW direction. . . . .	93
5.17 Diagram indicating IW activity within all Radon transform boxes. Green and blue boxes were determined to contain IW signatures, i.e. they have dominant Radon directions that are within $10^\circ$ of our first rough IW direction estimate. For the green boxes, a minimum of 75% of the neighboring boxes were also determined to contain IW signatures. The blue boxes do not themselves satisfy the 75% criterion but have neighboring boxes that do satisfy it. Red boxes show no IW signal. . . . .	93
5.18 Time series of the IW direction computed as the median of the dominant directions associated with the Radon transform boxes that were determined to contain an IW signal. The time series starts August 14, 06:00 UTC. . . .	94
5.19 1-min average of pre-processed marine radar data starting August 14, 2006, 06:00 UTC. The image has been rotated so that the IW propagates along the x-axis (top). Image projection onto IW propagation axis (bottom). . . .	96
5.20 Hovmöller diagrams of image projections onto IW propagation axis before (top) and after correcting for the ship motion (bottom). . . . .	97
5.21 Time series of IW packet displacement (top) and corresponding speed (bottom). . . . .	98
5.22 Flow chart outlining steps leading towards IW-enhanced radar images. . . .	99
5.23 Raw marine radar image from August 14, 2006, 06:00:01 UTC (left) and IW-enhanced image obtained from 2 min of data starting with the same image (right). Both images are oriented such that the IW travels from bottom to top along the y-axis. . . . .	101
5.24 IW-enhanced radar image after convolution with a Gaussian smoothing kernel (top). The corresponding kernel is shown at the bottom. . . . .	101
5.25 Flow chart outlining our IW signature retrieval method. . . . .	102

5.26 Clusters of radar backscatter intensity peaks identified within the IW-enhanced marine radar image from August 14, 2006, 06:00 UTC. Clusters with less than 10 elements have been discarded (a). Clusters can be further thresholded based on a more stringent length criterion (b) or on their mean backscatter intensity (c). . . . .	104
5.27 Clusters found within the three IW-enhanced images from August 14, 2006, 06:00 to 06:02 UTC. Red clusters are from the first, green from the second, and blue from the last image (a). The results after filtering, where we used our knowledge of the IW packet speed and direction, are shown on the right (b). . . . .	106
5.28 The leading three IW solitons during 1-hour period starting August 14, 2006, 06:00 UTC, before (left) and after (right) interpolation. The color code gives the time, starting in black (06:00 UTC) and ending in red (06:59 UTC). . . . .	107
5.29 Sequence of IW soliton maps retrieved from marine radar data in 7 min intervals from Aug 14, 2006, 06:00 UTC to 06:56 UTC. The solitons are color-coded by order of appearance with the leading soliton in black and the last (15 <sup>th</sup> ) in red. . . . .	108
5.30 Time series of mean soliton displacement starting Aug 14, 2006, 06:00 UTC. The solitons are color-coded by order of appearance with the leading soliton in black and the last (15 <sup>th</sup> ) in red. . . . .	109
5.31 Time series of leading soliton's speed from Aug 14, 2006, 06:00 UTC. . .	110
5.32 Mean soliton speed for 1-hour period from August 14, 2006, 06:00 UTC. .	111
5.33 Mean soliton wavelength for 1-hour period from August 14, 2006, 06:00 UTC. . . . .	112
5.34 Mean soliton normalized radar return for 1-hour period from August 14, 2006, 06:00 UTC. . . . .	112

6.1	Map of ship track from August 17, 19:00 UTC to August 18, 07:00 UTC. The ship positions are shown in red, every full hour is marked by a black dot. Mooring positions are marked by white crosses. The color scale rep- resents water depth. . . . .	118
6.2	Time series of ship over ground speed and heading from August 17, 19:00 UTC to August 18, 07:00 UTC. . . . .	119
6.3	Time series of wind speed and direction measured from <i>Oceanus</i> during our 11.5 hour period starting August 17, 19:00 UTC. . . . .	120
6.4	Scheme of IW radar imaging mechanism. Source: [67]. . . . .	121
6.5	Current profiles along IW direction (a) and vertical current profile (b) as measured by ship-based ADCP from <i>R/V Oceanus</i> on August 17, 2006, around 22:00 UTC. . . . .	122
6.6	Normalized radar backscatter intensity (red) and corresponding surface cur- rent velocity gradient along IW direction (blue) as recorded from <i>R/V Oceanus</i> on August 17, 2006, around 22:00 UTC. The IW propagates from left to right. . . . .	123
6.7	Marine radar image from <i>R/V Knorr</i> collected on August 14, 2006, 04:14:00 UTC. The zoom area covering the ASIS and tether buoys is marked by a red frame (a). Zoom into area with ASIS and tether buoy. The data shown are a 1 min average of georeferenced data starting with the image at the top (b). . . . .	124
6.8	Deviation of ASIS buoy from initial position in 1-min intervals for period from August 14, 2006, 04:14 through 05:59 UTC. The best-fit line is shown in blue. . . . .	125
6.9	Component of buoy motion along IW propagation direction (a) and corre- sponding speed (b). The times at which the buoy was on top of a soliton are marked by red bars. . . . .	127

6.10 Marine radar image from August 18, 04:00 UTC (a) and 1-min average of pre-processed images starting with the one on top (b). . . . .	128
6.11 Time series of IW Rosey's propagation direction starting August 17, 19:05 UTC. Raw estimates are shown in black. The red curve shows the 60 min running average. . . . .	129
6.12 Projection of 1-min averaged radar image onto the IW propagation axis. The radar data were recorded on August 18, 04:00 UTC. The position of the leading soliton is marked by a dashed line. . . . .	130
6.13 Hovmöller diagram of pre-processed and 1-min averaged radar images projected onto the IW propagation axis. The individual projections were shifted to account for the ship motion along the IW propagation direction. The diagram's first projection corresponds to August 17, 19:05 UTC. . . . .	131
6.14 Time series of IW packet speed obtained using cross-correlation techniques. The red curve shows the 60 min running average. The time series starts August 17, 19:05 UTC. . . . .	132
6.15 Hovmöller diagram of image projections. The individual projections were arranged to be ship-centered. The black dashed line marks the image origin (i.e. ship position). The position of the leading soliton is shown for each individual projection, with times during which the leading soliton had traveled past the ship marked in blue and times when the ship was ahead of the packet marked in red. The diagram's first projection corresponds to August 17, 19:05 UTC. . . . .	133
6.16 Same as Fig. 6.14, but times during which the ship was ahead of the IW packet are marked in red, blue indicates times when the leading soliton was more advanced than the ship. The time series starts August 17, 19:05 UTC. . . . .	134

6.17 Time series of mean radar backscatter intensity along the leading soliton's crest (as extracted from the image projections shown in Fig. 6.15). Red data points mark times during which the ship was ahead of the IW packet, blue indicates that the leading soliton was more advanced than the ship. The time series starts August 17, 19:05 UTC. . . . .	135
6.18 Time series of leading soliton speed obtained from the mean of estimates that were made independently for four different data categories (based on whether antenna look direction and ship heading were up- or downwave). The red curve shows the 60 min running average. The time series starts August 17, 19:05 UTC. . . . .	137
6.19 Hovmöller diagram of leading soliton speed estimates obtained from our four data categories, starting August 17, 19:05 UTC. For data points where more than one estimate was available the diagram shows the mean value. . .	138
6.20 Hovmöller diagram of radar images projections centered around the IW packet's leading soliton. The projections were smoothed with a 60 min window. The diagram's first projection corresponds to August 17, 19:05 UTC. . . . .	139
6.21 1-min average of pre-processed marine radar images from August 18, 01:20:01 through 01:20:55 UTC. . . . .	140
6.22 Time series of background current speed (top) and direction (middle) obtained from shipborne ADCP at times when the <i>Oceanus</i> was in front of the IW group. The corresponding water depth, also obtained from the ADCP record, is shown at the bottom. The time series starts August 17, 19:05 UTC.	141
6.23 Time series of IW direction and speed before (red) and after (blue) correction for background current. The time series starts August 17, 19:05 UTC. . . . .	142

6.24 Evolution of surface signatures of IW Rosey with peaks marked in red and troughs in blue. . . . .	145
6.25 Mean leading soliton backscatter intensity for different offsets from the image origin. A negative offset indicates that the ship is ahead of the leading soliton. . . . .	149
6.26 Time series of the leading soliton's backscatter intensity obtained from the mean of estimates that were made independently for four different data categories (based on whether antenna look direction and ship heading were up- or downwave). The red curve shows the 60 min running average. The time series starts August 17, 19:05 UTC. . . . .	150
6.27 Time series of radar backscatter intensity (red) and surface velocity gradient (blue) for IW Rosey's leading soliton, starting August 17, 19:05 UTC. .	152
6.28 Time series of radar backscatter intensity (red) and IW amplitude (blue) for Rosey's leading soliton, starting August 17, 19:05 UTC. . . . .	152
6.29 Scatter plots of surface velocity convergence (a) and divergence (b) versus corresponding radar backscatter intensity peaks and troughs. Results are shown with corresponding best-fit lines for IW Rosey's leading three solitons. (The different dot sizes ensure visibility of all data.) . . . . .	154
6.30 Scatter plot of IW amplitude and radar backscatter intensity for leading three solitons of IW Rosey with corresponding best-fit lines. . . . .	155
6.31 Radar backscatter peaks (red) and troughs (blue) for August 17, 22:06 UTC. The measurement location is marked by a black dashed line (a). Corresponding diagram illustrating the extended KdV equation, linking IW amplitude and p-p-distance for a water depth of 83.5 m and a mixed layer depth of 16 m (b). . . . .	157

6.32 Transect through an undisturbed section of IW Rosey. Radar backscatter peaks and troughs are shown by red and blue bars, respectively, and p-p-distances for each soliton are printed. The data were collected during a 4-min period starting August 17, 19:59 UTC. . . . .	158
6.33 Time series of p-p-distances and water depth (dashed line) for leading three solitons starting August 17, 19:05 UTC. . . . .	159
6.34 Scatter plot of measured and radar-derived amplitudes for leading three solitons for IW Rosey. . . . .	159
B.1 File creation time in black and estimated image acquisition time marked by red dashed line (a). Creation time difference for consecutive files (b). Resulting temporal error if file creation time is mistaken for image acquisition time (c). . . . .	195
B.2 Pulse migration between consecutive POL files. . . . .	199
B.3 Gyro compass measurements as recorded by WaMoS in red and from an external source in black (a). Gyro compass error without correction (b). . .	200
B.4 GPS measurements as recorded by WaMoS in red and from an external source in black (a). Ship location error without correction (b). . . . .	202
B.5 Average of 2-min worth of geolocated and IW-motion corrected radar images before (a) and after correction of image acquisition time, ship heading, and location (b). The data were acquired from August 17, 22:34:49 to 22:36:47 UTC. . . . .	203
B.6 Overview of WaMoS <i>Oceanus</i> data availability. . . . .	204
B.7 Histogram detailing number of WaMoS <i>Oceanus</i> POL files available for each full hour during 1-week period starting August 13. The dashed line indicates the number of POL files expected for a 2.55 s antenna rotation time.	205

C.1	Example of a single <i>Oceanus</i> radar image from August 17, 2006, 22:02:02 UTC (a) and the IW-enhanced version compiled from 86 consecutive images starting at the same time (b). . . . .	210
C.2	Transect with IW peaks and troughs marked by dashed lines (a) and corresponding image with the transect position marked by a yellow dashed line and the detected IW signatures marked by white and red solid lines (b). . .	213
C.3	Maps of IW signatures with peaks in black and troughs in red retrieved from 10-min worth of marine radar data starting August 17, 2006, 22:00 UTC. . . . .	213

# Chapter 1

## Introduction

### 1.1 Background and Motivation

Marine X-band radars work by transmitting microwave pulses to the sea surface and measuring the backscattered signal, known as sea clutter, at the instrument. The dominant imaging mechanism is Bragg scattering, i.e. the transmitted microwaves interact with surface waves that have roughly the same length scale [124]. The marine X-band radar return is therefore controlled by the capillary and surface gravity wave regime, or the cm-scale sea surface roughness.

The marine X-band radar return from the sea surface has long been regarded as a source of noise for navigation. This has changed when a method to determine directional wave spectra from marine radar data was first introduced [136]. Marine radars can be used as wave sensors because the orbital currents and tilt associated with surface gravity waves modulate the backscatter through wave-current interactions and by modifying the local incidence angle, resulting in radar images with bright and dark bands (e.g. [142]). In addition, shadowing due to the blocking of the radar's line of sight by the highest waves, may play an important role for grazing incidence marine radars and contribute to the wave patterns that can be observed in the images [129]. Today, marine radar data are widely used for surface wave monitoring and commercial systems are available for this purpose.

While marine radar-based wave measurements are now well established, the use of marine radars to gain knowledge on other environmental parameters is far less developed. In this work, the focus lies on the retrieval of wind and internal wave (IW) information from marine radar data. Since marine radars image the sea surface roughness, the radar backscatter strength has a strong dependency on the prevailing wind conditions [24, 66]. The imaging of IWs has some similarity with that of surface gravity waves: IWs are associated with zones of converging and diverging surface currents, which modulate the sea surface roughness, resulting in bright and dark bands within our marine radars images [2]. However, the IW radar signatures can easily be told apart from the surface gravity wave signal because they generally have larger scales and propagate much slower.

Just like for navigation, the surface wave signal in the marine radar data represents a source of noise for the retrieval of both wind and IW information. However, thanks to marine radar's short antenna revolution times, typically ranging from 1.5 to 2.5 s, this issue can easily be overcome by temporal averaging (or, for wind retrieval, by pulse averaging). In fact, the high temporal resolution represents a big advantage for marine radar over satellite data. While a typical satellite-borne synthetic aperture radar (SAR) has revisit time intervals of the order of days, marine radars are capable of monitoring oceanic and atmospheric changes that occur over the course of seconds. This advantage largely compensates for marine radar's relatively limited spatial coverage. In comparison with in-situ data, marine radars have the advantage that they offer spatial coverage, providing information on phenomena that are very difficult to study with single “point” measurements, e.g. IW interactions.

Wind plays an important role for gas, mass, momentum, and energy transfer between the air-sea interface. While an improved understanding of surface wind processes serves a scientific purpose, accurate wind information is also important for navigation and to ensure safety during offshore operations. Radar-based wind estimates have the advantage over traditional sensors that they are not at all, or to a much lesser extent, affected by air flow

distortion due to the instrument’s platform. For example, Moat et al. [75] estimate that shipborne anemometer measurements, even at well-exposed locations, may have errors of up to 10% due to air flow distortion caused by the ship’s hull and superstructure. Marine radar wind sensors have the additional advantage over in-situ measurements that they are independent of the sensor height and motion. Furthermore, they may help improve our understanding of short-lived and spatially-varying wind events, such as gusts, or of air-sea interaction processes, such as Langmuir circulation.

The importance of IWs in the ocean became well-established only when satellite data became widely available (e.g. [38]). Today it is known that IWs are ubiquitous in both coastal and deep oceans [49]. They represent an important mechanism for tidal energy transport and induce intensive vertical mixing, which in extreme cases may result in the resuspension of bottom sediments [77]. They also modify underwater acoustics, produce strong shear currents that may pose threats to navigation as well as offshore constructions, and affect biological processes through the distribution of nutrients, larvae, and plankton [21, 48]. When deployed on a ship, marine radar’s high temporal resolution has great potential for IW studies, in that it allows for the tracking of IWs. Marine radars thus offer the unique capability of studying the spatio-temporal evolution of IWs.

While both marine radar-based wind and IW studies must correct for the impact of surface waves on the radar return, some IW analyses require in addition a correction for the wind signal. The radar backscatter strength is mostly controlled by the wind, and has a strong dependency on range and antenna look direction. This dependency needs to be corrected for two reasons: (i) To enhance the IW signal, that would otherwise risk being obscured; (ii) to determine the IW-induced enhancement of the backscatter, which yields information on the dynamics of the interior ocean. In this regard, the chapters that discuss the retrieval of IW information from marine radar data build directly on findings from our wind retrieval.

This work focuses on marine radar data that were collected during three ONR-sponsored research experiments. Most of these data were acquired from moving platforms, which creates some challenges, as will be discussed in section 1.2. The wind retrieval methods developed here are applied to data that were collected from *R/V Roger Revelle* during ITOP in the western Pacific Ocean in 2010. Additional wind-related work is done with data from the 2010 Hi-Res experiment off the southern coast of California. Within Hi-Res, marine radar data were collected from *R/V Sproul* and *R/P Flip*, the only quasi-stationary platform used within this thesis. Finally, the IW-related work presented here, draws from data that were collected during NLIWI/SW06 off the New Jersey coast in 2006. A more detailed overview of the available data is given in the individual chapters.

## 1.2 Research Objectives and Overview

The main purpose of this dissertation is to develop and evaluate new algorithms for the retrieval of wind and IW parameters from shipborne marine radar data. In the following, the research objectives of this work are listed in detail and an overview of the subsequent chapters and appendices is given.

Regarding wind, the main objective of this work is to develop a methodology to obtain wind speed and direction from moving platform marine radar data. The wind information within marine radar data can be determined through different means: Dankert and Horstmann [30] proposed a method that is based on so-called wind streaks, that are aligned with the wind and can thus be used to infer its direction (with a  $180^\circ$  ambiguity). However, this approach cannot be directly applied to data that were acquired from a ship. This is because wind streaks become visible only after averaging a sequence of radar images, and therefore risk getting obscured due to the horizontal platform motion. Alternatively, the upwind peak in the radar backscatter strength, which is unique to grazing incidence radar measurements with horizontal polarization [47, 121], can be used to determine the wind

direction. This approach faces the challenge that in most cases the radar field of view is obstructed in some directions, e.g. due to the ship's main mast or smokestack. In this work, a new best-fit approach is developed that helps overcome this issue, and proves equally useful for estimating the wind speed. This new method allows for real-time radar-based wind monitoring from a ship.

A secondary objective is to evaluate the different existing wind retrieval methods and determine the most reliable one. With this goal in mind, a technique to geolocate shipborne marine radar data is developed, thus enabling the visualization and hence exploitation of wind streaks within such data. The different methods are then applied to both moving and fixed platform data. The results from this study can be used to determine the best technique of deriving winds from marine radar data.

Regarding IWs, the main objective is the development of techniques to automatically retrieve IW-induced surface signatures from marine radar data. Only few IW studies have been carried through that have their main focus on marine radar data (e.g. [128, 23, 96]). Until today, no method to retrieve IW surface signatures has been suggested. The approach proposed here begins by determining the IW group speed and direction, which is accomplished using a combination of localized Radon transform and cross-correlation techniques. It is demonstrated that the temporal averaging of geolocated marine radar images significantly enhances the IW signal. By correcting for the IW group velocity, the averaging period can be extended, which further enhances the IW signal. To retrieve IW soliton maps from the IW-enhanced images, a search for local backscatter peaks and troughs is carried through. The high temporal resolution of marine radar data combined with our knowledge of the IW group velocity can then be used to separate signal from noise. The resulting IW soliton maps provide a unique view of the spatio-temporal IW evolution. In addition, the signature retrieval technique proposed here may prove valuable from an operational perspective. For example, it could be used to identify areas of interest and improve the tracking of IWs during field studies.

As a secondary objective, marine radar data from the 11.5 hour-long tracking of a particularly energetic IW event are analyzed, to illustrate marine radar's potential for IW studies in general, and the promise of the newly developed tools in particular. As part of this study, the evolution of the IW velocity is studied, and a time series of IW soliton maps is obtained. For the shallow water conditions encountered within NLIWI/SW06, Xue et al. [132] employed both SAR and marine radar data to demonstrate that the distances between neighboring IW-associated positive and negative backscatter peaks (p-p-distances) can be used to estimate the IW amplitude via an extended Korteweg-de-Vries (eKdV) equation. Following the methodology introduced by Xue et al., the radar-derived IW soliton maps are used to estimate the amplitudes of the leading three solitons, and the results are compared with in-situ measurements. In addition, the IW-induced enhancement (and weakening) of the radar backscatter strength is correlated with the corresponding measured surface velocity convergence and IW amplitude.

This work is organized as follows: Chapter 2 relates the history of marine X-band radar as an oceanographic instrument from first observations of sea clutter to the current state-of-the-art. In addition, marine radar technical specifications are provided and the imaging mechanism is discussed. In chapter 3, a new technique for the retrieval of wind information from moving platform marine radar data is developed and evaluated. This work has been published in IEEE Transactions on Geoscience and Remote Sensing [69]. An alternative method of obtaining wind directions from shipborne marine radar data is developed and evaluated in chapter 4. Here, results are obtained for both moving and fixed platform data, and an attempt is made at determining the best techniques for both types of data. This work has been published in the proceedings for the 2012 IEEE International Geoscience and Remote Sensing Symposium [68]. Chapter 5 introduces a new tool for the automated retrieval of IW surface signatures from marine radar data. This work has been submitted to IEEE Transactions on Geoscience and Remote Sensing [70]. In chapter 6, the newly developed techniques to retrieve IW information from marine radar data are applied to

a particularly energetic IW that was tracked over a distance of almost 40 km across the continental shelf. The conclusions and future work are given in chapter 7.

Three appendices provide additional details and supplementary results. Appendix A gives a detailed description of the newly developed technique to correct marine radar data for the backscatter ramp, i.e. the backscatter's dependency on range and antenna look direction. This technique builds on results from chapter 3 and is employed in both chapters 5 and 6. For shipborne marine radar data, determining the correct antenna look direction of any given radar pulse may pose a challenge. This would be a non-issue if the radar pulse orientation relative to the ship, the exact time of a full antenna revolution, and the corresponding ship heading were correctly sampled. Sadly, this was not the case for the NLIWI/SW06 marine radar data. Appendix B therefore discusses the necessary correction of the NLIWI/SW06 marine radar data. Finally, appendix C describes and gives results for a previous method to retrieve IW surface signatures from marine radar data. This method is purely based on localized Radon transform techniques. This work has also been published in the proceedings for the 2012 IEEE International Geoscience and Remote Sensing Symposium [68].

# Chapter 2

## Marine X-Band Radar Background

### 2.1 History of Marine Radar as Oceanographic Instrument

Marine X-band radar systems operating at grazing incidence are widely used on ships for navigation. The radar backscatter from the sea surface, called sea clutter, may obscure small target echoes, and is thus generally considered as noise. In this sense, sea clutter has been discussed for decades (e.g. [27]).

Among the first to derive ocean surface wave information from marine radar data were Oudshoorn [82], Ijima et al. [57], and Mattie and Harris [74]. They used the method of visual inspection to obtain wave parameters. The digitization of marine radar images helped extend these early findings. Ziemer et al. [142] found the two dimensional Fourier transform of radar images and noted similarities to conventional buoy data. However, two dimensional spectra have an inherent  $180^\circ$  ambiguity. This ambiguity can be removed by considering two consecutive images [7].

A more advanced method of determining non-ambiguous surface wave spectra has been introduced by Young and Rosenthal [136]. They analyze marine radar data in the three-dimensional wavenumber frequency space, and apply the dispersion relationship to

distinguish between signal and noise. Any deviation of the wave signal from the dispersion relationship is attributed to surface currents, which induce a Doppler shift. Young and Rosenthal find that the wave period and direction derived from such filtered spectra is in excellent agreement with buoy reference data. To obtain calibrated two-dimensional wave energy spectra from marine radar data, Ziemer and Rosenthal [141] proposed an inverse wave to image transfer function. Finally, Ziemer [139] found a linear relationship between the significant wave height and the square-root of the signal-to-noise ratio in the three dimensional image spectrum. With these findings, the complete two dimensional wave energy spectrum can be retrieved from a sequence of marine radar images. An advantage over traditional buoy measurements, which are based on the analysis of the buoy motion using accelerometer and tilt sensors, is the capacity to detect multi-modal structures within the wave fields [140].

At the time, the images as displayed on the radar's screen were recorded on photographic film using a camera with a motor drive and shutter that was synchronized with the radar sweep. The photographic images were then digitized using an image processor. This technique has two major disadvantages: (i) It requires a high degree of maintenance and time-consuming processing; and (ii) by photographing the conventional black and white radar image displays, most information about the backscatter intensity gets lost [128]. It would be much better if the radar signal was digitized directly with an 8-bit or better radiometric resolution. Such a system, enabling the routine collection of marine radar data by means of an analog-to-digital converter, was first developed by Hirakuchi and Ikeno [51]. Buckley et al. [20] and Trask et al. [116] use marine radar data collected by a similar system to estimate the directional spectrum of the sea surface.

To allow for real-time radar-based wave measurements, a combined hard- and software system called WaMoS (Wave Monitoring System) was developed at the GKSS research centre (today Helmholtz-Zentrum Geesthacht) [33, 139]. The system consists of a standard navigation ship radar, an analog-digital conversion device, a personal computer for

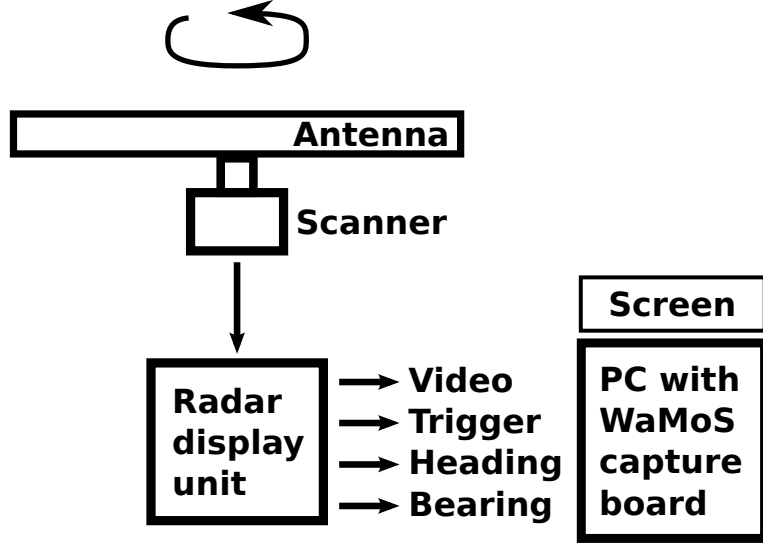


Figure 2.1: WaMoS hardware components.

data storage and analysis, and a screen to display results (see Fig. 2.1). After a calibration period, WaMoS can be used as a stand alone wave and surface current measuring device. Some important improvements have since been made to the wave and surface current retrieval techniques: Senet et al. [106] introduced an iterative technique to improve the accuracy of current estimates. The radar-based wave and surface current estimates are further improved by considering the harmonic (nonlinear) modes of the image spectrum and correcting for aliasing due to temporal undersampling [104].

Today, WaMoS is further developed and marketed by OceanWaveS [97]. It has been validated for offshore [72], coastal [13], and moving platform [104] applications. Similar marine radar based measuring capabilities are offered by MIROS' Wavex instrument [46]. In addition, MIROS commercially offers a marine radar based system to automatically detect oil spills [115, 6, 41]. Finally, the SeaDarlq system, which has been developed at the Dutch Governmental Institute TNO and was acquired by Nortek in 2011, uses marine radar technology to detect oil spills [60], monitor sea surface features, and extract hydrographic information from radar waves.

Today, marine radar data are used to derive shallow water bathymetry [10, 36, 105, 125, 119], determine maps of the sea surface elevation [15, 32], estimate surface currents

[40, 106], retrieve wind information [30, 31], or study internal waves (IWs) [23, 96, 128]. Catálan et al. [22] introduce a method that combines marine radar and optical data to detect wave breaking in the surf zone. Further oceanographic uses of marine radar technology are discussed by Robinson et al. [99]. Radar images of the sea surface are often noisy. As Robinson et al. demonstrate, averaging over several images, provided they overlay geographically, strongly enhances the signal of any permanent underlying features. In their article, they present case studies to illustrate the location of the surface signature of coastal discharge from rivers and from sewage outfalls as well as the location of a submerged sandbank, among others.

## 2.2 Marine Radar Technical Specifications

The goal of this section is to define the imaging capabilities of marine radar systems. Here, the focus lies on Furuno marine radars and WaMoS' data acquisition system. However, the following discussion applies equally to oceanographic marine radar systems offered by different manufacturers.

To capture radar images, WaMoS requires four signals from the radar: (i) A heading marker, which signals each full revolution of the antenna; (ii) a trigger pulse, signaling the emission of a microwave beam; (iii) a bearing pulse, carrying information on the antenna look direction; (iv) the demodulated, logarithmically compressed video signal (see Fig. 2.1). The WaMoS capture board digitizes the time history of the return signal. Typically, a single radar pulse is stored within 256 or 512 discrete cells. This may be repeated, integrating the signal of consecutive pulses. The resulting numbers are then stored, before the next pulse is processed [80].

Standard marine radars are fitted with logarithmic amplifiers that are designed to increase the dynamic range of the video signal and reduce the risk of near range saturation. WaMoS stores the backscatter intensity as a 12-bit number, i.e. intensities range from 0

(no return) to 4095 (maximum return). The radar backscatter intensity recorded for each range bin represents the power received at the antenna from the sea surface illuminated by the antenna at that range. For a unit area of sea surface, the ratio of the backscattered power to the incident power defines the surface's normalized radar cross section (NRCS) [43]. As a non-dimensional variable that spans a wide range of values over several orders of magnitude, it is usually expressed on the decibel scale [98]. Determining the NRCS for standard marine radars is not straightforward, since the video output is not radiometrically calibrated. However, using a low-budget marine X-band radar with a Wavex capture board, Gommenginger et al. [43] have found a way to calibrate the composite system in a single step. They conclude that marine radars are capable of routinely providing reliable quantitative measurements of the sea surface roughness.

It is important to distinguish between the sampling cell size and the radar-inherent resolution (see e.g. [140, 99]). The latter depends on the radar and determines the smallest feature size it can image, while the former is controlled by the data acquisition system. To allow for efficient operation, it is recommended to match resolution and sampling cell size.

The resolution in range is limited by the pulse length,  $\tau$ ,

$$\delta r = \frac{\tau c}{2}, \quad (2.1)$$

where  $c = 3 \times 10^8$  m/s is the speed of light. For example, the shortest pulse length supported by Furuno's FAR2117BB (which is one of the radars that is commonly used by WaMoS) is 0.07  $\mu\text{s}$  [39]. This corresponds to a pulse-averaged range resolution of 10.5 m. As a consequence, two objects that are separated by less than 10.5 m will be imaged as a single object. Note that such a short pulse length implies a relatively low output power, which limits the maximum radar range to 3 to 4 km. If greater ranges are desired, the radar must be set to a longer pulse duration (with higher output power), leading to a lower range resolution.

In contrast, the cell size in range is controlled by the sampling frequency,  $\sigma$ , of the digital capture board:

$$dr = \frac{c}{2\sigma}. \quad (2.2)$$

WaMoS offers a 20 MHz sampling frequency, which corresponds to a cell size of 7.5 m.

The azimuthal resolution,  $\delta\theta$ , is limited by the horizontal antenna beam width,  $\beta$  (see Fig. 2.2a). The beam width is proportional to the radar wave length,  $\lambda$ , and reciprocally proportional to the antenna length,  $l$ ,

$$\beta = \frac{\lambda}{l}. \quad (2.3)$$

The azimuthal resolution is then defined as

$$\delta\theta = 2r \tan(\beta/2). \quad (2.4)$$

Marine X-band radars typically operate at 9.4 GHz, i.e. a wavelength of  $\sim 3$  cm. For an 8-foot antenna, the longest antenna available for Furuno's FAR2117BB, the antenna beam width is therefore  $0.75^\circ$ . At a range of 4 km, this translates into an azimuthal resolution of 52 m. As illustrated by Fig. 2.2b, the radar's vertical beam width is with  $20^\circ$  much larger [39]. This allows a ship-mounted radar to illuminate the sea surface even when the vessel pitches and rolls in heavy seas.

The cell size in azimuth angle is determined by the antenna rotation period,  $T$ , the azimuth step,  $n$ , and the pulse repetition frequency,  $f$ :

$$d\theta = \frac{2\pi n}{Tf}. \quad (2.5)$$

The maximum pulse repetition frequency supported by Furuno's FAR2117BB is 3 kHz. For an antenna repetition rate of 42 rpm, and an azimuth step of 4, the WaMoS default

setting, the cell size in azimuth angle is therefore  $0.34^\circ$ . The WaMoS resolution cell size is illustrated in Fig. 2.2c.

Note that some of the radar parameters are interdependent. For example, a short pulse length of  $0.07 \mu\text{s}$  is available only up to a range of 2 nautical miles. A high pulse repetition frequency of 3 kHz is offered only up to a range of 4 nautical miles. To monitor the sea surface at a range that is greater than 4 nautical miles, a minimum pulse length of  $0.15 \mu\text{s}$  and maximum pulse repetition frequency of 1.5 kHz must be selected [39]. In addition, both pulse length and pulse repetition frequency determine the level of emitted power.

WaMoS stores the marine radar data as records of backscatter intensity from a series of ranges at each specific antenna look direction. Many oceanographic applications require such polar data to be converted to Cartesian coordinates. Robinson et al. [99] achieve this by placing each data point into its mapped output pixel and then averaging all such contributions. The WaMoS wave analysis software package accomplishes this task by nearest neighbor interpolation [104]. Alternatively, a bilinear interpolation technique can be chosen. The choice of output pixel size depends on the size of the range and azimuth cells as well as on the radial geometry. Generally, it is recommended that radar and WaMoS settings are chosen such that at the mid-range the azimuth and range cell are of about the same size. If then the square Cartesian cell is given sides equal to the range cell size, azimuthal oversampling occurs in the near range, whereas pixels in the far range are undersampled.

## 2.3 Imaging Mechanism

The radar backscattering mechanism at grazing incidence angles is not very well understood [19]. The purpose of this section is to summarize the current knowledge. Standard marine radars are non-coherent (i.e. they measure only amplitude and not Doppler modulation) and operate with horizontal polarization on transmit and receive (HH). So, Doppler modulation and vertical polarization will not be discussed here.

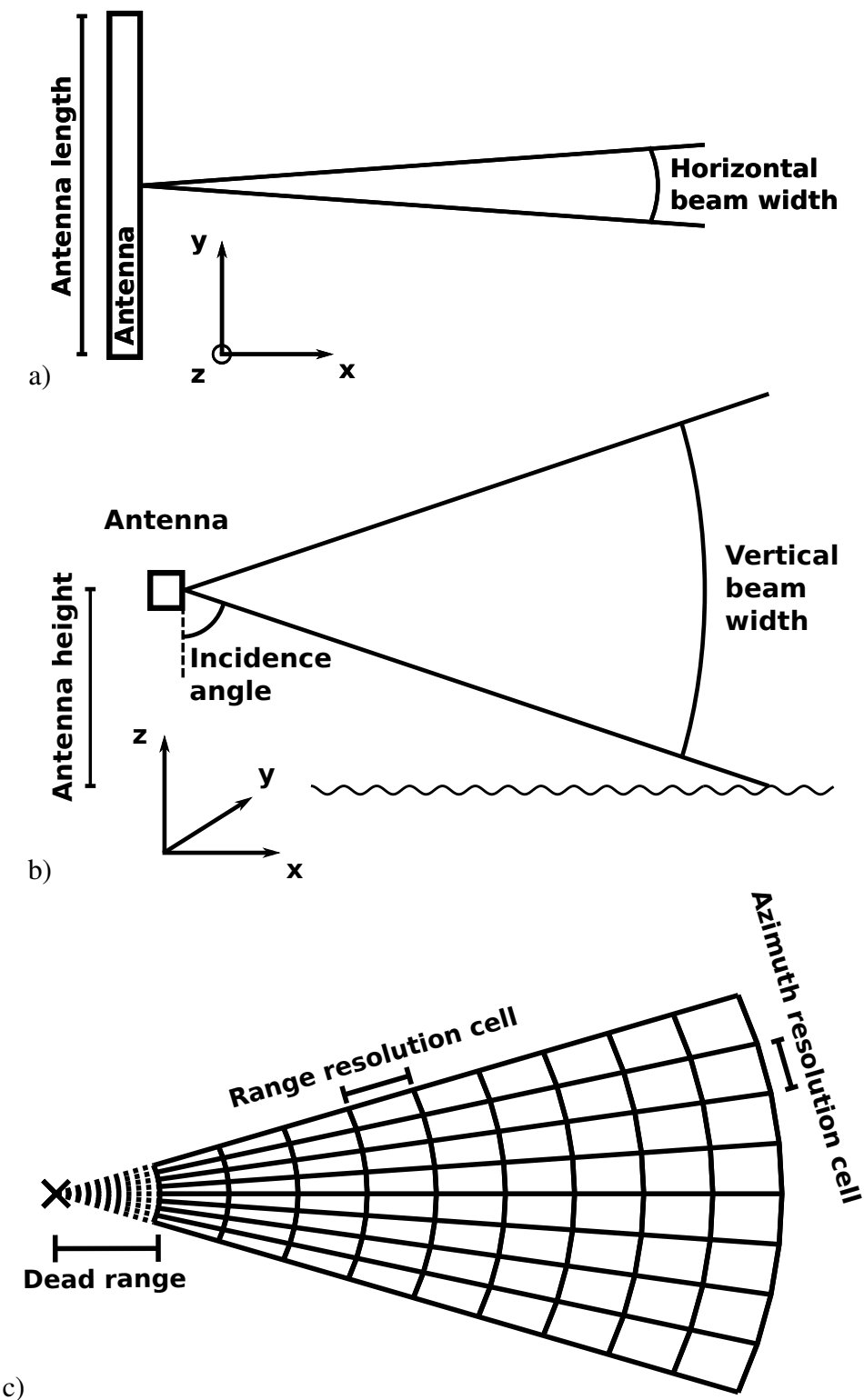


Figure 2.2: Illustration of radar antenna horizontal and vertical beam width (a, b) and WaMoS resolution cell size (c).

The radar backscatter intensity can be taken as a measure of the sea surface roughness, which is dominantly controlled by the wind. For obliquely viewing radars, the scattered power increases with wind speed. For nadir-viewing radars, where the incidence angle is zero, this relationship is inverted. The incidence angle therefore plays an important role for the microwave interaction with the sea surface [98].

At low incidence angles, specular reflection is the dominant process. In this context, it is important to introduce the concept of the sea surface being made up of a large number of small facets oriented at different angles. The sea surface changes its shape in space and time. The facets that are normal to the incident radar energy will generate strong specular reflection. Brown [18] extensively discusses the quasi-specular scattering from the air-sea interface.

Unlike quasi-specular scattering, which depends mostly on the larger scale ocean waves, oblique incidence scattering from the ocean surface appears to be highly dependent on the small scale surface waves. It is generally accepted that the most important mechanism contributing to the interaction between radar and ocean surface waves is resonant, or Bragg, scattering [124]. Bragg resonance by ocean waves was first observed by Crombie [26] for radio waves of 22 m. He found that the strongest grazing incidence backscatter occurred from ocean waves whose wavelength was 11 m or exactly one half that of the incident electromagnetic waves. In the original theory, using crystal lattices, representing an array of isolated scatterers, Bragg [16] found that if the round trip distance between successive scatterers equals an exact number of wavelengths, the radar waves reinforce each other. The Bragg condition, expressed in terms of the spacing between scatterers,  $L$ , the incidence angle,  $\theta$ , and the wavelength,  $\lambda$ , is given by

$$\frac{2L \sin \theta}{\lambda} = n \quad n = 1, 2, \dots \quad (2.6)$$

If this condition is not met, destructive interference occurs and the backscattered power is greatly reduced. For X-band radar, Wright [130] performed a laboratory experiment

to show that the backscatter from water waves agrees well with Bragg theory. The radar backscatter from the sea surface is thus controlled by Bragg-selected waves of the wavelength

$$\lambda_w = \frac{n\lambda}{2 \sin \theta}. \quad (2.7)$$

The surface waves the radar interacts with are therefore those of comparable wavelength to the microwaves [98]. For a marine X-band radar operating at 9.4 GHz (i.e. a wavelength of 3 cm) and grazing incidence, cm-scale surface capillary waves are responsible for the backscatter. Note that for such short waves, both gravity and surface tension are important restoring forces in the wave motion.

It is important to realize that Bragg resonance generally occurs in small isolated patches. For imaging radars (as opposed to scatterometers or altimeters), the number of such patches within a resolution cell is generally very small, which explains the grainy appearance of radar images, called clutter noise.

To explain the scattering of microwaves from a realistic sea surface, a composite surface theory was proposed by Wright [131] and Bass et al. [9]. Basically, they distinguish between short and long waves. The large scale ocean surface is approximated by an array of plane surfaces, or facets, each of which is displaced and tilted by the long waves. To obtain the scattered signal Bragg theory is applied to each small facet. Assuming that the short wave structure decorrelates in distances that are short compared to the long wavelengths, the net radar backscatter can then be obtained by summing over all facets. These studies find that the frequency, incidence angle, and polarization dependence of the sea echo at microwave frequencies can be well explained by the theory [85]. Today's state-of-the-art models use a radar backscatter model in conjunction with a model of the ocean processes which modulate the surface wave spectrum [101, 102, 71, 127].

Bragg theory predicts a reduction of the backscatter intensity with increasing incidence angle (e.g. [124]). However, the observed backscatter intensities from the sea surface

at grazing incidence are significantly higher than what is predicted by composite radar backscatter models. It is now widely accepted that a significant contribution comes from breaking wave events at a variety of scales, generating so-called sea spike echoes [122, 117, 65, 121]. Hwang et al. [54] find that the sea spike coverage is considerably higher than whitecap coverage and attribute this to steep features that produce quasi-specular facets and short-scale waves bounded to intermediate waves during breaking.

The ocean waves modulate the surface roughness, which explains why waves can be imaged with a radar. Tilt modulation and hydrodynamic modulation are well established imaging mechanisms at moderate incidence angles [92, 3, 4]. When the radar incidence angle is greater than the slope angle of the long ocean waves, parts of the sea surface become hidden from the radar's direct line of sight, and shadowing occurs. Shadowing is thought to reinforce the trend of reducing backscatter with increasing incidence angle. While Bragg scattering remains important at grazing incidence, shadowing is assumed to be the dominant modulation mechanism [8, 110].

A good overview of radar backscattering mechanisms is given by Robinson [98]. Plant [85] provides an extensive discussion of Bragg and composite surface theories and their application to research in air-sea interaction. The review by Wetzel [129] addresses the physics of grazing incidence radar backscatter.

## 2.4 Discussion and Recent Developments

For a long time, radar sea clutter was regarded as a source of noise, hindering navigation. This has changed with the advent of oceanographic marine radar applications, most notably regarding surface wave detection.

Marine radars cover a much smaller area than SAR images. However, the capability to sample an area at high frequency (25 to 40 images per minute) and continuously over hours and days gives marine radars a significant advantage over satellite SARs that can at best

revisit a site once a day. Thus, marine radars can monitor the evolution of oceanographic processes over much shorter timescales than satellite remote sensing methods. Furthermore, marine radar's capability to sample images, albeit much smaller than typical SAR images, represents an excellent complement to in situ “point” measurements, which are limited in spatial coverage to sparse arrays. For example, one commonly used analytical method to obtain the wave direction from heave-pitch-roll buoy data assumes that waves have a  $\cos^2 s \theta / 2$  distribution about the mean wave direction [135]. This assumption does not allow for the existence of multi-modal seas (wave energy contributions from more than two directions). In contrast, marine radars have no such limitations and bimodal wave distributions are regularly observed [136].

Marine radars can image only sea surface phenomena, or those that have a surface signature. For grazing incidence, the mechanisms responsible for the backscatter from such features are not yet fully understood. However, there is no doubt about the link between the periodic character of the radar backscatter and surface gravity waves, and Young and Rosenthal's [136] spectral analysis technique to retrieve wave period and direction from marine radar data is well established. What still represents a big challenge is the determination of spectral density or wave height from the backscatter intensity. It is extremely difficult to relate the radar backscatter intensity to the wave height because the radar image transfer function is influenced by many factors, including radar wavelength, incidence angle, look direction, wind, wave conditions, and surface currents [88].

Standard non-coherent marine radars measure backscatter intensity only, while coherent radars also preserve the phase information of the return signal. Recent studies by Johnson et al. [61] and Hwang et al. [56] suggest that coherent radars are capable of reliably estimating the wave height. The Doppler frequency shift, determined from the phase information, can be processed to yield the line-of-sight (radial) velocity of the scattering elements [61, 86]. The derived radial velocity has many contributing factors: Currents of all sources, the phase velocity of Bragg waves, and the oscillatory motion of the long sur-

face waves. However, the oscillatory portion of the radial velocity is generated primarily by ocean surface waves. Spectral analysis of the radial velocity therefore yields the wave-induced velocity spectrum, which can more easily be converted to a surface wave elevation spectrum [56]. This is because, in contrast to wave height retrieval from the backscatter intensity, no empirical parameters are required [61]. Using an upwind pointing nonrotating radar antenna, Hwang et al. [56] found that reliable information of dominant wave period and significant wave height can be derived from radar data of a few seconds with range coverage on the order of 10 wavelengths. With a scanning coherent radar system, the wave direction can be determined [120].

Another recent study by Cui et al. [28] suggests that for surface wave and current monitoring, antennas with vertical polarization are superior over standard horizontally-polarized ones. Huang and Gill [53] collected low sea state data using a dual polarized marine radar and analyzed them regarding surface currents. They also conclude that vertical polarization leads to better results. These studies support findings by Nortek, who use vertically-polarized radars for their oil spill and hydrography monitoring system SeaDarq. The Italian marine radar company GEM now routinely manufactures vertically polarized radar antennas, significantly reducing their cost relative to custom-made ones [62]. In general, images from vertically-polarized radars have a more spatially homogeneous character than what is observed for horizontal polarization. This can be explained by differences in the backscatter mechanisms for the two polarizations: The more evenly distributed Bragg-resonant scattering facets are believed to dominate the vertically polarized backscatter, while the spiky features due to localized wave breaking events are much more important for horizontal polarization. For an extensive discussion of the differences between horizontal and vertical polarization at grazing incidences, the reader is referred to [65, 121, 55, 89].

Recent upgrades to marine radar technology include solid-state transmitters. Traditional radar transmitters are based on magnetrons, which generate electromagnetic waves at microwave frequencies by a special vacuum tube that requires high voltages and strong

magnetic fields. While magnetrons have a short life expectancy, solid-state transmitters require much lower voltages and use no components with short operational lives, which improves reliability and helps reducing maintenance costs. In addition, solid state systems are capable of measuring the phase of the received echo relative to the phase of the transmission. This is because, unlike magnetrons, solid-state transmitter produce a very stable signal. Marine radar manufacturers like Kelvin Hughes now routinely offer such Doppler radar systems, advertising their enhanced performance in sea clutter [79]. What is more, state-of-the-art marine radars now offer a digital output of the received backscatter signal, thus eliminating the necessity of an external analog-to-digital converter, as offered by companies like OceanWaveS and its competitors.

From our perspective, solid-state radar systems offer the advantage that the calibration parameters required to retrieve wind speeds would need no adjustments over time. This is because solid-state transmitters have a much longer operational life than magnetrons. Regarding IWs, the phase information recorded by coherent radars can be used to derive the IW-induced surface velocity convergence, and would thus provide a direct link between radar measurements and interior ocean dynamics. In addition, as discussed above, the additional phase information may significantly improve radar-based estimates of the significant wave height. Finally, the new digital radars offer the potential to improve data quality and reduce noise.

Finally, conventional marine radar systems could most likely produce better oceanographic results if they offered a higher resolution. The use of 12 foot antennas, instead of the 8 foot antennas employed within this work, would improve the azimuthal resolution. The range resolution could be improved with radar scanners of greater output power, allowing for shorter pulse lengths. The resulting higher resolution would, for example, enable the imaging of shorter surface gravity waves. This could improve wave estimates under low-wind, short-wavelength conditions. Furthermore, a higher resolution could improve

current measurements. This is because the existing algorithms rely heavily on the signal that is due to the shorter surface waves, which exhibit the most notable Doppler shift.

# **Chapter 3**

## **Wind Retrieval from Shipborne Marine Radar Data**

### **Summary**

In this chapter we study the retrieval of wind information from nautical X-band radar data. In contrast to previous studies, where data from stationary research platforms were used, this study focuses on data from a moving platform, encountering a larger variety of conditions than a platform at a fixed location. Compared to traditional in situ sensors, wind data derived from nautical radar images are much less susceptible to air flow distortion by the platform, since the images cover a large area around the ship. Images collected with a standard nautical HH-polarized X-band radar operating at grazing incidence exhibit a single intensity peak in upwind direction. The wind retrieval method developed here uses a harmonic function that is least-squares fitted to the radar backscatter intensity as a function of antenna look direction. The upwind direction is given by the direction that corresponds to the peak of the fitted function. An empirical model function is derived to retrieve the wind speed from the average radar backscatter intensity. Contrary to wind retrieval methods that have been proposed before, this approach is well suited for data acquired from a moving platform, as it functions well even if the radar field of view is partially shadowed and does

not require ship motion correction. Here, we focus on data that were collected during two storms, using the first storm to derive and the second to test the empirical model functions. The method is validated using measurements from two ship-based anemometers.

### 3.1 Introductory Remarks

This chapter studies the retrieval of wind information from X-band radar images collected from *R/V Roger Revelle* during the Impact of Typhoons on the Ocean in the Pacific (ITOP) program in 2010. Ocean wind measurements are crucial for the study of energy and momentum transfer from the atmosphere to the ocean as well as for gas-exchange processes at the air-sea interface. On ships, wind measurements are important for navigation and safety. Wind measurements from ship-mounted anemometers are affected by the effect of the ship's hull and superstructures on the flow of air to the instrument. Errors due to air flow distortion are highly dependent upon anemometer position, ship shape, and relative wind direction. However, even for anemometers at well-exposed locations wind speed measurements may have an error of up to 10% [75, 93, 134]. In addition to the distortion of the wind field, further errors are introduced due to the ship's pitch and roll [95]. Contrary to ship-mounted anemometers, nautical X-band radars can acquire wind vectors in areas where the flow distortion due to the ship is strongly reduced or not present. Furthermore, the retrieval of wind information from the radar backscatter intensity of the ocean surface is independent of the sensor's installation height and motion. And since practically all ships are already equipped with X-band radars, these wind data can be obtained at a small extra cost.

Nautical X-band radars operate by transmitting and receiving pulses of microwaves that interact with the cm-scale sea surface roughness. The radar return from the sea surface has a strong dependence on both wind direction and speed [24, 66]. The backscatter intensity images collected with an HH-polarized X-band radar operating at grazing incidence exhibit

a peak in upwind direction, which can be used to retrieve the wind direction [47, 121]. Nautical radar images that are averaged over about 1 min may also show linear features, which are usually well-aligned with the mean surface wind direction [30, 31]. However, wind streaks are difficult to exploit for estimating the wind direction from shipborne radar data because of the platform’s horizontal motion. After a calibration is performed, the radar backscatter intensity can be used to infer the wind speed [58].

The hydrodynamic modulation of the surface roughness and tilt modulation associated with long surface waves lead to a pattern of adjacent regions with weak and strong radar echo, a phenomenon called sea clutter. Common oceanographic nautical radar applications exploit the sea clutter to determine directional wave spectra and significant wave height [136, 14], surface currents [106], bathymetry [10, 105, 36], and individual wave parameters [15, 32]. More recent studies use nautical X-band radar images to determine internal wave properties [96] and detect wave breaking [22].

Here, we focus on data that were collected during two storms in August and September 2010, with wind speeds above 20 m/s and significant wave heights up to 6 m. Data from the August storm are used to derive the empirical model functions needed to retrieve radar-based wind information. The September storm data are used to test these model functions. Both storms are characterized by several periods of heavy rain, which modifies the radar backscatter characteristics, and therefore complicates a radar-based wind estimate. To address this problem, we have performed a histogram analysis of radar images, which led to a new quality control parameter that is used to identify images collected during rain.

The accuracy of wind measurements from nautical X-band radar images has been studied by various investigators, most notably Dankert et al. [30, 31]. In contrast to previous studies, where data from stationary research platforms or coastal stations were used, the X-band radar images used for the present work were collected from a moving platform, the *R/V Roger Revelle*. Ships are confronted with a greater variability of wind and sea state conditions than fixed platforms or coastal stations, which operate under specific local

conditions. It is therefore of interest to study whether the application of radar-based wind retrieval methods to shipborne data produces results that are comparable with those found for fixed platforms. Furthermore, the wind retrieval method proposed by Dankert et al. determines the wind direction from quasi-stationary wind streaks, which become visible by averaging radar images over about 1 min. This approach cannot be directly applied to ship data, because the radar's field of view changes with the ship motion. As the spacing between wind streaks is of the order of 100 m, averaging a sequence of radar images without correcting for ship motion would risk obliterating the wind streak signal. We have developed a new method to retrieve the wind direction from the upwind peak in the radar data. Our approach is well suited for data acquired from a moving platform as it does not require a correction for ship motion.

The wind retrieval algorithm presented here has similarities to the wind-backscatter transfer function derived for scatterometry at C-band frequency with vertical polarization and moderate incidence angles [113]. To retrieve the wind direction from a single image, the radar backscatter intensities from the non-obstructed antenna look directions are averaged over range. The resulting azimuthal backscatter intensities are then used to derive a best-fit harmonic function. The upwind direction is given by the direction that corresponds to the fit function's peak. With this novel approach based on a least-squares fit, the upwind peak can be found even if it is located in a shadowed area. The average backscatter intensity obtained from the same fit function correlates with the wind speed. An empirical model function is derived to retrieve the wind speed from this average backscatter value.

This chapter is organized as follows. In section 3.2 the X-band radar system and available data are described. A histogram analysis of radar images is performed to identify images collected during rain, the results of which are presented in section 3.3. Section 3.4 introduces our least-squares-fit method to retrieve wind information from X-band radar data. It is validated using measurements from two ship-mounted anemometers. This chapter ends with a summary and discussion of the results (section 3.5).



Figure 3.1: Pictures of *R/V Roger Revelle* in Kaohsiung harbor, taken on June 16, 2010, and of the ship’s main mast with the X-band radar antennas for wind retrieval (bottom) and navigation (top) [photo credit: Wolfgang Hüneburg, OceanWaveS GmbH].

## 3.2 Data Overview

The data used for the present work were collected within the field study for the Impacts of Typhoons on the Ocean in the Pacific (ITOP) program from August to October 2010. The ITOP program, a multi-institutional effort supported by the U.S. Office of Naval Research and the Taiwan National Science Council, focuses on the ocean response to typhoons in the western Pacific Ocean. Its experimental plan included a moored buoy array, two U.S. Air Force C-130 aircraft and a DOTSTAR Astra jet to deploy floats and drifters, two EASI/ASIS buoy pairs, United States and Taiwanese research vessels, satellite data, numerical forecast models, as well as a control center at the Naval Postgraduate School in Monterey, California, and a flight operations center in Guam.

Here, we use X-band radar data that were collected from *R/V Roger Revelle*. The data were acquired with a standard Furuno FAR2117BB nautical X-band radar, operating at grazing incidence with horizontal polarization in transmit and receive (HH), installed on the main mast above the pilot house. This radar system was installed in addition to the already present X-band radar that is being used for navigation, also located on the main mast (see Fig. 3.1). The wind retrieval radar operates at 9.4 GHz with a sampling frequency of

20 MHz. It was modified to allow for an increased antenna repetition frequency of 42 rpm with a pulse repetition frequency of 3 kHz. With this configuration, radar backscatter images were collected every 1.5 s, covering a range from 240 to 2,145 m with a range resolution of 7.5 m. The radar was connected to a wave monitoring system (WaMoS) [33, 139], which digitizes and stores the spatial and temporal radar backscatter information as a sequence of images with a 12-bit gray scale depth, i.e. digitized backscatter intensities range from 0 to 4,095. The true radar cross section (in dB) is not available since standard nautical radars are not radiometrically calibrated. WaMoS is capable of measuring the spatial and temporal evolution of the surface wave field [136]. It determines the significant wave height from the signal-to-noise ratio (SNR) in the image spectrum [140, 14].

The reference data used to validate the radar-based wind retrieval scheme developed here, were acquired from two ship-based anemometers. The primary wind sensor (Anemometer-1) was an R.M. Young Ultrasonic 85000 in a well-exposed location on the meteorological mast on the bow of the ship at a height of 17 m. The secondary wind sensor (Anemometer-2) was an R.M. Young 5300 “airplane”, located on the main mast at a height of 25 m.

The data we use for this study cover two storms from August 6, 00:00 UTC to August 9, 23:59 UTC and September 12, 15:53 UTC to September 17, 15:56 UTC, 2010. A map of the corresponding ship track is shown in Fig. 3.2. During the August storm, the ship stayed in the vicinity of the two EASI/ASIS buoy pairs, located at 127° E, 19.5 and 21° N, respectively. On September 12, the ship departed from Kaohsiung, Taiwan, traveled east to the ASIS/EASI deployment sites, where it stayed for three days, and then returned towards its point of departure on September 17. The color code in the figure gives the significant wave height as measured by WaMoS, ranging from 0.5 to 7 m. Note that the significant wave height data have not been calibrated and therefore give only a first order estimate.

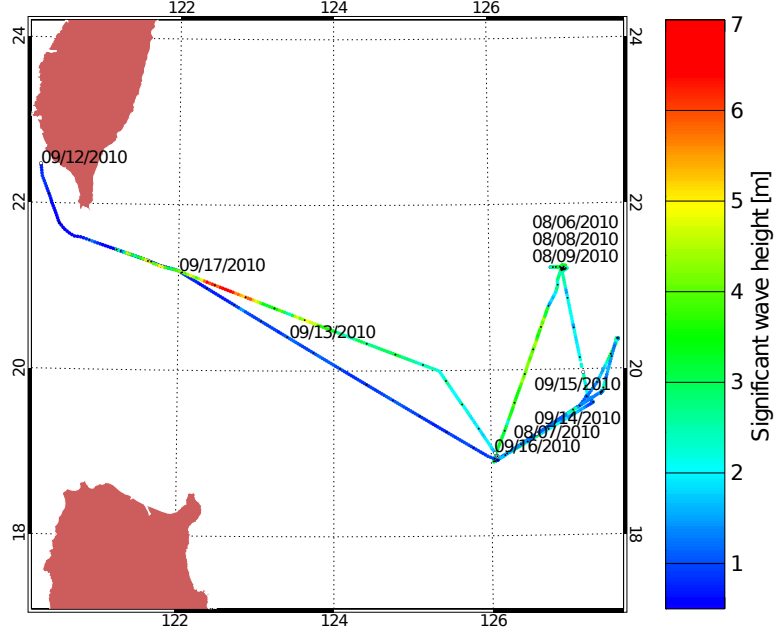


Figure 3.2: Map of the track of *R/V Roger Revelle* during the storms from August 6, 00:00 UTC to August 9, 23:59 UTC and from September 12, 15:53 UTC to September 17, 15:56 UTC, 2010. The corresponding significant wave height estimates by WaMoS are color coded.

### 3.3 Rain Recognition

The two storms studied here produced several periods of heavy rain, which modifies the radar backscatter characteristics, and therefore complicates radar-based wind estimates. Fig. 3.3 compares X-band radar image data that were collected in absence of rain (top left) and during rain (top right). The image on the left was recorded on August 8, 2010, 06:40 UTC, when Anemometer-1 measured a 16 m/s wind coming from 200°. The image on the right was recorded 10 min later, with an increased wind speed of 20 m/s coming from 224°. The corresponding histograms (bottom left and right) have a bin size of 25. The average intensity for the image collected in absence of rain is 467, for the image collected during rain it is almost twice as bright at 807. If no rain recognition was implemented, this change in the image intensity would be mistaken for a much more significant rise in the wind speed than the 4 m/s increase measured by Anemometer-1. When comparing the histograms from the two cases, the greatest difference can be found in the overall percentage of first bin

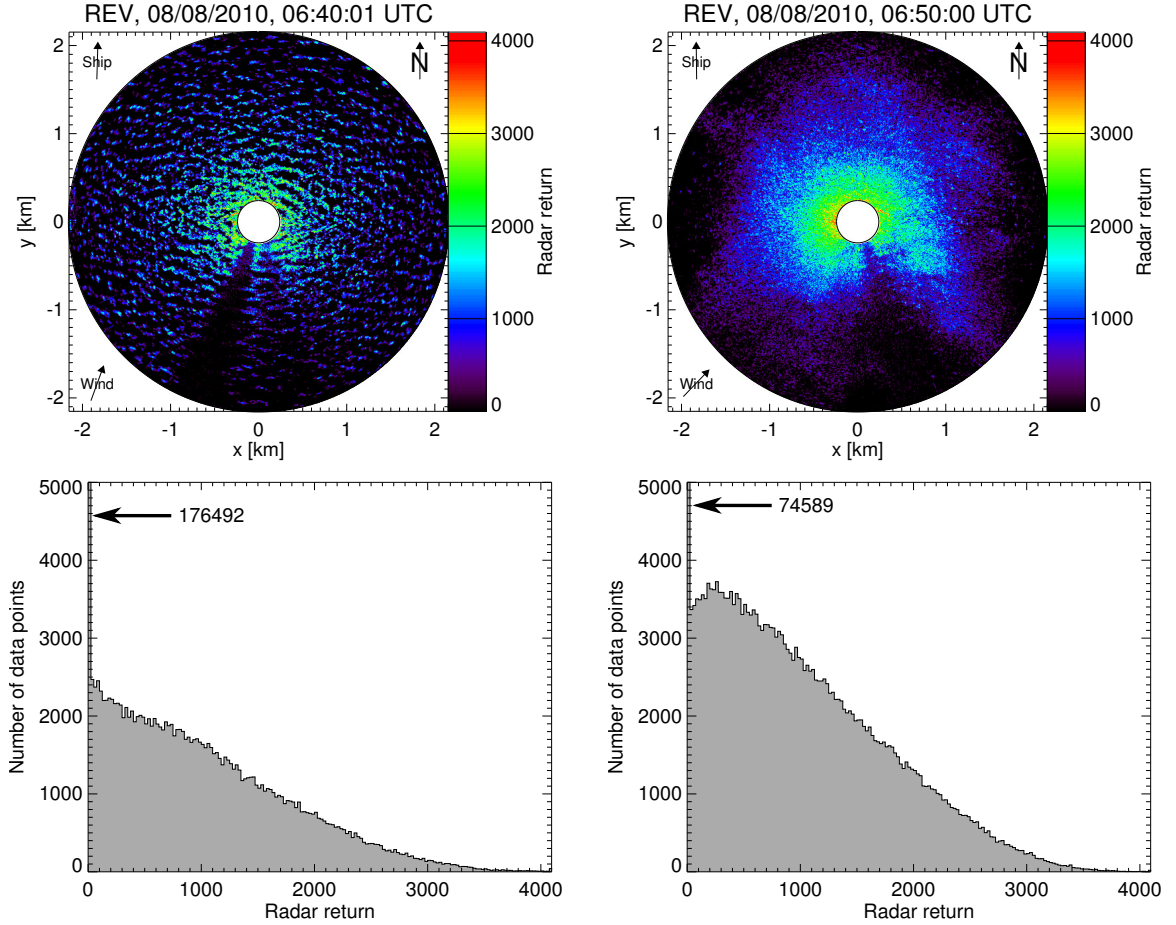


Figure 3.3: Radar images collected in absence of rain on August 8, 2010, 06:40 UTC (top left) and during rain on August 8, 2010, 06:50 UTC (top right). Histograms of the radar backscatter intensities are shown below. The numbers with arrows indicate the lengths of the first bars, including pixels with zero intensity, which exceed the range of the y-axis.

pixels with intensities from 0 to 24: While for the case in absence of rain 56% of all image pixels were found to belong to the first bin (99% of which had zero intensity), for the case during rain only 24% had intensities smaller than 25 (with 95% having zero intensity). Note that for both histograms in Fig. 3.3 the length of the bar that includes pixels with zero intensity exceeds the range of the y-axis.

Little is known about the dominant backscatter mechanism for nautical X-band radars operating at grazing incidence in presence of rain. However, it can be observed that for areas shadowed by surface wave crests (no radar return) under no-rain conditions, the radar backscatter in presence of rain is quite significant, greatly reducing the sea clutter. The

resulting fairly uniform radar backscatter, in particular at medium ranges, suggests that volume scattering by rain drops in the air plays a role.

Due to the strong impact of rain on the number of pixels with zero intensity, the zero pixel percentage (i.e. ratio of the number of image pixels with zero intensity to the overall number of pixels) was identified as a quality control parameter to determine the presence of rain. Radar image data where the zero pixel percentage was below 50%, a value that we chose because it yields satisfactory results, were flagged as rain cases and excluded from wind retrieval. Fig. 3.4 shows time series of the percentage of image pixels with zero intensity for radar images that were collected during our two storms in August and September 2010. The rain threshold is marked by a dashed line. From a total of 542,672 radar images, 138,616 or just above one quarter of the measurements were found to have been acquired during rain.

In addition, data that were collected right after the passage of two rain fronts, one around August 6, 23:00 UTC, the other around August 7, 01:30 UTC, and characterized by low wind speeds with large local gradients, were considered outliers and discarded.

## 3.4 Wind Retrieval

In the following, our method to retrieve wind direction and speed from shipborne nautical X-band radar data is introduced. We begin with a brief description of the measurement principle for radar based wind retrieval (section 3.4.1). Wind measurements obtained by ship anemometers are susceptible to air flow distortion. To improve our understanding of flow distortion effects due to the ship, section 3.4.2 compares data from the two reference sensors. In order to obtain wind information from the radar data, empirical model functions that relate the observed backscatter intensities to wind direction and speed must be derived. We use nautical X-band radar and ship anemometer data acquired during the August storm to derive the model functions (section 3.4.3). The model functions are tested using data

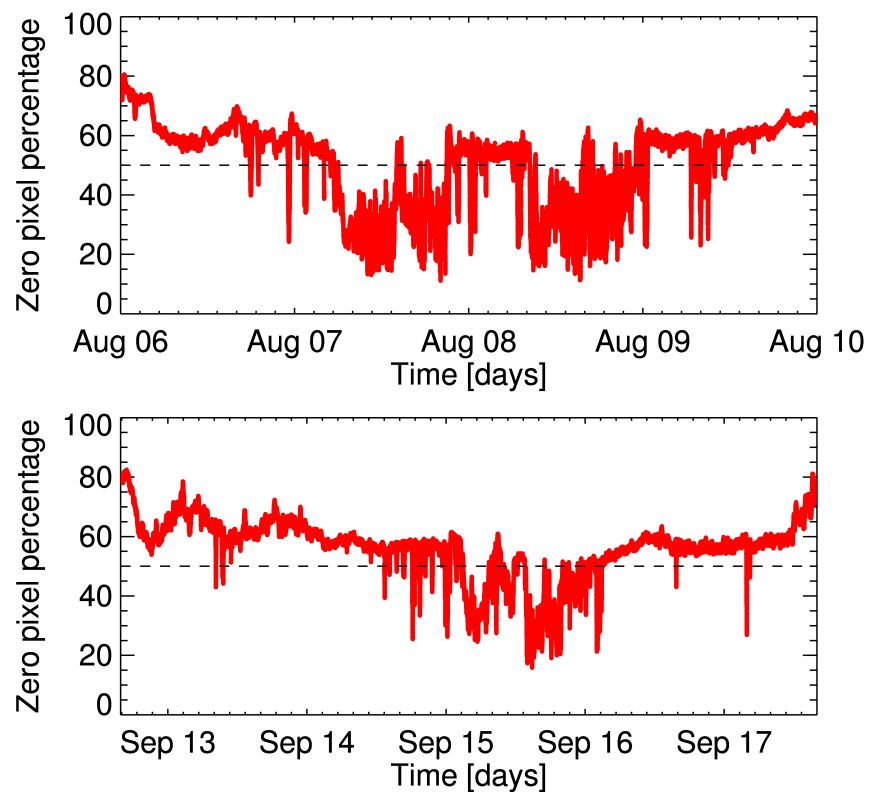


Figure 3.4: Time series showing percentage of image pixels with zero backscatter intensity for radar images collected from August 6, 00:00 UTC to August 9, 23:59 UTC (top) and September 12, 15:53 UTC to September 17, 15:56 UTC, 2010 (bottom).

that were collected during the September storm (section 3.4.4). This section ends with a study of the sensitivity of our radar-based wind retrieval scheme to wind speed and relative orientation between wind direction and ship heading (section 3.4.5).

### 3.4.1 Measurement Principle

Nautical X-band radars have been used for many years to collect images of the sea surface. Small wind-induced ripples on the sea surface cause Bragg scattering of the incident microwave energy. For HH-polarized X-band radars operating at grazing incidence, the backscatter intensity has a single peak in upwind direction [47, 121]. This is in contrast to the radar backscatter at moderate incidence angles, where a second peak appears in downwind direction [87]. The single peak for grazing incidence can be explained by scattering due to small scale breaking waves that are most prominent forward of the crest of the long waves [118].

The backscatter intensity can be related to the wind speed [58]. The stratification conditions in the boundary layer between the ocean and lower atmosphere, i.e. air-sea temperature differences, have an influence on the radar backscatter intensity from the sea surface. Keller et al. [63] found that the radar return from the sea surface in unstable conditions is higher than for neutral and stable conditions. A simple measure of the boundary layer stability is given by the bulk Richardson number  $Ri_b$

$$Ri_b = \frac{gz(\theta_v - \theta_0)}{\theta_v(u^2 + v^2)}, \quad (3.1)$$

where  $\theta_v$  is the virtual potential temperature,  $\theta_0$  the potential surface temperature,  $u$  and  $v$  the wind components in the x- and y-direction, respectively,  $g$  the acceleration due to gravity, and  $z$  the height above sea level [42]. Values close to zero are indicative of neutral conditions. In the area studied here, air-water temperature differences are small, and during

the two storms of interest wind speeds are generally high. Therefore, a neutral boundary layer can be assumed.

### 3.4.2 Comparison Between Reference Sensors

The air flow distortion due to the hull and superstructures of *R/V Roger Revelle* can be studied by comparing the measurements made by the two reference sensors, installed at different locations on the ship. Fig. 3.5 shows time series of wind speed and direction measured by the two ship anemometers. The data presented here are 1-min running averages with a 30-s overlap and cover the two storms we are interested in. The velocity due to the ship motion was subtracted from the anemometer data. An iterative approach was used to correct the wind speeds to 10 m above sea surface ( $U_{10}$ ), with friction velocity and drag coefficient computed according to Smith [111]. Note that neutral conditions and wind sea must prevail for this wind-speed-correction method to be applicable, which is assumed to be the case for the data presented here (see section 3.4.1). In both storms, the corrected wind speeds ( $U_{10}$ ) from the two reference sensors range from under 5 to around 20 m/s. However, especially during the peak of the August storm, wind speeds measured by the two anemometers differ significantly. As will be demonstrated below, these differences are due to air flow distortions that are increased for specific orientations of the ship relative to the wind direction. For the first storm, wind directions change on August 6 from northeast to predominantly southern. The second storm is characterized by a change from predominantly eastern to western wind directions, occurring on September 15, before the peak of the storm.

The scatter plots in Fig. 3.6 show wind speed and direction data from the two storms, each consisting of 25,817 data points. The correlation coefficient for the wind speed measurements is determined to be 0.89, with a bias of -0.72 m/s, a root-mean-square (RMS) difference of 1.57 m/s and a standard deviation of 1.40 m/s. The negative bias can be explained by the ship's hull and superstructures compressing the air flow streamlines, leading

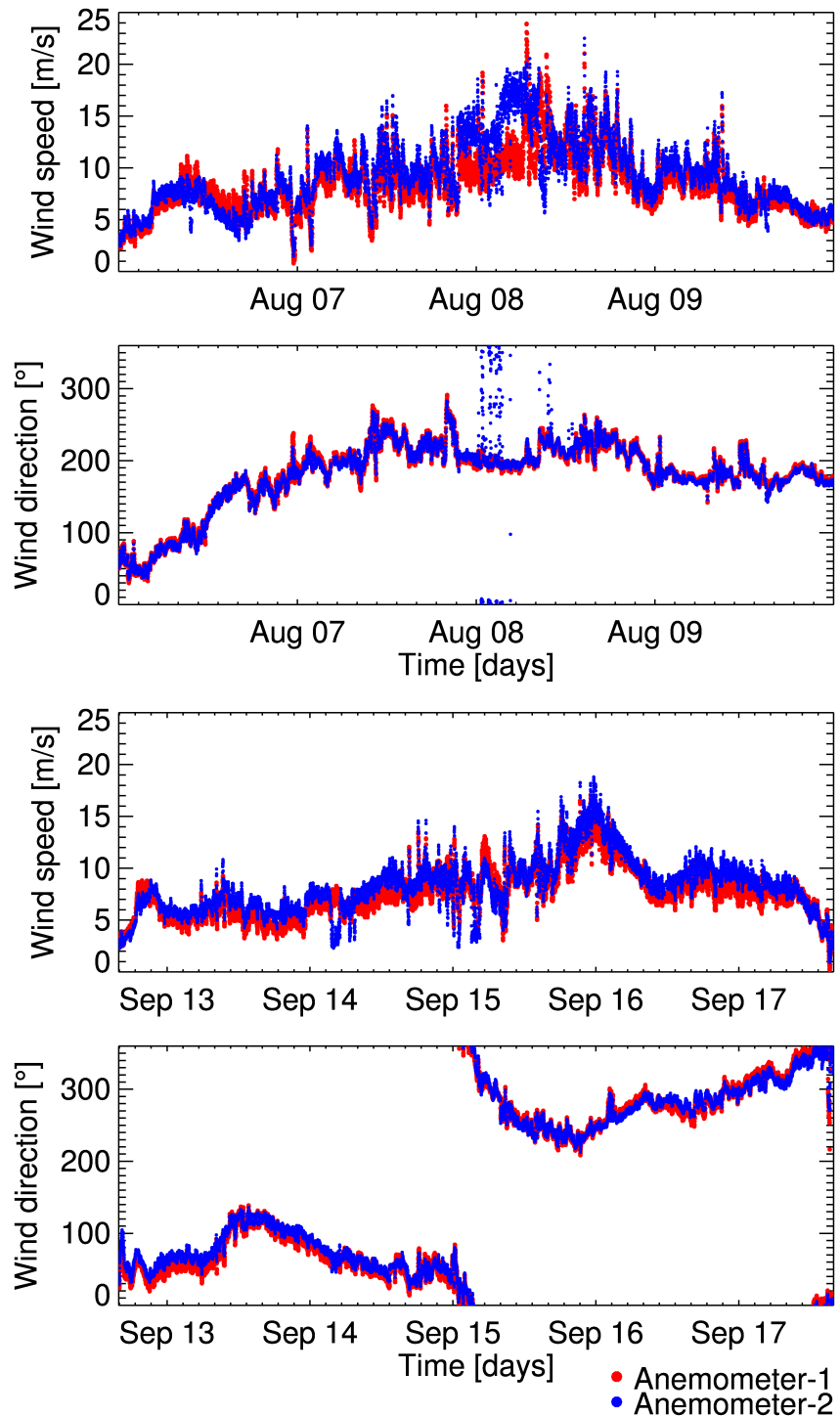


Figure 3.5: Time series of wind speed and direction measurements from ship anemometers 1 and 2 from August 6, 00:00 UTC to August 9, 23:59 UTC and September 12, 15:53 UTC to September 17, 15:56 UTC, 2010.

to an increased wind speed around the main mast, where Anemometer-2 is located. For the wind direction measurements, a mean directional difference length of 0.99, a bias of  $-1.79^\circ$ , an RMS difference of  $11.10^\circ$  and a standard deviation of  $10.95^\circ$  is found. The mean directional difference length is obtained by combining the unit difference vectors via vector summation and dividing the resulting vector's length by the number of data points (e.g. [12]).

To gain a better understanding of the impact of the relative orientation between ship heading and wind direction on the measurements made by the two ship anemometers, a sensitivity study was carried out. A histogram considering all possible angles between ship and wind direction was composed with  $10^\circ$  bins. For each bin, bias and standard deviation were computed. Fig. 3.7 shows these two statistical parameters as a function of the difference between ship heading and wind direction for wind speed and direction. The histograms showing the number of data points per bin is plotted in the background. Bias and standard deviation are omitted for ship-wind-orientations where the number of measurements was smaller than 20. For both wind speed and direction, the standard deviation increases significantly when the ship is heading downwind. For the wind speed, the bias is negative when the ship is heading upwind or downwind, meaning that Anemometer-2 on the main mast measures greater wind speeds than Anemometer-1. But when the wind is coming from either side of the ship, the bias is positive. For the wind direction, the bias is positive for wind coming from the starboard side of the ship and negative for wind coming from the port side. There is no directional bias when the ship is heading upwind, but a negative bias for situations when the ship is heading downwind.

The differences between the wind measurements acquired by the two reference sensors indicate that the air flow around the ship is distorted and that flow distortions vary with changing orientations towards the wind. In the following, data from Anemometer-1, located on the more exposed forward mast and therefore less susceptible to air flow distortions, will be used as main reference for the wind information retrieved from X-band

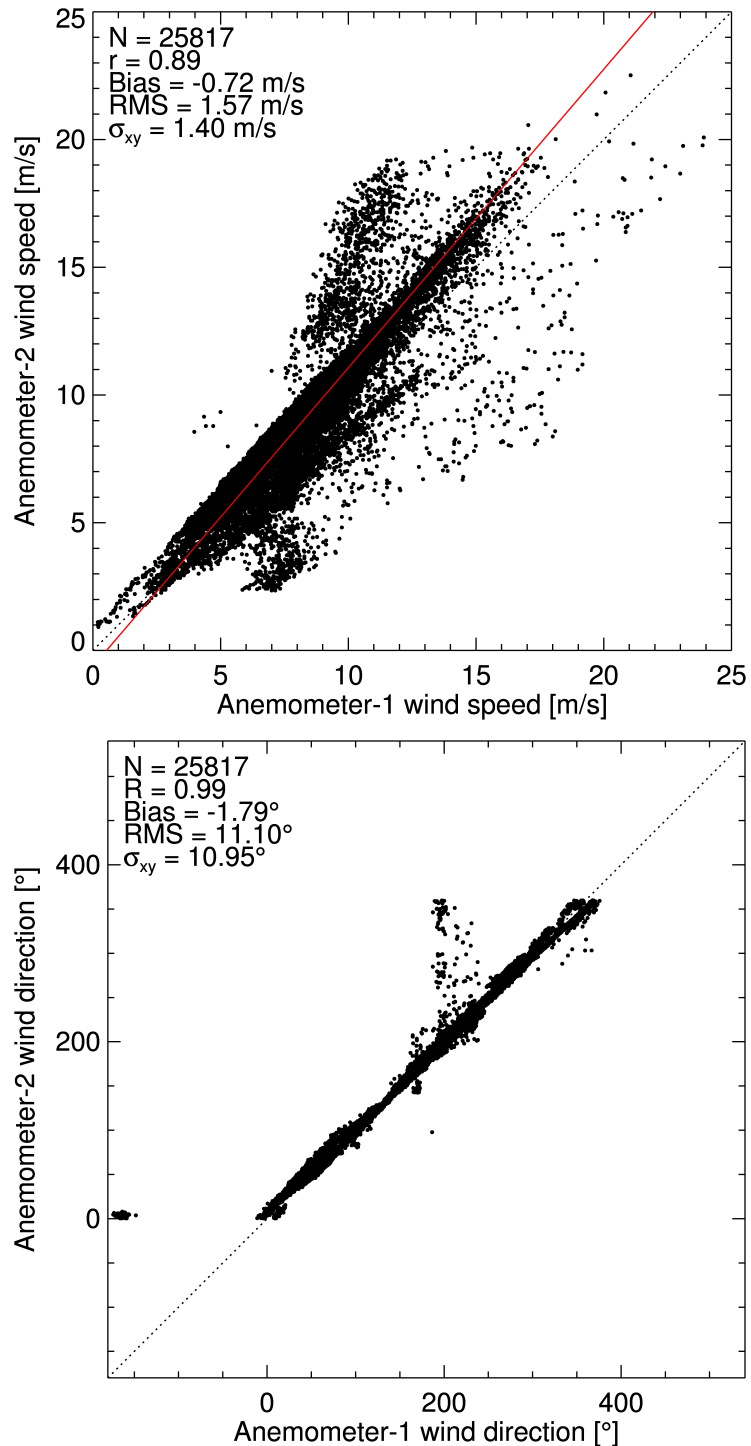


Figure 3.6: Scatter plots and statistical parameters of wind speed (top) and wind direction (bottom) measurements by ship anemometers 1 and 2 during the August and September storms.

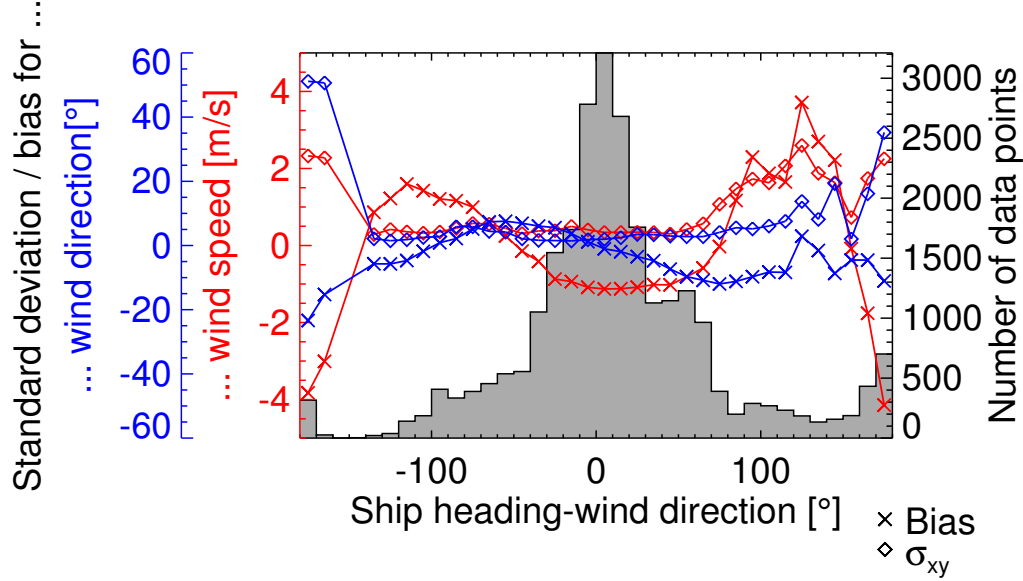


Figure 3.7: Standard deviation (marked by diamonds) and bias (crosses) for wind speed (red curves) and direction (blue curves) measurements acquired by the ship anemometers as a function of the angle between the ship's heading and the wind direction measured by Anemometer-1. A histogram showing the number of data points per  $10^\circ$  bin is plotted in the background.

radar data. Furthermore, data points where the difference between the wind speed or direction measurements made by the two ship anemometers was greater than 2 times the respective standard deviations, taking the biases into account, are considered to be affected by flow distortions. This was the case for 1,703 out of 25,817 measurements, or almost 7% of the reference data. Under such conditions, radar-based wind estimates that are not affected by air flow distortions would be of particular value. However, in order to allow for a quantitative comparison between radar and reference wind data, these data points will be disregarded during the derivation and testing of our empirical model functions.

### 3.4.3 Derivation of the Empirical Model Functions

To derive the empirical model functions needed to retrieve wind information from nautical X-band radar images, we use data that were collected during the August storm. Of the total 11,456 measurements (representing 1-min running averages with 30-s overlap), 5,174 mea-

surements or approximately 45% of the data had to be excluded due to rain and/or strong disagreements between the two reference wind measurements. Note that cases where only a subset of measurements within an averaging interval did not pass this quality control were still discarded. The remaining 6,282 data points are characterized by wind speeds ranging from 2 to 17 m/s.

#### **3.4.3.1 Shadowing of the Radar Field of View**

Before the radar backscatter intensity images can be used to determine the wind speed and direction, the shadowing influence of ship structures on the radar data must be investigated. Fig. 3.8 shows an image of the average radar backscatter intensity, compiled from data collected on August 09, 2010 between 03:00 and 03:30 UTC, when the ship was heading upwind. Areas where the radar field of view is obstructed by ship structures are marked by red frames. The forward looking area of the radar field of view is mostly unobstructed, with the exception of a small 6°-wide slice towards the bow due to the meteorological mast. In the radar's backward looking area the main mast causes a 65°-wide shadow. The smaller structures on the starboard and port sides of the ship were found to have a negligible impact on the radar backscatter intensity. Our wind retrieval scheme is therefore limited to an image section covering 289°.

#### **3.4.3.2 Radar Backscatter Dependency on Range and Antenna Look Direction**

Fig. 3.9 shows a ship-heading-oriented X-band radar image collected on August 9, 18:23:41 UTC. At this time, Anemometer-1 measured a wind of 6.2 m/s coming from south. On the radar image, the sea clutter becomes visible as dark and bright lines aligned with the long surface wave crests. The significant wave height estimate by WaMoS was 2.7 m, with a peak wave period of 8.0 s and a peak wave direction of 201°. The presence of another X-band radar on the ship manifests itself by the regular occurrence of interference spikes within the radar imagery. These spikes have been removed to prevent artificial biases.

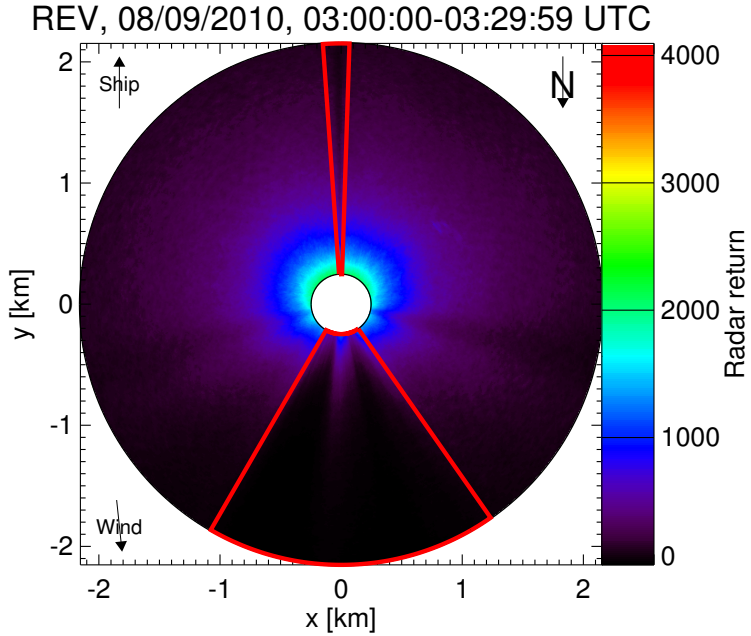


Figure 3.8: Image of the average radar backscatter intensity measured from 03:00 to 03:30 UTC on August 09, 2010, with the ship heading upwind. The image was composed out of 1270 individual radar images. The slices of the image where the radar field of view is obstructed are framed in red.

Since interference spikes show in the raw polar radar data as clusters of pixels with maximum backscatter intensity, they can be easily identified through a thresholding operation and replaced by the average of the unaffected adjacent pixels.

For the same radar image, Fig. 3.10 shows the radar backscatter intensity as a function of range and antenna look direction (where  $0^\circ$  corresponds to the ship's heading). The backscatter dependency on antenna look direction was obtained by integrating all radar pulses over range. Data points marked in gray correspond to areas shadowed by ship structures. A cosine-squared function

$$\sigma_\Theta = a_0 + a_1 \cos(0.5(\Theta - a_2))^2 \quad (3.2)$$

was least-squares fitted to the unmasked data (marked in red). Here,  $\sigma_\Theta$  is the average radar backscatter intensity as a function of antenna look direction,  $a_0$ ,  $a_1$ ,  $a_2$  are the regression

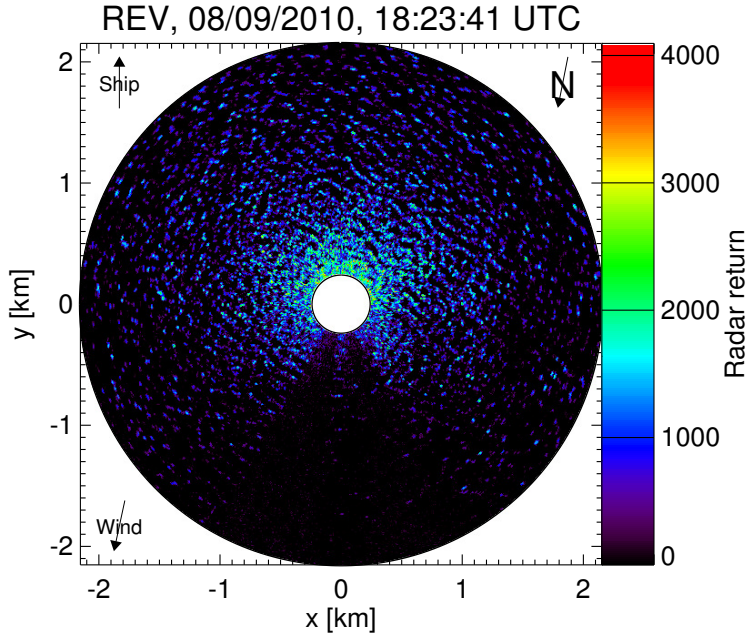


Figure 3.9: Radar backscatter intensity image collected on August 9, 2010, 18:23:41 UTC.

parameters, and  $\Theta$  is the antenna look direction. The best-fit curve is shown in blue. The peak of the best-fit curve is located upwind.

To obtain the backscatter dependency on range, all unobstructed radar pulses were integrated over antenna look direction. The model function used to obtain the best-fit curve in Fig. 3.10 is given by

$$\sigma_\rho = \frac{b_0}{(b_1 + \rho^{b_2})}, \quad (3.3)$$

where  $\sigma_\rho$  is the average radar backscatter intensity as a function of range,  $b_0, b_1, b_2$  are the regression parameters, and  $\rho$  is the range distance from the antenna.

### 3.4.3.3 Wind Direction

For each individual radar image, the wind direction can be retrieved from the upwind backscatter peak. To achieve this, we use Eq. (3.2) as our model function. The model function is least-squares fitted to the radar backscatter intensity as a function of antenna look direction, disregarding shadowed pulses, as illustrated by Fig. 3.10. The upwind peak

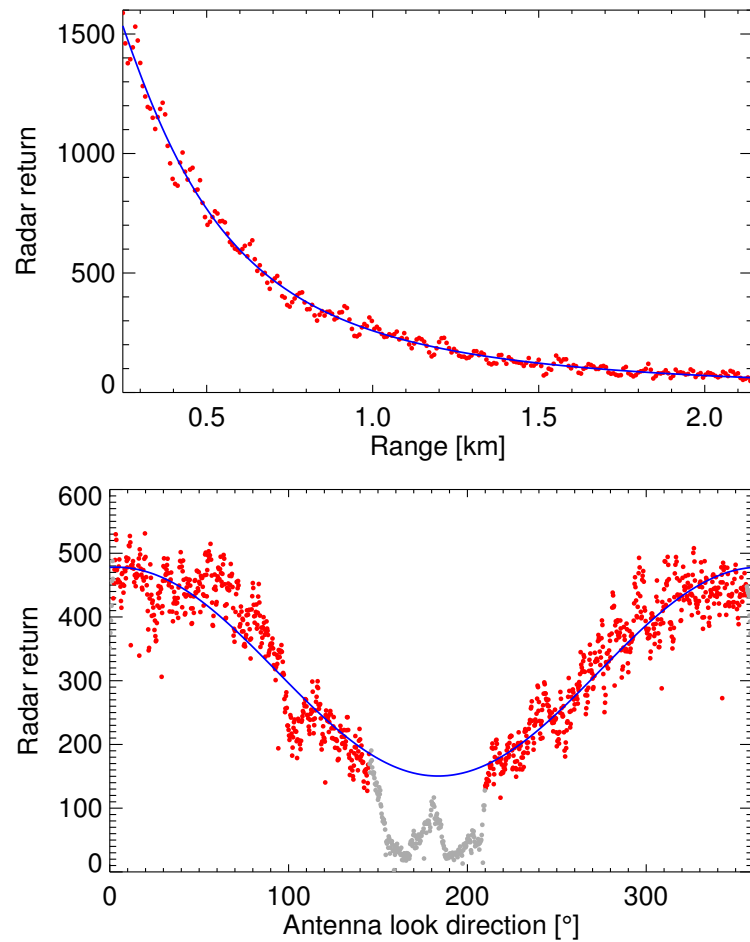


Figure 3.10: Average radar backscatter intensity as a function of range (top) and antenna look direction (bottom) for image collected on August 9, 2010, 18:23:41 UTC. The backscatter dependency on range does not include the shadowed antenna look directions that are shown in gray for the backscatter dependency on antenna look direction. The corresponding best-fit curves are shown in blue.

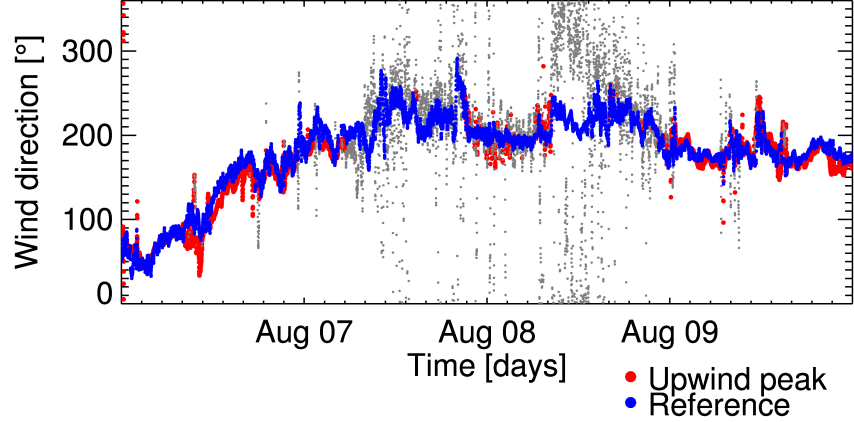


Figure 3.11: Time series of wind direction estimates obtained from the upwind peak in the radar data (red) and measurements made by Anemometer-1 (blue) during the storm from August 6, 00:00 UTC to August 9, 23:59 UTC, 2010. Radar measurements made during rain and at times when the wind data from the two ship anemometers strongly disagreed, i.e. discarded data points, are shown in gray.

direction is given by regression parameter  $a_2$ , which corresponds to the peak of the best-fit curve. The advantage of this approach is that the upwind peak can be determined even if it is located in a section of the radar image that is shadowed by ship structures. It is therefore no longer necessary that the ocean surface is imaged over the full azimuth, as suggested by Dankert and Horstmann [30].

For the following comparison, both radar-retrieved and reference wind directions represent 1-min running averages with a 30-s overlap. Fig. 3.11 shows wind directions obtained from the upwind peak in the radar data in red and measured by Anemometer-1 in blue. Fig. 3.12 shows the same data as a scatter plot. For the 6282 measurements that passed quality control, a mean directional difference length of 0.97, a bias of  $4.0^\circ$ , an RMS difference of  $14.2^\circ$ , and a standard deviation of  $13.6^\circ$  is found.

#### 3.4.3.4 Wind Speed

The most straight-forward method of obtaining a radar backscatter intensity value that can be related to the wind speed would be to evaluate the average backscatter intensity of each individual radar image. However, in our case this is bound to yield less than perfect results,

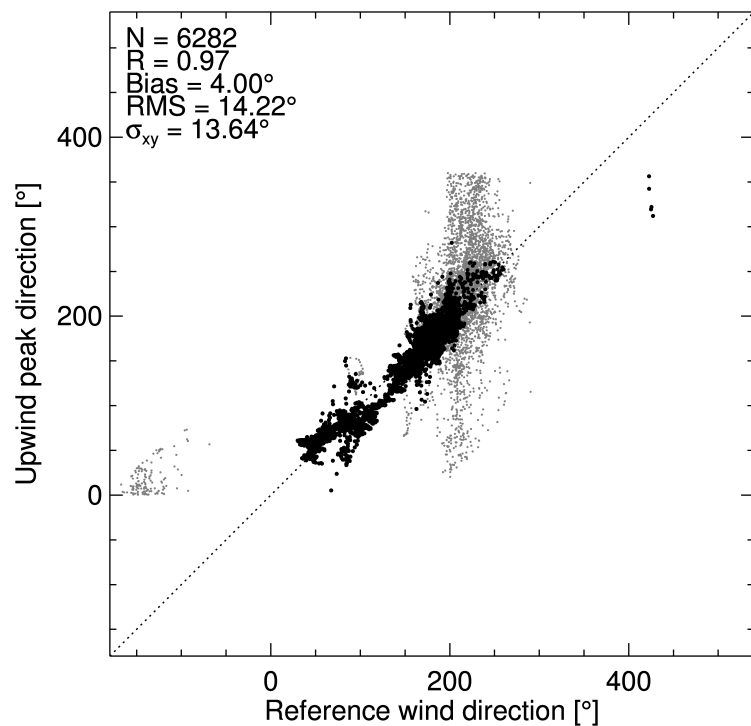


Figure 3.12: Scatter plot and statistical parameters of wind direction measurements acquired by Anemometer-1 and estimates derived from the upwind peak in the radar data for the August storm. Again, discarded data points are shown in gray.

since a 71°-wide section of the radar field of view was found to be obstructed by ship structures (see section 3.4.3.1). This is because changes of the relative angle between ship's heading and wind direction would provoke a change of the average image intensity. For example, we would expect an increased backscatter intensity as the shadowed image section moves from an upwind to a downwind location.

We have evaluated various methods to compute mean radar backscatter intensities: One approach is to consider only radar pulses that were collected with the antenna looking in crosswind direction, in order to prevent possible blocking effects by the ship from influencing the radar data. Another approach uses the mean intensity associated with the best-fit curve that is obtained by fitting the model function of Eq. (3.3) to the radar backscatter dependency on range. This can be done for each radar image, considering all pulses or just the unobstructed ones. However, it was found that best results are obtained by averaging the best-fit curve that is obtained by fitting Eq. (3.2) to the radar backscatter intensity as a function of antenna look direction, excluding all obstructed pulses (as has been done to estimate the wind direction). This does not come as a surprise since the fit function helps filling the gap that occurs due to shadowing by ship structures. The most suitable quantity for the following model function derivation is therefore obtained by evaluating

$$\sigma_{wSpd} = \frac{1}{2\pi} \int_0^{2\pi} (a_0 + a_1 \cos(0.5(\Theta - a_2))^2) d\Theta. \quad (3.4)$$

In contrast to the neural network approach introduced by Dankert et al. [30], this method uses a single parameter, which simplifies the wind speed retrieval significantly. Furthermore, it is physically more intuitive than a neural network, which does not require an explicit model for the radar imaging mechanism. Finally, by relying on a least-squares-fit approach, the Chi-Square values associated with the fit can be used as quality control parameters, e.g. to detect the presence of bright targets such as ships in the radar field of view, which could potentially bias our radar-based wind estimates.

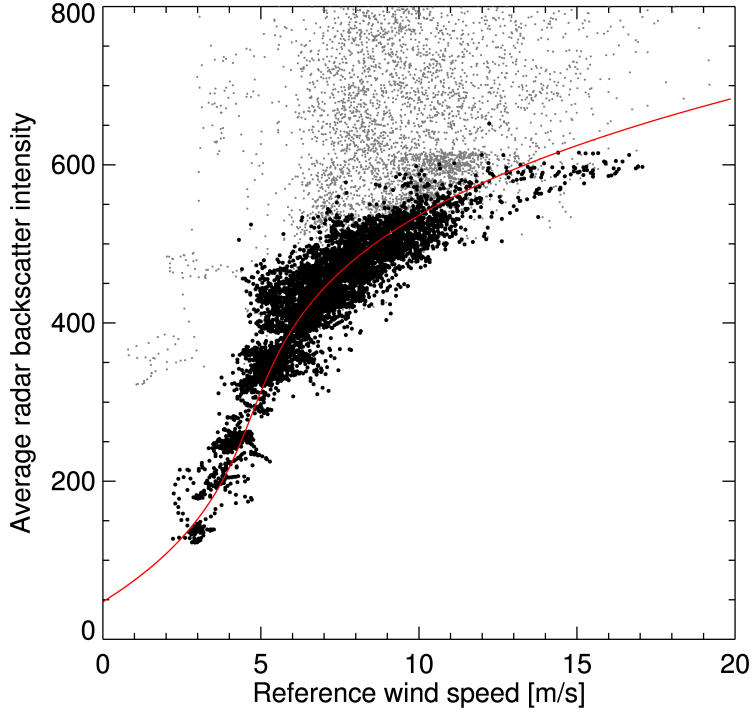


Figure 3.13: Scatter plot showing the wind speed from Anemometer-1, corresponding radar backscatter intensity, and the best-fit curve based on a third-degree polynomial function for data acquired during the August storm. Discarded data points are shown in gray.

As for the wind direction, both radar-retrieved backscatter intensity value ( $\sigma_{wSpd}$ ) and reference wind speeds are 1-min running averages with a 30-s overlap. For the data collected during the August storm, Fig. 3.13 shows a scatter plot of the wind speed measurements made by Anemometer-1 and the corresponding radar backscatter intensities obtained as described above. The best-fit curve is shown in red. It was derived using a least-squares method based on a third-degree polynomial function.

The time series in Fig. 3.14 shows the wind speed obtained from the radar backscatter intensities through the proposed model function and from Anemometer-1. Fig. 3.15 shows a scatter plot of the same data. For the 6282 valid data points, a correlation coefficient of 0.90 and a standard deviation of 0.88 m/s are found. Since this data set was used to derive the model function, the RMS difference equals the standard deviation and the bias is 0.00 m/s.

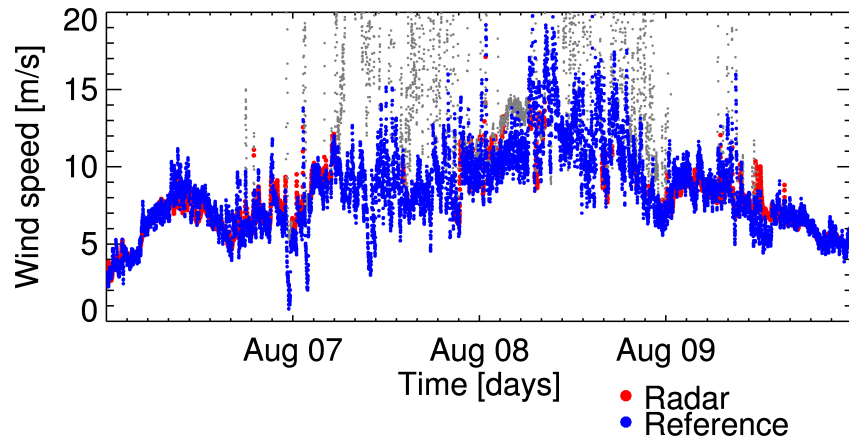


Figure 3.14: Time series of wind speed obtained from the radar data through the proposed model function (red) and Anemometer-1 (blue) during the storm from August 6, 00:00 UTC to August 9, 23:59 UTC, 2010. Discarded radar data points are shown in gray.

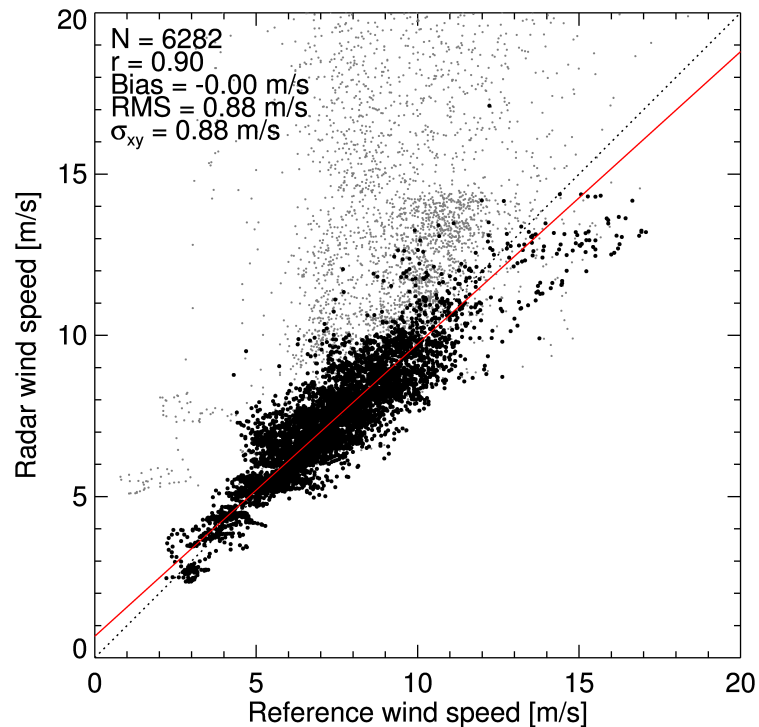


Figure 3.15: Scatter plot and statistical parameters of wind speed measurements acquired by Anemometer-1 and estimates obtained from the radar backscatter intensities for the August storm. Discarded data points are shown in gray.

As mentioned before, standard nautical radars are not radiometrically calibrated. Therefore, an empirical model function must be derived for every individual radar system. However, this is a simple procedure that can be accomplished with only a few days worth of data covering a preferably wide range of wind speeds.

### 3.4.4 Test of the Empirical Model Functions

In section 3.4.3, empirical model functions to retrieve wind information from nautical X-band radar data have been derived using data from the August storm. Here, we test these empirical model functions by applying them to radar data collected during the September storm. From a total of 14,361 measurements (representing 1-min running averages with 30-s overlap), 3,040 data points, or approximately 21% of the data, had to be excluded due to rain and/or strong disagreements between the two reference wind measurements. The remaining 11,321 data points have wind speeds ranging from just above 0 to almost 15 m/s.

#### 3.4.4.1 Wind Direction

The time series in Fig. 3.16 shows wind directions obtained from the upwind peak in the radar data in red and measured by Anemometer-1 in blue. Fig. 3.17 shows the same data as a scatter plot. For the 11,321 measurements considered, a mean directional difference length of 0.95, a bias of  $0.1^\circ$ , an RMS difference of  $17.4^\circ$ , and a standard deviation of  $17.4^\circ$  are found. The bias of the September storm data is smaller in magnitude than the one that was found for the August storm. However, RMS difference and standard deviation have increased slightly. Dankert and Horstmann [30] analyzed 4786 X-band radar data sets from the research platform FINO-I in the German Bight, using a method based on the derivation of local gradients. They obtained a correlation coefficient of 0.99, a bias of  $0.3^\circ$ , and a standard deviation of  $12.8^\circ$ . Our results for shipborne data and based on a least-squares-fit technique are therefore of comparable quality as the statistics found by a local gradients method applied to fixed platform data.

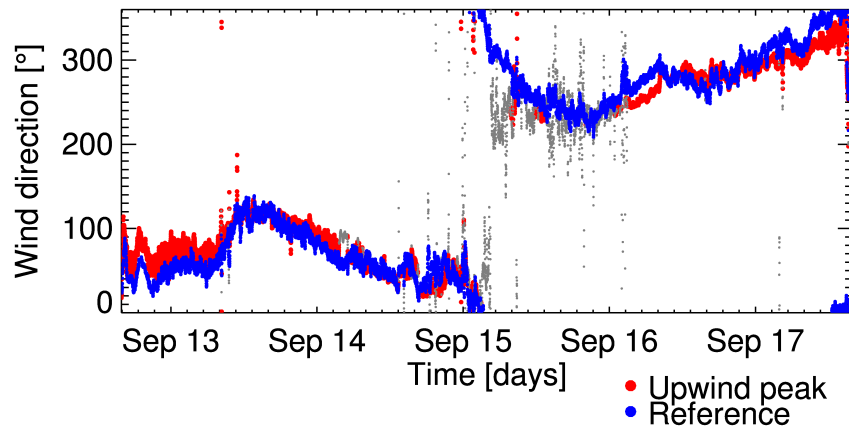


Figure 3.16: Time series of wind direction estimates obtained from the upwind peak in the radar data (red) and measurements made by Anemometer-1 (blue) during the storm from September 12, 15:53 UTC to September 17, 15:56 UTC, 2010. Discarded radar data points are shown in gray.

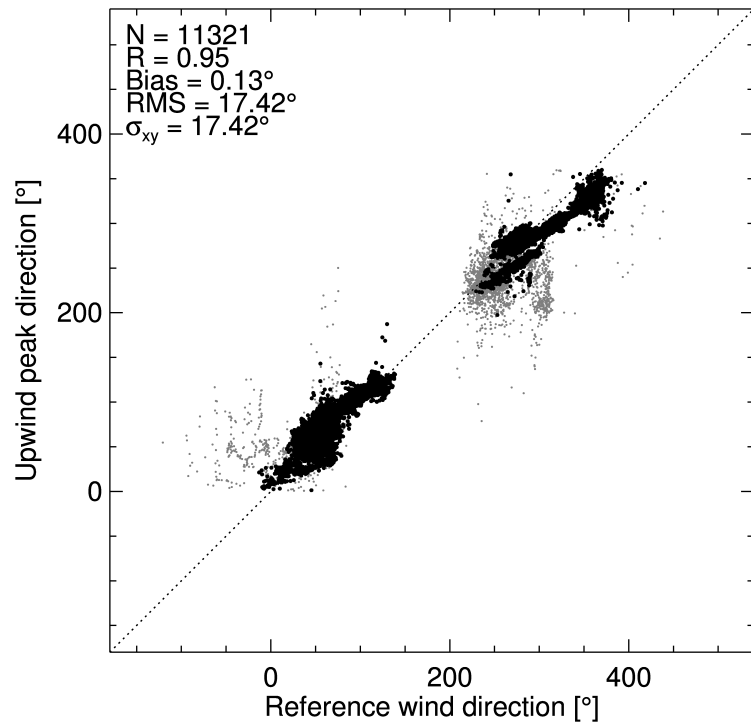


Figure 3.17: Scatter plot and statistical parameters of wind direction measurements acquired by Anemometer-1 and estimates derived from the upwind peak in the radar data for the September storm. Discarded data points are shown in gray.

### 3.4.4.2 Wind Speed

Fig. 3.18 shows a time series of the wind speed obtained from Anemometer-1 and from the radar data using the empirical model function derived from the August storm data. The scatter plot of Fig. 3.19 shows the same data. For the 11,321 measurements considered in the comparison, the correlation coefficient is found to be 0.91, the bias -0.10 m/s, the RMS difference 0.79 m/s, and the standard deviation 0.78 m/s. In comparison to the August storm, the standard deviation improved. Using a neural network approach with the average backscatter intensity in both crosswind directions, the corresponding antenna look direction, and the collocated anemometer data as input parameters, Dankert and Horstmann [30] obtained similar statistics for their fixed platform data set: correlation coefficient of 0.96, bias of 0.01 m/s, and standard deviation of 0.90 m/s. By adding the SNR, as well as the air-sea temperature difference, and relative air humidity obtained from external sensors to the input parameters, they further improved their statistics, resulting in a correlation coefficient of 0.99, a bias of 0.00 m/s, and a standard deviation of 0.41 m/s. We decided to limit our wind retrieval scheme to the radar backscatter intensity as this is the physically most intuitive parameter and allows for a more general application. This is in accordance with wind scatterometry, where a model function dependency on geophysical parameters other than wind (e.g. stability, waves) is generally assumed to be non-substantial (e.g. [113]).

### 3.4.5 Sensitivity Study

In this section we analyze the influence of wind speed and the relative orientation between wind direction and ship heading on the nautical X-band radar-based wind retrieval. For this study we use data from both storms, omitting rain cases as identified via our zero pixel threshold (see section 3.3) as well as cases when the ship anemometer measurements strongly disagreed, reducing the total of 25,817 data points (representing 1-min running averages with 30-s overlap) by approximately one third to 17,603.

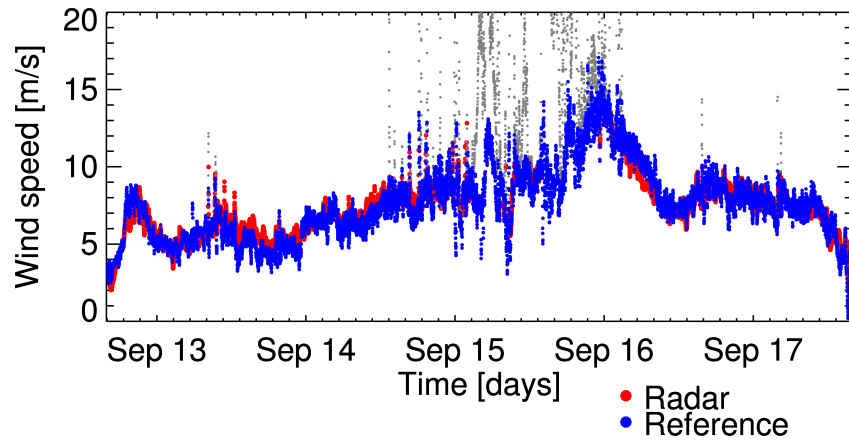


Figure 3.18: Time series of wind speed obtained from the radar data through the proposed model function (red) and Anemometer-1 (blue) during the storm from September 12, 15:53 UTC to September 17, 15:56 UTC, 2010. Discarded radar data points are shown in gray.

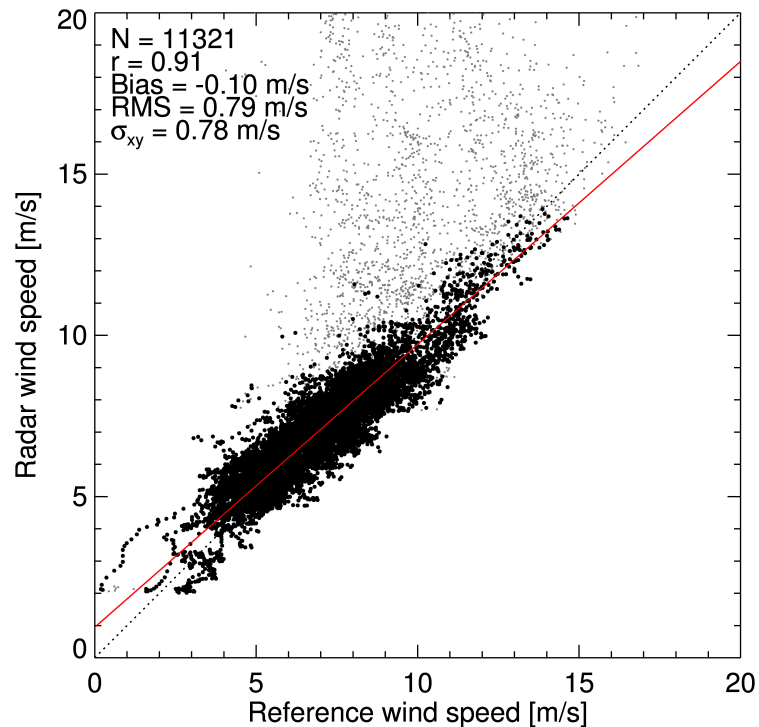


Figure 3.19: Scatter plot and statistical parameters of wind speed measurements acquired by Anemometer-1 and estimates obtained from the radar backscatter intensities for the September storm. Discarded data points are shown in gray.

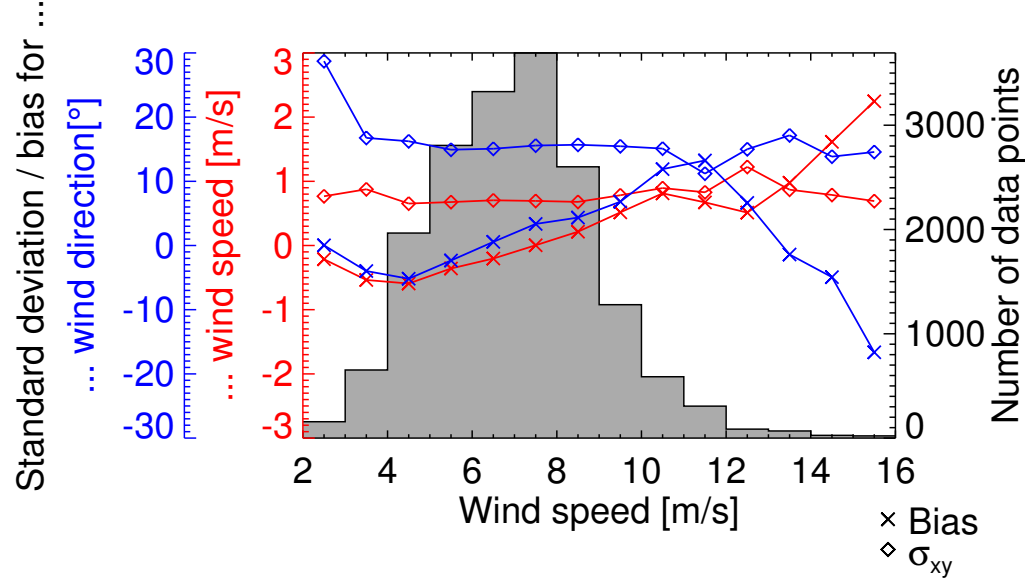


Figure 3.20: Standard deviation (marked by diamonds) and bias (crosses) for wind speed (red curves) and direction (blue curves) measurements acquired by Anemometer-1 and estimates from the radar data as a function of the wind speed. A histogram showing the number of data points per 1 m/s bin is plotted in the background.

The influence of wind speed on standard deviation and bias of the wind speed and direction measurements made by Anemometer-1 and estimates derived from the radar data is depicted in Fig. 3.20. A histogram showing the number of data points per 1 m/s bin is plotted in the background. Measurements from Anemometer-1 were used to compile the histogram. For the wind direction, the standard deviation is greatest at almost  $29^\circ$  under calm wind conditions. For the wind speed, the standard deviation reaches its maximum at just above 1.2 m/s for the 10 to 11 m/s bin, which has a limited number of data points. For all other histogram bins the standard deviation is below 1.0 m/s. For both wind direction and speed the bias reaches its largest magnitude for the highest wind speeds between 15 and 16 m/s. However, this bin consists of only 21 data points. The wind speed bias is negative for wind speeds under 7 m/s and positive for wind speeds above.

Fig. 3.21 shows standard deviation and bias for the wind measurements as a function of the absolute value of the angle between ship's heading and wind direction from Anemometer-1. The histogram in the background shows the number of measurements per

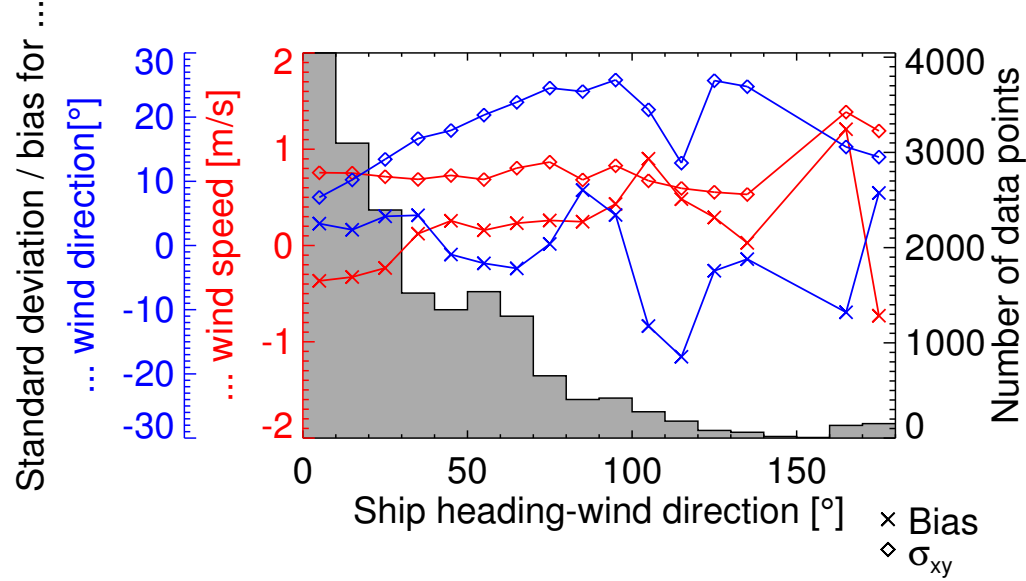


Figure 3.21: Standard deviation (marked by diamonds) and bias (crosses) for wind speed (red curves) and direction (blue curves) measurements acquired by Anemometer-1 and estimates from the radar data as a function of the angle between the ship’s heading and the wind direction. A histogram showing the number of data points per  $10^\circ$  bin is plotted in the background.

$10^\circ$  bin. No statistics are shown for the  $140^\circ$  to  $160^\circ$  bins because they had under 20 data points. For the wind speed, assuming an even distribution of wind speeds over all bins, the data suggest that bias and standard deviation are mostly independent of the ship’s orientation towards the wind. This is an encouraging result as it indicates that our wind speed retrieval scheme successfully resolves the shadowing of the radar field of view issue discussed in section 3.4.3.1. For the wind direction retrieval, statistics are best when the ship is heading upwind or downwind and deteriorate slightly for a cross-wind heading. However, it must be noted that the ship had its heading upwind for the longest time period. Thus, additional data are needed to obtain more comprehensive results.

## 3.5 Discussion

A new method to determine wind speed and direction from nautical X-band radar images has been developed. Wind measurements from ship-mounted anemometers are affected

by the effect of the ship's hull and superstructures on the flow of air to the instrument. Even for anemometers at well-exposed locations, the wind speed error may reach up to 10%. Nautical radars can retrieve wind vectors from areas where the flow distortion due to the ship is strongly reduced or not present, and therefore present a viable alternative to traditional ship-based wind measurements.

Our wind retrieval algorithm has been applied to nautical X-band radar data collected within the 2010 Field Study for the ITOP program from *R/V Roger Revelle* over a period of nine days and covering two storms. The data set contains several long periods of heavy rain, which negatively affects the radar-based wind retrieval. To address this limitation, the percentage of radar image pixels with zero intensity has been identified as a rain criterion. Images where the zero pixel percentage is under 50% have been flagged as rain cases and excluded from the wind retrieval. Using wind measurements acquired by two ship-based anemometers, it has been demonstrated that the air flow is strongly distorted by the ship's hull and superstructures. The flow distortion depends on the relative orientation between ship heading and wind direction, which makes a correction difficult.

The wind direction is determined from the upwind peak in the radar backscatter dependency on antenna look direction, using a least-squares-fit method. The advantage of this novel approach with similarities to wind scatterometry is that the wind direction can be computed from radar data where significant image portions are shadowed by ship structures. By using the best-fit curve of the radar backscatter dependency on antenna look direction, the wind direction (direction of the maximum) can be determined even if it is located in the shadowed section of the image. Furthermore, our method does not require a correction for ship motion and can therefore be directly applied to data acquired from a moving platform. This is in contrast to previously proposed methods that retrieve the wind direction from wind streaks, which become visible in averaged radar images only. If the ship's position changes during an averaging period, averaging radar images without correcting for ship motion would risk obliterating the wind streak signal.

To retrieve wind speeds from radar backscatter images, an empirical model function has been derived using data from a storm that the ship encountered in August. The model function allows to determine the wind speed from a single image intensity value derived from the best-fit curve associated with the radar backscatter dependency on antenna look direction. It was successfully tested with another storm data set acquired in September. The radar based wind estimates agree well with the reference data.

The standard deviations found for the test data set are 0.78 m/s for the wind speed and 17.4° for the wind direction. These results for shipborne data are comparable with the 0.90 m/s and 12.8° standard deviations found by Dankert and Horstmann for X-band radar data collected from a fixed platform with similar wind speed ranges [30].

Future work will focus on extending this study to the full X-band radar data set from the 2010 ITOP Field Study on *R/V Roger Revelle*. A greater number especially of high and low wind speed scenarios is likely to improve the empirical model function for the wind speed retrieval. However, if a greater range of data is considered, the boundary layer stability may need to be included in the model function. Furthermore, it would be of interest to study the sensitivity of our wind retrieval scheme to variations in surface wave conditions. The wind direction retrieval, in particular under low wind speed conditions, might be improved by including the wind speed in our model for the radar backscatter dependency on the antenna look direction. This is because the assumed harmonic model function might not be accurate for low wind situations. The radar-based wind retrieval could be further improved if the rain recognition was applied to image subsections instead of using the full image. This would enable the identification and masking of local rain occurrences that are limited to small areas within the image. Finally, the Chi-Square values associated with each best-fit curve could be used to identify outliers due to bright targets such as ships in the radar field of view.

# **Chapter 4**

## **Ocean Surface Wind Retrieval from Stationary and Moving Platform Marine Radar Data**

### **Summary**

In this chapter we evaluate different methods to retrieve wind information from marine radar data. In contrast to traditional in-situ sensors, marine radar wind data cover a large area and therefore are much less susceptible to air flow distortion by the platform. Unlike previous studies that have been limited to fixed-platform data, this study includes data from a quasi-stationary and moving platform. Images collected with a standard marine HH-polarized X-band radar operating at grazing incidence angle exhibit a single intensity peak in the upwind direction. Marine radar images that are averaged over about 1 min may also show wind streaks, which are usually well-aligned with the mean surface wind direction. Here, we use both phenomena to retrieve wind directional information and compare results to determine the best approach under the given conditions. To retrieve wind speeds, an empirical model function which relates average backscatter intensity to wind speed is developed.

## 4.1 Introductory Remarks

This chapter studies the retrieval of wind information from marine radar data collected from *R/P Flip* and *R/V Sproul* during the ONR High Resolution Air-Sea Interaction (Hi-Res) experiment in June 2010.

Ocean wind measurements are crucial for the study of energy and momentum transfer from the atmosphere to the ocean as well as for gas-exchange processes at the air-sea interface. On ships, wind measurements are important for navigation and safety. Wind measurements from traditional in-situ sensors are influenced by the platform's effect on the flow of air to the instrument. Errors due to air flow distortion are highly dependent upon anemometer position, platform shape and motion, and relative wind direction. However, even for anemometers at a well-exposed location wind speed measurements may have an error of up to 10% [75]. Contrary to in-situ sensors, marine X-band radars can acquire wind vectors in areas where flow distortion due to the platform is not present or strongly reduced. Furthermore, the retrieval of wind information from the radar backscatter intensity of the ocean surface is independent of the sensor's installation height and motion.

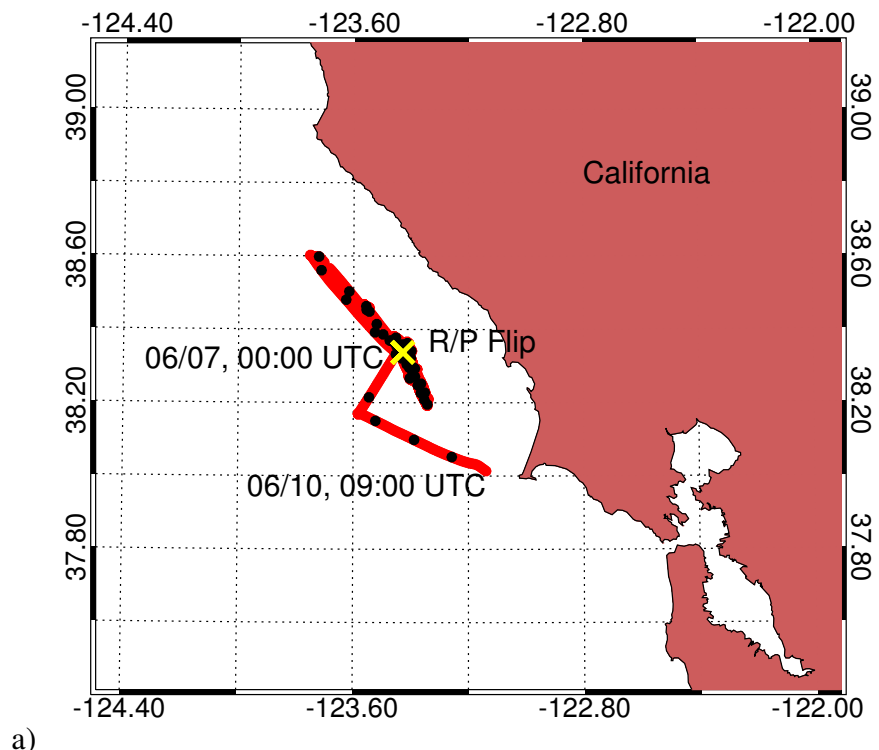
Marine X-band radars operate by transmitting and receiving pulses of microwaves that interact with the cm-scale sea surface roughness. The radar return from the sea surface has a strong dependence on both wind direction and speed [24]. Backscatter intensity images collected with HH-polarized X-band radars operating at grazing incidence angles exhibit a single peak in the upwind direction [118]. Radar images that are averaged over about 1 min may also show linear features, which are usually well-aligned with the mean surface wind direction. Furthermore, the radar backscatter intensity can be used to infer the wind speed [31].

Previous studies were limited to fixed-platform data and focused on wind streaks (e.g. [30]). Here, we use data from both a quasi-stationary and a moving platform. Therefore, in order to determine the best approach for either platform type, we have developed methods

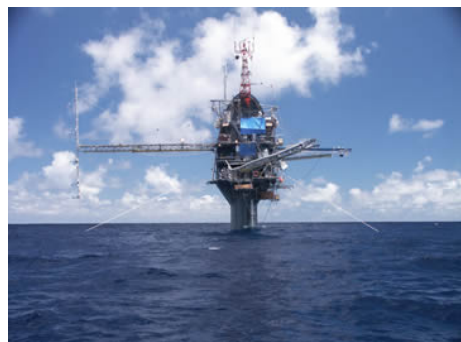
to retrieve wind directions from both the upwind peak and wind streaks. An empirical model function is derived to compute the wind speed from the average backscatter intensity.

## 4.2 Data Overview

The data used for the present work were collected during the ONR field experiment on High Resolution Air-Sea Interaction (Hi-Res) off the southern coast of California in June 2010. Our data were acquired from *Sprout* and *Flip* using standard Furuno marine X-band radars operating at 9.4 GHz with HH-polarization at grazing incidence angles. The radars have an antenna repetition frequency of 42 rpm with a sampling and pulse repetition frequency of 20 MHz and 3 kHz, respectively. With this configuration, radar backscatter images were collected every 1.5 s, covering a range from 120 to 3,960 m with a range resolution of 7.5 m. Each radar was connected to a wave monitoring system (WaMoS), which digitizes and stores the spatial and temporal radar backscatter information as a sequence of 12-bit images, i.e. digitized backscatter intensities range from 0 to 4,095 [139]. Note that for standard marine radars the backscatter intensity is not radiometrically calibrated. The reference data used to validate the radar-retrieved winds were acquired from anemometers at exposed locations on both platforms. The *Sprout* data were collected continuously from June 7 to 10, 2010 (a 5.5 hour-long period had to be disregarded because wind speeds were below 3 m/s, a minimum value for radar-based wind retrieval [47]), and the *Flip* data from June 7 to 16, 2010 (with several data gaps due to mechanical issues with the radar system). The *Sprout* and *Flip* data used here cover in total over 8 days, during which winds of 2 to 19 m/s coming mainly from northwest were encountered. Fig. 4.1 shows a map of the Hi-Res experiment with the location of *Flip* and the track of *Sprout* during the period studied here. Finally, note that we use 10-min running averages when comparing our radar winds with anemometer measurements.



a)



b)



c)

Figure 4.1: Map of Hi-Res experiment (a) and pictures of *Flip* (b) and *Sproutl* (c). Photo sources: <http://www.mpl.ucsd.edu/resources/flip.intro.html> and [http://shipsked.ucsd.edu/Ships/Robert\\_Gordon\\_Sproutl/photos.php](http://shipsked.ucsd.edu/Ships/Robert_Gordon_Sproutl/photos.php).

## 4.3 Wind Direction Retrieval

### 4.3.1 Wind Streaks

Wind streaks, which may be due to Langmuir circulation, are usually well-aligned with the wind direction. They become visible in marine radar images after averaging over about 1 min. The averaging is necessary to remove the otherwise dominating surface wave signal. To retrieve their orientation, we use a Radon transform based method [94]. The Radon transform is defined as

$$f(\rho, \alpha) = \iint_D I(x,y) \delta(\rho - x \cos \alpha - y \sin \alpha) dx dy, \quad (4.1)$$

where  $I$  represents the intensity level of the image at position  $(x,y)$ ,  $\delta$  denotes the Dirac delta function,  $\rho$  is the length of the normal from the origin to a straight line, and  $\alpha$  represents the angle between the normal and the x-axis. The main advantage of the Radon transform is that it enhances the signal-to-noise ratio of poorly defined linear features, facilitating their detection in marine radar images, which suffer from radar-inherent speckle noise. A similar approach has been used previously to retrieve wind directions from wind-induced streaks in synthetic aperture radar (SAR) imagery [126].

Fig. 4.2 shows the average of 32 radar images collected from *Flip* starting June 11, 2006, 00:00:28 UTC. For this image, the decrease of the radar backscatter intensity with range as well as its dependency on wind direction were removed by subtracting the radar backscatter ramp, which was obtained by convolving the averaged image with a Gaussian smoothing kernel. This is necessary because the Radon transform requires a homogeneous image to allow for an optimal detection of linear features. An additional processing step is required for data from the moving platform *Sprout*: As the spacing between wind streaks is of the order of 100 m, averaging a sequence of radar images without removing the ship motion would risk obliterating the wind streak signal. Therefore, we geolocated each in-

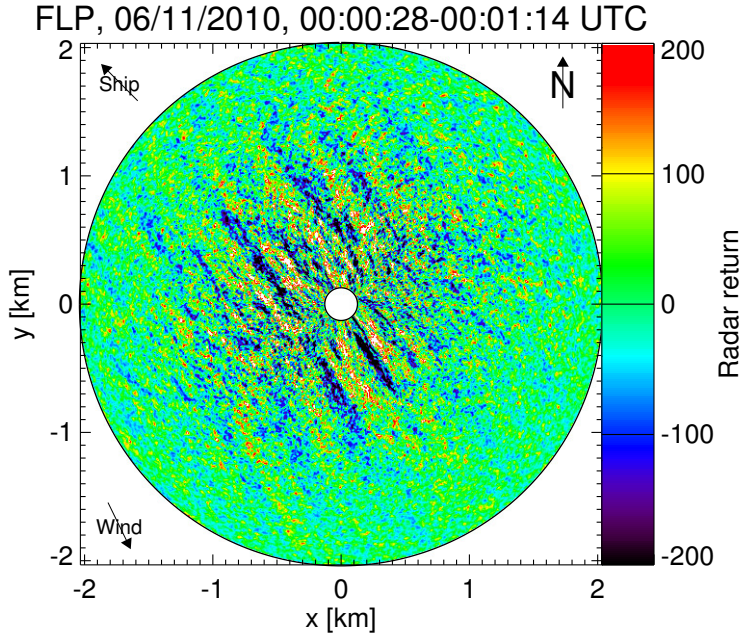


Figure 4.2: Average of 32 radar images collected from *Flip* starting June 11, 2006, 00:00:28 UTC.

dividual radar image to correct for the above-ground ship motion before averaging and simulate a fixed platform. Finally, our wind-streak analysis is limited to ranges from 120 to 2,000 m because wind streaks do not show well in far ranges, where the radar backscatter intensity is significantly reduced.

The Radon transform is performed for multiple circular boxes that cover the entire averaged image (up to a range of 2 km). Here, we use transform boxes of 360 m (48 pixels) radius and 32-image averages (48 s). Fig. 4.3 shows the average backscatter intensity within such a box in Cartesian (a) and Radon space (b) (both with the same scale as Fig. 4.2). Note that we divided each data point in Radon space by the number of image pixels along its projection line. This is to prevent the subsequent linear feature detection from being biased towards projection lines that are characterized by the greatest number of pixels. Furthermore, we limited the Radon transform to projection lines that cover at least 68 image pixels. The plot on the right shows the standard deviation as a function of Radon projection angle. We use the average of the directions associated with the standard devia-

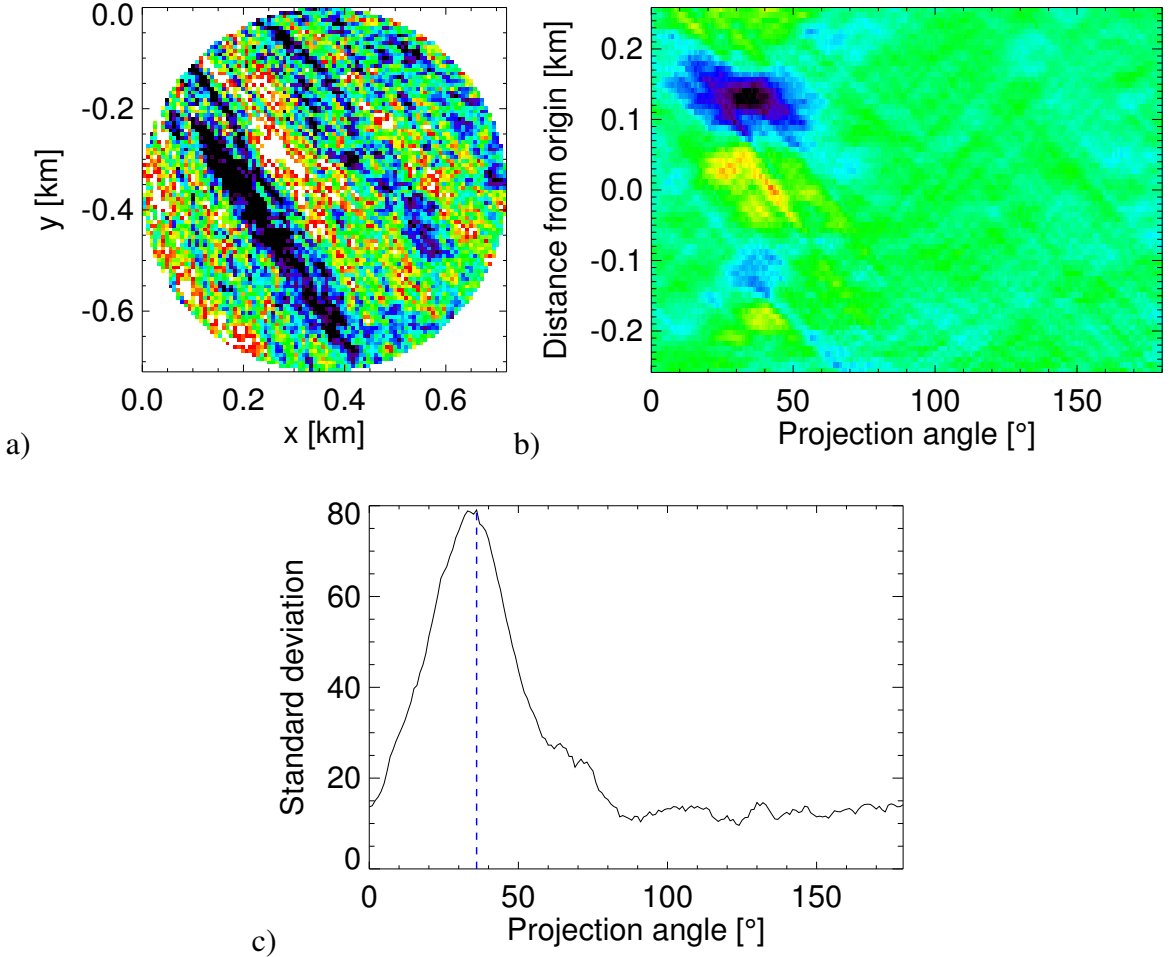


Figure 4.3: Example of average backscatter intensity for a given transform box in Cartesian (a) and Radon (b) space. The standard deviation as a function of Radon projection angle is given on the right (c).

tion peaks from each box as the wind streak direction (counter-clockwise from north). The inherent  $180^\circ$  ambiguity of this approach is resolved using a rough estimate of the upwind peak (see below).

For the 15,078 (6,059) *Flip (Sprout)* radar and anemometer wind direction measurements, a mean directional difference length of  $0.99$  ( $0.97$ ), a bias of  $-2.1^\circ$  ( $-9.0^\circ$ ), an RMS difference of  $9.9^\circ$  ( $17.1^\circ$ ), and a standard deviation of  $9.6^\circ$  ( $14.5^\circ$ ) is found. The mean directional difference length is obtained by combining the unit difference vectors via vector summation and dividing the resulting vector's length by the number of data points.

The differences between the fixed and moving platform data suggests that the ship motion correction has a detrimental impact on the streak-based wind direction retrieval.

### 4.3.2 Upwind Peak

For HH-polarized X-band radars operating at grazing incidence angles a single intensity peak is observed upwind, which can be explained by scattering due to small scale breaking waves that are most prominent forward of the crest of the long waves [118]. The advantage of an upwind peak based approach is that no geolocation is required. However, the azimuthal coverage must be at least 180°.

Fig. 4.4 shows the radar backscatter intensity as a function of antenna look direction (where 0° corresponds to north) for a *Flip* image that was collected on June 11, 2006, 00:00 UTC. It was obtained by integrating all radar pulses over range. A cosine-squared function

$$I_\Theta = a_0 + a_1 \cos(0.5(\Theta - a_2))^2 \quad (4.2)$$

was least-squares fitted to the data. Here,  $I_\Theta$  is the average radar backscatter intensity as a function of azimuth,  $a_0$ ,  $a_1$ ,  $a_2$  are the regression parameters, and  $\Theta$  is the antenna look direction. The best-fit curve is shown in blue. The upwind peak direction is given by regression parameter  $a_2$ , which corresponds to the peak of the best-fit curve. For this case, the upwind peak direction is 324° and the reference wind direction is 332°. Note that with this approach, the upwind peak can be determined even if it is located in a section of the radar image that is shadowed by platform structures or masked due to land (see chapter 3). The pronounced dips in the backscatter intensity at 155° and 325° roughly correspond to the downwind and upwind directions and are due to the wind streaks (compare Fig. 4.2).

For the 494,602 (193,899) *Flip (Sproul)* radar and anemometer wind direction measurements, a mean directional difference length of 0.99 (0.99), a bias of 1.5° (-3.0°), an RMS difference of 6.2° (6.9°), and a standard deviation of 6.0° (6.2°) is found.

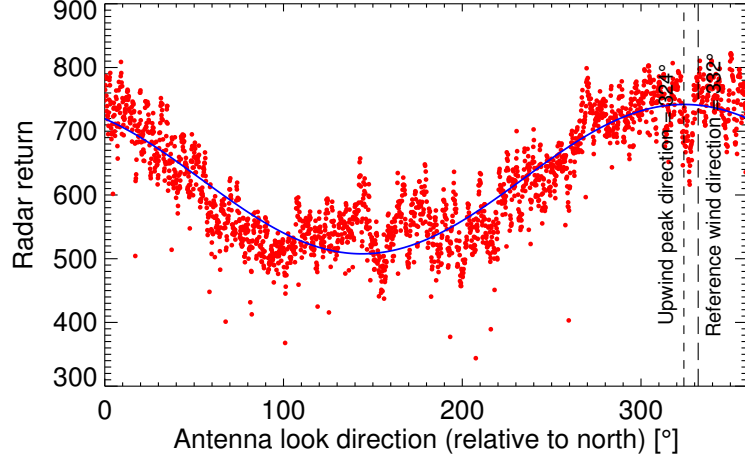


Figure 4.4: Radar backscatter intensity as a function of antenna look direction (relative to north) for *Flip* image collected on June 11, 2006, 00:00 UTC. The corresponding best-fit curve is shown in blue.

## 4.4 Wind Speed Retrieval

We have evaluated various radar backscatter parameters to determine which correlates best with the wind speed (e.g. the average radar backscatter intensity within specific ranges or from cross-wind directions only). Best results are obtained by using the most straightforward method, which is to evaluate the average backscatter intensity of the entire radar image. However, the data sets used here are special in that the radar fields of view cover 360°, which is generally not the case (e.g. due to shadowing by platform structures or masking of land areas for coastal stations). For a station where a significant portion of the radar field of view is shadowed, it has been found that results improve if instead one uses the average of the best-fit curve that is obtained by fitting Eq. (4.2) to the radar backscatter intensity as a function of antenna look direction, excluding all obstructed pulses [69].

An empirical model function to retrieve wind speeds from the radar backscatter intensity values is obtained by fitting a second-degree polynomial function to the reference wind speed and radar backscatter data pairs. (Note that in chapter 3, a third-degree polynomial fit was used instead, as it yielded wind speeds that were in better agreement with the reference

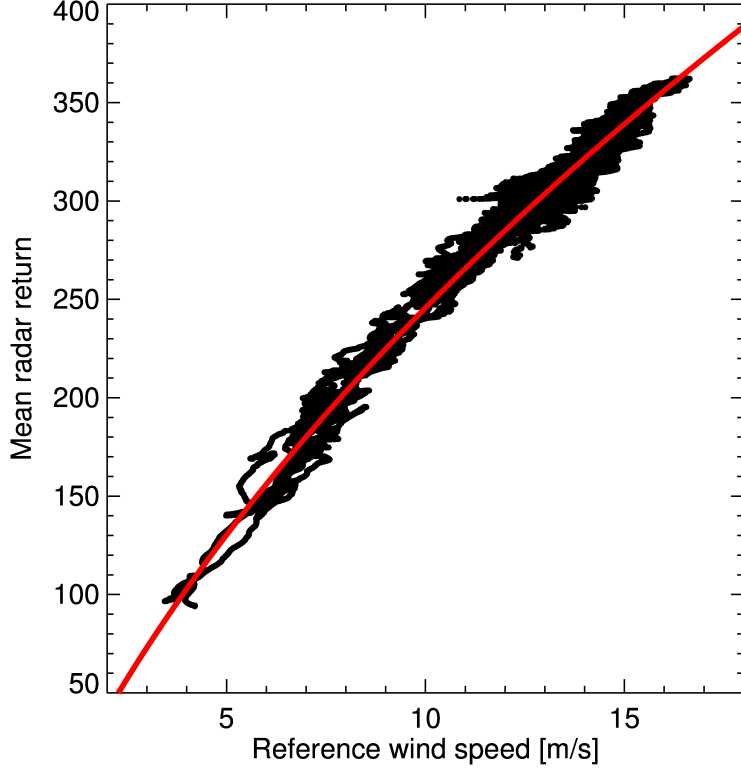


Figure 4.5: Scatter plot of radar backscatter intensity and reference wind speed for *Flip*. The empirical model function is shown in red.

data. This indicates that the choice of model function depends on the given radar installation. For example, a higher gain setting may result in image saturation, which weakens the radar return especially at high wind speeds.) The model function for *Flip* is shown in Fig. 4.5. In contrast to the neural network approach introduced by Dankert and Horstmann [30], this method uses a single parameter, which simplifies the wind speed retrieval significantly. Since marine radars are not radiometrically calibrated, an empirical model function must be derived for every individual radar system. However, this is a simple procedure that can be accomplished with only a few days worth of data covering a preferably wide range of wind speeds.

For the 311,807 (181,973) *Flip* (*Sprout*) radar and anemometer wind speed measurements, a correlation coefficient of 0.99 (0.99) and a standard deviation of 0.42 m/s (0.62 m/s) is found.

## 4.5 Discussion

We have developed new methods to retrieve wind vectors from marine radar images and have applied them to moving and fixed platform data collected during the 2010 Hi-Res experiment. Marine radar wind data are much less likely to be influenced by air flow distortion around the platform, and therefore present a viable alternative to traditional in-situ wind measurements.

Fig. 4.6 shows a time series of radar wind estimates and reference measurements for *Sprout* and *Flip*. Time gaps are indicated by vertical dashed lines and the transition from *Sprout* to *Flip* data by a solid line. Wind directions that were obtained using the upwind peak method show a better agreement with the reference data than those obtained from the wind streaks (standard deviation of  $6.0^\circ$  ( $6.2^\circ$ ) versus  $9.6^\circ$  ( $14.5^\circ$ ) for *Flip* (*Sprout*)). For the wind streak based approach, the difference between fixed and moving platform indicates that the ship motion correction affects the wind retrieval negatively. The wind speed results, with a standard deviation of  $0.42$  m/s ( $0.62$  m/s) for *Flip* (*Sprout*), show that marine radars with an unobstructed field of view yield highly reliable wind speed estimates for both fixed and moving platforms.

In our future work, we will continue developing marine radar wind retrieval methods and try to determine the best methods for different scenarios. For example, a wind streak based method may be preferable for stations where a significant portion of the radar field of view is obstructed. And even though the upwind peak method appears to yield best results, our Radon transform based wind streak analysis allows us to study the spacing and temporal evolution of such linear features, which may improve our understanding of the underlying oceanic (or atmospheric) phenomenon. For the wind speed, we will explore alternative methods that do not require a calibration, e.g. based on the local image flow.

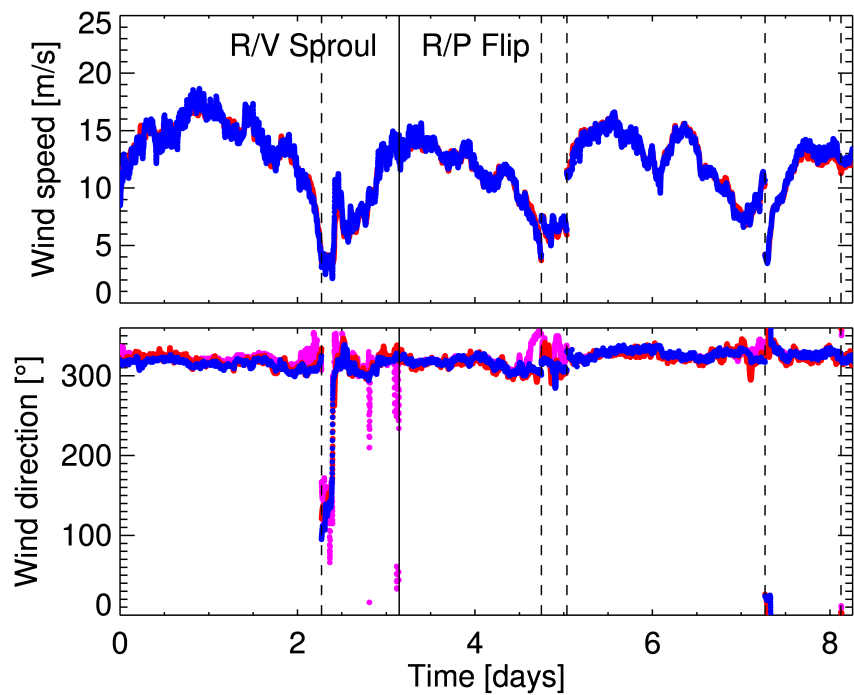


Figure 4.6: Time series of wind measurements from reference sensors (blue) and radars (wind speed and upwind peak direction in red, wind streak direction in magenta) for *Sproul* and *Flip*.

# **Chapter 5**

## **Analysis of Internal Wave Signatures in Marine Radar Data**

### **Summary**

Satellite images have long been used to study surface manifestations of internal waves (IWs). More recently, marine X-band radar data have been employed to retrieve IW packet parameters. Marine radars have the advantage over satellite systems that their high temporal resolution enables the study of the IW evolution. Until today, no method to automatically detect IW surface signatures in marine radar data has been suggested. In this study, we present a new fully automated tool to retrieve IW signatures from marine radar image sequences. First, after various pre-processing steps, the IW packet velocity is determined using a combination of localized Radon transform and cross-correlation techniques. Temporal averaging of the marine radar data significantly enhances the IW signatures. The knowledge of the IW packet velocity is used to correct for the IW motion, enabling us to extend the averaging period, which further enhances the IW signal. An IW-motion correction is necessary because otherwise the IW signal would become smeared if the averaging period were much longer than the time it takes the IW to propagate between radar resolution cells. The IW-enhanced images are then utilized for the IW signature analysis. Here, we

identify local backscatter peaks and exploit the marine radar’s high temporal resolution to distinguish signal from noise. The resulting series of IW soliton maps provides information on changes in soliton wavelength, velocity, and backscatter intensity. Our marine radar IW signature analysis tool therefore offers a great opportunity of studying the spatio-temporal evolution of IWs as they grow and decay.

## 5.1 Introductory Remarks

This chapter presents a novel tool to automatically detect and retrieve IW signatures within marine radar image sequences. IWs are ubiquitous features of coastal oceans and play an important role in tidal energy transport [49]. Their dissipation induces intense vertical mixing that may result in resuspension of bottom sediment [77] and affect biological processes such as the supply of nutrients [48] or the distribution of larvae and plankton [103, 84]. Furthermore, IWs affect underwater acoustics and the strong currents and shears associated with them pose a potential threat to offshore structures [21].

Satellite images have long been used to study IW surface manifestations in coastal oceans and derive IW parameters such as propagation direction, crest length, wavelength, and number of solitons (e.g. [38, 5, 67, 59]). Thanks to their wide geographic coverage, satellite images may furthermore contain information on the spacing between individual wave packets. Assuming a tidal generation mechanism, the inter-packet spacing can be used to estimate the IW phase speed.

In contrast to satellite data, where an IW packet is generally imaged only once, and in-situ measurements that provide “point” observations, marine radars with their high spatio-temporal resolution make it possible to study the evolution of a packet. This is particularly the case for shipborne marine radars, since a ship can follow an IW over long distances. Marine radar data were first used by Watson and Robinson in 1990, to study the evolution of IWs at the Strait of Gibraltar using photographs of the marine radar screen [128], and

later in 2003 by Orr and Mignerey, who used marine radar data to track IWs in the South China Sea [81]. While drawing attention towards the potential of marine radar data for studying the IW evolution, both studies retrieved IW signatures manually with low temporal resolution and significant errors. Furthermore, they observed IWs that are characterized by a single prominent soliton that is easier to detect than a packet of solitons with partly very weak surface manifestations. More recently, it has been shown that the marine radar backscatter intensity can be used to estimate IW horizontal velocity convergence and amplitude [23]. Pan and Jay used marine radar images to track IW packets at the Columbia River plume [83]. Ramos et al. [96] have introduced a method to retrieve IW packet parameters from marine radar data, which has since been employed by Zha et al. [137] to estimate the force exerted by IWs on a cylindrical pile. Finally, Plant et al. [91, 90] employed a dual-polarized, coherent, X-band radar to study the modulation of the normalized radar cross section by IWs, as well as the characteristics of IWs in the South China Sea.

Marine radars operate by transmitting and receiving pulses of microwaves that interact with the rough sea surface. IWs are accompanied by a spatially and temporally varying surface current field. The radar echo from the sea surface is primarily dependent on small-scale ripple waves due to Bragg scattering. Marine radars generally show IWs as adjacent bands of weak and strong backscatter that propagate at the IW packet's velocity. Like for synthetic aperture radar (SAR) images, such features result from hydrodynamic interactions between the short surface waves and the horizontal surface currents caused by IWs [2]. Alternatively, at low wind speeds IW surface manifestations can result from surfactants that accumulate in flow convergence zones, where they dampen the short surface waves, producing a series of dark bands on a uniform background in a radar image [29, 35].

Here, we introduce a fully automated tool to retrieve IW signatures from marine radar data. With this goal in mind, we first determine IW packet direction and speed using localized Radon transform and cross-correlation techniques, respectively. The IW signal is enhanced by temporal averaging after correcting for horizontal platform and IW packet

motion. The IW-enhanced images are then utilized for the signature retrieval, taking advantage of marine radars' high temporal resolution. The resulting series of IW soliton maps provides a unique view of the spatio-temporal evolution of IWs. Beyond IW packet characteristics, such maps detail changes in wavelength, velocity, and backscatter intensity for each individual soliton. We use marine radar data collected from *R/V Oceanus* during the 2006 ONR Non-Linear Internal Wave Initiative (NLIWI) off the New Jersey coast to evaluate the tool and illustrate its capabilities.

This chapter is organized as follows: In section 5.2 we provide a description of the data used here. Our methodology is presented in section 5.3, which explains the individual steps necessary to obtain IW soliton maps from raw marine radar data. First results are presented in section 5.4. The chapter concludes with a discussion and outlook in section 5.5.

## 5.2 Data Overview

The data used for the present work were collected from *R/V Oceanus* during the NLIWI experiment off the coast of New Jersey from August 12 to September 11, 2006. NLIWI's goal is to investigate the impact of non-linear IWs on acoustic propagation and scattering in shallow water [114]. The experiment combined a great variety of instruments on different platforms including research vessels, moorings, aircraft, shore-based HF radar, Air–Sea Interaction Spar (ASIS) buoys, and satellite imagery.

During NLIWI, *Oceanus* sampled velocities and amplitudes associated with 27 distinct IW packets using shipboard acoustics at various locations over the continental shelf [107]. Fig. 5.1 shows a map of the NLIWI study area and mooring locations. It also shows the *Oceanus* track and local bathymetry as the ship was following an IW packet on August 14, 2006 from 04:00 to 23:00 UTC. During this period the IW packet was sampled in water depths ranging from 80 m, where IWs are typically still in the process of growing, to less

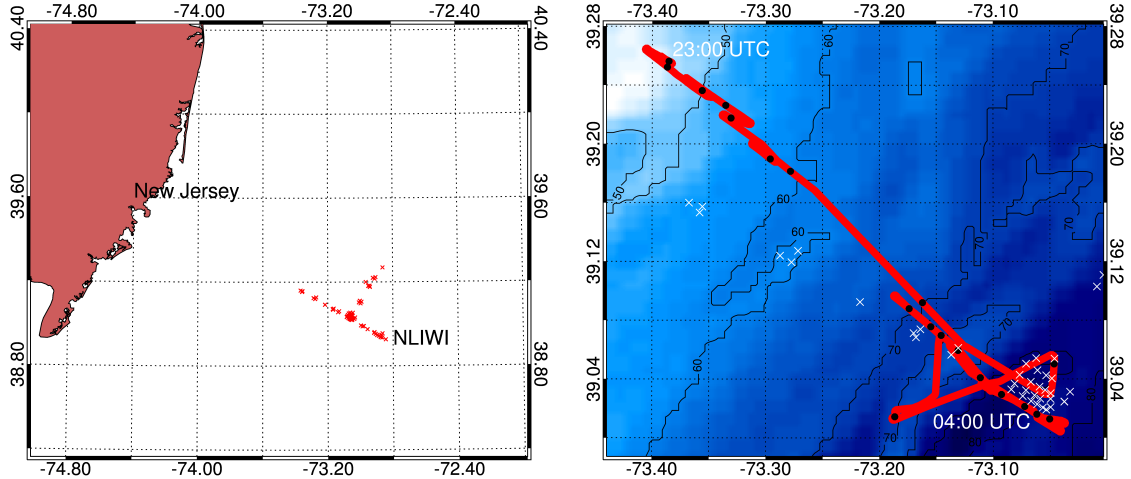


Figure 5.1: Overview map of NLIWI study area with mooring locations marked by crosses (left). Map detailing local bathymetry and *R/V Oceanus* track as it was following an IW packet on August 14, 2006, from 04:00 to 23:00 UTC. The ship track is shown in red, with each full hour marked by a black dot. Mooring locations are marked by white crosses (right).

than 50 m, where they start dissipating [107]. In this chapter, we will focus on a 1-hour period of data that were collected in approximately 80 m depth, starting 06:00 UTC.

Our marine radar data were acquired using a standard Furuno marine X-band radar operating at 9.4 GHz with HH-polarization and grazing incidence angle. The radar has an antenna repetition frequency of 24 rpm with a sampling frequency of 20 MHz. With this configuration, radar backscatter images were collected every 2.5 s, covering a range from 60 to 3,900 m with a range resolution of 7.5 m. The radar was connected to a Wave Monitoring System (WaMoS), which digitizes and stores the spatial and temporal radar backscatter information as a sequence of 12-bit images, i.e. digitized backscatter intensities range from 0 to 4,095 [140]. Note that for standard marine radars the backscatter intensity is not radiometrically calibrated.

Depending on the radar antenna's position on the ship, a section of the radar field of view may be obstructed by ship structures. To eliminate random speckle noise and determine the area over which the radar has an unobstructed field of view, radar images can be averaged. Fig. 5.2 shows a 10-min averaged ship-heading-oriented radar backscatter image

collected from *Oceanus*. Here, we consider antenna look directions with range-averaged backscatter intensities below 700, corresponding to a 22°-wide window towards the ship’s stern, to be masked by the main mast. This threshold was chosen manually to maximize the amount of data available for the subsequent IW signature retrieval. Furthermore, data collected in the near range from 60 to 350 m are saturated with backscatter values at or near the maximum of 4,095. In the following, our IW retrieval is limited to unmasked and unsaturated image sections.

## 5.3 Methodology

The retrieval of IW soliton maps from raw marine radar data consists of the following steps: Pre-processing of the data (Section 5.3.1), determining IW packet characteristics (5.3.2), producing IW-enhanced radar images (5.3.3), and retrieving IW surface signatures from IW-enhanced images (5.3.4).

### 5.3.1 Data Pre-processing

The goal of the marine radar data pre-processing described here is to ensure correct mapping of the radar pulses in space-fixed (versus ship-fixed) Cartesian coordinates and to remove radar image artifacts as well as sources of backscatter that are unrelated to the sea surface. The flow chart in Fig. 5.3 details our pre-processing scheme. Note that these pre-processing steps could easily be implemented in the marine radar data acquisition system. However, as of now, except for a bearing control that tracks antenna speed changes with wind loading, the standard WaMoS software provides no such capabilities.

#### 5.3.1.1 Azimuthal Position of Radar Pulses

Starting with the raw marine radar data in polar coordinates, we must first determine the correct azimuthal position of each radar pulse accounting for both ship heading changes

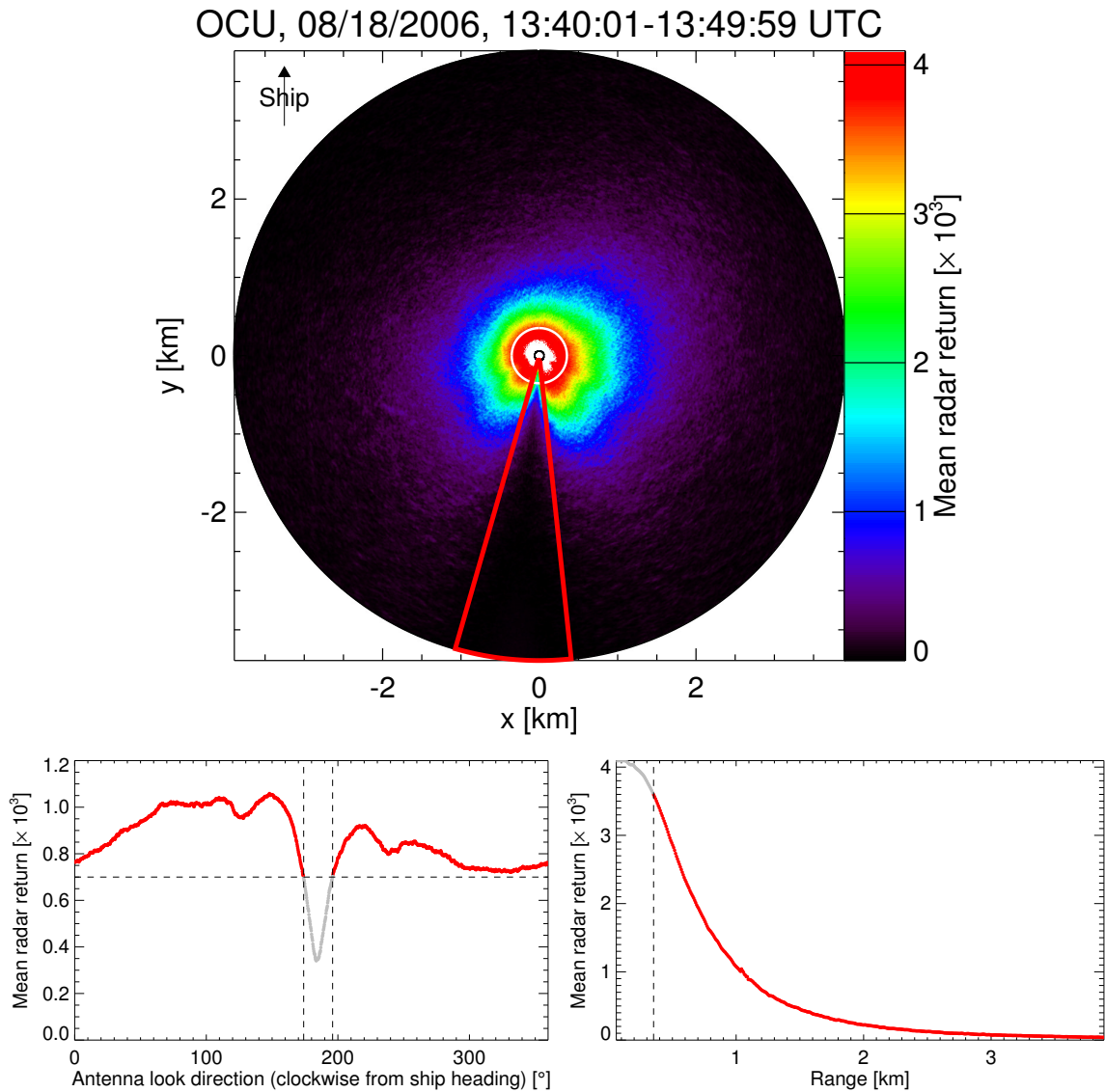


Figure 5.2: Average of ship-heading-oriented radar backscatter images collected from *Oceanus* on August 18, 2006, from 13:40 to 13:50 UTC, with masked area framed in red and saturation area marked by white circle (top). The corresponding mean backscatter intensities as functions of antenna look direction (left) and range (right) are shown at the bottom with masked or saturated data, respectively, marked in gray.

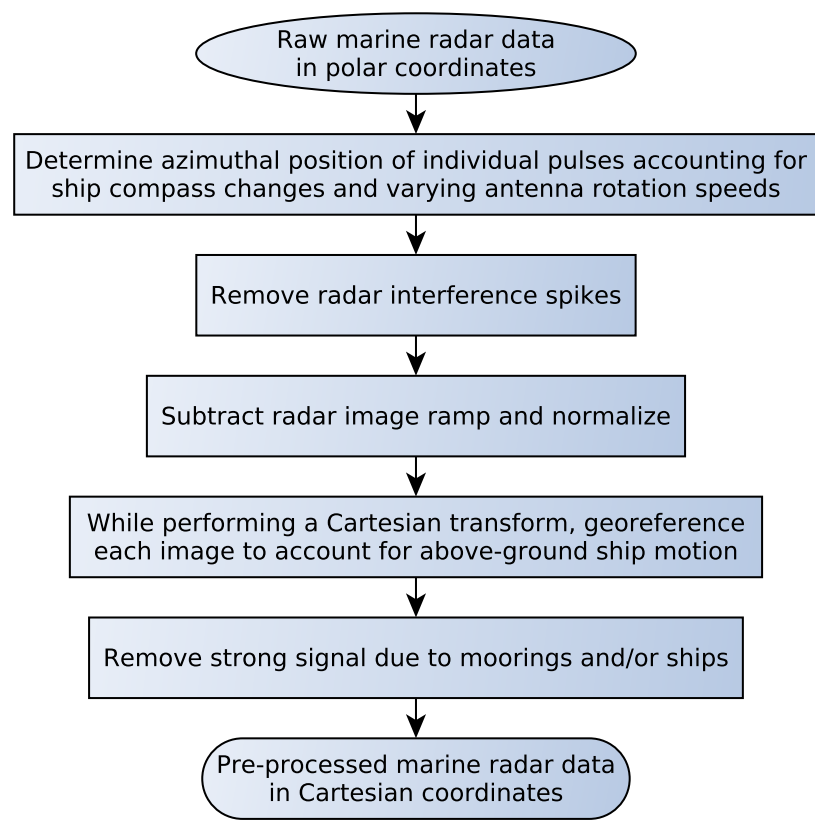


Figure 5.3: Marine radar data pre-processing scheme.

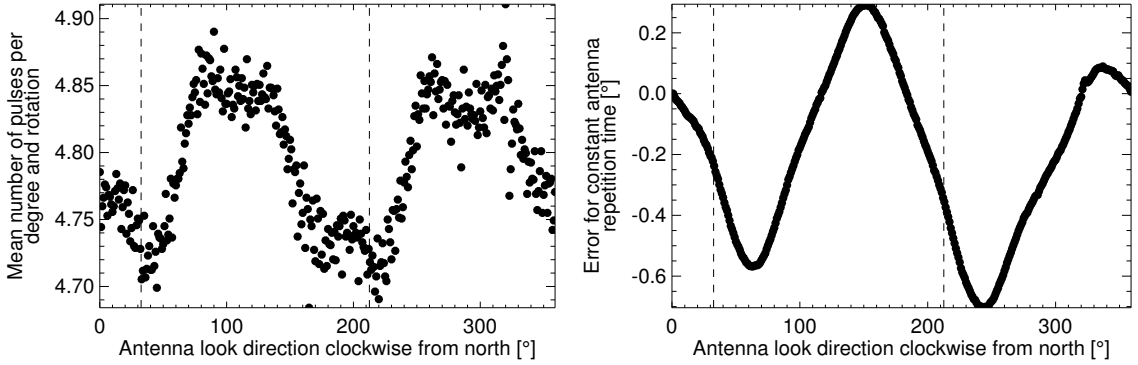


Figure 5.4: Mean number of radar pulses per degree clockwise from north obtained from *Oceanus* over a 1-hour period starting August 15, 2006, 12:00 UTC (left). Corresponding pulse position error if a constant antenna repetition time is assumed (right). Vertical bars mark the up- and downwind directions.

and varying antenna rotation speeds. This is important because at a later stage we will average our radar data in order to enhance the IW signal, and incorrect mapping of the individual radar pulses would result in a blurred signal. For example, at the maximum range of 3.9 km, a  $1^\circ$  error in the azimuthal pulse position results in a pixel being placed  $\sim 70$  m from its true position. With a typical wavelength of about 200 m, this is a significant error for IWs.

Fig. 5.4 shows the mean number of radar pulses per degree clockwise from north obtained from *Oceanus* over a 1-hour period starting August 15, 2006, 12:00 UTC. During this period a strong wind averaging 12 m/s was coming from south-southwest. The figure illustrates the antenna rotation speed's dependency on the wind, with the number of pulses per degree reaching troughs when the antenna is looking up- or downwind and peaks at the two cross-wind positions. In addition, the figure gives the resulting error, ranging from  $0.3^\circ$  to  $-0.7^\circ$ , if a constant antenna repetition time is assumed. Therefore, we can conclude that neglecting the antenna rotation speed's variability would result in significant errors. However, since our marine radar data contain a record of every  $1^\circ$ -change in the antenna orientation relative to the ship heading, we can easily determine the correct azimuthal position for each radar pulse, resulting in an irregularly gridded polar image.

The histogram in Fig. 5.5 shows ship heading changes within the antenna repetition time of 2.5 s for August 14, 2006, from 04:00 to 23:00 UTC. As the ship was tracking an IW packet during this period, it regularly reversed course, resulting in heading changes of up to  $\pm 4^\circ$  during a single antenna revolution. In order to obtain north-oriented radar images, we must determine the ship's heading change during each antenna revolution and adjust the azimuthal position of each pulse accordingly. This correction is complicated by the fact that the software version of the WaMoS digitization system at the time of the experiment updated the gyroscope record only in 15-s intervals and logged the time at which each radar image was sampled with only 1-s accuracy. Therefore, we had to do a correction using the ship's gyroscope record (with 1-s resolution), which we collocated with our (inaccurate) image acquisition times. From the ship heading change during each antenna revolution we then derive a rate of change (assumed to be constant) to determine each radar pulse's correct orientation relative to north. Since we do not know the exact image acquisition time, a small error in the resulting corrected radar pulse orientations is bound to remain. But because we will consider a large number of images when retrieving IW signatures, this error can be assumed to average out. Note that the antenna look direction may furthermore be influenced by the ship's pitch and roll, which we do not account for. This may introduce an additional error in the assigned pulse position. We assume this error to be small on average, however, it could be corrected in the future using data from a motion sensing package [50].

### 5.3.1.2 Radar Interference Spikes

The presence of other marine radars on ships in the area can manifest itself by interference spikes in the raw radar data. Fig. 5.6 shows a zoom into a raw marine radar image in polar coordinates with multiple interference spikes, which appear as high backscatter intensity pixels neighboring in range direction. Such spikes represent noise that needs to be removed because it may overshadow our IW signal, especially in the far range where backscatter

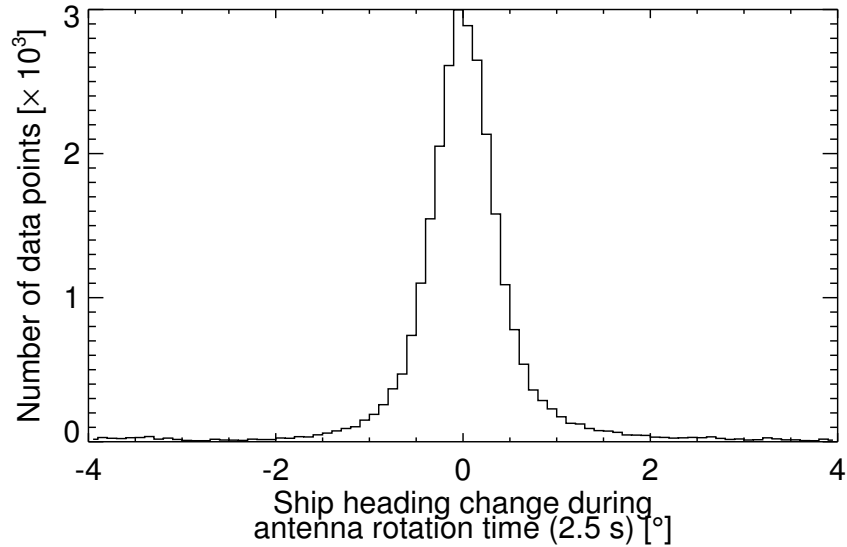


Figure 5.5: Histogram of ship heading changes within antenna repetition time (2.5 s) for August 14, 2006, from 04:00 to 23:00 UTC.

intensities are low. This can be achieved by convolving a  $3 \times 3$ -pixel kernel, where the first and last row are set to -1 and the middle row is set to 2, with the raw polar image. In the resulting image, interference spikes can easily be identified as data points that are greater than 4,095 (the raw data's maximum intensity) and that form a range-oriented cluster with a minimum length of 4 pixels. Each pixel element of the thus identified interference spikes is then replaced by the mean of its neighboring non-spikes pixels, generally originating from the previous and subsequent radar pulse. As Fig. 5.6 illustrates, this procedure successfully removes interference spikes.

### 5.3.1.3 Radar Backscatter Ramp Correction and Normalization

In a next step, the radar backscatter ramp, i.e. the general dependency of the radar backscatter intensity on range and antenna look direction, must be removed from the marine radar data. This is necessary since the IW retrieval techniques we develop in sections 5.3.2 and 5.3.4 require homogeneous radar images.

For a 1-min-long sequence of marine radar images collected on August 14, 2006, 06:12 UTC, Fig. 5.7 illustrates the radar backscatter dependency on range and antenna look

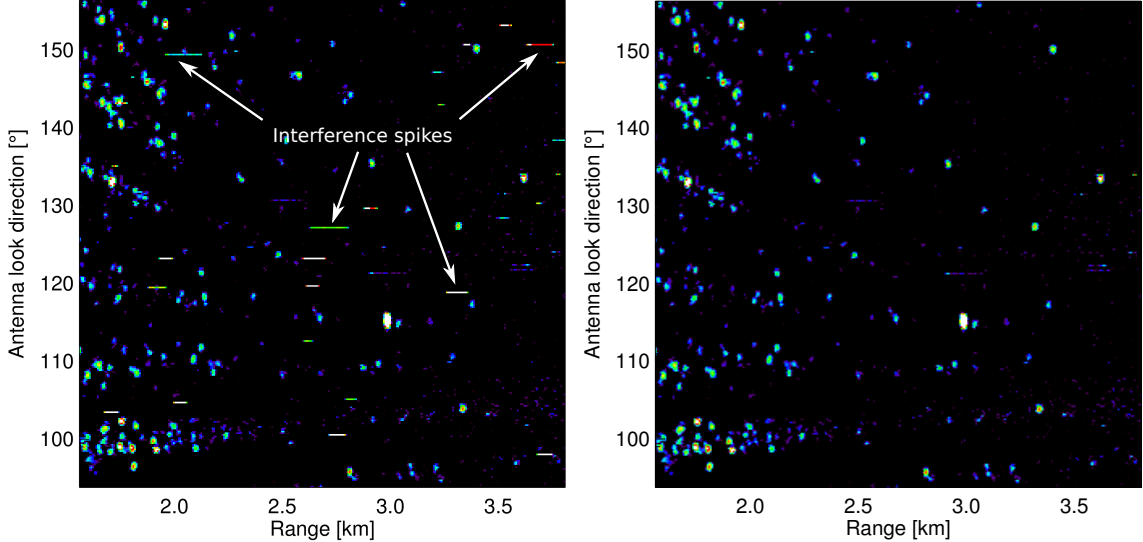


Figure 5.6: Zoom into raw polar marine radar image with radar interference spikes (left) and after correction (right). The data were collected on August 14, 2006, 00:01 UTC.

direction. Best-fit-curves, obtained using empirical model functions, are shown for each dependency. At the time, the ship anemometer measured a 7.7 m/s wind coming from west-southwest. To obtain the backscatter dependency on range (Fig. 5.7a), all unobstructed radar pulses were averaged over antenna look direction. The figure shows that the radar image intensity decreases rapidly in the near-range and more slowly in the mid- to far-range, which can be explained by the decay of received electromagnetic energy with distance. The backscatter dependency on antenna look direction (Figs. 5.7b and c) was obtained by averaging all radar pulses over range. The best-fit curve has a peak in upwind direction, and its average intensity can be correlated with the wind speed. Therefore, it offers a means of estimating the wind speed and direction from marine radar data [69]. Fig. 5.7d shows how the amplitude of directional radar backscatter intensity variations depends on range: At first the amplitude increases, reaching a maximum of  $\sim 1,660$  at 750 m, then it decreases to values as low as  $\sim 10$  at 3900 m. The relatively low amplitude at the very near range can be explained by image saturation, which is not an issue at greater ranges.

To construct the radar backscatter ramp, we use a least-squares fit technique that combines our model functions for the backscatter dependency on range and antenna look di-

rection, accounting for directional radar backscatter intensity variations that are changing with range. The resulting ramp function has the following characteristics: Its intensity has a peak in upwind direction; the difference between up- and downwind intensity first increases and then decreases, as shown in Fig. 5.7d; its mean intensity in range is controlled by the fitted backscatter dependency on range (see Fig. 5.7a).

Our assumption that the backscatter intensity has an upwind peak at all ranges may not be evident, since the incidence angle changes with range. This may in turn result in varying backscattering mechanisms. However, the change in the incidence angle from near to far ranges is small, suggesting that any changes to the backscattering mechanisms would be minor. Furthermore, by averaging over a large number of images, it can be shown that an upwind-peak is in fact found at all ranges.

The polar radar image in Fig. 5.8a is the first image collected during our 1-min-long sequence from August 14, 2006, 06:12 UTC. An IW packet is clearly visible at antenna look directions from  $50^\circ$  to  $210^\circ$  and ranges greater than 1 km. The decrease in the backscatter intensity around  $115^\circ$  can be attributed to masking by ship structures. The corresponding ramp image shows similar characteristics (see Fig. 5.8b). However, it is much smoother, does not have a masked section, and shows no IW signal. By subtracting the ramp from the mean image, we obtain a ramp-corrected radar image with a mean intensity near zero (Fig. 5.7c).

Comparing ramp-corrected backscatter intensities in the image's near-range section with those from the far range, reveals that the variability is significantly enhanced for ranges less than  $\sim 1,500$  m. Fig. 5.9a shows the radar backscatter intensity's standard deviation as a function of range, computed from the same 1-min sequence of marine radar data we've studied before. The standard deviation curve has a similar shape as the amplitude (compare Fig. 5.7d). It reaches its peak of 1,510 at  $\sim 850$  m and then decreases towards its minimum of 110 at 3,900 m. As for the amplitude, the relatively low standard deviation at the very near range can be explained by image saturation. In order to obtain images with similar

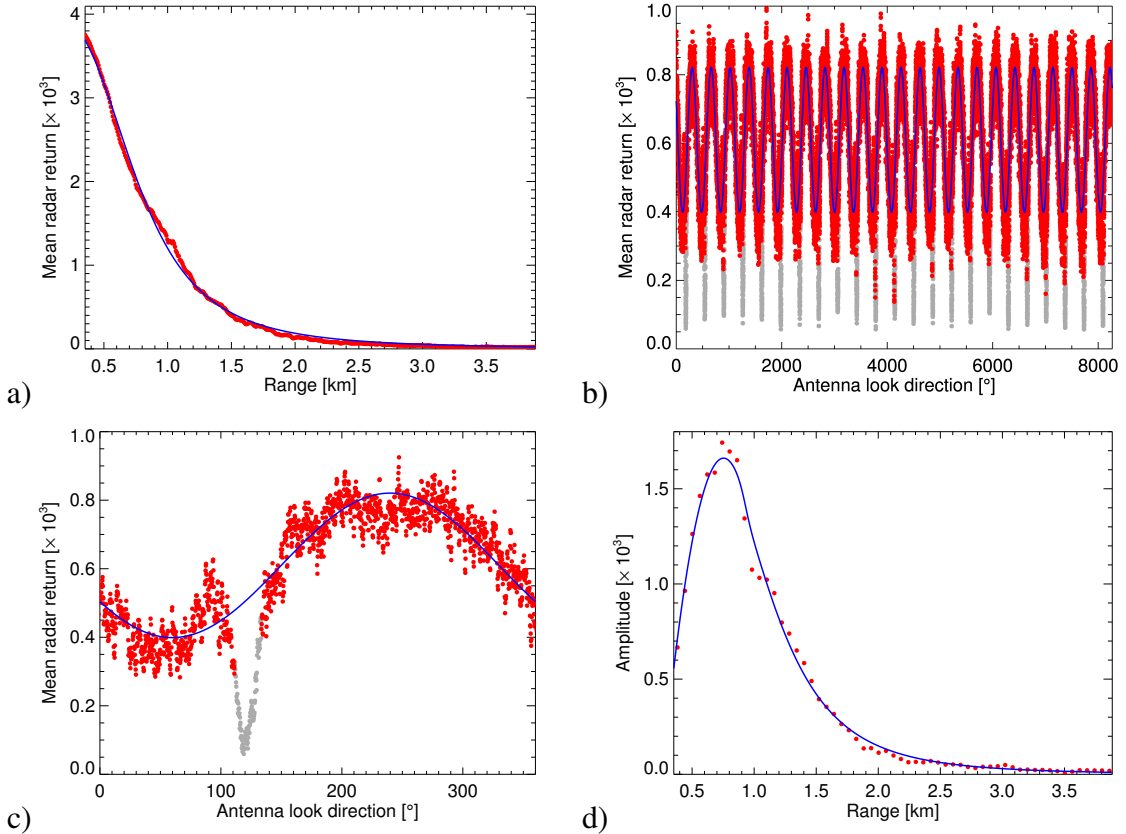


Figure 5.7: Mean radar backscatter intensity as function of range computed from 1-min-long sequence of marine radar images collected on August 14, 2006, 06:12 UTC (a). Corresponding mean radar backscatter intensity as function of antenna look direction (clockwise from north) (b). Zoom into data of first image (c). Amplitude of directional radar backscatter intensity variations computed for a range-shrunk version of same 1-min data set (d). In all four plots, the radar measurements are shown in red and the least-squares-fit curves in blue. Measurements from masked antenna look directions are displayed in gray.

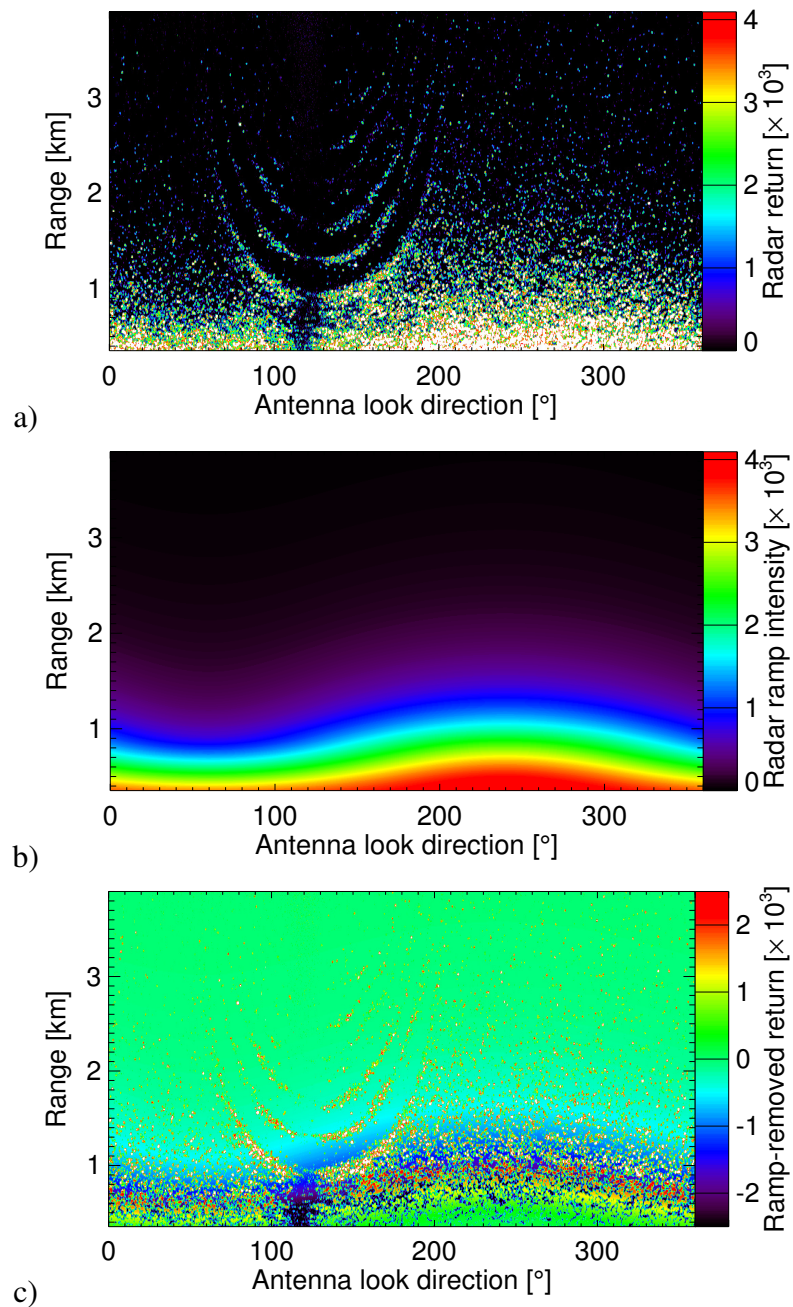


Figure 5.8: Marine radar image in polar coordinates from August 14, 2006, 06:12 UTC (a). Corresponding ramp image obtained from empirical model function (b). Resulting ramp-subtracted image (c).

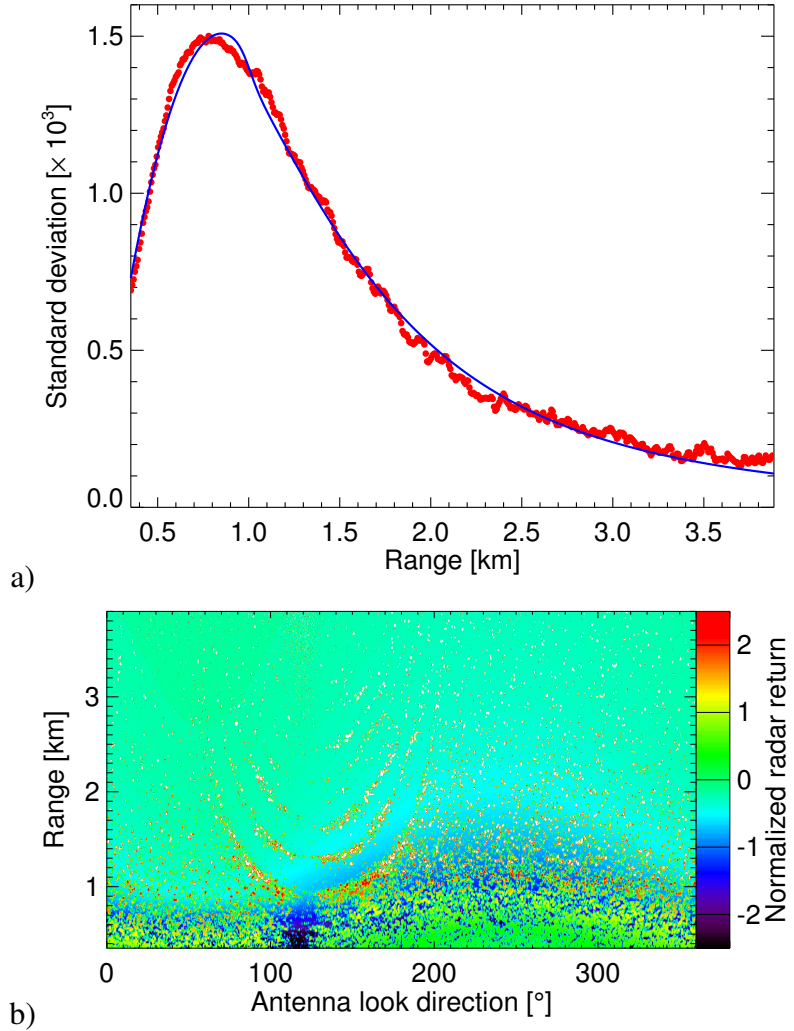


Figure 5.9: Standard deviation as function of range for 1-min sequence of marine radar images from August 14, 2006, 06:12 UTC (a). Ramp-subtracted and normalized image from same sequence (b).

backscatter intensity levels from near to far range, we divide each pixel in range by its corresponding fitted standard deviation, which is obtained in the same way we derived our amplitudes [52]. Fig. 5.9b shows the resulting normalized image. The bulk of the normalized image's intensities ranges from  $-1$  to  $1$ , with occasional outliers that can be attributed to the masking by ship structures, the IW, surface waves, or bright targets such as ships or moorings (see Section 5.3.1.5).

The remaining image heterogeneities can be attributed to imperfections in the ramp model function and normalization approach. For example, Fig. 5.10 shows an image of

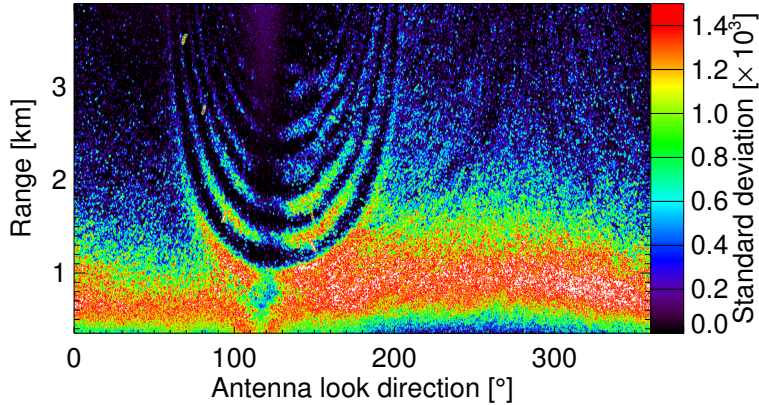


Figure 5.10: Image of standard deviation for 1-min sequence of marine radar images from August 14, 2006, 06:12 UTC.

the standard deviation computed from our 1-min sequence of pre-normalized marine radar data. It can be observed that the radar backscatter intensity's standard deviation changes depending on the relative angle between antenna look direction and wind direction. The range where the standard deviation reaches its maximum value is greatest where the antenna looks upwind ( $\sim 240^\circ$ ). Our assumption of a standard deviation that varies only as a function of range but not antenna look direction is thus inaccurate. Further research is required to derive a general rule from this observation. However, for this chapter's purpose, the resulting normalized radar images are sufficiently homogeneous.

#### 5.3.1.4 Georeferencing

By averaging a sequence of marine radar images, the IW signal becomes much stronger, and the radar's inherent speckle noise is reduced. Since the data used for this study were acquired from a moving platform, they have to be properly georeferenced before averaging. In section 5.3.1.1 we discussed how the correct azimuthal position of each radar pulse is determined. We now have to account for the horizontal ship motion. To simplify the georeferencing, we assume the ship to be stationary during each antenna revolution. This is in accordance with the georeferencing method suggested by Bell and Osler, who use shipborne marine radar data to derive the local bathymetry [11].

Here, we use ship positions with 1-s resolution that are obtained from the existing ship navigation system. The record of the ship position is then collocated with the image acquisition times. For a sequence of marine radar images, we can now easily determine the horizontal distance traveled by the ship relative to the ship position associated with the sequence's first image. With this information, our irregularly gridded north-oriented polar images can finally be transformed to Cartesian space. This is accomplished using a bilinear interpolation technique that takes the horizontal ship motion into account.

Fig. 5.11 shows a 1-min average of marine radar data from August 14, 2006, 06:12 UTC. Before averaging, the radar images were ramp-corrected, normalized, georeferenced, and transformed to Cartesian coordinates. The image's origin corresponds to the initial ship position. An IW packet propagating in a northwestern direction with the ship being as close as  $\sim 1\text{km}$  to the leading soliton is clearly visible. Note that image locations where radar data from less than 50% of the total number of radar images are available were disregarded. In addition, Fig. 5.11 shows an image that illustrates the data availability during the 1-min averaging interval. The image slice that contains no data corresponds to the masked area (see Section 5.2). Since the mask is due to the main mast, which relative to the radar antenna is located towards the ship stern, it provides a rough indicator of the ship's orientation. During the 1-min period studied here, the ship began traveling in a northwestern direction, but then changed course to north-northwest towards the end.

### 5.3.1.5 Bright Target Detection

Bright targets such as ships or moorings are the signal for most marine radar users, but in the context of this study they represent a source of noise. Within our normalized, georeferenced, and then averaged radar images, bright targets can easily be detected through a simple thresholding operation. Without radar ramp correction (and normalization), such a global operation would be impossible as it would always point towards near-range locations where the backscatter intensity is about two orders of magnitude greater than at far

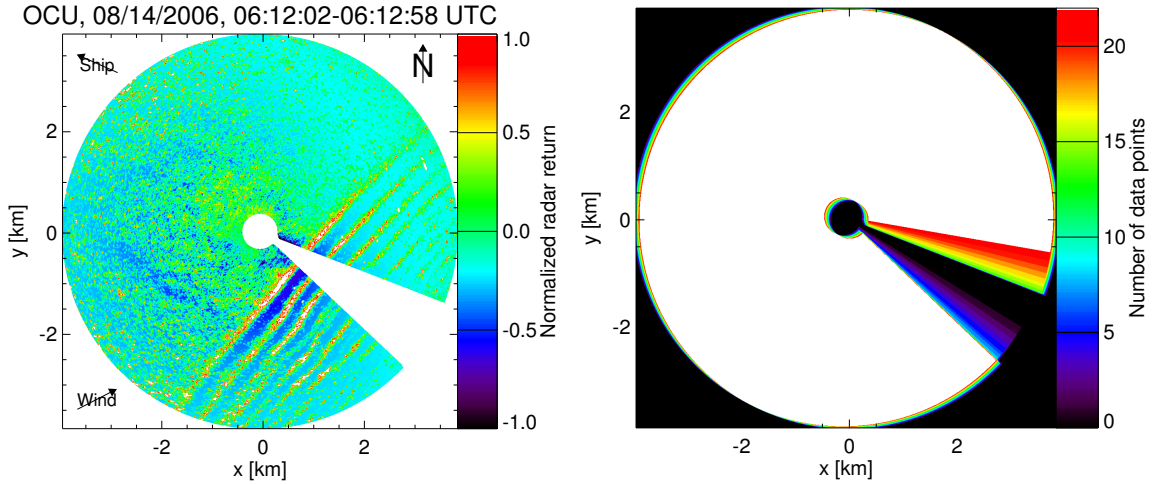


Figure 5.11: Normalized and georeferenced marine radar data averaged over a 1-min interval in Cartesian coordinates (left). The image origin corresponds to the ship position on August 14, 2006, 06:12:02 UTC. The sequence's last image was acquired at 06:12:58 UTC. Image locations at which radar data are available from less than 50% of the total number of radar images have been treated as if no data are available. The image on the right illustrates the data availability. For the white area, data from the full sequence (23 images) are available.

ranges. Here, we identify image clusters consisting of a minimum of 5 neighboring pixels with normalized backscatter intensities greater or equal 3 as bright targets. These clusters are dynamically extended by including adjacent pixels with intensities that are below the threshold of 3 but still significantly above the background. This is to ensure complete removal of the bright targets from the image. The thus identified bright targets are then removed as follows: First, rectangular frames surrounding them at some distance are defined. Next, we randomly select pixel intensity values from these frames, and then use these values to replace the bright targets' intensity values. Fig. 5.12 shows a 1-min average of normalized and georeferenced marine radar data with and without backscatter signal from bright targets, in this case moorings. The figure also shows closeups of the area where most moorings were detected and includes an illustration of the bright target detection scheme.

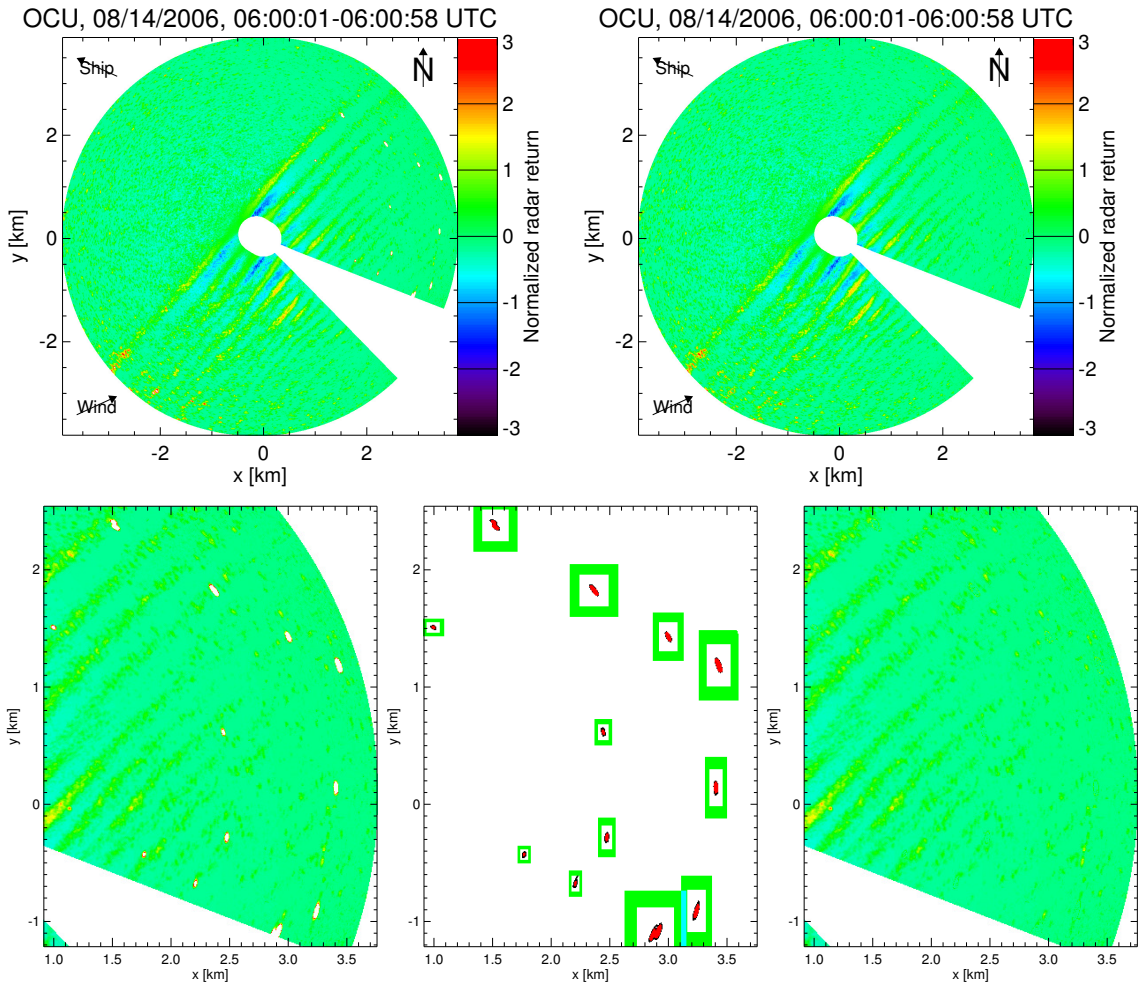


Figure 5.12: 1-min average of marine radar data collected starting August 14, 2006, 06:00 UTC with (top left) and without backscatter signal from moorings (top right). Zoom into images from top (bottom left and right, respectively) and corresponding image to illustrate mooring detection (bottom center). In the latter, pixel clusters with normalized backscatter intensities greater or equal 3 are marked in red. Neighboring pixels with intensities below the threshold but still well above the background are assumed to belong to the bright targets and marked in black. Finally, the green frames around each individual cluster mark pixels that are considered as replacement values.

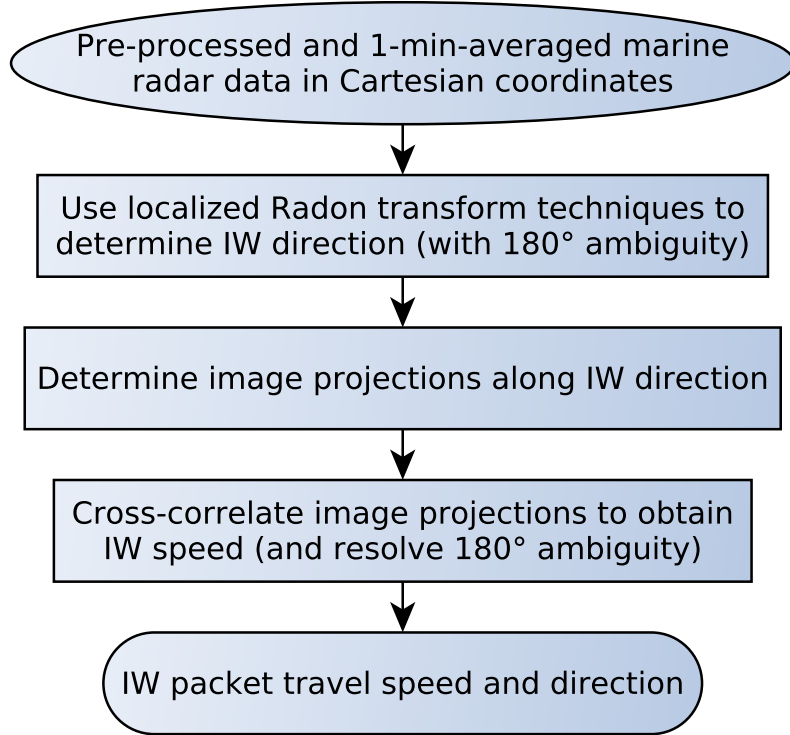


Figure 5.13: Flow chart detailing retrieval of IW packet speed and direction from pre-processed marine radar data.

### 5.3.2 Retrieval of IW Packet Parameters

In order to enable the retrieval of IW soliton maps from marine radar data, the IW signal must be enhanced, which requires in turn knowledge about IW packet parameters. The flow chart in Fig. 5.13 illustrates the steps involved to determine IW packet speed and direction from our pre-processed marine radar data. As Radon transform techniques play an integral role in our IW packet parameter retrieval scheme, we begin this section with a brief discussion of the Radon transform.

#### 5.3.2.1 Radon Transform

The Radon transform maps the spatial domain of an image into the two-dimensional Euclidean space [94]. It is defined as

$$f(\rho, \alpha) = \iint_D I(x, y) \delta(\rho - x \cos \alpha - y \sin \alpha) dx dy, \quad (5.1)$$

where  $I$  represents the intensity level of the image at position  $(x, y)$ ,  $\delta$  denotes the Dirac delta function,  $\rho$  is the length of the normal from the origin to a straight line, and  $\alpha$  represents the angle between the normal and the x-axis. The Dirac delta function forces the integration of  $I(x, y)$  along the line  $\rho = x \cos \alpha + y \sin \alpha$ . Consequently, the Radon transform yields integrals across the image at varying orientations  $\alpha$  and offsets  $\rho$  relative to the image center.

The Radon transform facilitates the detection of linear features as it maps a straight line in image space to a single point in transform space. Detection of a bright (dark) linear feature in an image thus becomes detection of a bright (dark) point in the Radon domain. As the Radon transform essentially involves the integration of an image intensity function along a set of lines, it is particularly well suited for application to marine radar images, which suffer from radar-inherent speckle noise. This is because the intensity fluctuations due to speckle tend to be canceled out by integration. The main advantage of the Radon transform is therefore that it enables the detection of poorly defined linear features in noisy images as it enhances their signal-to-noise ratio significantly [78].

Radon transform techniques have previously been applied to SAR data to retrieve wind directions from wind-induced streaks, IW information, and ship wakes [126, 100, 25]. Here, we use them to determine IW packet speed and direction from marine radar data.

### 5.3.2.2 IW Packet Direction

Fig. 5.14 shows a 1-min average of pre-processed marine radar data starting August 14, 06:00 UTC. An IW packet propagating in a northwesterly direction is clearly visible with the signal strength of the individual solitons decreasing from front to back.

The Radon transform enhances the signal-to-noise ratio of linear features, but is much less effective for the detection of curved features. IW surface manifestations may exhibit a

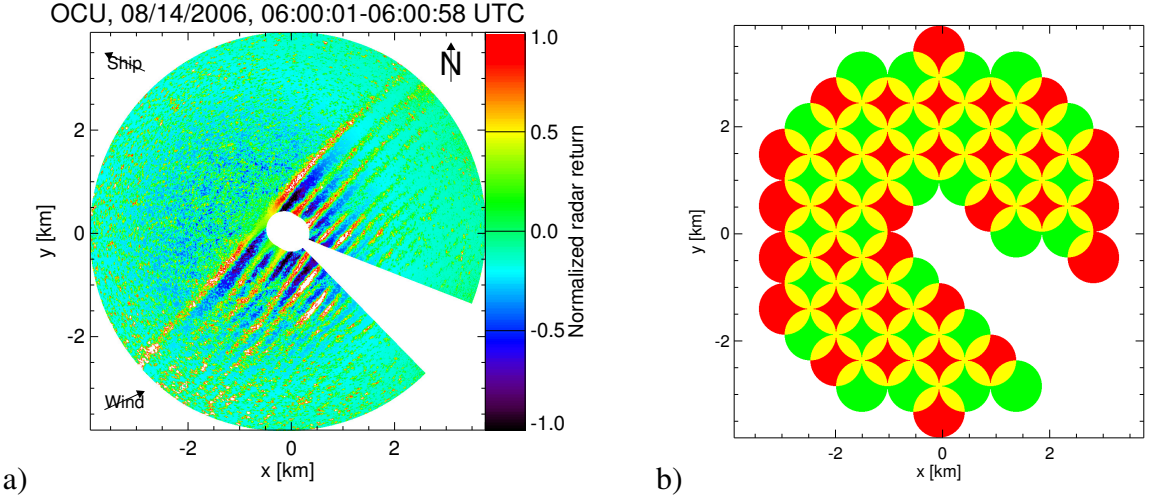


Figure 5.14: Pre-processed marine radar data averaged over a 1-min interval starting August 14, 2006, 06:00 UTC (a). Overlapping Radon transform boxes (b).

significant amount of curvature. By localizing the Radon transform, even curved features can be detected. This is because inside boxes that are significantly smaller than the radar field of view, they approximate straight lines. Furthermore, localization enables the detection of features that are significantly shorter than the image dimensions [25]. To determine the IW packet direction, we therefore define a set of overlapping circular Radon transform boxes. The boxes are limited to the image area containing valid data, i.e. non-masked pixels that are within the radar's range. The box diameter should be at least twice the dominant IW wavelength. Here, we chose a 960 m (128 pixels) diameter.

In our north-oriented and averaged images, the location of the mask that is due to the ship main mast changes with the ship heading and, due to the georeferencing, the image dimensions may vary slightly as a function of horizontal ship motion. The transform box positions therefore need to be reevaluated for each image average, and the number of boxes may change. In this case, a total of 63 boxes was defined (see Fig. 5.14).

Fig. 5.15 shows the radar backscatter intensity within a select Radon transform box in Cartesian coordinates and the corresponding image in Radon space. The box shows three bright lines that are due to the IW and that get mapped to bright points in Radon coordinates. Each data point in Radon space is divided by the number of image pixels along

its projection line. This is to prevent the subsequent analysis from being biased towards projection lines that are characterized by the greatest number of pixels across the Radon transform box. Furthermore, we have limited the Radon transform to projection lines that cover at least 91 pixels. Fig. 5.15 also depicts the standard deviation of Radon transform intensities as function of projection direction. The Radon projection direction that is associated with the maximum standard deviation is retained as the dominant direction. For the transform box shown in the figure, the dominant Radon direction is  $133^\circ$ . Note that Radon directions have an inherent  $180^\circ$  ambiguity. This issue will be addressed below (Section 5.3.2.3).

The histogram in Fig. 5.16 gives an overview of the dominant Radon directions found for all 63 boxes. Assuming that the IW packet is responsible for the most prominent linear features in the image, the histogram peak position represents a first rough estimate of the overall IW propagation direction. As the histogram shows, 23 boxes, more than one third of the total number of boxes, have their dominant peak at directions between  $130^\circ$  and  $140^\circ$ . This result suggests that the IW propagation direction is roughly  $135^\circ$ . With this knowledge, we can determine what regions of the image contain IW signals. Here, we consider all boxes with a dominant Radon direction within  $10^\circ$  of our rough IW direction estimate to contain an IW signal. This approach is further refined by checking whether the neighboring boxes also contain IW signatures. This helps eliminating the occasional outlying boxes with dominant Radon directions that accidentally coincide with the IW direction even though they do not contain IW signatures. The diagram in Fig. 5.17 indicates the IW activity for all transform boxes. With this information we can finally make our best estimate of the IW propagation direction, which is the median dominant Radon direction for all boxes that were determined to contain an IW signal. In our case, 31 boxes contain IW information, and the resulting IW direction is  $136^\circ$  (with  $180^\circ$  ambiguity).

Fig. 5.18 shows a 1-hour time series of the IW propagation direction starting with the data set discussed above. The median of all IW propagation directions during this period

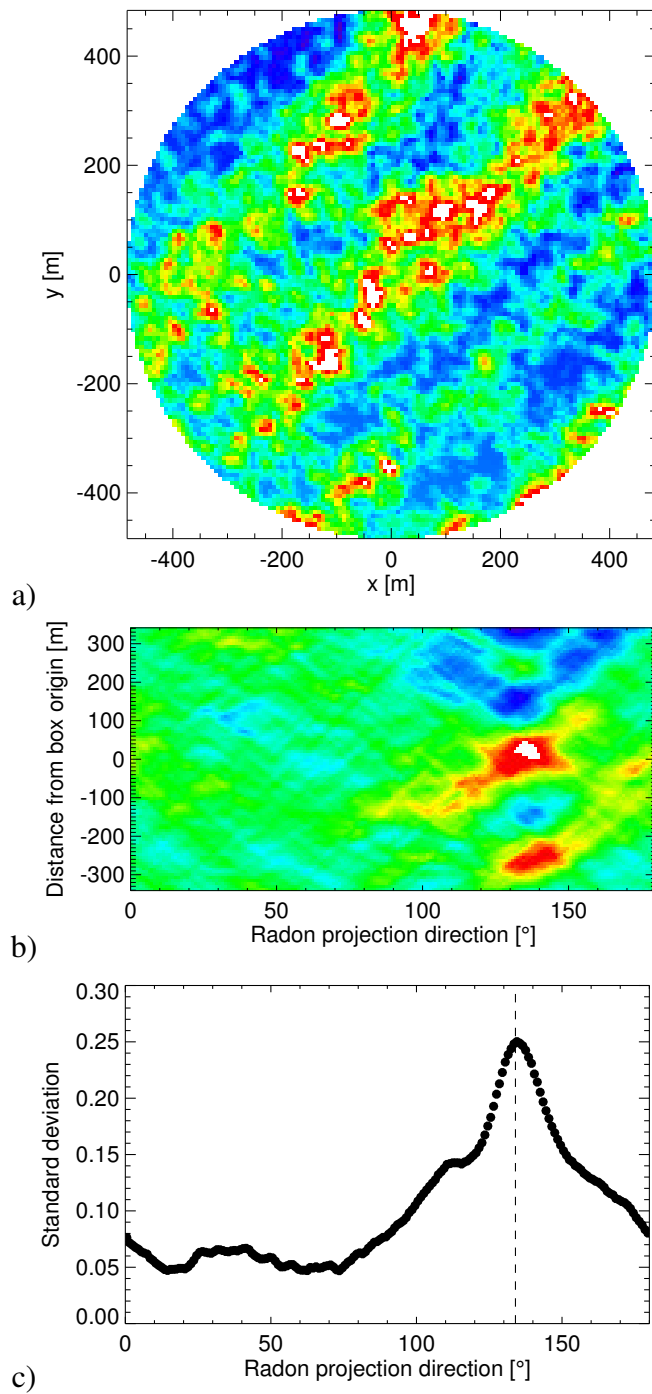


Figure 5.15: Radar backscatter intensity within select Radon transform box in Cartesian coordinates (a). Corresponding image in Radon space (b). Standard deviation of Radon transform intensities as function of projection direction. The dominant direction, associated with the maximum standard deviation, is marked by a dashed line (c).

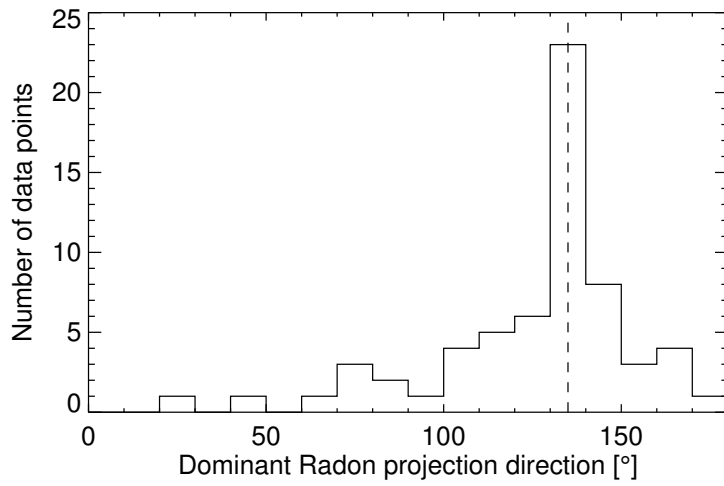


Figure 5.16: Histogram of dominant directions from all 63 Radon transform boxes. The dashed line marks the first rough estimate for the IW direction.

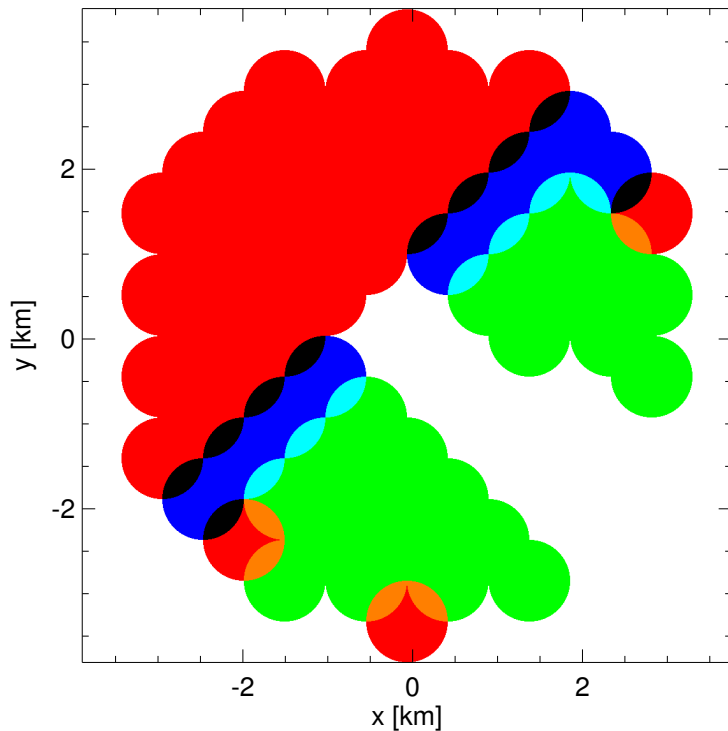


Figure 5.17: Diagram indicating IW activity within all Radon transform boxes. Green and blue boxes were determined to contain IW signatures, i.e. they have dominant Radon directions that are within  $10^\circ$  of our first rough IW direction estimate. For the green boxes, a minimum of 75% of the neighboring boxes were also determined to contain IW signatures. The blue boxes do not themselves satisfy the 75% criterion but have neighboring boxes that do satisfy it. Red boxes show no IW signal.

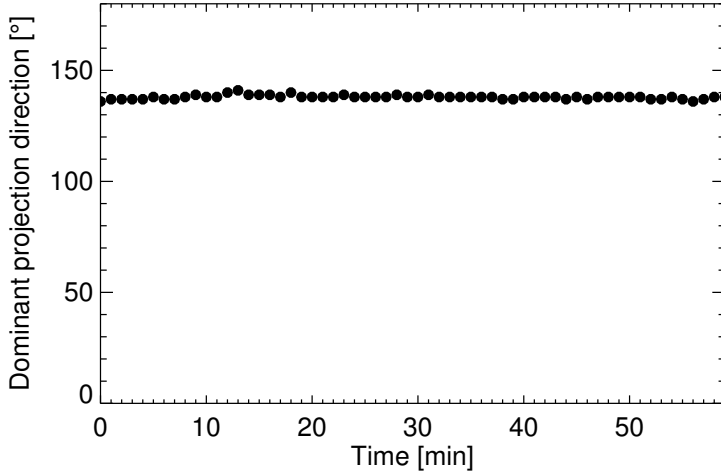


Figure 5.18: Time series of the IW direction computed as the median of the dominant directions associated with the Radon transform boxes that were determined to contain an IW signal. The time series starts August 14, 06:00 UTC.

is  $138^\circ$ . Converted to clockwise from north it becomes  $132^\circ$ . We will retain this value for the subsequent retrieval of IW surface signatures.

### 5.3.2.3 IW Packet Speed

Knowing the IW direction, we can rotate our pre-processed and 1-min averaged marine radar images such that the IW packet propagates along the x-axis. Averaging such a rotated image over the y-axis yields the mean normalized backscatter intensity along the IW propagation axis. Fig. 5.19 shows the rotated and 1-min averaged image from August 14, 06:00 UTC, as well as its projection onto the IW propagation axis. The projection's backscatter intensity has its peak at a distance of  $\sim 500$  m from the ship, which corresponds to the leading soliton. The smaller peaks following the first one indicate the positions of the subsequent solitons. In front of the leading soliton, the image projection has intensities around 0, as could be expected from the radar ramp correction (see Section 5.3.1.3). Note that IW parameters such as the wavelength, the peak intensity, or the number of peaks are difficult to retrieve from this projection. This is because the solitons are not perfectly linear features but have curvature, which may lead to neighboring solitons appearing as a single

soliton in the projection or canceling each other out. However, the projection does show a clear IW signal that we will use in the following to determine the IW speed.

Fig. 5.20 shows a Hovmöller diagram of image projections onto the IW propagation axis covering the period from August 14, 06:00 to 07:00 UTC. The top diagram is ship-centered while the bottom one has been corrected for the ship motion along the IW propagation direction. The ship-motion-corrected diagram clearly depicts the IW packet's propagation from left to right with more than 10 peaks (solitons) visible at all times. During the 1-hour period studied here, the leading soliton traveled a distance of roughly 1900 m, which corresponds to a speed of 0.52 m/s.

To obtain a more accurate estimate of the IW packet speed, we divide our ship-motion-corrected Hovmöller diagram into 10-min segments. Dividing the diagram in such a way makes sense because it can be assumed that the IW characteristics change only insignificantly in this short a period. For any given segment, we then cross-correlate each projection with the segment's first one. The lag associated with the peak in the cross-correlation function represents the average distance traveled by the packet. Fig. 5.21 shows the resulting IW packet displacement and corresponding speed. The figure shows that the IW packet speed at first rapidly increased up to  $\sim 0.8$  m/s and then decreased to  $\sim 0.5$  m/s, a value around which it hovered during the data set's last  $\sim 45$  min. We retain the mean IW speed of 0.52 m/s for the subsequent analysis. Finally, we use the IW speed's sign to resolve the directional ambiguity of our IW direction estimate. The positive sign confirms that our IW packet is propagating in a northwesterly direction, so that our IW propagation direction must be  $312^\circ$  (and not  $132^\circ$ ).

### 5.3.3 IW-enhanced Radar Images

As a final preparatory step towards the retrieval of IW soliton maps, we use our newly acquired knowledge about the IW packet speed and direction to produce IW-enhanced radar images. The individual steps leading towards IW-enhanced images are outlined in Fig.

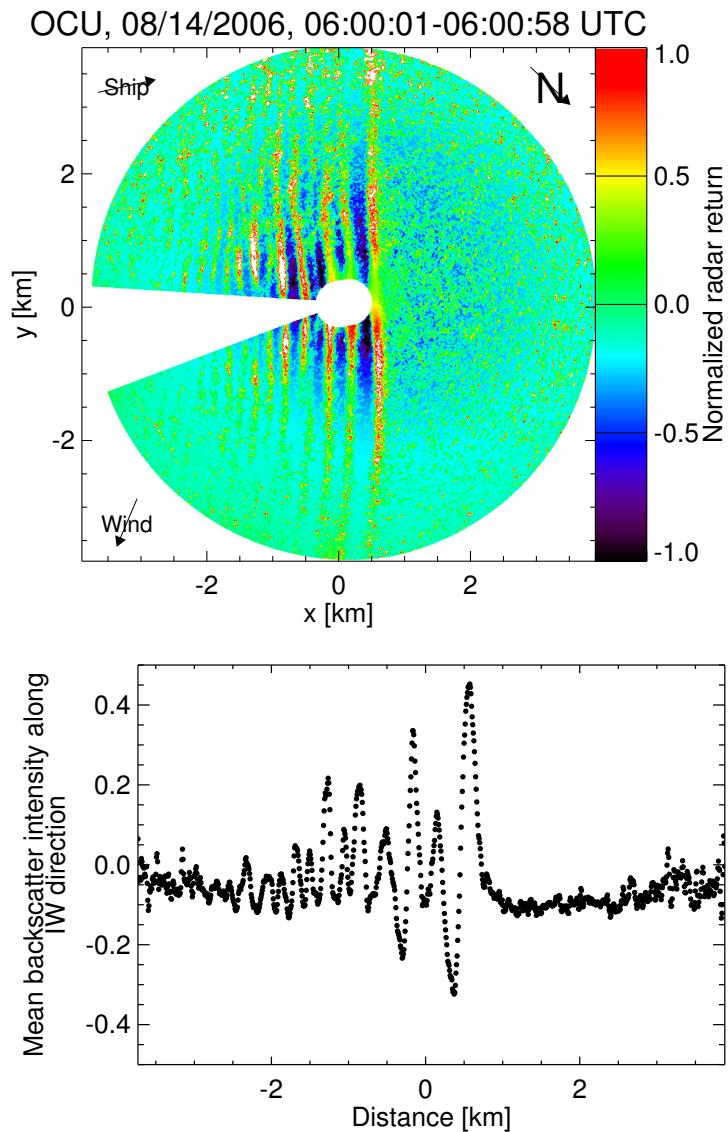


Figure 5.19: 1-min average of pre-processed marine radar data starting August 14, 2006, 06:00 UTC. The image has been rotated so that the IW propagates along the x-axis (top). Image projection onto IW propagation axis (bottom).

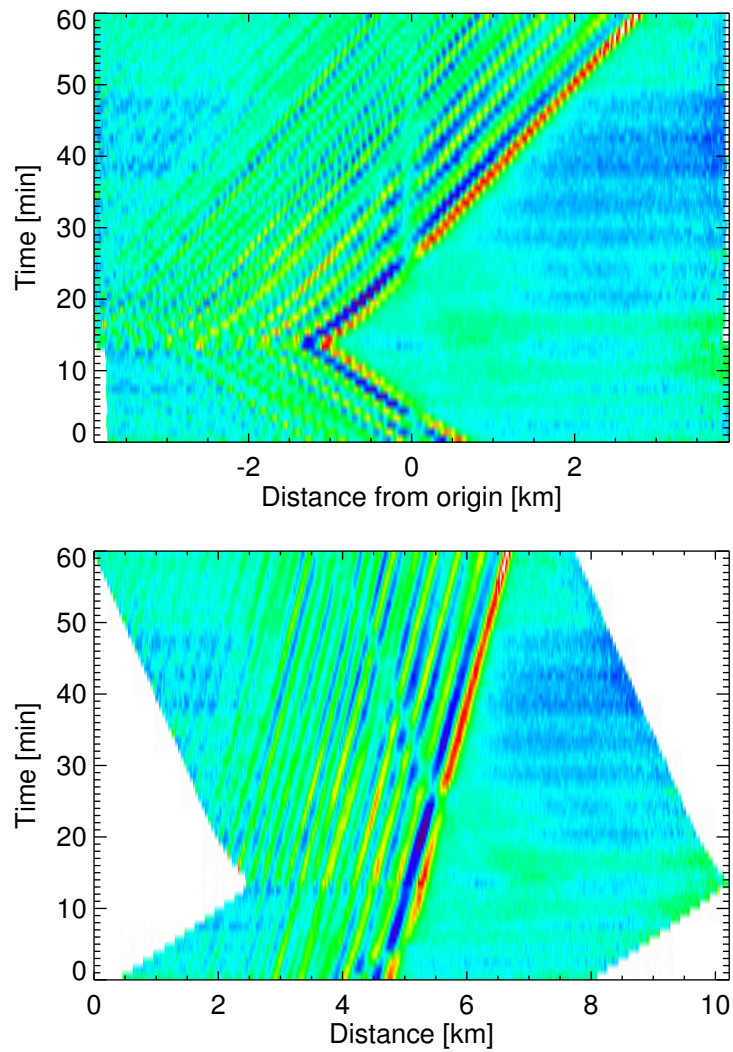


Figure 5.20: Hovmöller diagrams of image projections onto IW propagation axis before (top) and after correcting for the ship motion (bottom).

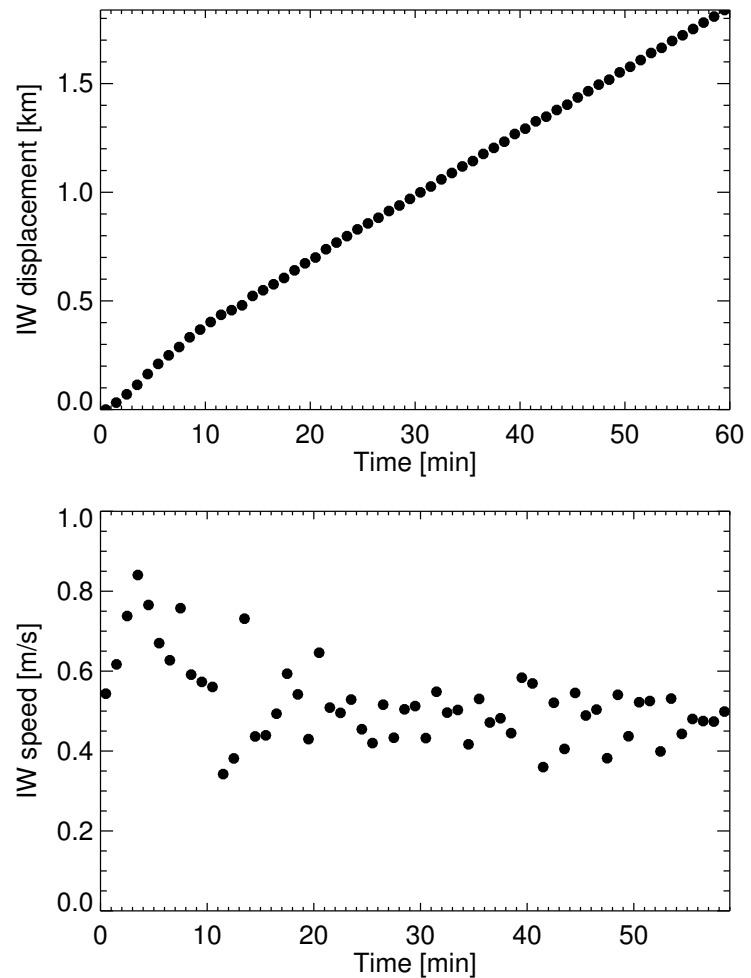


Figure 5.21: Time series of IW packet displacement (top) and corresponding speed (bottom).

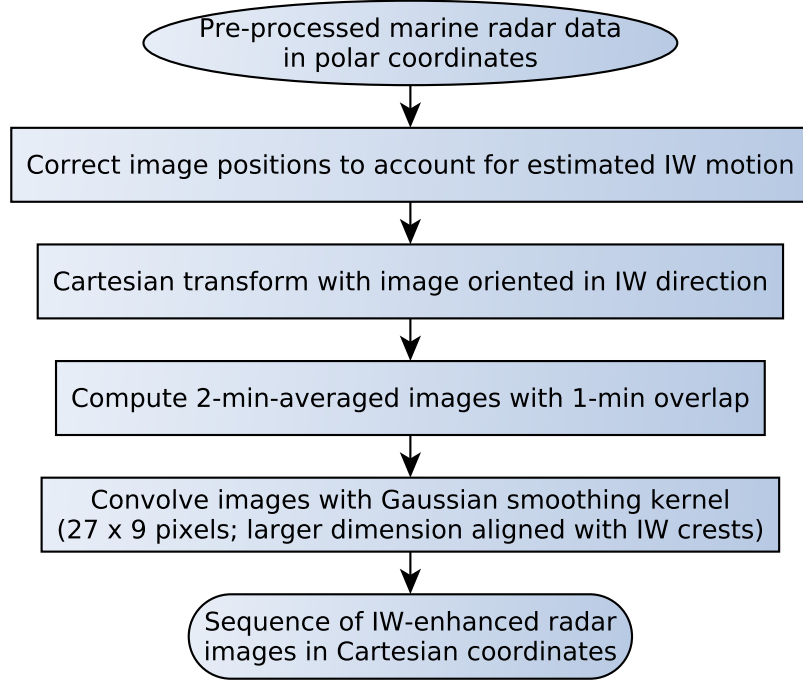


Figure 5.22: Flow chart outlining steps leading towards IW-enhanced radar images.

5.22. Note that contrary to section 5.3.2, here our analysis begins with pre-processed marine radar data in polar (and not Cartesian) coordinates. In section 5.3.1, the only step that requires a conversion to Cartesian coordinates is the identification of bright targets (which in turn requires the data to be georeferenced). For this section, we altered the pre-processing in such a way that the georeferenced bright target locations are transferred back to our raw polar coordinates, where the correction is being performed in the same fashion as described above (compare Section 5.3.1.5). This is useful because our georeferencing step, which is embedded in the polar to Cartesian transform, will be modified here in order to account for the IW motion. Doing this in one step allows us to take advantage of the polar radar data's full resolution and helps minimize the number of interpolations applied to the data.

### 5.3.3.1 IW Motion Correction

As has been discussed above, temporal averaging of our marine radar data greatly enhances the images' signal-to-noise ratio. However, since IWs are not stationary, their radar signatures will be "smeared" if the averaging period becomes too long. An IW packet traveling at a speed of 0.5 m/s needs 15 s to pass from one resolution cell to the next. For a 1-min averaged image this smearing effect is still fairly small, however, for longer averaging periods correcting for the IW motion before averaging becomes necessary. In the following, since we do not know over what time scales the solitons change their characteristics, we will use a 2-min averaging period. In the future, this could be extended to 5 min or even longer. Fig. 5.23 shows a raw marine radar image from August 14, 2006, 06:00:01 UTC and an IW-enhanced image obtained from 2 min of data starting with the same image. To produce the IW-enhanced image, we removed the previously determined IW motion (the IW packet was determined to travel at 0.52 m/s in a direction of  $312^\circ$ ) in addition to the ship motion when performing the polar to Cartesian transform. As part of the transform, we furthermore rotated the images such that the IW propagates along the y-axis. When comparing the raw single radar image with our IW-enhanced image, it becomes clear that the processing described here greatly enhances the IW signatures.

### 5.3.3.2 Gaussian Smoothing

Finally, the image is convolved with a Gaussian smoothing kernel. Fig. 5.24 shows the IW-enhanced image from Fig. 5.23 after the smoothing. Note that the corresponding  $27 \times 9$ -pixel kernel has its larger dimension aligned with the IW crests. Since we aim at exploiting marine radar's high temporal resolution, the above steps are repeated for the full 1-hour data set with a 1-min overlap between consecutive images. The resulting sequence of smoothed and IW-enhanced images will be used within our IW signature detection scheme.

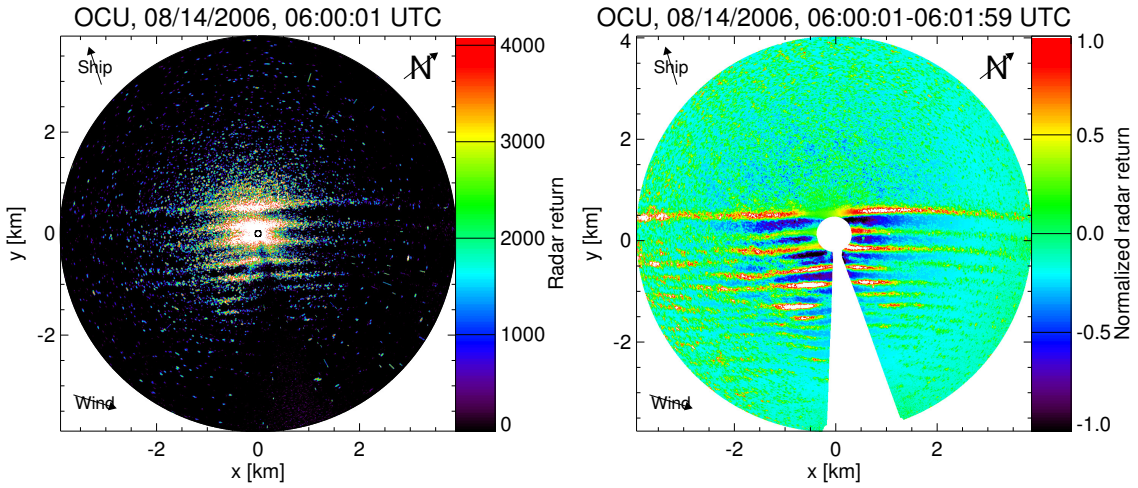


Figure 5.23: Raw marine radar image from August 14, 2006, 06:00:01 UTC (left) and IW-enhanced image obtained from 2 min of data starting with the same image (right). Both images are oriented such that the IW travels from bottom to top along the y-axis.

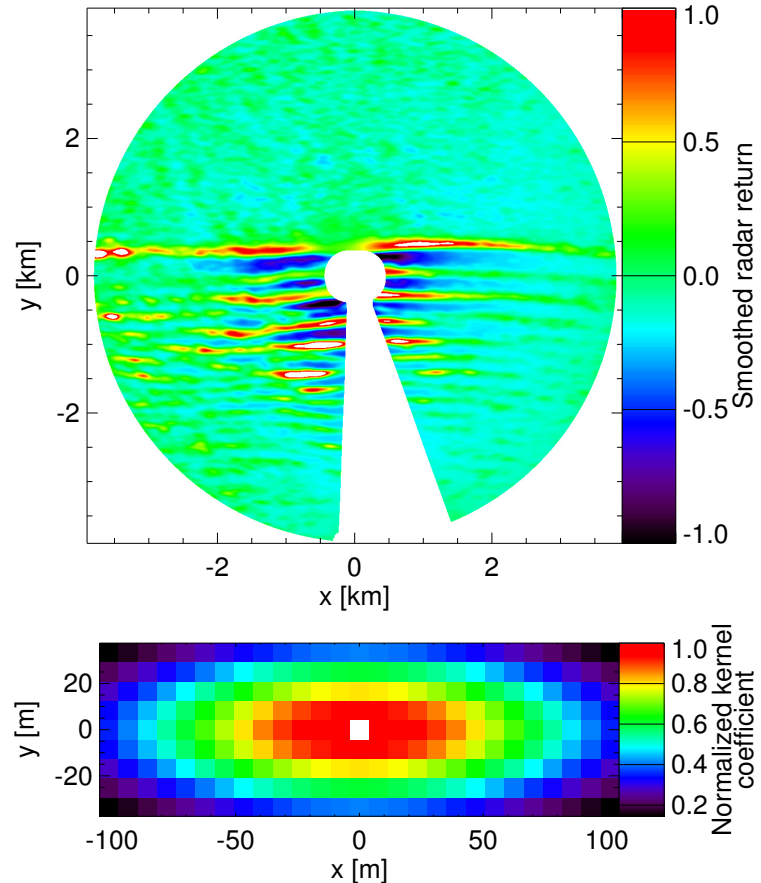


Figure 5.24: IW-enhanced radar image after convolution with a Gaussian smoothing kernel (top). The corresponding kernel is shown at the bottom.

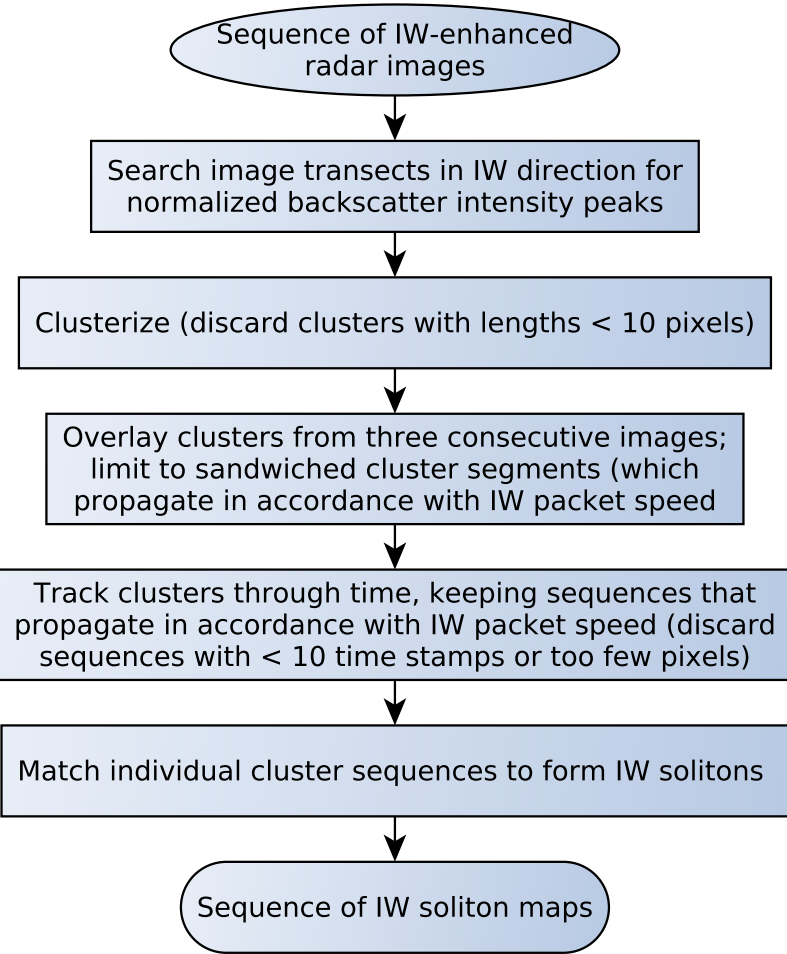


Figure 5.25: Flow chart outlining our IW signature retrieval method.

### 5.3.4 IW Signature Retrieval

The flow chart in Fig. 5.25 gives an overview of our IW signature retrieval approach. In the following sections, the individual steps are described in detail.

#### 5.3.4.1 Clusterization of Radar Return Peaks

We begin our IW signature analysis by searching for radar backscatter intensity peaks in our IW-enhanced radar images. This is done in 1-pixel intervals over image transects along the IW propagation axis, covering the entire image. In this first step, we simply retain all pixel locations that have a greater backscatter intensity than their two neighboring pixels

(in IW direction). In case of a flat peak, we retain the plateau's center location as the peak position. Neighboring backscatter peaks are then connected to form peak clusters. For any given peak location, we have six potential connecting points, three to the left and three to the right. After clusterizing our individual peaks, we discard clusters that have less than 10 elements, assuming that the IW produces much longer peak clusters than noise.

Fig. 5.26a shows the peak clusters that were identified within the IW-enhanced image from August 14, 06:00 UTC. Clusters with less than 10 elements have been discarded. The IW signal has been fully retained after this first filtering, however, a large number of clusters that are unrelated to the IW remains. Furthermore, filtering the clusters based on a more stringent length requirement, as in Fig. 5.26b, where all clusters with less than 100 elements have been discarded, yields unsatisfactory results. This is because some clusters that are not part of the IW remain, while other clusters that potentially represent IW signatures are discarded. Discarding clusters with mean backscatter intensities below e.g. 0.1, would lead to similar issues (see Fig. 5.26c). The following sections explain how our IW signature retrieval method overcomes these challenges. At this stage, we retain all clusters with a minimum length of 10, independent of their mean backscatter intensity.

### 5.3.4.2 Cluster Filtering

As a simple thresholding of our clusters based on their length or mean backscatter intensity yields less than satisfactory results, we suggest an alternative method. This method takes advantage of marine radars' high temporal resolution, and uses the previously determined IW packet speed and direction to separate peak clusters that are due to the IW from noise. Fig. 5.27a shows clusters from three consecutive IW-enhanced images in a fixed coordinate system. While clusters that are due to noise are very disorderly, the IW-related clusters, visible over the entire x-domain for y-values less than  $\sim 300$  m, are highly repetitive and show a clear propagation pattern. Therefore, to reduce noise, we limit our further analysis to clusters that are “sandwiched” by peaks from the previous and subsequent time stamp.

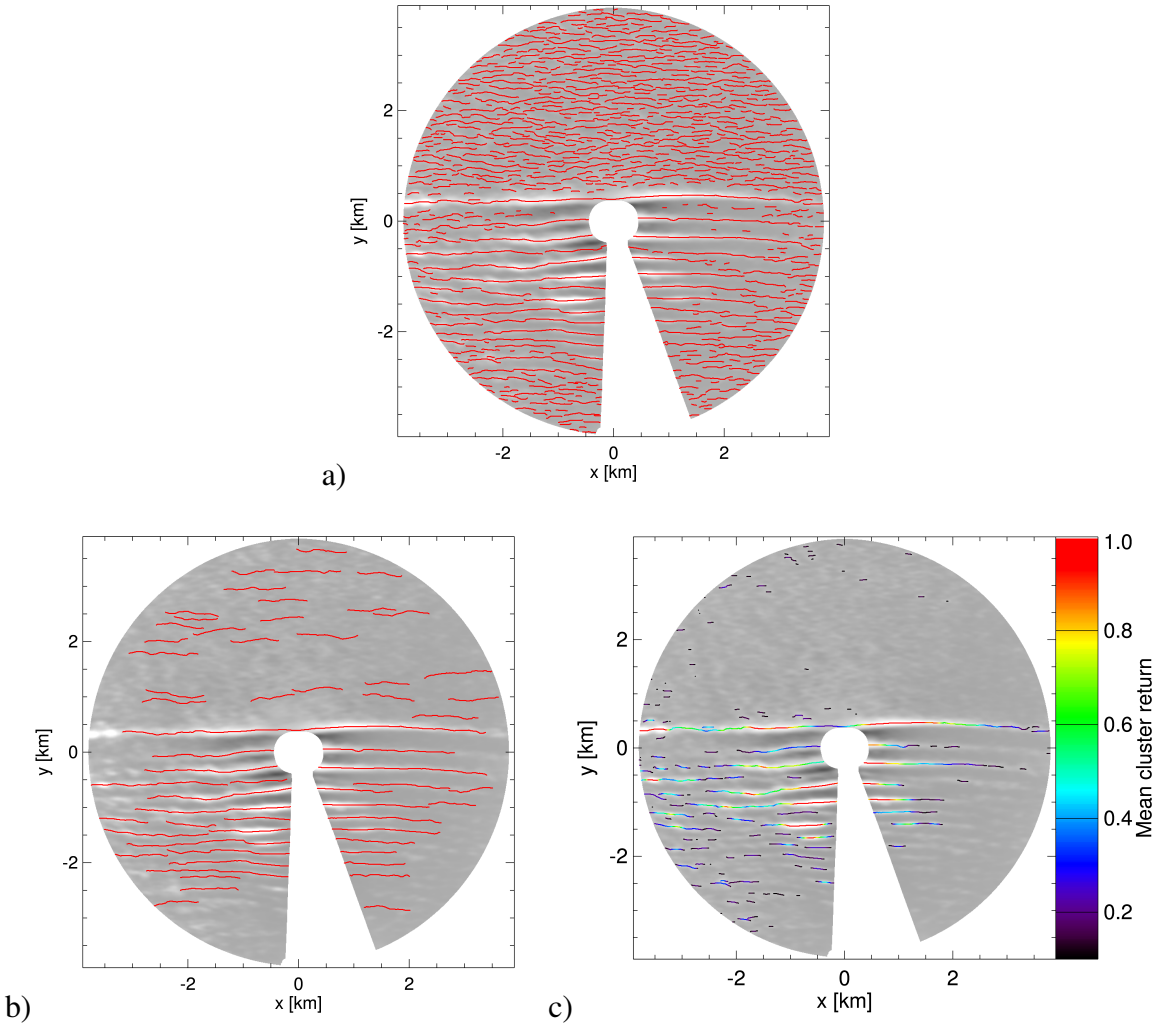


Figure 5.26: Clusters of radar backscatter intensity peaks identified within the IW-enhanced marine radar image from August 14, 2006, 06:00 UTC. Clusters with less than 10 elements have been discarded (a). Clusters can be further thresholded based on a more stringent length criterion (b) or on their mean backscatter intensity (c).

Assuming that the three clusters contributing to such a “sandwich” (with each cluster being 1 min apart) are due to the same IW soliton, we furthermore require the distance between the clusters to be no greater than 75 m (10 pixels). This limit is based on the previously determined IW packet speed of 0.52 m/s – a travel distance of 10 pixels within the 60 s between two consecutive data sets corresponds to a soliton speed of 1.25 m/s, which we assume cannot be exceeded by this IW. Note that this analysis is being done by cluster elements, i.e. it can result in clusters being fragmented. To further reduce noise, the resulting filtered and partially fragmented clusters are once again length-filtered, keeping clusters with a minimum of 10 pixel elements. For the same data set, Fig. 5.27b gives the results of this “sandwich”- and subsequent length-filtering. As can be seen, the IW signal is largely retained while the noise is significantly reduced. This procedure is being repeated in 1-min intervals, and during each iteration the sandwiched pixels from all three consecutive time stamps are retained. This means that at any given time, radar backscatter intensity peaks from up to 5 consecutive IW-enhanced radar images are considered. As a result, Fig. 5.27b may show cluster segments that do not appear to be “sandwiched”. In the next section we will explain how the remaining noise is eliminated by cluster sequencing.

#### 5.3.4.3 Cluster Sequencing

In a final step, the “sandwiched” clusters, that were determined to propagate in accordance with the IW packet parameters during three consecutive time stamps, must be sequenced in time and merged in space to form IW solitons. Here, we operate cluster-by-cluster and search for sequence and merge candidates throughout our full 1-hour period. For a sequencing operation to be effective, we require the distance towards the subsequent time stamps’ clusters to be no greater than 75 m (10 pixels). Again, this is in accordance with the previously determined IW packet speed. Cluster sequences that share elements are assumed to be part of the same soliton and automatically merged. In this fashion, clusters are sequenced and merged to form cluster groups that resemble IW solitons. In order to

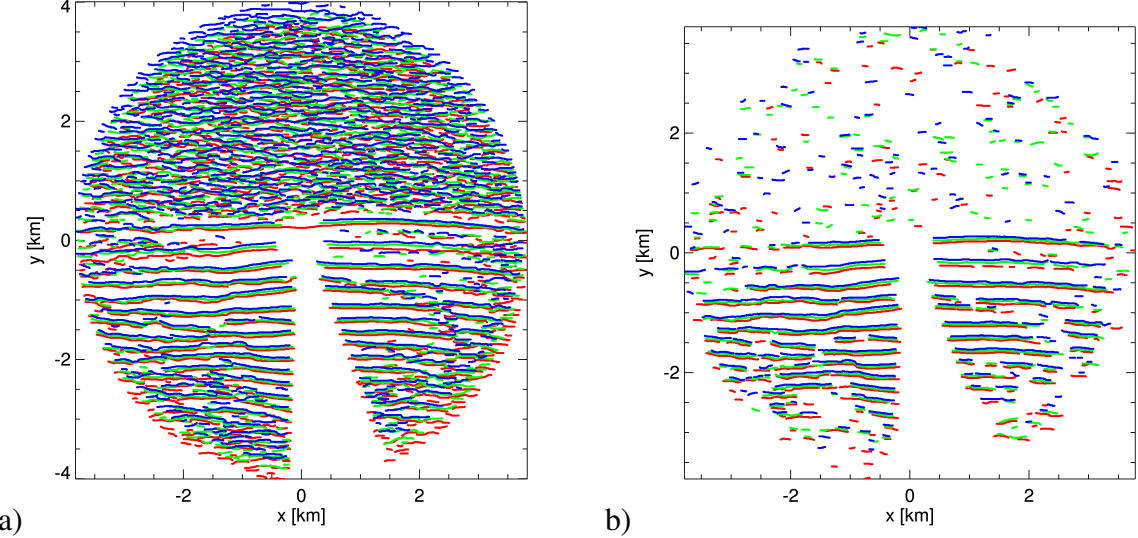


Figure 5.27: Clusters found within the three IW-enhanced images from August 14, 2006, 06:00 to 06:02 UTC. Red clusters are from the first, green from the second, and blue from the last image (a). The results after filtering, where we used our knowledge of the IW packet speed and direction, are shown on the right (b).

eliminate the remaining noise, we discard all cluster groups that last for less than 10 min or have on average fewer than 50 pixel elements per time stamp. Finally, the remaining cluster groups are analyzed to determine whether they belong to the same soliton. In this context, we require the mean along-crest distance between the ends of two matching groups to be no greater than 1.5 km (200 pixels). The maximum mean distance between matching ends along the IW direction is 75 m. The resulting merged cluster groups, when viewed as a whole, mimic the IW packet's propagation and contain no discernible noise.

To fill the gaps between the individual clusters that each soliton consists of, a Delaunay triangulation with bilinear interpolation is performed, such that at each time stamp the solitons form continuous lines from one end to the other [64]. Fig. 5.28 illustrates the leading three IW solitons' propagation during our 1-hour period starting August 14, 06:00 UTC, before and after interpolation.

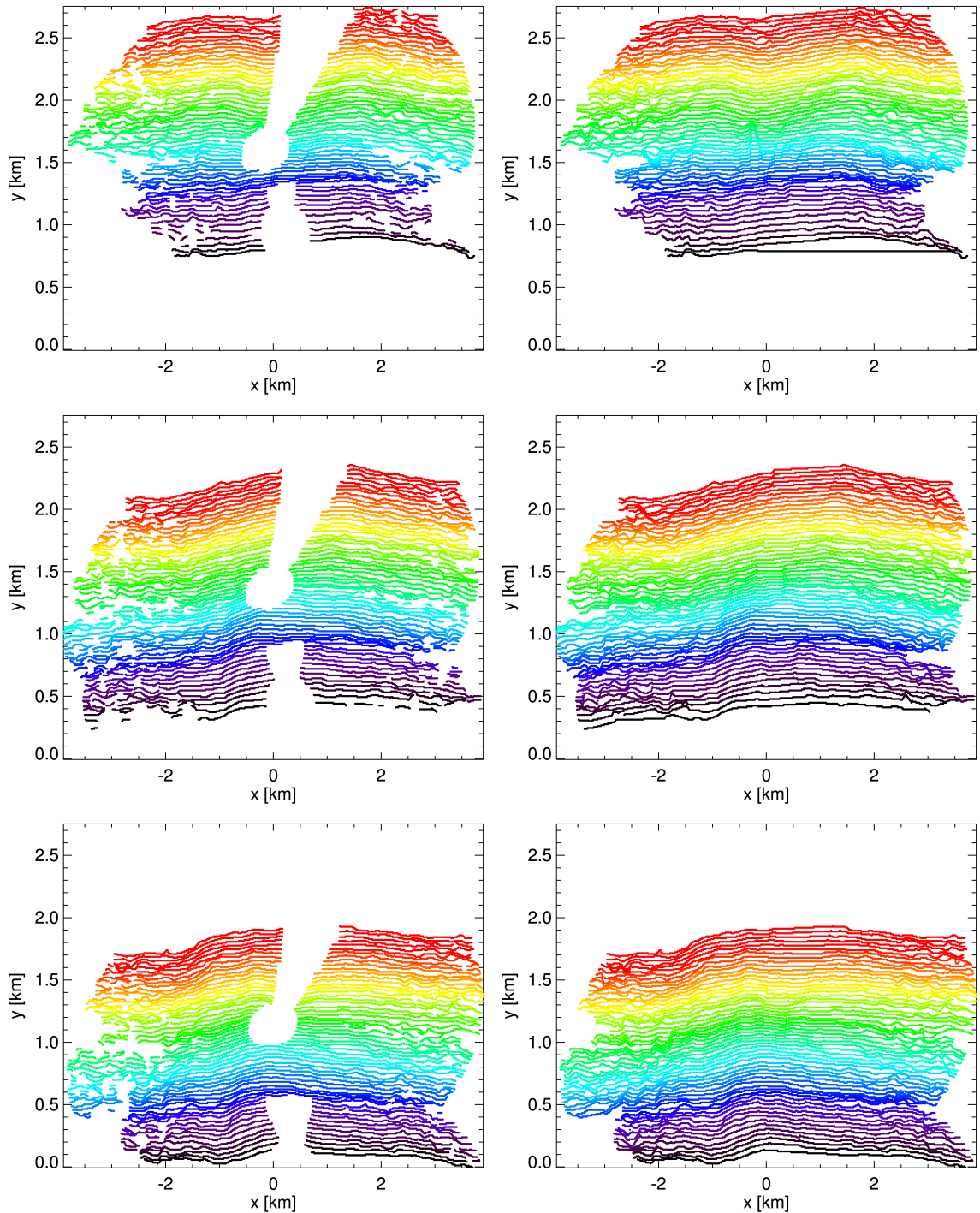


Figure 5.28: The leading three IW solitons during 1-hour period starting August 14, 2006, 06:00 UTC, before (left) and after (right) interpolation. The color code gives the time, starting in black (06:00 UTC) and ending in red (06:59 UTC).

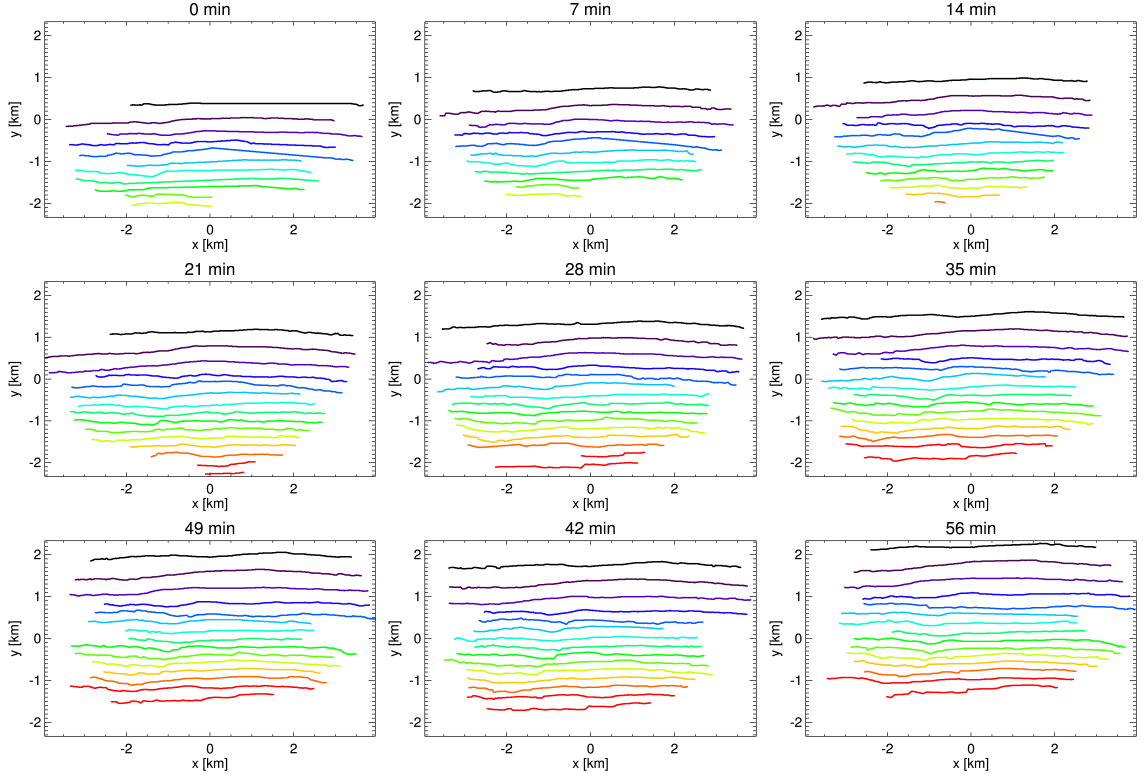


Figure 5.29: Sequence of IW soliton maps retrieved from marine radar data in 7 min intervals from Aug 14, 2006, 06:00 UTC to 06:56 UTC. The solitons are color-coded by order of appearance with the leading soliton in black and the last (15<sup>th</sup>) in red.

## 5.4 Results

A sequence of IW soliton maps, the result from the IW signature retrieval technique introduced above and applied to our 1-hour long marine radar data set, is shown in Fig. 5.29. The figure illustrates the propagation of the 15 leading solitons. Each soliton has been assigned a unique color for identification.

Using the same color code, Fig. 5.30 illustrates each soliton's mean displacement in 1-min resolution. As is clear from the figure, the individual solitons do not propagate in perfect unison. Furthermore, it can be observed that each solitons' speed is not constant but changes as a function of time. This is especially obvious for the leading soliton (shown in black), which propagates at an accelerated pace during the time series' first  $\sim 10$  min.

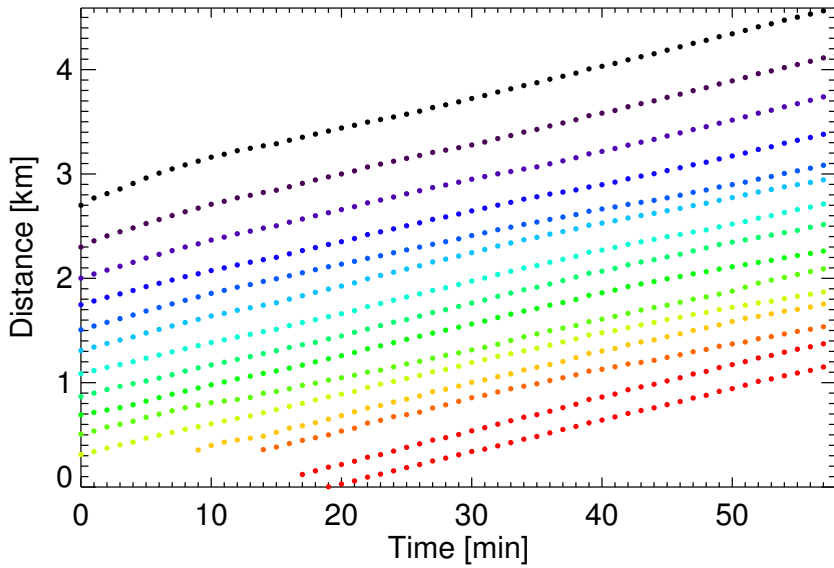


Figure 5.30: Time series of mean soliton displacement starting Aug 14, 2006, 06:00 UTC. The solitons are color-coded by order of appearance with the leading soliton in black and the last (15<sup>th</sup>) in red.

Fig. 5.31 shows a time series of the leading soliton's speed. It has a striking resemblance with our IW packet speed (compare Fig. 5.21): The speed increases at first to  $\sim 0.8$  m/s and then decreases to  $\sim 0.5$  m/s, which it holds during the remaining period. This result indicates that our IW packet speed (see Section 5.3.2.3) is most representative of the leading soliton. The sudden increase in speed may be the result of a wave-wave interaction, but further research is necessary to provide conclusive explanations.

Figs. 5.32 to 5.34 show the mean speed, wavelength (i.e. distance to trailing soliton), and normalized backscatter intensity for each soliton. Here, each data point represents a spatio-temporal mean, summarizing the soliton characteristics within the radar's field of view during our 1-hour period. All three parameters vary significantly within the IW packet. In general, speed, wavelength, and backscatter intensity decrease from IW front to back. The leading soliton is propagating fastest at a mean speed of 0.54 m/s. It also has the greatest mean normalized backscatter intensity and wavelength with 421 m. Speed and wavelength decrease continuously from the first to the fourth soliton and then hover above 0.45 m/s and just around 200 m, respectively. It can therefore be concluded that only the

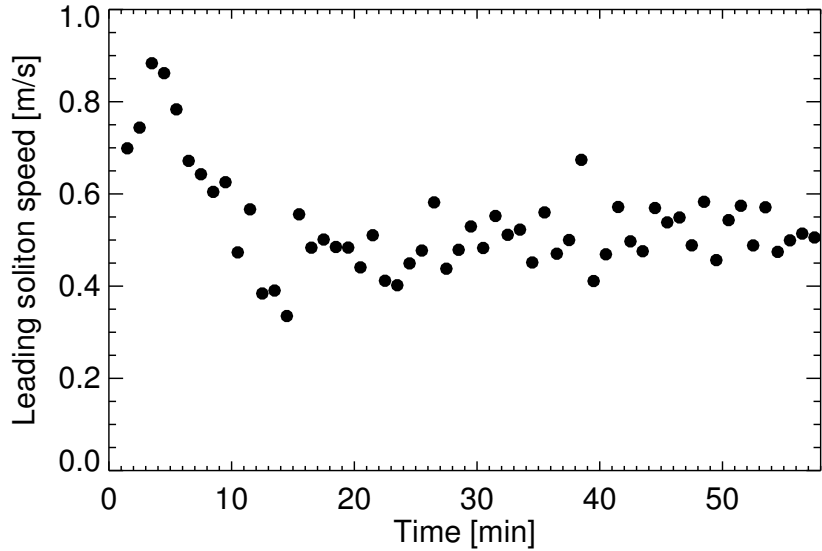


Figure 5.31: Time series of leading soliton's speed from Aug 14, 2006, 06:00 UTC.

leading three solitons exhibit dispersive behavior. Interestingly, the trailing two solitons (number 14 and 15) are significantly faster and slightly wider than their predecessors, as they appear to be catching up with the IW packet. Finally, backscatter intensity is most elevated for the first three solitons, decreases significantly for the fourth and fifth soliton, but then exhibits a sudden increase to a level just below that of the third soliton, only to decrease again, with the tenth soliton having the lowest intensity of the whole package. Note that marine radar backscatter intensities are difficult to interpret quantitatively because of their strong dependence on wind and imperfections in our ramp-removal and normalization procedure (see Section 5.3.1.3). However, the general decrease in backscatter intensity from front to back agrees with the understanding that the IW package's energy is greatest at the front [107]. Higher-order Korteweg-de Vries (KdV) theory suggests that larger amplitude solitons travel faster [83]. For a complete discussion of the higher-order KdV equation refer to Stanton and Ostrovsky [112] or Grimshaw et al. [45]. Shroyer et al. have successfully used a higher-order KdV equation to study the influence of the background fluid state on IWs over New Jersey's continental shelf [109]. Our marine radar measurements of soliton speed and wavelength are therefore in good agreement with predictions from non-linear IW

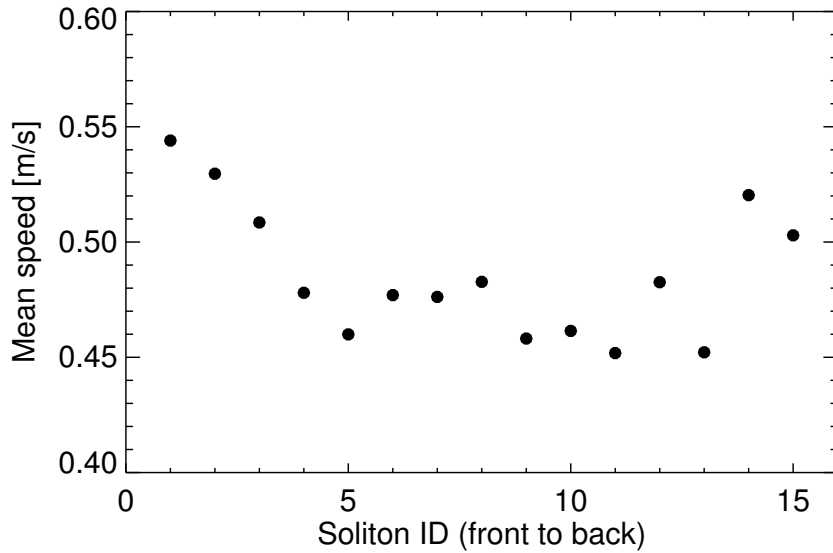


Figure 5.32: Mean soliton speed for 1-hour period from August 14, 2006, 06:00 UTC.

theory. Future work will focus on estimating the IW amplitude and studying its evolution from the soliton characteristic half width [132, 138].

## 5.5 Discussion

The divergent and convergent surface currents associated with IWs modulate the surface waves, creating alternating smooth and rough bands which can be observed by radar. This chapter introduces a new method to retrieve IW surface signatures from marine radar data. The IW radar signatures are first enhanced using georeferencing and averaging. IW signatures can then be identified by localized Radon transform, yielding their general propagation direction (with  $180^\circ$  ambiguity). Cross-correlation techniques are employed to determine the IW packet speed and resolve the directional ambiguity. The thus obtained IW packet characteristics are used to further enhance the IW signatures by extending the averaging period while correcting for the IW motion. The resulting IW-enhanced radar images are then channeled into our newly developed IW signature retrieval algorithm. Knowing the IW packet speed and direction, we can focus our efforts on peak clusters that are ori-

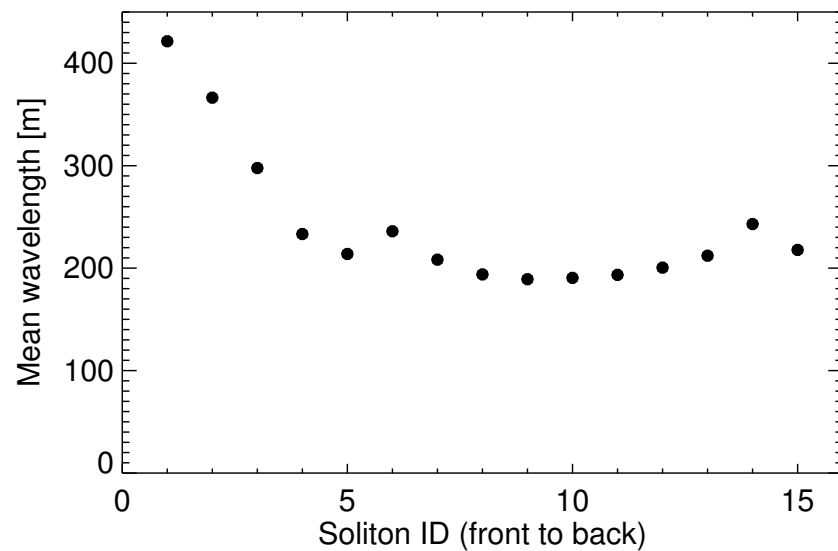


Figure 5.33: Mean soliton wavelength for 1-hour period from August 14, 2006, 06:00 UTC.

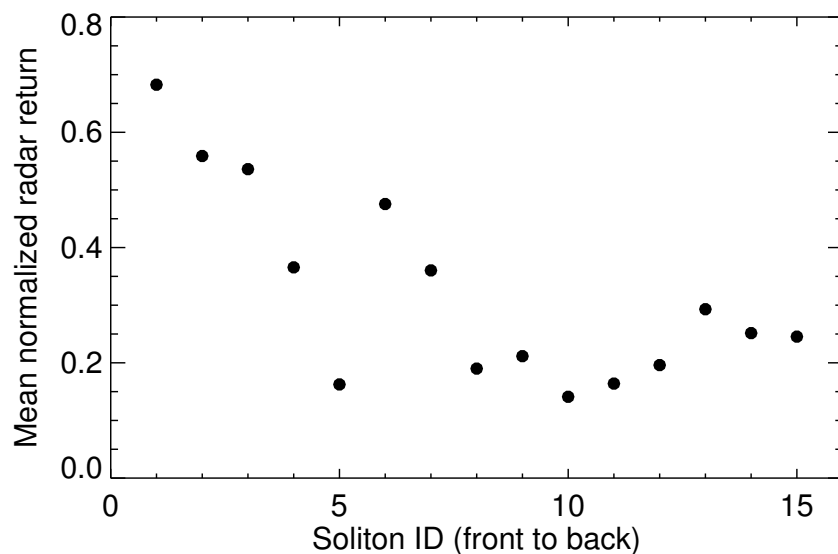


Figure 5.34: Mean soliton normalized radar return for 1-hour period from August 14, 2006, 06:00 UTC.

ented across the IW propagation direction. Marine radar's high temporal resolution allows us to track the peak clusters in time. Clusters that do not move in agreement with the general IW packet characteristics are discarded, leaving clusters that, if they persist in time, are due to the IW. These remaining peak clusters can finally be merged into cluster groups, which are combined to form IW soliton maps. Such analysis of IW signatures in marine radar data provides a first means of studying the spatio-temporal evolution of IW surface manifestations as the underlying wave grows and later decays while propagating across the shelf.

IW signatures that are not apparent in single radar images become visible through our IW-enhancement technique. In this context, diligent georeferencing of the raw polar marine radar data, correcting for both ship heading changes and horizontal ship motion, plays an important role. Data quality can be further improved by removing noise due to interference with other radars or bright targets such as moorings.

Our IW signature retrieval algorithm is fully automated and works reliably even for radar data that are characterized by a significant amount of noise. In principle, the processing could be done in near real-time on any computer with a processor of at least 2 GHz, a minimum of 2 GB memory, an IDL license, and a connection to a device that collects marine radar data, e.g. WaMoS. This algorithm could therefore prove to be useful in IW research field campaigns, especially if the goal is to track an IW packet, as in NLIWI.

In the future, we are hoping to relate the IW characteristics obtained from our IW soliton maps to the velocity, density, and turbulence measurements made from *R/V Oceanus* using shipboard acoustics and a microstructure profiler. In particular, it would be interesting to study changes in soliton wavelength, velocity, and backscatter intensity during IW growth and decay. For example, Chang et al. have proposed empirical model functions that relate marine radar backscatter intensity to IW horizontal velocity convergence and amplitude measurements made in the South China Sea [23]. Furthermore, they found that the IW-related backscatter intensity enhancement exhibits a strong asymmetry with the

enhancement observed when looking in IW propagation direction being 24% smaller than that observed when looking against it. The IW signature retrieval algorithm presented here makes it easy to investigate whether similar relationships can be established for the shallow water data collected during NLIWI. However, radar backscatter intensities have a strong dependence on wind, and the backscatter mechanism for grazing incidence applications is generally not well understood. The use of backscatter intensities to derive IW characteristics must therefore be treated with caution. What we believe to be a more promising approach in shallow water is to make use of the radar-retrieved soliton characteristic half width with the higher-order KdV equation to retrieve IW amplitudes [132, 138]. Last but not least, our radar-derived IW soliton maps can be used to study wave and packet-packet interactions.

Further improvements are required regarding the marine radar ramp removal and normalization. Our empirical radar ramp model function needs to be subjected to further testing, in particular under very low- and high-wind conditions. For the normalization, we assume the standard deviation to depend on range only, which is inaccurate as it appears in fact to vary with antenna look direction. Additional research is required in this regard, however, early results indicate that the range where the standard deviation reaches its maximum value is greatest in upwind direction. On the long term, it would be desirable to develop a ramp model function that can be expressed in terms of wind speed and direction, and, if necessary, other environmental or radar system parameters. This is because it would allow us to compute a radar ramp that is independent of the radar measurement, which would in our case prevent the IW signal from influencing the ramp and thus the resulting backscatter intensities.

# Chapter 6

## Study of Internal Wave Evolution by Marine Radar

### Summary

During ONR’s Non-Linear Internal Wave Initiative / Shallow Water ’06 experiment (NLIWI/SW06), *R/V Oceanus* tracked internal wave (IW) packets over large distances across the continental shelf off the coast of New Jersey. *R/V Oceanus* was equipped with a marine radar which recorded backscatter intensities from the sea surface up to a range of 4 km with 7.5 m resolution. With an antenna rotation rate of 24 rpm, the radar allows a detailed analysis of the spatio-temporal evolution of IW surface signatures. This chapter focuses on the campaign’s most energetic IW, named Rosey by Oregon State University’s Shroyer et al. [109], which has been tracked by the ship over a period of about 12 hours. During this period, the IW traveled almost 40 km in a northwesterly direction, covering water depths from above 80 m to under 60 m. Here, the methods developed in the previous chapter are applied to the full data set, to study the evolution of IW Rosey as it propagates across the continental shelf. The resulting time series of IW speed, direction, and soliton maps yield information on the wave’s growth and subsequent decay. A higher-order (extended) Korteweg-de-Vries (eKdV) equation is used to derive IW amplitudes from the

distances between IW-induced positive and negative radar backscatter intensity peaks, following the techniques introduced by Xue et al. [132]. The radar-derived amplitudes are compared with in-situ measurements made with a microstructure profiler [76]. In addition, the measured radar backscatter intensities are correlated with the IW-induced surface current gradients obtained from a shipborne ADCP as well as with the measured IW amplitudes.

## 6.1 Introductory Remarks

Over the course of the NLIWI/SW06 experiment, *R/V Oceanus* sampled velocities and amplitudes associated with 27 distinct IW packets using shipboard acoustics at various locations over the continental shelf [107]. In addition, some packets were profiled using Oregon State University's microstructure profiler, yielding density and turbulent kinetic energy dissipation [76]. Generally, the IW tracking was carried out as follows: The ship was stationed ahead of the packet, the first few solitons were sampled as the wave propagated past the ship, after which the ship was repositioned ahead of the packet. In this fashion, IW packets were tracked over large distances across the continental shelf. Using visual and marine radar sightings, the ship course was held roughly in IW propagation direction.

Here, the focus lies on IW Rosey, the largest IW packet observed during the experiment [109]. IW Rosey was tracked over a distance of almost 40 km during an 11.5 hour period starting August 17, 2006, 19:00 UTC. During this period, 13 profiling time series were obtained, i.e. the ship was repositioned ahead of the IW roughly every 3 km or 1 hour. The 2006 IW season over New Jersey's continental shelf has been extensively studied [107, 108, 109]. For the period from August 17-21, Shroyer et al. [109] note that wave arrival times were roughly phased with the barotropic M2 tidal current measured at mooring SW40.

This chapter aims at studying IW Rosey's evolution through its surface signatures as observed by marine radar. Section 6.2 gives an overview of the available radar data, the ship

track, and the environmental conditions. In a brief excursus from this chapter’s main topic, section 6.3 consults both radar and ADCP measurements to determine the marine radar imaging mechanism for IW Rosey. The radar-derived time series of IW Rosey’s speed and direction as well as a correction for the background current are discussed in sections 6.4 to 6.6. Section 6.7 provides results from the IW surface signature retrieval. In section 6.8, an attempt is made to correlate IW-induced radar backscatter intensities with measured surface current gradients and pycnocline displacements. The radar-derived distances between subsequent backscatter peak and trough (p-p-distances) are used in section 6.9 to obtain IW amplitudes via an extended KdV equation, as suggested by Xue et al. [132]. This chapter concludes with a discussion in section 6.10.

## 6.2 Marine Radar Data Availability and Environmental Conditions

Marine radar data were collected with a standard Furuno marine X-band radar operating at 9.4 GHz with HH-polarization and grazing incidence angle. With an antenna repetition frequency of 24 rpm and a sampling frequency of 20 MHz, radar backscatter images were collected every 2.5 s with a range resolution of 7.5 m. The radar data were digitized and stored as a sequence of 12-bit images, using a Wave Monitoring System (WaMoS) [140]. The system was set to collect approximately 1800 radar pulses per image up to a maximum range of 3,900 m. Note that standard marine radars are not radiometrically calibrated, i.e. a quantitative interpretation of backscatter intensities can be challenging.

The map in Fig. 6.1 shows the track of *R/V Oceanus* as it was sampling IW packet Rosey. During the 11.5 hour period considered here, the IW traveled over almost 40 km across the continental shelf, covering water depths from above 80 m to under 60 m. The ship track roughly follows the IW propagation direction. For the same time period, Fig. 6.2 shows a time series of ship speed over ground and heading. During profiling, the ship was

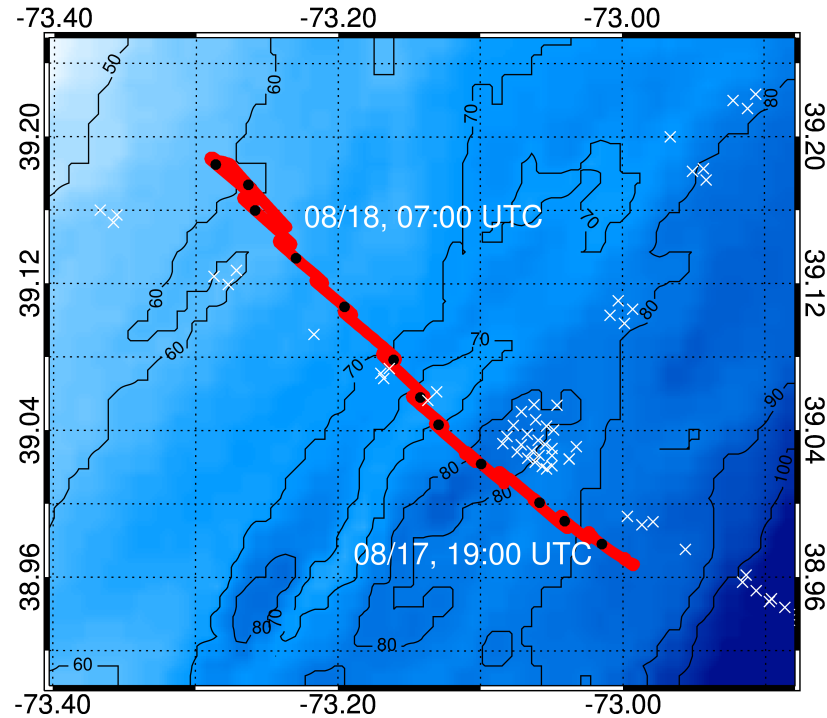


Figure 6.1: Map of ship track from August 17, 19:00 UTC to August 18, 07:00 UTC. The ship positions are shown in red, every full hour is marked by a black dot. Mooring positions are marked by white crosses. The color scale represents water depth.

heading into the IW and traveling at low speeds (below 1 m/s). A change of the profiling station is easily identifiable in the time series by the periods during which the ship advanced in IW direction (northwest) at greater speeds (3 to 4 m/s). During the period studied here, 13 profiling time series were collected.

Fig. 6.3 shows a time series of shipboard wind measurements made during our 11.5 hour period. Wind speed is an important parameter for this analysis, since the wave-current interactions that are responsible for the remotely sensible IW sea surface signatures require the presence of some ripple waves. As for marine radar-based wind and wave measurements, for wind speeds smaller than 3 m/s the backscatter intensity is too low to derive meaningful parameters [47]. Here, the wind comes constantly from east with speeds that are fairly stable, slightly decreasing from about 7 to 6 m/s during the period of interest. Note that the wind measurements show regularly occurring outliers that are most likely

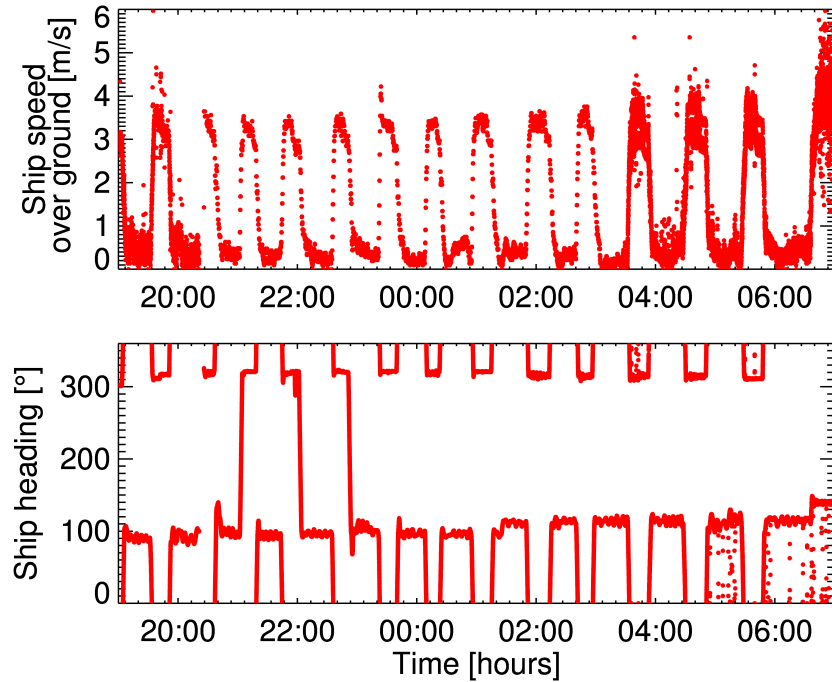


Figure 6.2: Time series of ship over ground speed and heading from August 17, 19:00 UTC to August 18, 07:00 UTC.

due to airflow distortion by the ship, which depends on the relative angle between ship heading and wind direction.

### 6.3 Marine Radar Imaging Mechanism of IWs

Different mechanisms have been proposed to explain the imaging of IWs by synthetic aperture radar (SAR). Alpers [2] has suggested that the hydrodynamic modulation of the small-scale surface waves due to the varying surface current field associated with IWs is the dominant SAR imaging mechanism. Hydrodynamic modulation leads to a radar backscatter peak in convergence zones and minimum backscatter in areas of divergence. Fig. 6.4 illustrates the radar imaging of IWs due to hydrodynamic modulation. Alternatively, in presence of surfactants, convergence zones may be associated with a negative radar backscatter

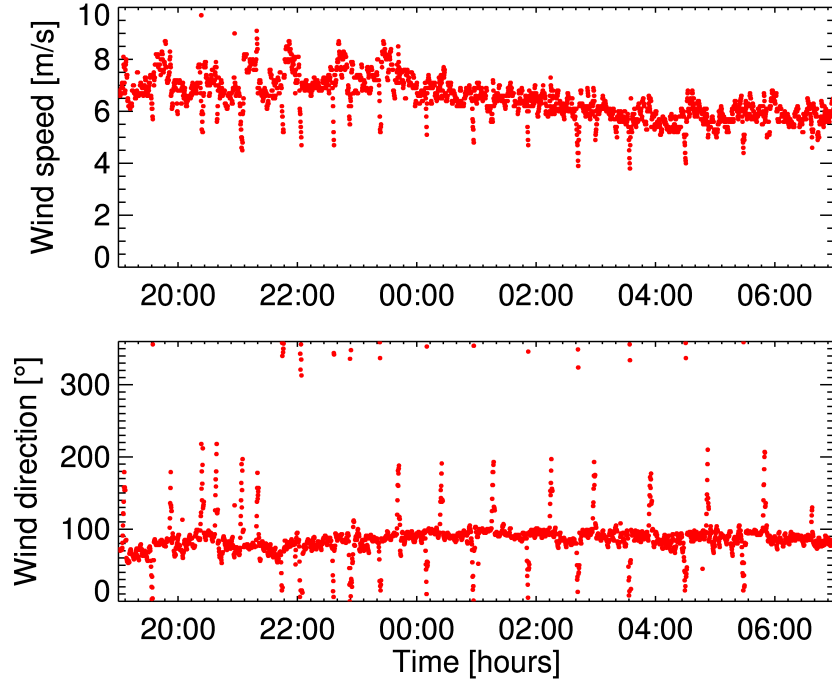


Figure 6.3: Time series of wind speed and direction measured from *Oceanus* during our 11.5 hour period starting August 17, 19:00 UTC.

peak. This is because surfactants have a dampening effect on the radar-resonant short surface waves, and they accumulate in convergence zones [29, 35].

In the following, radar backscatter and ADCP measurements are collocated to determine the dominant marine radar IW imaging mechanism. In addition, the radar-observed response of an ASIS buoy to the passage of an IW is consulted to provide further evidence regarding the imaging mechanism and illustrate the IW-induced forcing on the buoy.

### 6.3.1 Current Measurements as a Tool to Determine Dominant IW Imaging Mechanism

Fig. 6.5a shows the along-IW-direction current profile for the leading three solitons of IW Rosey as measured by ADCP from *R/V Oceanus* on August 17, around 22:00 UTC. The surface currents are highly variable with peak values greater than 0.6 m/s. The corresponding vertical current profile is shown in Fig. 6.5b. The IW-induced vertical currents are less

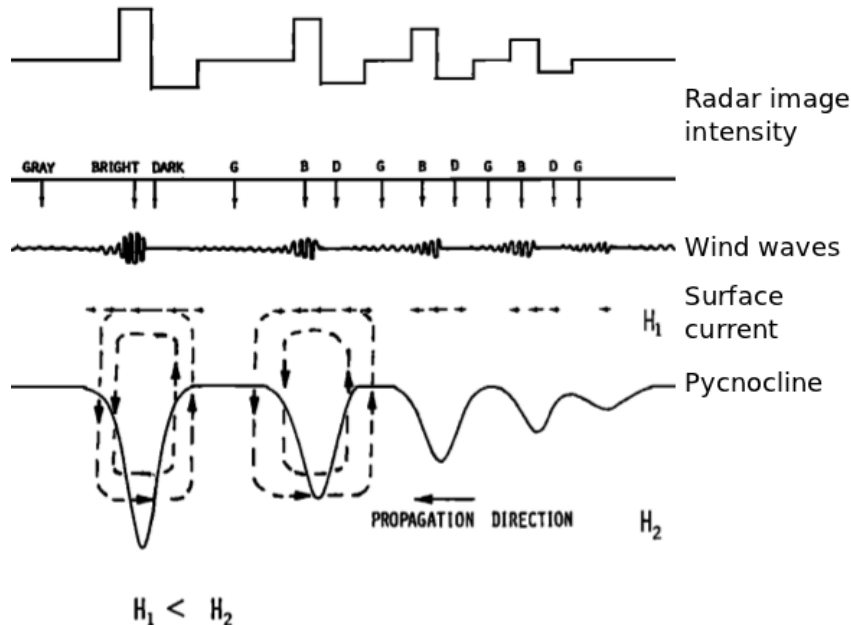


Figure 6.4: Scheme of IW radar imaging mechanism. Source: [67].

pronounced with absolute values below 0.1 m/s. However, the profile clearly shows narrow bands of down- and upwelling associated with each soliton. As the two graphs illustrate, the solitons impart an orbital motion to the water particles. Surface currents travel in IW direction, currents below the mixed layer in the opposing direction.

Convergence zones are characterized by a negative velocity gradient and divergence zones by a positive one. Fig. 6.6 shows the current velocity gradient at the sea surface as obtained from the ADCP record's 10 m bin and the corresponding normalized marine radar return. Here, a positive (negative) peak in the radar backscatter intensity coincides with a negative (positive) velocity gradient peak, suggesting an imaging mechanism that is dominated by hydrodynamic modulation. Note that the radar return measurement was made slightly earlier than the velocity gradient one. Furthermore, the radar record was obtained from a 4-min averaged image, while the ADCP profile was measured during a much longer time period. The difference in the time of measurement represents the most likely explanation for the differing radar return and velocity gradient peak locations found for the third soliton.

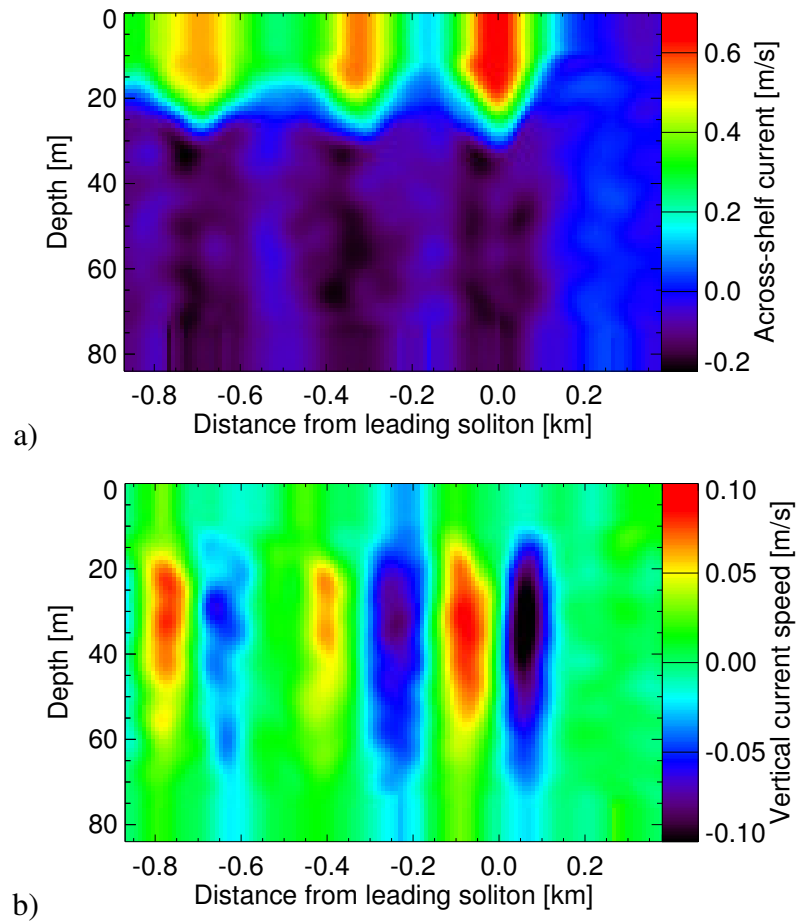


Figure 6.5: Current profiles along IW direction (a) and vertical current profile (b) as measured by ship-based ADCP from *R/V Oceanus* on August 17, 2006, around 22:00 UTC.

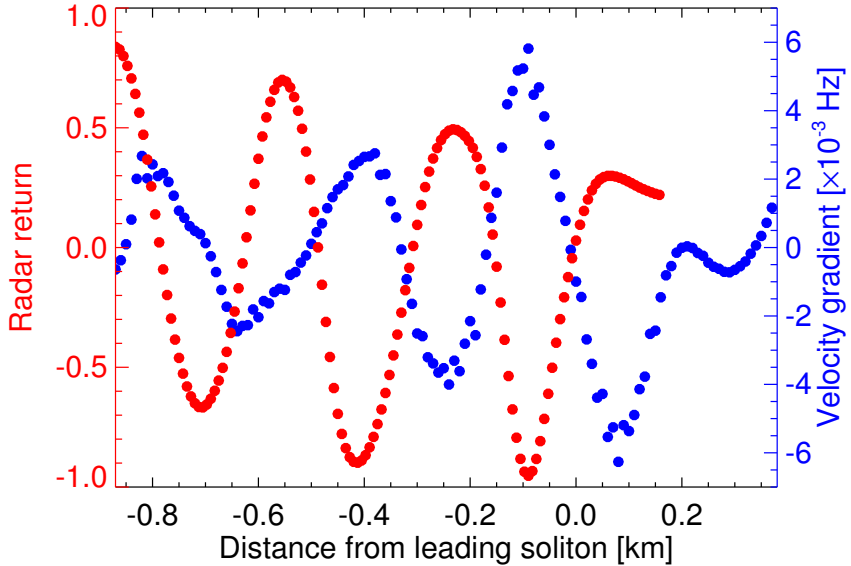


Figure 6.6: Normalized radar backscatter intensity (red) and corresponding surface current velocity gradient along IW direction (blue) as recorded from *R/V Oceanus* on August 17, 2006, around 22:00 UTC. The IW propagates from left to right.

### 6.3.2 ASIS Response to IW as Observed by Marine Radar from *R/V Knorr*

A different way of determining the marine radar IW imaging mechanism consists of studying the response of a floating radar target to the passage of an IW. Fig. 6.7a shows a marine radar image collected from *R/V Knorr* on August 14, 2006, 04:14 UTC. The Air-Sea Interaction Spar (ASIS) buoy [44] Yankee and its surface tether are located inside the red frame at a distance of about 1.7 km from the ship. The radar image was collected shortly before the IW packet reached the buoy. In the image, the IW is clearly visible as a group of bright and dark bands traveling in a northwesterly orientation. During the period studied here, a steady wind of 7 m/s was coming from west-southwest as measured by *R/V Knorr*'s anemometer. Fig. 6.7b shows a zoom into the framed area with the ASIS buoy and surface tether. The data shown in the zoom represent a 1 min average of georeferenced images to enhance the buoy and tether signal, which show as bright points against a dark background. Before the IW's arrival, the ASIS buoy was acting like a weather vane, with the line connecting it to the tether buoy pointing in wind direction.

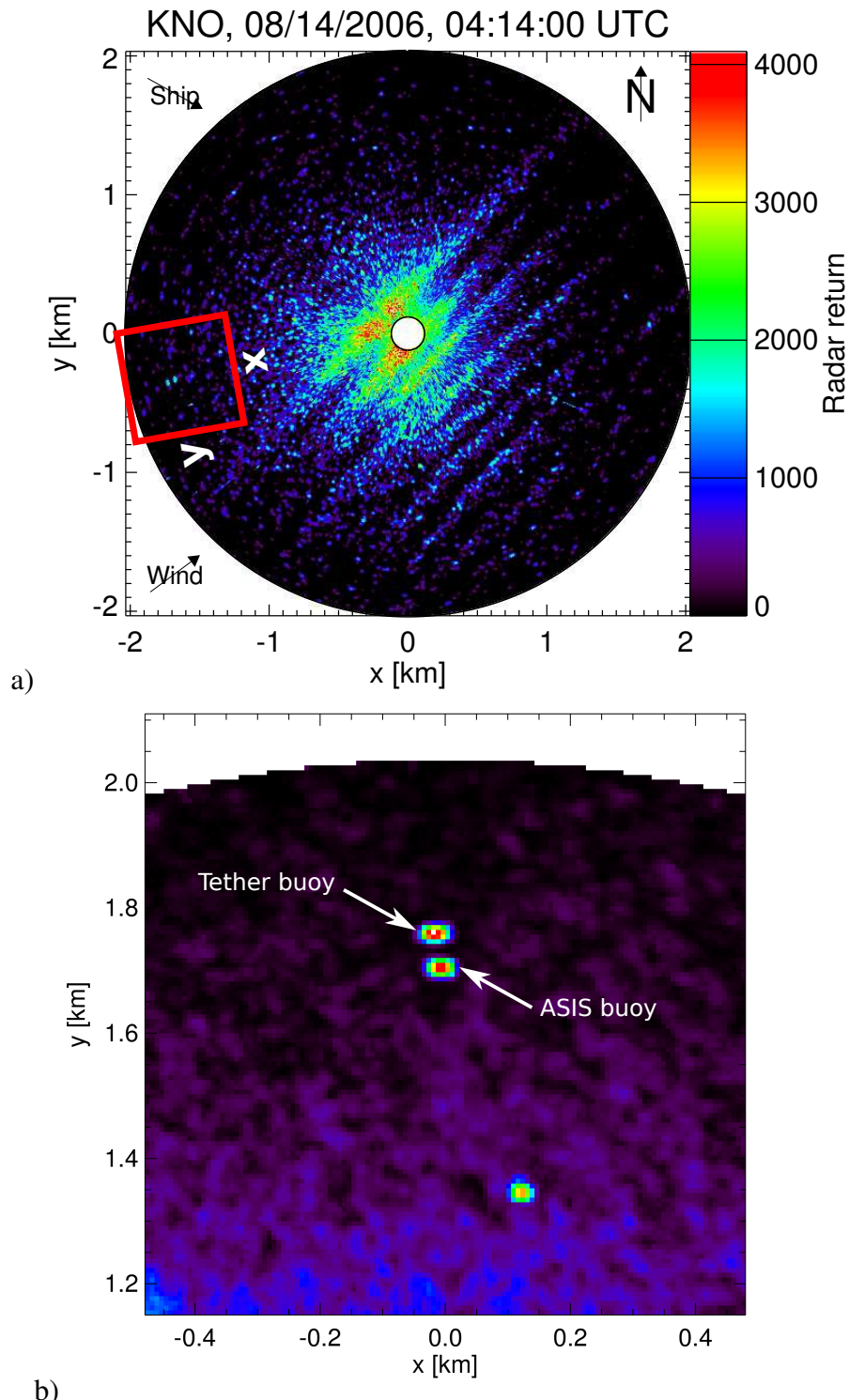


Figure 6.7: Marine radar image from *R/V Knorr* collected on August 14, 2006, 04:14:00 UTC. The zoom area covering the ASIS and tether buoys is marked by a red frame (a). Zoom into area with ASIS and tether buoy. The data shown are a 1 min average of georeferenced data starting with the image at the top (b).

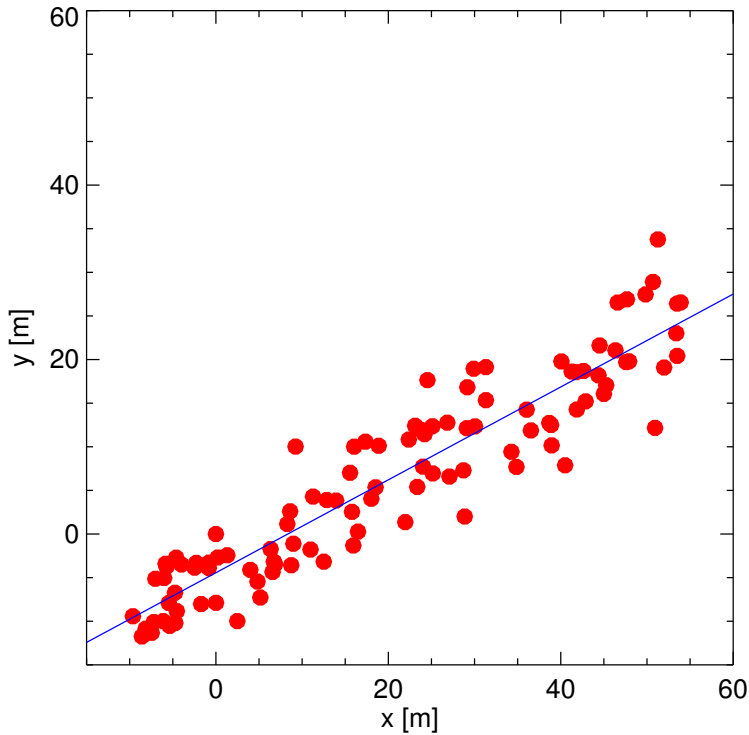


Figure 6.8: Deviation of ASIS buoy from initial position in 1-min intervals for period from August 14, 2006, 04:14 through 05:59 UTC. The best-fit line is shown in blue.

The motion of the ASIS buoy in response to the IW passage may reveal some information on the dominant imaging mechanism. In this context, we need to take into account that the ASIS buoy is attached to a surface tether via a 60 m long line and therefore not freely floating. Furthermore, the ASIS buoy is designed to be driven mostly by wind- and only to a lesser extent by current-forcing, as demonstrated by its orientation in wind direction. Fig. 6.8 shows the deviation of the ASIS buoy from its initial position in 1-min intervals for the 1:45 hour period during which the buoy was under the IW's influence. The mean buoy motion, as illustrated by the best-fit line, is in direction of the IW propagation, suggesting that the IW-induced surface currents are strong enough to take precedence over the wind forcing on the buoy.

Fig. 6.9a shows a time series of the along-IW-direction component of the buoy's motion during the first 50 min of the same period. The buoy's velocity, derived from the same data, is shown in Fig. 6.9b. The vertical red bars mark the times at which an IW-induced radar

backscatter intensity peak reached the buoy location. The speed of the buoy, reaching peak values just under 0.3 m/s right after the passage of the leading soliton, shows that the IW exerted significant hydrodynamic forcing. The fact that the radar backscatter intensity peaks at times when the buoy accelerates, suggesting converging surface currents, indicates again that hydrodynamic modulation is responsible for the marine radar imaging of the IWs observed here.

To conclude, both ADCP measurements from *R/V Oceanus* and the ASIS buoy response to an IW passage as observed from *R/V Knorr* suggest that hydrodynamic modulation represents the dominant marine radar IW imaging mechanism.

## 6.4 IW Propagation Direction

The image in Fig. 6.10a shows the raw radar data as recorded by WaMoS on August 18, 04:00:01 UTC. Fig. 6.10b shows a ramp-corrected, normalized, georeferenced, and 1-min averaged image from the same time. The surface signatures of IW Rosey are visible in both images, however, the signal is clearly enhanced in the averaged version. The work detailed in the following will use such pre-processed and 1-min averaged radar images. A detailed outline of the individual processing steps can be found in [70, 96]. Note that the IW surface signatures exhibit some curvature as well as phase shifts due to packet-packet interactions.

Fig. 6.11 shows a time series of IW Rosey's propagation direction starting August 17, 19:00 UTC. The propagation direction was determined using localized Radon transform techniques. It changed from  $300^\circ$  to  $310^\circ$  during the first four hours, then went back to under  $305^\circ$  by hour 7, and up to  $315^\circ$  towards the end of the time series. Shroyer et al. [109] find that the across-shelf mean speed of the IWs they sampled was significantly correlated with across-shelf barotropic velocity. They therefore conclude that waves were advected with the barotropic tide. This suggests that the IW propagation direction changes observed in the marine radar data are related to the barotropic tide. Alternatively, IW interactions

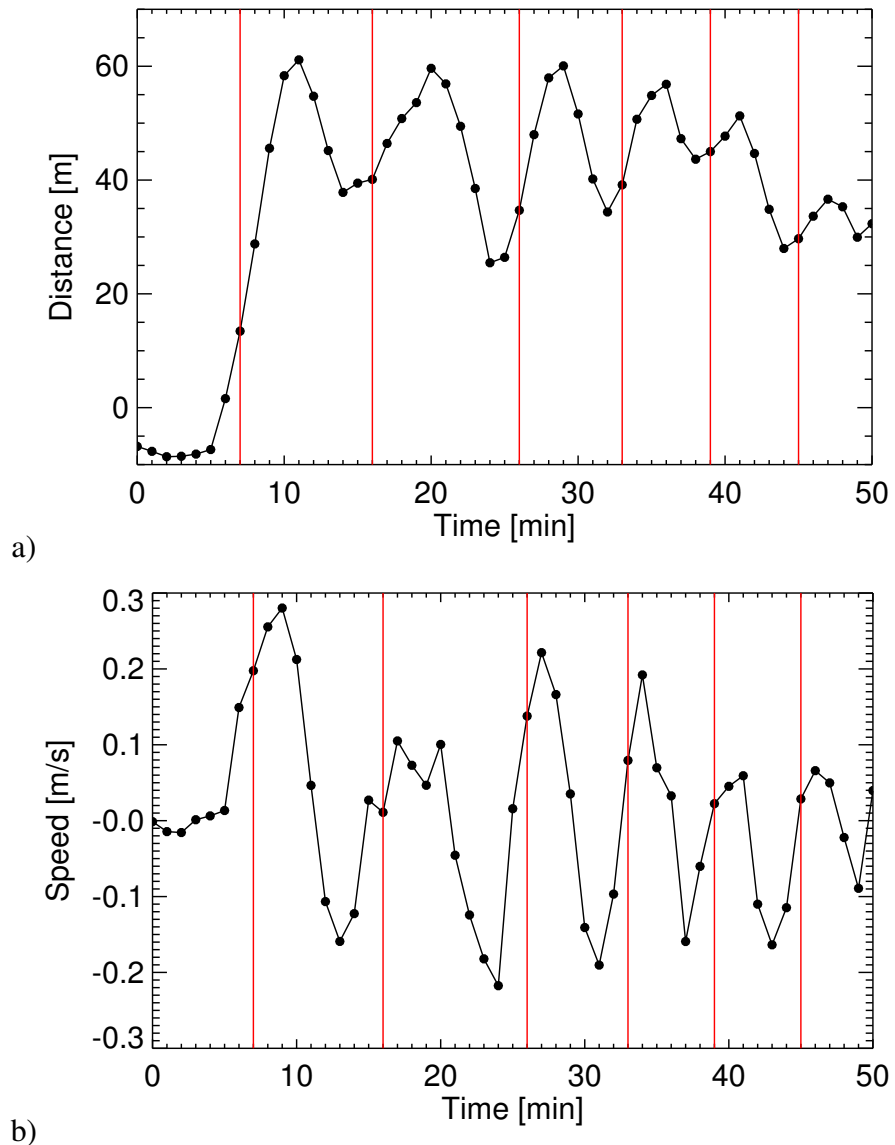


Figure 6.9: Component of buoy motion along IW propagation direction (a) and corresponding speed (b). The times at which the buoy was on top of a soliton are marked by red bars.

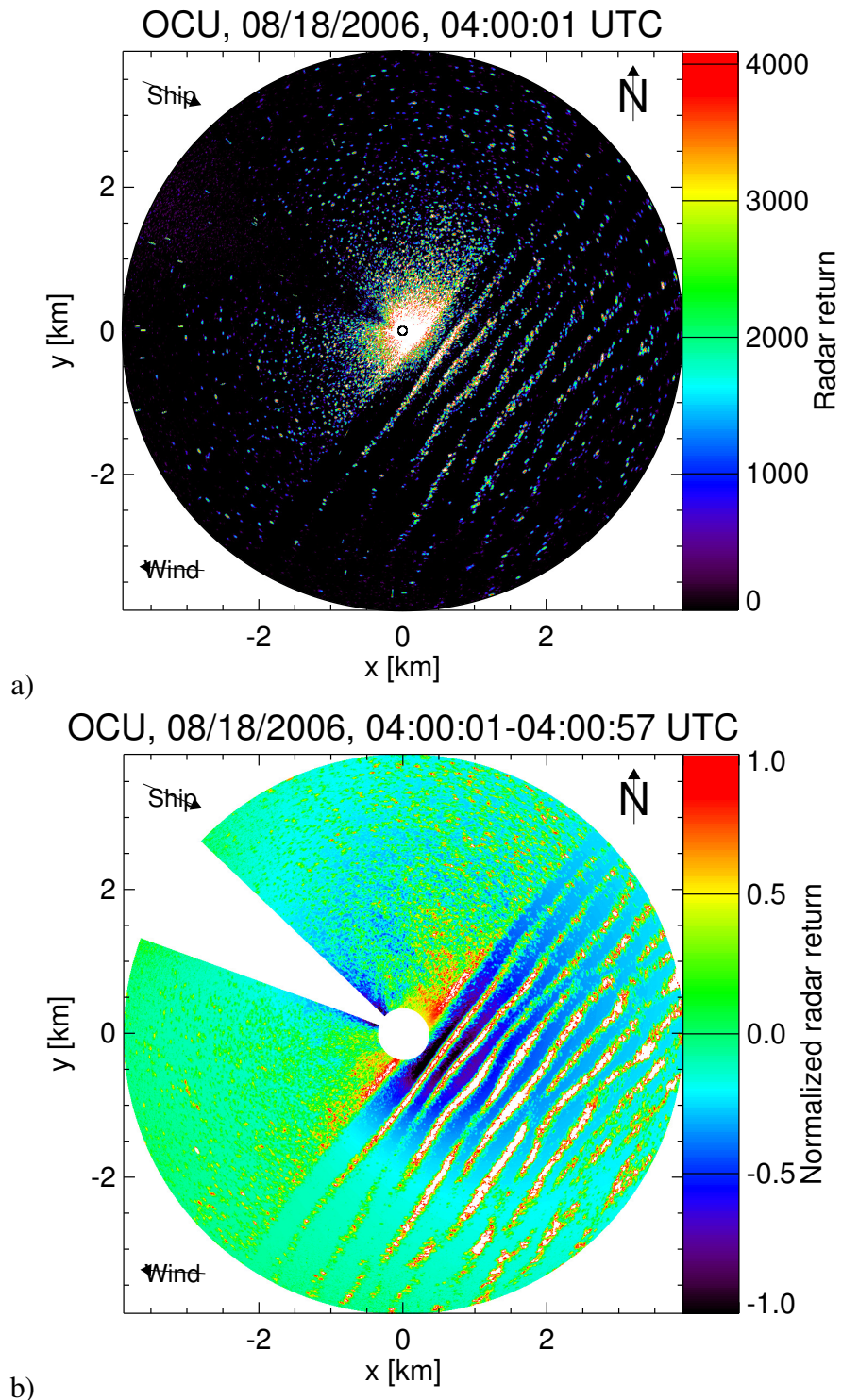


Figure 6.10: Marine radar image from August 18, 04:00 UTC (a) and 1-min average of pre-processed images starting with the one on top (b).

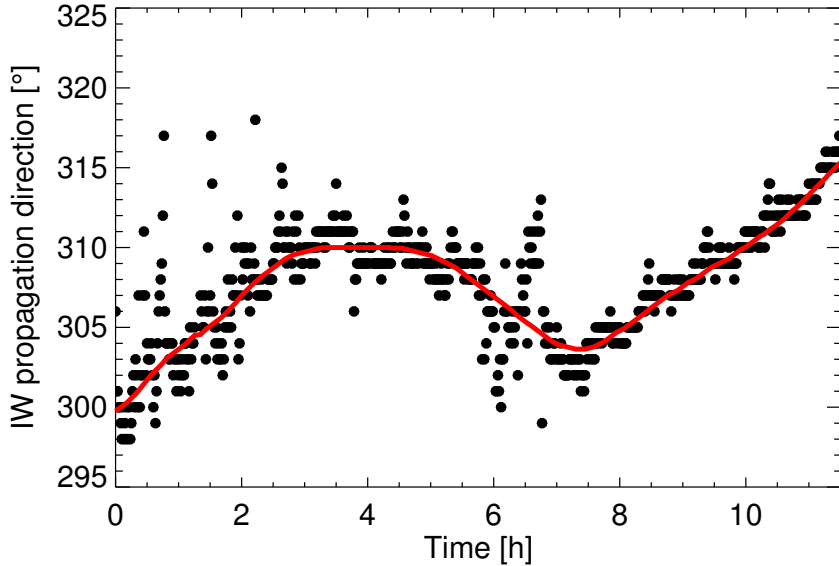


Figure 6.11: Time series of IW Rosey's propagation direction starting August 17, 19:05 UTC. Raw estimates are shown in black. The red curve shows the 60 min running average.

with the bottom topography could be responsible for the observed directional changes. Finally, IW interactions could induce some changes to the propagation direction. This question merits further research.

## 6.5 IW Propagation Speed

In a next step, the IW packet speed is retrieved. To this end, the pre-processed and 1-min averaged radar images are projected onto their IW propagation axes. Here, we use the 60 min running average of our previously determined IW propagation direction for the projections. Fig. 6.12 shows the projection of the image from Fig. 6.10b onto its IW propagation axis. At the time, the IW propagated in a direction of  $307.6^\circ$ . The signal due to the IW is very prominent, with the leading soliton close to the image origin (i.e. the location of the ship).

Fig. 6.13 shows a Hovmöller diagram of radar image projections onto the IW propagation axis for the 11.5 hour period studied here. The individual projections were positioned such that they reflect the ship's motion along the IW propagation direction. A 5 min data

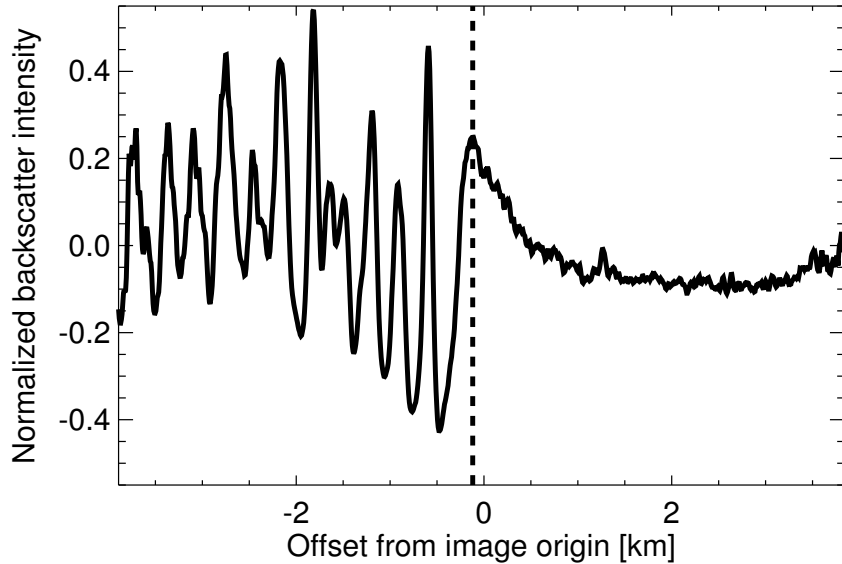


Figure 6.12: Projection of 1-min averaged radar image onto the IW propagation axis. The radar data were recorded on August 18, 04:00 UTC. The position of the leading soliton is marked by a dashed line.

gap during the second hour shows as a white horizontal band in the figure. The figure shows that the IW was tracked over a distance of approximately 37 km across the continental shelf. Furthermore, the figure illustrates how the number of solitons increases and how their surface signatures become clearer over time. Note that the diagram shows a strong signal that remains almost stationary from hours 1.5 to 3 (visible as a vertical line). This is due to a ship in the radar field of view. The bright target recognition and correction proposed in [70] is obviously not working as a global approach. This issue could easily be resolved by using a dynamic threshold, e.g. one that targets the 0.1 % brightest pixels.

The IW packet speed retrieval technique employed in [96, 70] is based on the cross-correlation of consecutive image projections. The IW speed can be derived from the lag associated with the peak in the cross-correlation function. The results obtained using this approach are shown in Fig. 6.14. The 60 min averaged time series of the IW speed appears to have a periodicity that resembles the one observed for the IW propagation direction (see Fig. 6.11), which may be due to the barotropic tide (or wave-bottom or packet-packet interactions). However, the raw estimates are of a much noisier character with values ranging

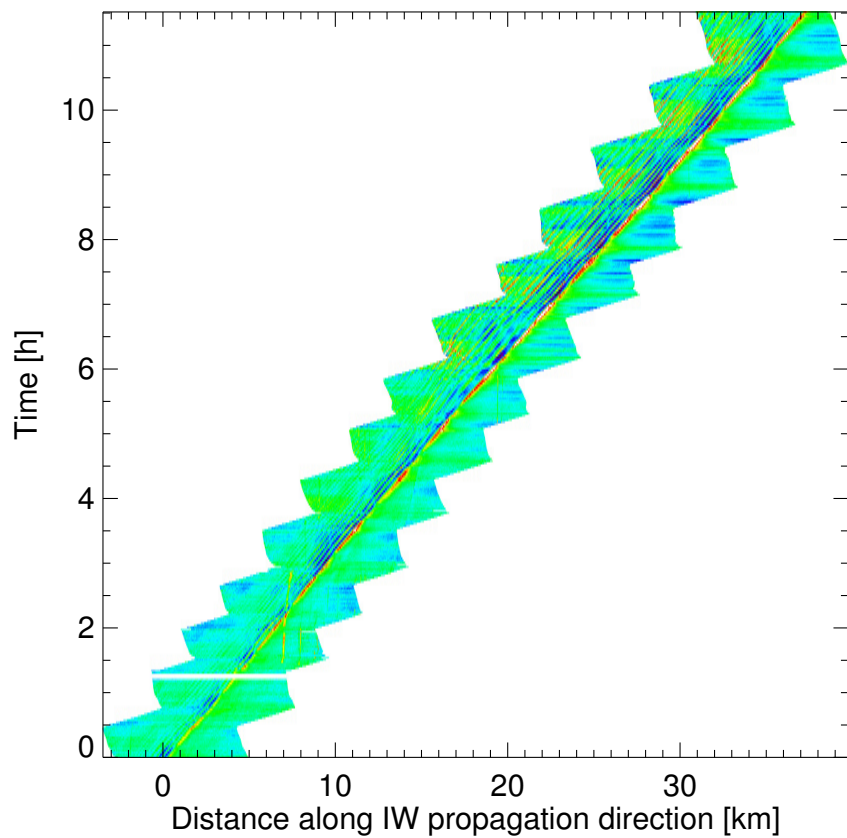


Figure 6.13: Hovmöller diagram of pre-processed and 1-min averaged radar images projected onto the IW propagation axis. The individual projections were shifted to account for the ship motion along the IW propagation direction. The diagram's first projection corresponds to August 17, 19:05 UTC.

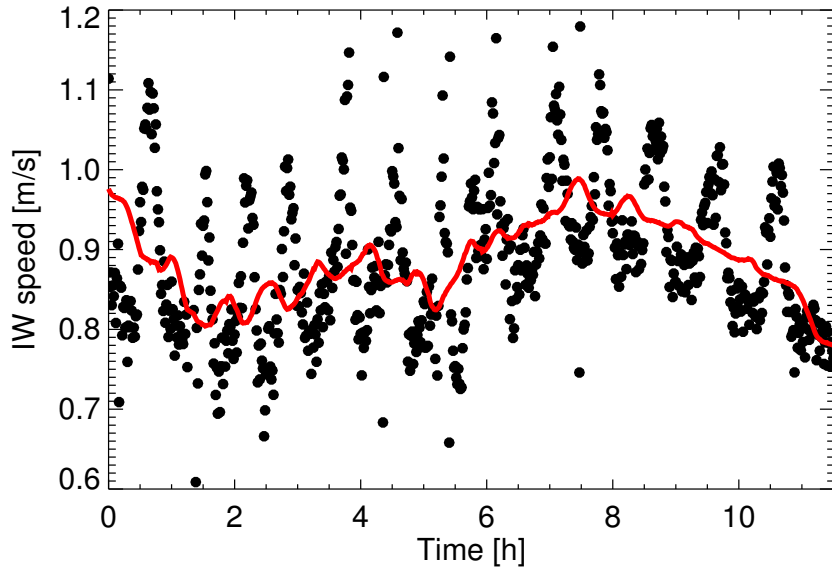


Figure 6.14: Time series of IW packet speed obtained using cross-correlation techniques. The red curve shows the 60 min running average. The time series starts August 17, 19:05 UTC.

from 0.6 to 1.2 m/s. And, most strikingly, the data show a regularly occurring pattern that seems to be in sync with the ship track (compare Fig. 6.2).

To gain a better understanding of the ship track's impact on our IW speed estimates, we identify the position of the leading soliton for each time stamp. Fig. 6.15 shows a Hovmöller diagram of ship-centered image projections. For each individual projection, the position of the leading soliton is shown. Times during which the leading soliton was more advanced than the ship are marked in blue, times when the ship was ahead of the IW are marked in red.

Fig. 6.16 shows again a time series of the IW packet speed. As before, periods when the leading soliton was more advanced than the ship are shown in blue, periods during which the ship was ahead of the IW packet are marked in red. The speed estimates clearly depend upon the relative position between ship and IW packet. In general, the speed either reaches a peak or a trough at times when the leading soliton is at the same level as the ship. This behavior depends on whether the ship is moving up- or downwave (i.e. against or in IW propagation direction). An upwave motion results in a speed trough, a downwave motion

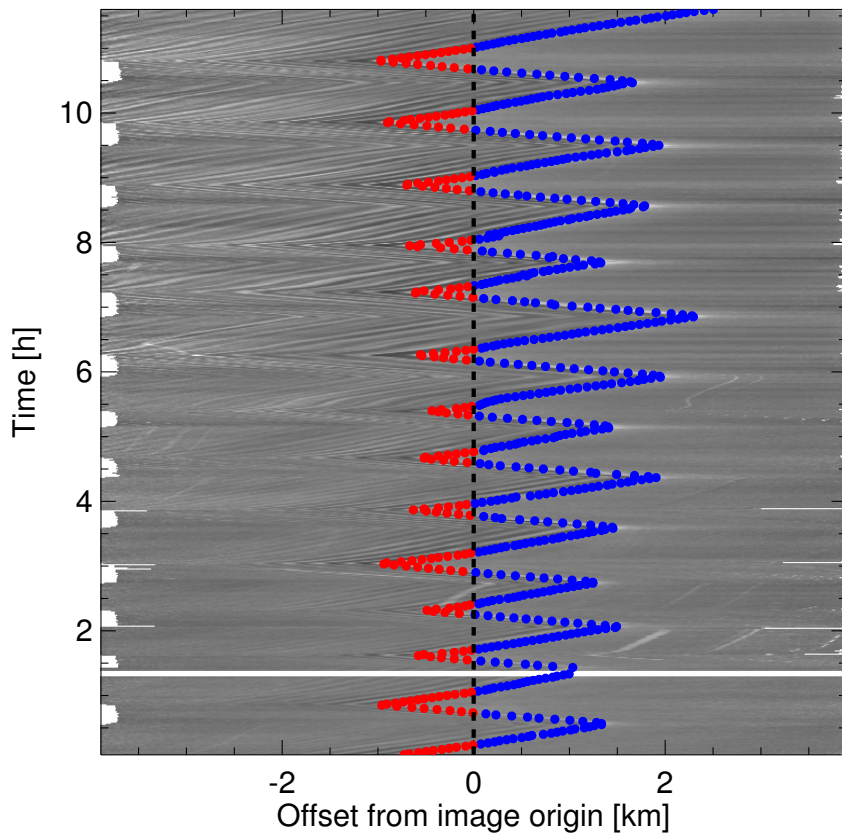


Figure 6.15: Hovmöller diagram of image projections. The individual projections were arranged to be ship-centered. The black dashed line marks the image origin (i.e. ship position). The position of the leading soliton is shown for each individual projection, with times during which the leading soliton had traveled past the ship marked in blue and times when the ship was ahead of the packet marked in red. The diagram's first projection corresponds to August 17, 19:05 UTC.

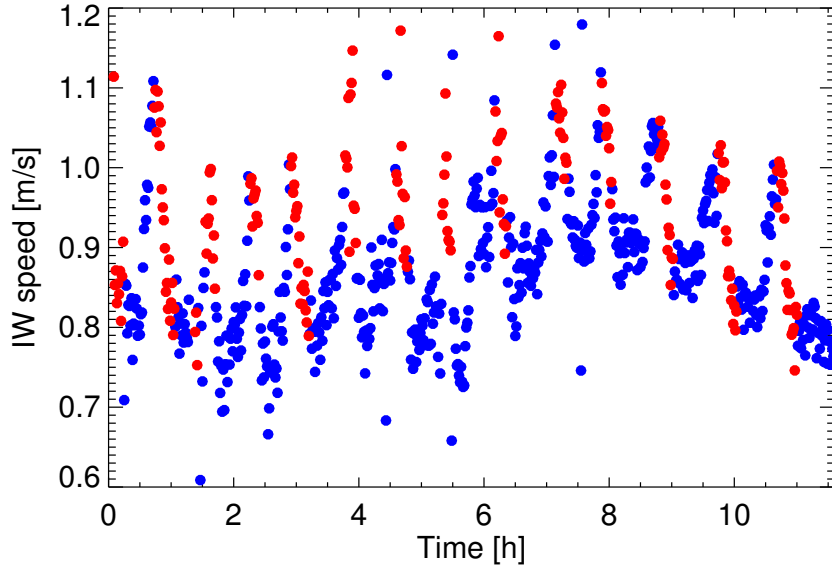


Figure 6.16: Same as Fig. 6.14, but times during which the ship was ahead of the IW packet are marked in red, blue indicates times when the leading soliton was more advanced than the ship. The time series starts August 17, 19:05 UTC.

in a peak. We can thus divide our data into four distinct categories, with the speeds of each category depending on the distance between ship and leading soliton: Uplooking and -traveling; uplooking and downtraveling; downlooking and -traveling; downlooking and uptraveling. Note that a similar behavior of the propagation speed is found if one derives it directly from the leading soliton position (or the position of the trough that follows the leading peak) instead of employing a cross-correlation technique.

To shed further light on this problem, Fig. 6.17 shows a time series of the mean radar backscatter intensity along the leading soliton's crest, obtained from the image projections shown in Fig. 6.15. As before, the figure uses blue and red to distinguish between times when the ship was behind or ahead of the leading soliton. A general trend of increasing backscatter intensity over time can be observed. What is more noteworthy in this context, however, is that the IW-associated backscatter intensity shows a dependency on the ship track that is similar to that found for the IW speed. In particular, the backscatter intensity appears to be greater at times when the IW is ahead of the ship.

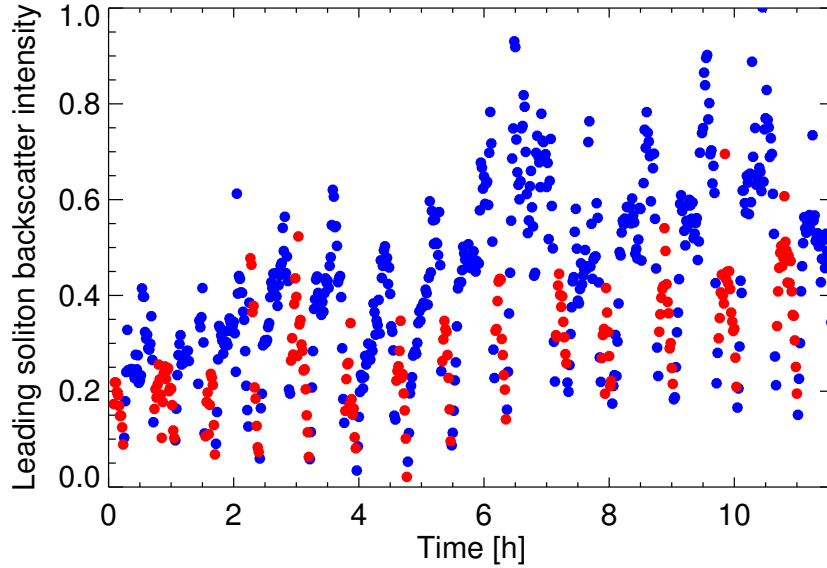


Figure 6.17: Time series of mean radar backscatter intensity along the leading soliton's crest (as extracted from the image projections shown in Fig. 6.15). Red data points mark times during which the ship was ahead of the IW packet, blue indicates that the leading soliton was more advanced than the ship. The time series starts August 17, 19:05 UTC.

A combination of different factors appears to be responsible for this issue, and a detailed examination is beyond the scope of this work. In the following, a few possible explanations will be discussed:

- The fact that the observed speed changes are in-sync with the ship track, makes it clear that they do not reflect the IW behavior. A possible explanation would be a bug in the georeferencing of the image projections. A close inspection of the code, however, showed no errors. What is more, the speed generally either peaked or reached a trough at times when ship and soliton were at the same level. When this happened, the ship steered a steady course as it was either sampling the IW or traveling towards the next profiling station. It is therefore unlikely that the georeferencing is to blame.
- The backscatter intensity associated with the leading soliton exhibits a pattern that is similar to that of the IW speed. This could be due to different backscattering mechanisms, depending on whether the radar is positioned in front of or behind the IW packet. For example, small breaking waves that are known to enhance HH-

polarized grazing incidence backscatter might be more pronounced for an up- or downwave antenna look direction. Now, if the wave breaking occurred at a location that is slightly different from that of the Bragg scatterers, a phase shift in the peak backscatter intensity could occur as the ship travels in or against the wave. A phase shift would translate into a changing soliton speed. Also, since the relative angle between IW propagation and antenna look direction depends on the crest location, and, here, we are looking at along-crest averaged backscatter values, this change would occur gradually, as it does here. However, if this was the only reason for our issue, we would expect a reversal in the speed changes at times when the ship changed course, which is not evident here.

- The radar ramp correction and normalization could also play a role here. A significant section of the *Oceanus* radar images is masked by the ship mast. Here, we use the measured radar backscatter from outside the mask to construct a ramp that covers the full radar field of view. The position of the mask relative to the wind direction changes with the ship course. The course changes thus may have an impact on the ramp. Furthermore, the IW signatures may affect the ramp construction. It is therefore feasible that the course changes as well as the relative position between IW signatures and ship modify the ramp, which might in turn influence our IW speed estimates. This is because the ramp correction may change the IW's apparent position depending on the wave's location along the ramp's nonlinear slope.

To overcome the apparent dependency of the IW speed on the ship track, a new processing method has been developed. Fig. 6.18 shows a time series of the IW speed that was derived from the leading soliton positions shown in Fig. 6.15. The soliton positions were divided into four categories based on the relative position between ship and leading soliton (antenna looking up- or downwave) as well as on whether the ship was heading up- or downwave. The positions of each category were then divided into segments, i.e. profiling stations. For each category and offset from the image origin, the distance the leading

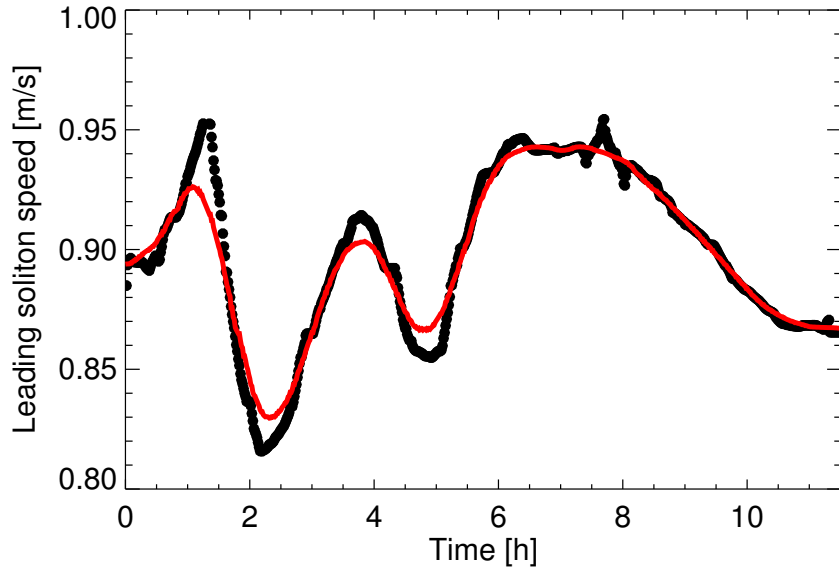


Figure 6.18: Time series of leading soliton speed obtained from the mean of estimates that were made independently for four different data categories (based on whether antenna look direction and ship heading were up- or downwave). The red curve shows the 60 min running average. The time series starts August 17, 19:05 UTC.

soliton traveled between subsequent segments was used to compute the IW propagation speed. Fig. 6.19 shows the leading soliton speed estimates from our four data categories in form of a Hovmöller diagram. The mean value is shown for data points where more than one estimate was available. The leading soliton speed time series in Fig. 6.18 shows the mean of all offsets. Compared with Fig. 6.14, the resulting speeds are more stable and the underlying trend is much better defined.

Finally, the radar image projections carry information on the IW packet's evolution that merits further discussion. The Hovmöller diagram in Fig. 6.20 was obtained by shifting the individual projections from our 11.5 hour period such that they are centered around the leading soliton's position. The diagram was subsequently smoothed over 60 min to enhance the most prominent and persistent features. The following observations can be made: Firstly, the IW signatures become more distinct over time as the contrast between peaks and troughs increases. Secondly, the number of solitons increases as time progresses. Lastly, the wavelength is highly variable and may increase and subsequently decrease with

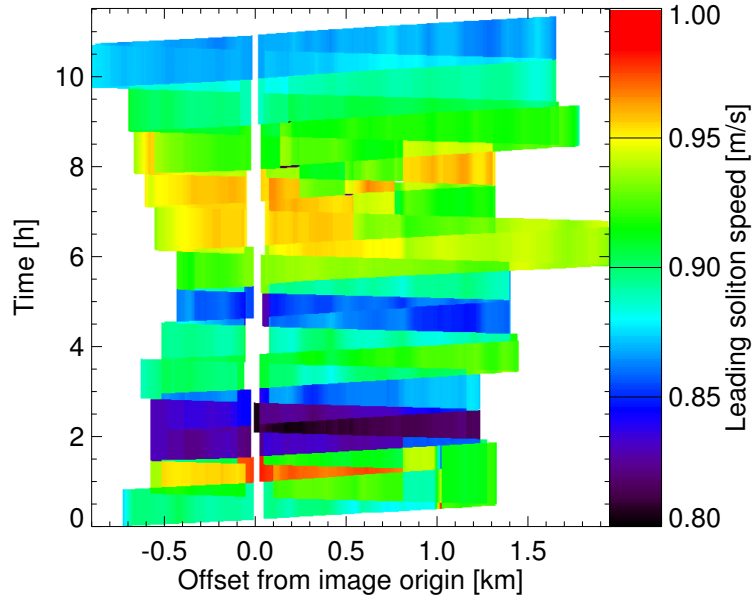


Figure 6.19: Hovmöller diagram of leading soliton speed estimates obtained from our four data categories, starting August 17, 19:05 UTC. For data points where more than one estimate was available the diagram shows the mean value.

time, which is at least partly the result of IW packet-packet or wave-wave interactions. In this context, we would like to draw the reader's attention to an apparent interaction between the second and third soliton of the packet. Here, the third wave appears to be overtaking the second. However, after inspection of the corresponding imagery (see, for example, Fig. 6.21), this is not the case. Instead, the enhanced curvature of solitons 2 and 3, most likely due to IW interactions, is to blame for this apparent overtaking.

## 6.6 Correction for Background Current

To determine the IW speed, one needs to subtract the background current due to tides, wind, and waves. Fig. 6.22 shows a time series of background current speed, direction, and water depth as measured by ADCP from *R/V Oceanus* while it was tracking IW Rosey. The time series starts August 17, 19:05 UTC. The current measurements were made at times during which the ship was in front of the IW, and represent 60-min smoothed values. The background current appears to be modulated by a 12-h tidal periodicity with currents go-

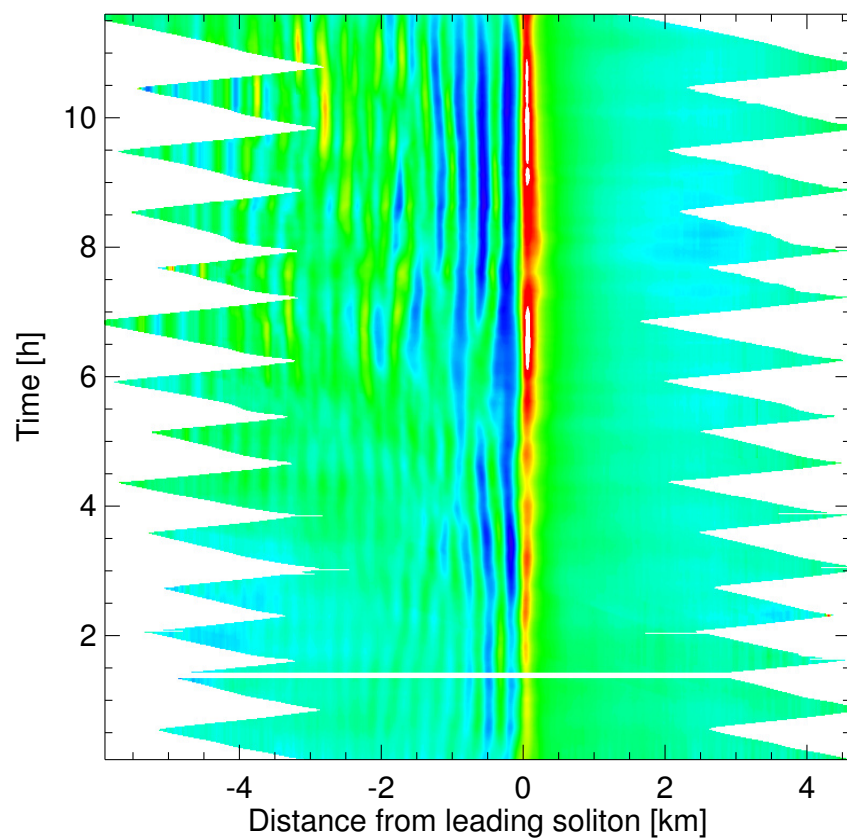


Figure 6.20: Hovmöller diagram of radar images projections centered around the IW packet's leading soliton. The projections were smoothed with a 60 min window. The diagram's first projection corresponds to August 17, 19:05 UTC.

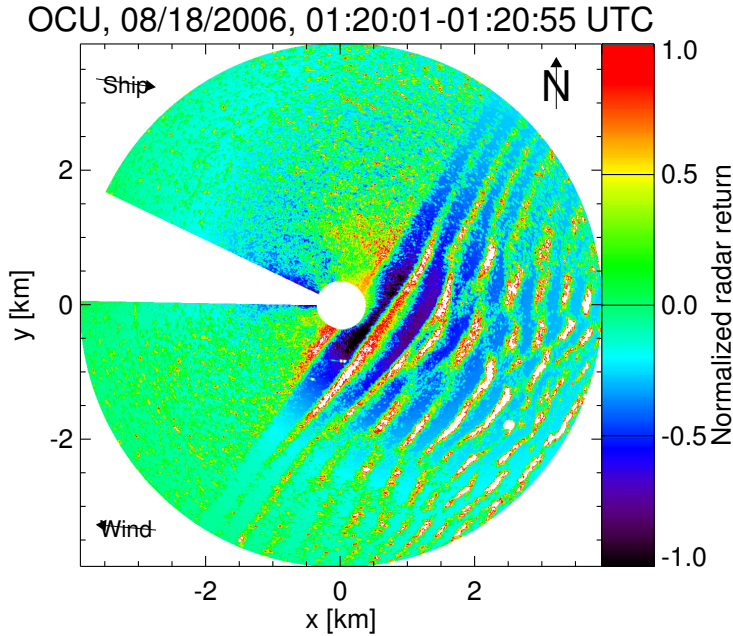


Figure 6.21: 1-min average of pre-processed marine radar images from August 18, 01:20:01 through 01:20:55 UTC.

ing in a western direction at first, turning south, and later returning to a western direction. Background current speeds are small, ranging from 0.03 to 0.18 m/s. During the 11.5 hours studied here, the water depth ranges from 85 m at the beginning to just under 60 m towards the end as the IW propagates onto the shelf. However, this change is not linear; the water depth increases during the third hour, remains stable for another 1.5 hours, and then decreases quite rapidly.

The top time series in Fig. 6.23 shows the 60-min averaged IW speed, as derived in section 6.5 (compare Fig. 6.18), before and after correction for the background current. The figure also shows the IW direction from section 6.4. The background-current-corrected speed is with 0.8 m/s relatively slow at first, then increases to 0.95 m/s over the course of 3 hours. This is followed by a “bump” in the speed, possibly due to the sudden decrease in the water depth, after which the maximum speed of 0.95 m/s is reached yet again. Starting from hour 6, the corrected IW speed decreases continuously to a value below 0.8 m/s at the end of the time series. The observed behavior of the IW speed can be seen as an indicator

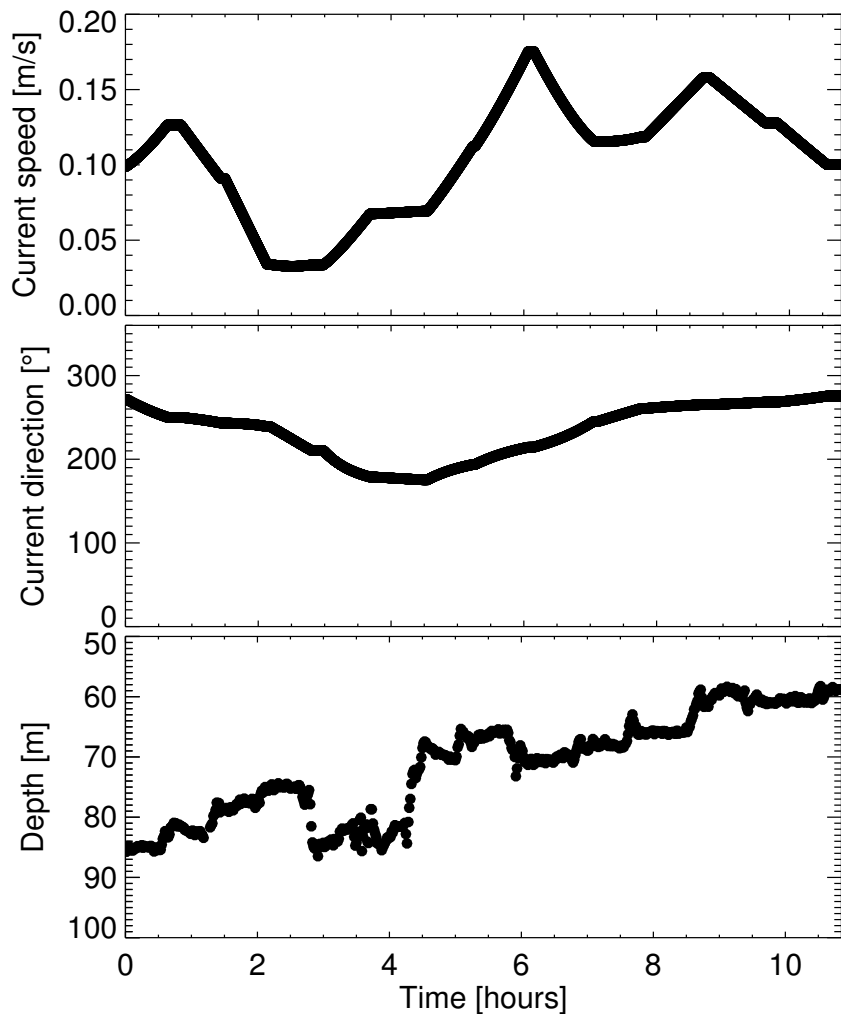


Figure 6.22: Time series of background current speed (top) and direction (middle) obtained from shipborne ADCP at times when the *Oceanus* was in front of the IW group. The corresponding water depth, also obtained from the ADCP record, is shown at the bottom. The time series starts August 17, 19:05 UTC.

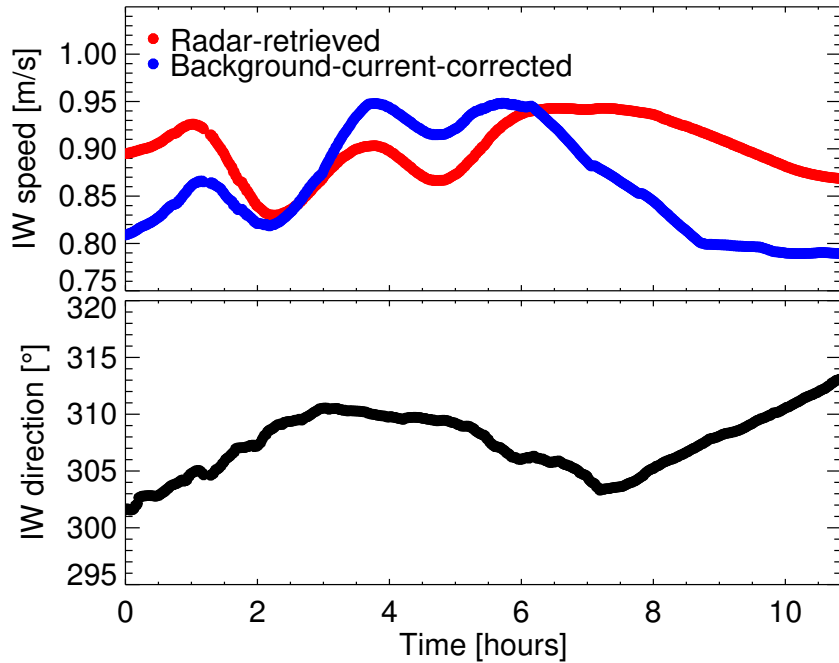


Figure 6.23: Time series of IW direction and speed before (red) and after (blue) correction for background current. The time series starts August 17, 19:05 UTC.

of IW growth and decay, since weakly nonlinear soliton theory predicts that IWs of greater energy travel faster [34, 1].

## 6.7 Evolution of IW Surface Signatures

As discussed in section 6.5, the image projections onto the IW propagation axis, as shown in the Hovmöller diagram of Fig. 6.20, provide a good overview of the IW evolution. However, they may conceal information on IW interactions that can only be studied by analyzing the full radar images. The same argument can be made for any attempt to derive IW characteristics from the radar backscatter intensity or from the distance between neighboring backscatter peak and trough. This is because for IW surface signatures that exhibit some curvature, e.g. due to wave-wave or bottom interactions, it becomes difficult to link the peaks and troughs within the image projections to a specific soliton.

Fig. 6.24 shows a sequence of IW-enhanced radar images (each image represents a 4-min average) with convergence bands marked in red and divergence bands in blue. The images were collected from *R/V Oceanus* during the tracking of IW Rosey and cover the time period from August 17, 2006, 19:00 UTC to August 18, 06:00 UTC. Here, we focus on images that were collected at times when the ship was ahead of the tracked IW group. To enhance and retrieve the IW surface signatures, the techniques introduced by Lund et al. [70] were employed. However, the radar ramp correction was slightly modified: Instead of subtracting the ramp from the individual radar images, and then dividing by the standard deviation, the images were solely divided by the ramp. The resulting images are therefore centered around 1 (as opposed to 0), and the variability of backscatter intensity values still exhibits a range dependency. Further research is required to determine which of the two approaches yields better results.

The following observations can be made regarding the retrieved IW surface signatures: Firstly, the number of solitons increases and the solitons become better defined with time. For example, during the first 2-3 hours of the time series, the surface signatures of the trailing solitons do not span over the entire image. Secondly, the distance between neighboring peaks and troughs tends to increase over time. Thirdly, the surface signatures are highly complex, exhibit a significant amount of curvature, and do not necessarily span across the whole image. Consequently, the assumption that they approximate straight lines within the radar field of view is an oversimplification. Finally, and related to the previous point, the surface signatures show some clear evidence of wave-wave interactions. In the following, the evidence of IW interactions within the IW soliton maps will be discussed in greater detail.

Depending on amplitude and propagation direction, interacting IWs may exhibit phase shifts [37, 123, 133]. The majority of the images shown in Fig. 6.24 have signatures of at least one additional IW packet. In particular during the first 5 hours of the time series, an IW packet at an interacting angle of approximately  $45^\circ$  (the angle is greater at the

beginning but decreases with time) is clearly visible. The rupture that all imaged solitons exhibit during this period and that is accompanied by a phase shift is most likely due to the dominant IW's interaction with this second packet. The image from August 17, 21:18 UTC, shows evidence that a third packet, at a  $90^\circ$  angle to the second packet, is present. Finally, towards the end of the time series, another IW packet at an interacting angle close to  $90^\circ$  becomes visible (the signatures are most clear in the image from August 18, 04:56 UTC). Note that our IW signature retrieval technique includes a step that enhances the signal associated with the dominant wave by correcting for its average motion before averaging. This enhancement step works less well for additional IW groups and may even have an adverse effect if they propagate in directions that are much different from the dominant group's propagation direction. However, if the additional groups have a strong enough signal, the techniques that have been developed for and applied to the dominant group, could easily be used to separately also enhance their signal. This is work in progress that, in combination with research done by Xue et al. [133], might yield information on IW amplitudes.

## 6.8 IW Characteristics from Radar Backscatter Intensity

For situations where hydrodynamic modulation is the dominant radar imaging mechanism of IWs, which is the case here (see section 6.3), the IW-associated areas of converging and diverging surface currents become visible as bright and dark bands on a gray background. It is clear that the IW-induced modulation of the radar backscatter intensity from the sea surface carries some information on the dynamics of the interior ocean. Work by Brandt et al. [17] based on SAR data and modeling results suggests that the complexity of radar imaging mechanisms makes it very difficult to extract valuable information about the interior ocean dynamics from the modulation depth of the backscatter intensity associated with IWs. In particular, they point out that the backscatter's dependency on wind

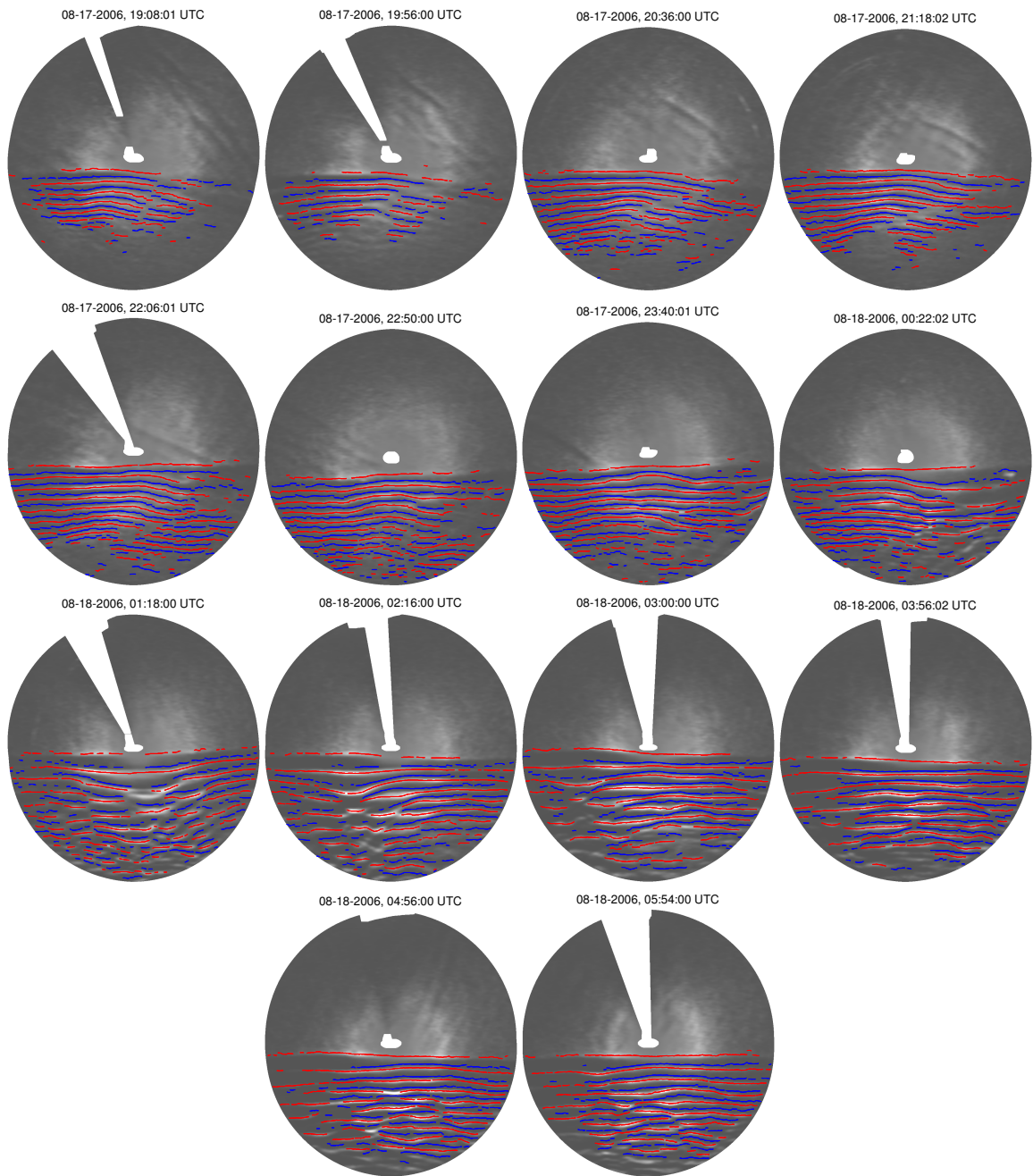


Figure 6.24: Evolution of surface signatures of IW Rosey with peaks marked in red and troughs in blue.

speed and direction is of the same order as its dependency on IW parameters. An accurate knowledge of wind conditions is therefore crucial for deriving IW characteristics from the backscatter modulation. While this is problematic for satellite-borne SAR images, where wind data are not readily available, marine radar and anemometer data can easily be collected together. With concurrent anemometer data available, even if negatively affected by platform-induced airflow distortions [69], it should be possible to derive a wind-dependent model function that describes the radar backscatter's dependency on IW characteristics. Such an attempt was made by Chang et al. [23], who analyzed marine radar data collected in the South China Sea. They found that IW horizontal velocity convergence and amplitude are positively correlated with the enhancement of the surface scattering strength. Based on this finding, they propose empirical formulas for estimating both IW parameters from the backscatter intensity within the convergence zone.

In the following, the backscatter intensity modulation associated with IW Rosey is analyzed. We begin by further analyzing the temporal evolution of the backscatter enhancement associated with Rosey's leading soliton (compare section 6.5). To shed further light on the observed asymmetry between the radar return that is measured in front of and from behind the IW, an attempt is made to quantify the backscatter intensity's dependency on the relative position between ship and soliton. The backscatter intensity enhancement associated with the leading three solitons is then correlated with the corresponding measured IW surface velocity convergence and amplitudes. The IW reference data collected with a shipborne ADCP and a microstructure profiler were processed and kindly provided by Oregon State University's Shroyer and Moum. Estimates of the surface velocity convergence were made with data from the ADCP's 10 m bin.

Before results are presented, a word of caution is necessary: As demonstrated by Brandt et al. [17], the radar backscatter intensity strongly depends on wind conditions. Here, it is assumed that the ramp removal and normalization procedure, introduced by Lund et al. [70] and further discussed in appendix A, removes the wind dependency such that the re-

maining enhancement of the backscatter intensity is purely IW-induced. This assumption is somewhat strengthened by the fact that the wind conditions during the tracking of IW Rosey were fairly constant (see section 6.2). However, it requires that our radar backscatter ramp correctly models the backscatter intensity in absence of IWs. Furthermore, the radar return's standard deviation must be modeled correctly for the normalization to work accurately. With the current state of knowledge on grazing incidence radar backscatter intensity, in particular regarding marine radar measurements that are not radiometrically calibrated, it is highly questionable whether these requirements are met with sufficient accuracy to enable estimating IW parameters.

In section 6.5, it is observed that the IW-associated backscatter enhancement is greater at times when the ship is trailing the IW than when it is ahead of the IW. It is suggested that this ship-track dependency is due to different backscattering mechanisms. In an attempt to quantify this asymmetry, we process the leading soliton's backscatter intensity, as obtained from the Hovmöller diagram of Fig. 6.13, using the same interpolation techniques that were employed to derive the IW propagation speed. This means, to remove the backscatter intensity's dependency on the relative position between ship and soliton (compare Fig. 6.17), the measurements were binned based on their offsets from the image origin and then interpolated, such that a time series is obtained for each offset. Since the resulting backscatter intensities stem from a sequence of radar image projections, they represent average values. It is therefore assumed that the leading soliton approximates a straight line. Note that the backscatter intensities were ramp-subtracted and divided by their respective standard deviations. For such normalized data, values greater than 0 indicate backscatter enhancement and values below 0 indicate backscatter weakening.

Fig. 6.25 shows the mean leading soliton backscatter intensity as function of the offset from the image origin. Here, negative offsets indicate that the ship is ahead of the leading soliton. The backscatter intensities were obtained from the full 11.5-hour time series shown in Fig. 6.17. This figure illustrates that the backscatter intensity is in general greater

when the ship is behind the leading soliton than when ahead of it. The figure furthermore shows that in both ways the backscatter intensity increases with the distance from the image origin. It has its minimum when ship and leading soliton are roughly at the same level. By comparing the backscatter intensities associated with negative offsets with the corresponding positive offsets, it can be found that the backscatter intensity observed from ahead of the leading soliton is on average 19% smaller than the intensity observed from behind. This result disagrees with findings by Chang et al. [23] who observed the opposite, a 24% decrease behind the IW relative to the scattering strength from ahead. They explain the asymmetry of the backscatter power by the IW-induced skewness and breaking of surface waves. However, their observations were made in the South China Sea during a period of weak wind ( $\sim 2$  m/s) and were characterized by large-amplitude waves with a single soliton. More importantly, their radar ramp correction does not account for the backscatter's dependency on the relative angle between antenna look and wind direction. In fact, their data were collected during a period of northeast winds, and the IWs they observed were traveling in a western direction. The increased radar backscatter intensity they observe with the ship ahead of the soliton and attribute to the IW, should therefore instead, at least in part, be attributed to the wind. While an asymmetry in the IW-induced backscatter enhancement due to small breaking waves is credible – the occurrence of an upwind peak in the radar backscatter at grazing incidence is generally explained by small-scale wave breaking [118] –, further work is needed to increase our understanding of how the surface currents associated with IWs generate the observed radar signatures. In addition, to gain more reliable results, the radar ramp correction and normalization may require some improvements. This is because any deviation of the measured backscatter from the ramp, which is basically assumed to mirror the mean radar backscatter for the given wind situation, will be attributed to the IW. A less than perfect ramp will therefore introduce errors into our estimate of the IW-induced backscatter enhancement. Finally, the fact that the

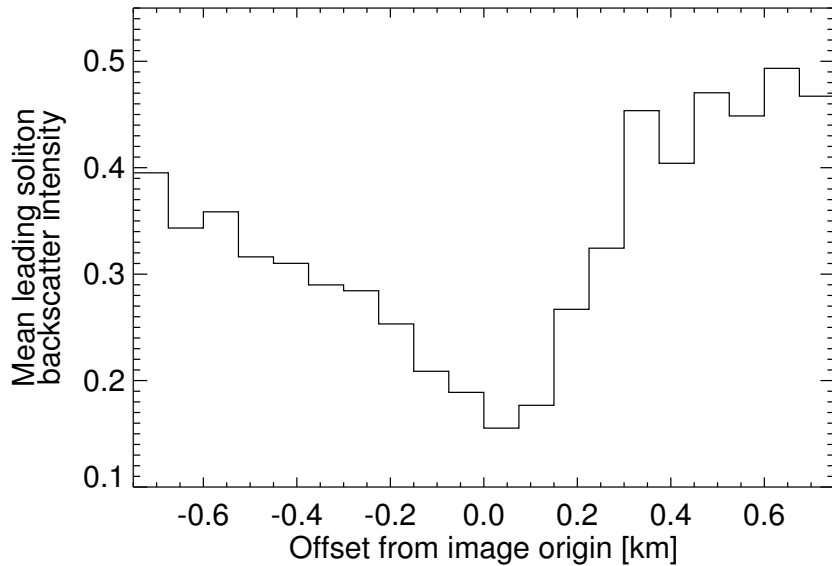


Figure 6.25: Mean leading soliton backscatter intensity for different offsets from the image origin. A negative offset indicates that the ship is ahead of the leading soliton.

findings presented here are in discordance with those presented by Chang et al. emphasizes the need for further research.

In spite of the asymmetry of the IW-induced radar backscatter enhancement and some uncertainty regarding the best radar ramp removal and normalization techniques, the backscatter intensity within a given soliton's convergence zone may still contain some valuable information on the IW evolution. Fig. 6.26 shows a time series of the leading soliton's mean backscatter intensity. The data shown here were obtained by averaging over estimates that were made independently for four cases based on the relative angle between antenna look direction / ship heading and IW propagation direction (see above). It is clear that this processing technique largely removed the backscatter's dependency on the ship track (compare Fig. 6.17). The backscatter intensity increases continuously during the first six hours and then levels off. In the following, the radar backscatter intensities associated with IW Rosey's leading three solitons are correlated with the corresponding measured surface velocity convergence and divergence. If these parameters do correlate, the surface velocity convergence can be assumed to follow a similar trend as the backscatter intensity.

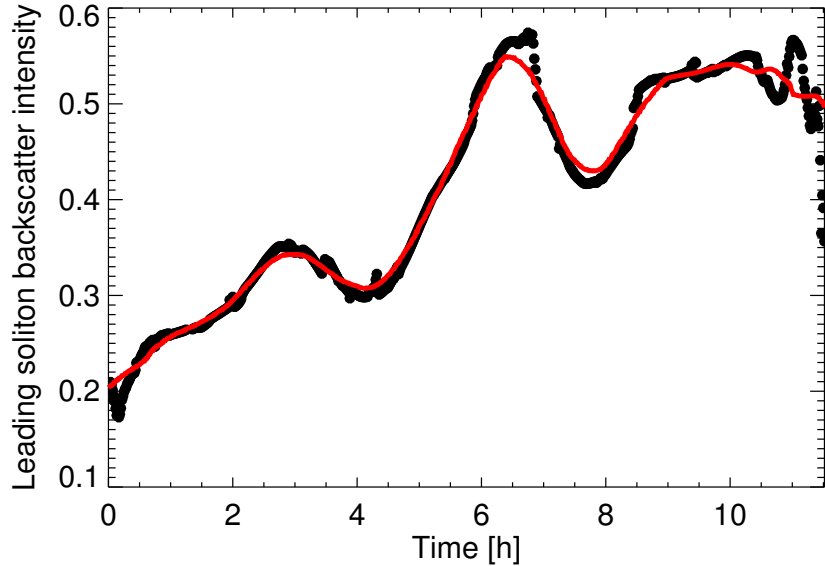


Figure 6.26: Time series of the leading soliton's backscatter intensity obtained from the mean of estimates that were made independently for four different data categories (based on whether antenna look direction and ship heading were up- or downwave). The red curve shows the 60 min running average. The time series starts August 17, 19:05 UTC.

The results presented so far in this section have the drawback that they were obtained from image projections, and are thus based on the assumption that our IW surface signatures approximate straight lines. While this assumption may be somewhat valid for the leading soliton, it definitely represents an oversimplification for the IW group as a whole (see section 6.7). For this reason, a different approach is used here: Backscatter intensities are extracted from 4-min averaged image transects through the leading three solitons along the IW propagation direction. The transects are taken from images that were acquired just before profiling, such that they can easily be matched with the subsequent measurements. The focus is on the peak positive and negative backscatter intensities and corresponding surface velocity gradients and IW amplitudes. Note that there will always be a temporal offset between the radar and reference measurements. Finally, as for the images shown in section 6.7, but in contrast to the results shown above, the radar ramp removal was accomplished by dividing the images by their respective ramps. This means that intensity values greater than 1 indicate backscatter enhancement and values below 1 weakening.

This method is similar to the range dependency corrections made by Chang et al. [23], which ensures comparability with their results. However, as mentioned above, Chang et al. do not account for the backscatter's dependency on the antenna look direction. Also, the resulting IW-induced backscatter modulation has a range dependency. Further research is required to address this issue.

Fig. 6.27 shows a time series of the peak radar backscatter intensity associated with IW Rosey's leading soliton and the corresponding surface velocity convergence. The figure shows radar and reference data points for all 14 profiling stations sampled during the tracking of IW Rosey. The radar backscatter measurements were all made at roughly the same distance from the ship, ensuring that the remaining post-ramp-removal range dependency of the radar backscatter modulation can be neglected. While both parameters seem to exhibit significant levels of noise, the measured increase in the backscatter intensity with time is reflected by an increasing surface velocity convergence (i.e. the absolute velocity gradient increases). Note that, while Figs. 6.26 and 6.27 both show a general trend of increasing backscatter intensity over time, they have differences. These differences can be attributed to the fact that the intensities shown in the former represent average values that were derived from full images, while the latter's intensities were obtained from image transects. Also, remember that the one shows normalized data from a multitude of ranges, while the other shows data that were solely ramp-divided and extracted at a fairly constant range.

The time series in Fig. 6.28 juxtaposes the leading soliton's peak backscatter intensity with the corresponding IW amplitude. The increasing trend observed for the backscatter intensity coincides with an increasing absolute IW amplitude. What is particularly striking here is that the measured increase in the backscatter intensity around hour 5 occurs only shortly after a relative sudden augmentation of the IW amplitude from about -16 to -22 m.

For the leading three solitons, the scatter plots in Fig. 6.29 compare the measured surface velocity convergence with the corresponding radar backscatter intensity peaks (a) and

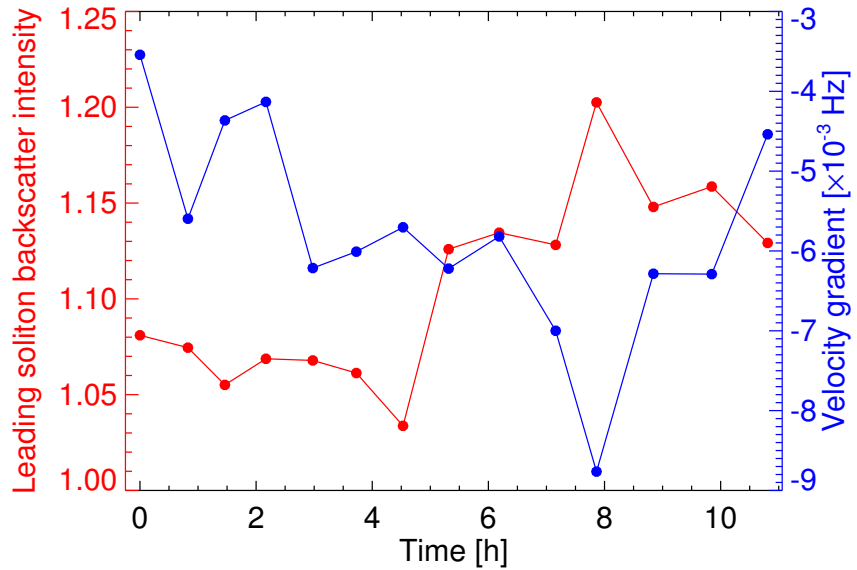


Figure 6.27: Time series of radar backscatter intensity (red) and surface velocity gradient (blue) for IW Rosey's leading soliton, starting August 17, 19:05 UTC.

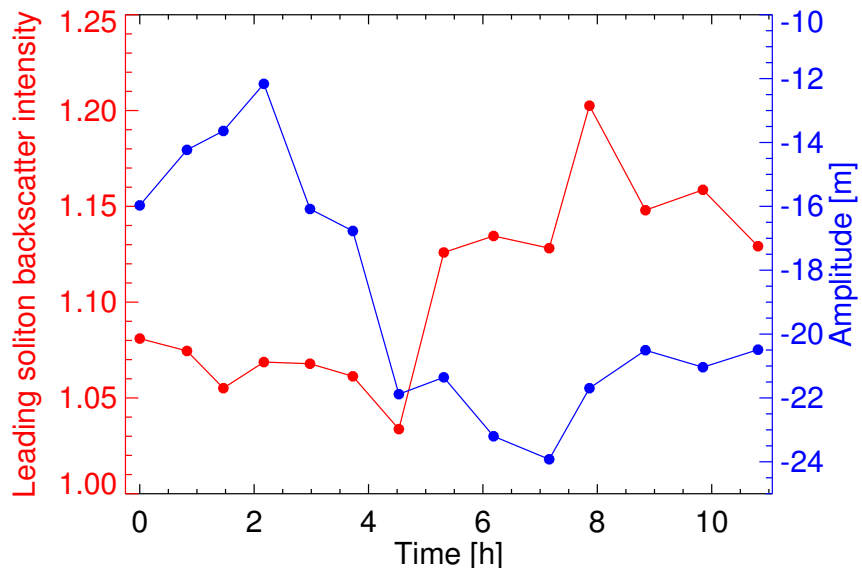


Figure 6.28: Time series of radar backscatter intensity (red) and IW amplitude (blue) for Rosey's leading soliton, starting August 17, 19:05 UTC.

the divergence with its backscatter troughs (b). The graphs include the corresponding best-fit lines. As could be expected, all 6 best-fit lines (for both convergence and divergence) have a negative slope, indicating that a decrease in the backscatter intensity is associated with a decreasing convergence or increasing divergence. However, in particular regarding velocity convergence, it must be noted that the radar backscatter intensities observed for the three solitons vary significantly and counter-intuitively: While one would typically expect the IW-associated enhancement of the radar backscatter to decrease from front to back, since the leading soliton generally is the most energetic, the opposite is the case here. This issue can be explained by the remaining range dependency of the radar backscatter intensity, and illustrates the need for further research in this regard.

Similarly, Fig. 6.30 shows a scatter plot comparing IW amplitude and peak radar backscatter intensity for the leading three solitons. As illustrated by the best-fit lines, the backscatter intensity generally increases with the absolute IW amplitude.

In summary, both IW amplitude and surface velocity convergence (and divergence) correlate with the corresponding IW-induced modulation of the radar backscatter intensity. This finding suggests that, as done by Chang et al. [23], empirical model functions can be derived to determine characteristics of the interior ocean from the IW-associated radar backscatter intensities. However, it is highly questionable whether these IW characteristics can be determined with sufficient accuracy. Further research is required to determine whether an empirical formula, derived under the given wind conditions, can be applied to data that were collected in a different environment. What is more, before a reliable empirical formula can be derived, several issues must be addressed satisfactorily: The IW-induced backscatter enhancement exhibits a strong asymmetry. This study suggests that the observed backscatter intensity is greater from behind the IW than ahead, which contradicts Chang et al., who reported the opposite. This result gives rise to the following questions: What is the origin of this asymmetry, and how can it be modeled? The radar backscatter ramp removal and normalization, which largely depend on the wind conditions,

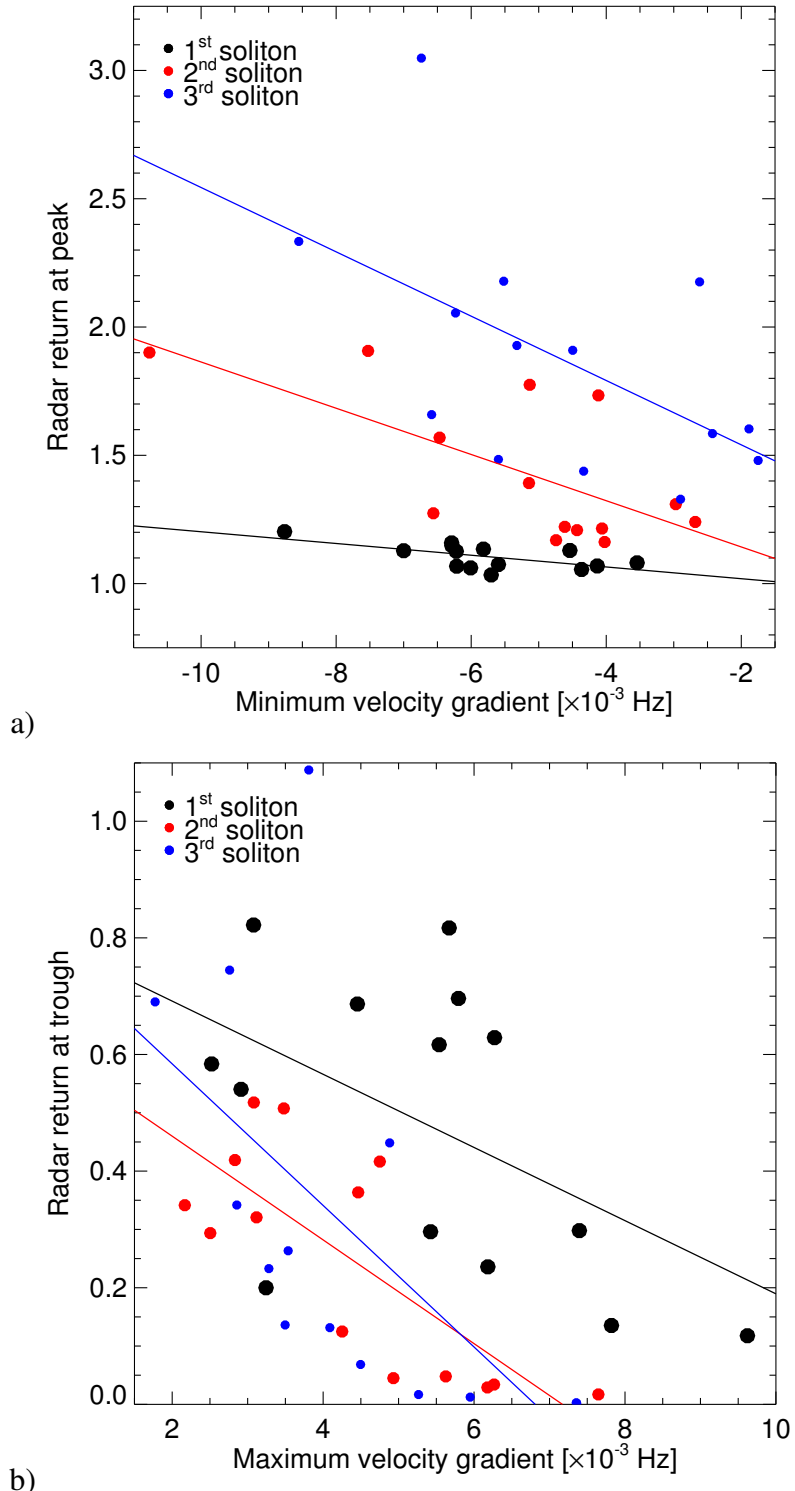


Figure 6.29: Scatter plots of surface velocity convergence (a) and divergence (b) versus corresponding radar backscatter intensity peaks and troughs. Results are shown with corresponding best-fit lines for IW Rosey's leading three solitons. (The different dot sizes ensure visibility of all data.)

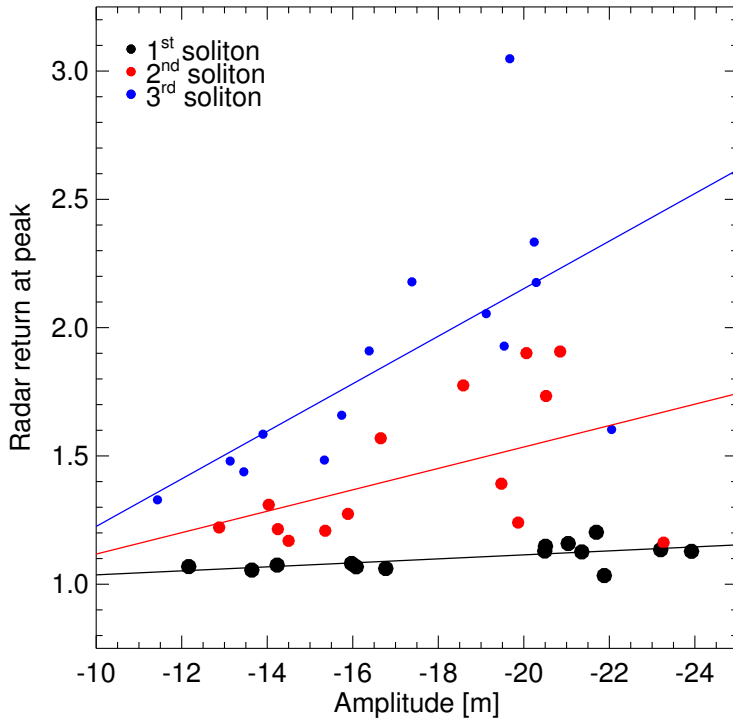


Figure 6.30: Scatter plot of IW amplitude and radar backscatter intensity for leading three solitons of IW Rosey with corresponding best-fit lines.

represent another issue. The existing approaches to construct such a ramp are suboptimal, particularly in presence of an IW, and errors in the ramp removal will negatively affect our estimate of the IW-induced radar backscatter enhancement. Different methods of removing the ramp exist: Divide the image by the ramp or subtract the ramp from the image? What is even less established, is an adequate way of normalizing the image. An optimal solution would require the construction of yet another ramp, this time one of the backscatter's standard deviation and not its mean value, the shape of which is still unknown. To conclude, this section on the relationship between the IW-induced radar backscatter modulation and interior ocean dynamics opens up more questions than it provides answers and underlines the need for further research in the field.

## 6.9 IW Amplitudes from Peak-to-Peak Distances via Extended Korteweg-de-Vries Equation

In the previous section, we analyzed the relationship between the radar backscatter intensity and the IW-induced modulation of the surface current field as well as the IW amplitude. While these parameters seem to correlate, several issues complicate the retrieval of IW characteristics from the backscatter intensity. Most importantly, since grazing incidence radar backscatter is not yet fully understood, it is difficult to separate the IW-induced backscatter enhancement from the influence of the wind, which is generally of the same order of magnitude. With this issue in mind, Xue et al. [132] developed a new technique to estimate amplitudes for IWs in the Mid-Atlantic Bight from the distance between the IW-associated positive and negative radar backscatter peaks (p-p-distance) via an eKdV equation. As demonstrated in the paper, using radar imaging models of varying complexity, the p-p-distance is much less affected by wind conditions than the radar backscatter modulation depth due to IWs. In the following, the methodology introduced by Xue et al. is applied to marine radar and reference data collected during the tracking of IW Rosey.

Fig. 6.31a shows an IW-enhanced radar backscatter image collected from *R/V Oceanus* on August 17, 22:06 UTC. On the image, IW-induced radar backscatter peaks are marked in red, troughs in blue. The IW signatures were retrieved using techniques introduced by Lund et al. [70]. The dashed black line roughly reflects the profiling track of the ship and spans across the leading three solitons. Here, the p-p-distances that were determined along the marked transect are fed into the eKdV-based amplitude estimation scheme. The diagram in Fig. 6.31b shows the eKdV relationship between IW amplitude and p-p-distance. Of the two solutions that can be found for the retrieved p-p-distances, the higher (absolute) amplitude ones apply. This is because IWs generally rank in order, i.e. the soliton amplitude decreases from front to back. Fig. 6.32 shows an image transect through a section of IW Rosey that is relatively undisturbed by packet-packet interactions. As the figure illus-

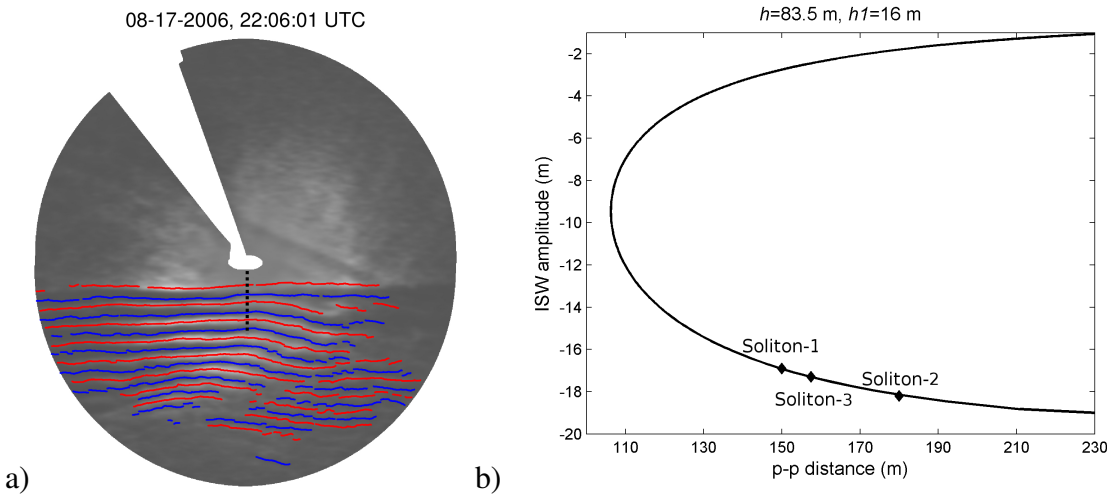


Figure 6.31: Radar backscatter peaks (red) and troughs (blue) for August 17, 22:06 UTC. The measurement location is marked by a black dashed line (a). Corresponding diagram illustrating the extended KdV equation, linking IW amplitude and p-p-distance for a water depth of 83.5 m and a mixed layer depth of 16 m (b).

brates, the p-p-distances decrease continuously from 188 m for the leading soliton to 98 m for the last one. P-p-distances thus tend to follow the same trend as the IW amplitudes. For this reason, the relationship in the lower part of the eKdV graph must apply [132]. For the case shown in Fig. 6.31a, however, the p-p-distances for the leading three solitons are 150 m, 180 m, and 158 m. This deviation from the general rule of decreasing p-p-distances from front to back can be explained by IW interactions, which will be discussed further below. For a water depth of 83.5 m and a mixed layer depth of 16.0 m, the higher-amplitude solution of the eKdV equation yields IW amplitudes of -16.9 m, -18.0 m, and -17.3 m for our leading three solitons. These results are in reasonably good agreement with the corresponding in-situ amplitudes of -16.1 m, -14.2 m, and -13.9 m, even though the radar-based estimates slightly overestimate the measured data.

Fig. 6.33 shows a time series of p-p-distances and corresponding water depths as measured during the tracking of IW Rosey. The p-p-distances are shown for the leading three solitons. A relatively sudden change of the p-p-distances can be observed around hour 5. Note that at roughly the same time both the radar backscatter intensity enhancement due to the leading soliton and the soliton's amplitude exhibited an equally sudden increase

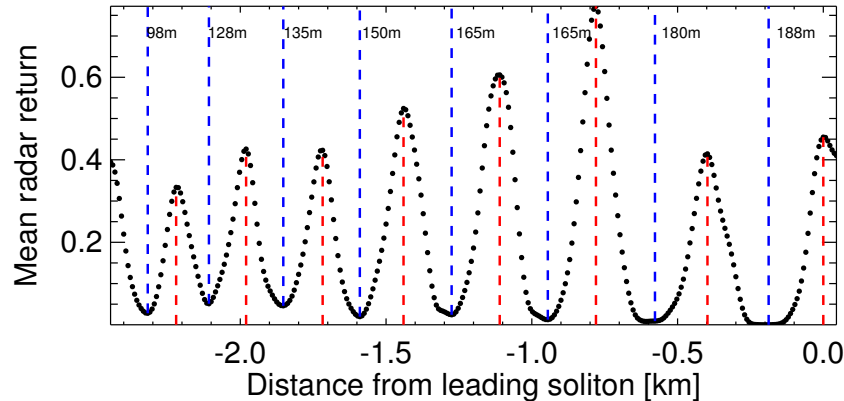


Figure 6.32: Transect through an undisturbed section of IW Rosey. Radar backscatter peaks and troughs are shown by red and blue bars, respectively, and p-p-distances for each soliton are printed. The data were collected during a 4-min period starting August 17, 19:59 UTC.

(compare Fig. 6.28, section 6.8). The water depth chart suggests that this change might in part be due to the fact that the IW entered much shallower water around this time (during the fifth hour of the wave tracking, the water depth decreased from above 80 m to below 70 m). However, our detailed study of the evolution of IW Rosey's surface signatures (see section 6.7) revealed that the wave's interaction with several other IW packets significantly influences its surface signatures and thus p-p-distances. For example, a close study of the surface signatures reveals that the outliers around hours 1 and 6, associated with the third soliton, can be attributed to wave-wave interactions (see Fig. 6.24, second image from top left and first image of third row; the location of the image transects, along which the p-p-distances were retrieved, was identical with that of Fig. 6.31a).

The scatter plot in Fig. 6.34 compares radar-derived IW amplitude estimates with reference measurements for Rosey's leading three solitons, covering the full 11.5 hours of data. Two distinct groups can be identified in the plot. In the first half of the tracking, the radar overestimates the reference measurements. During the tracking's second half, the opposite is the case, with the radar estimates being significantly lower than the in-situ measurements. The differences observed here are most likely due to wave-wave interactions, which are not accounted for in the eKdV equation.

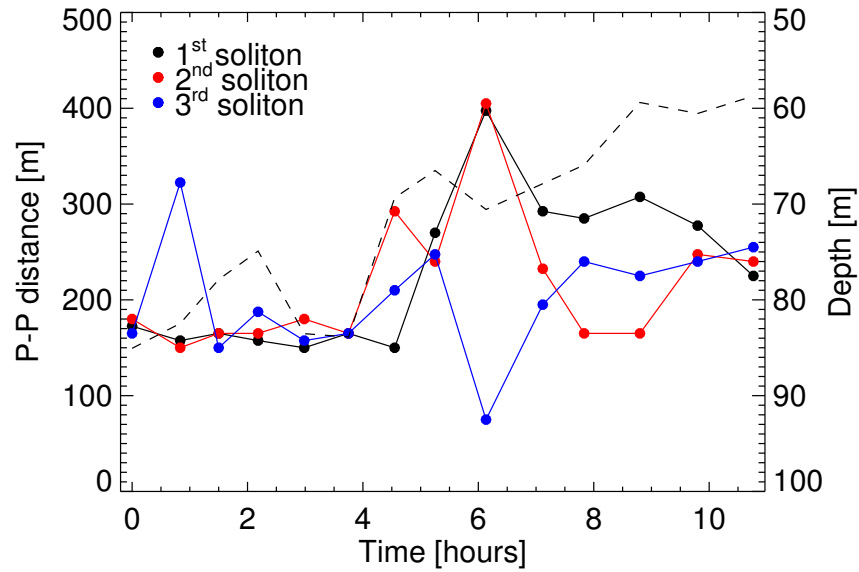


Figure 6.33: Time series of p-p-distances and water depth (dashed line) for leading three solitons starting August 17, 19:05 UTC.

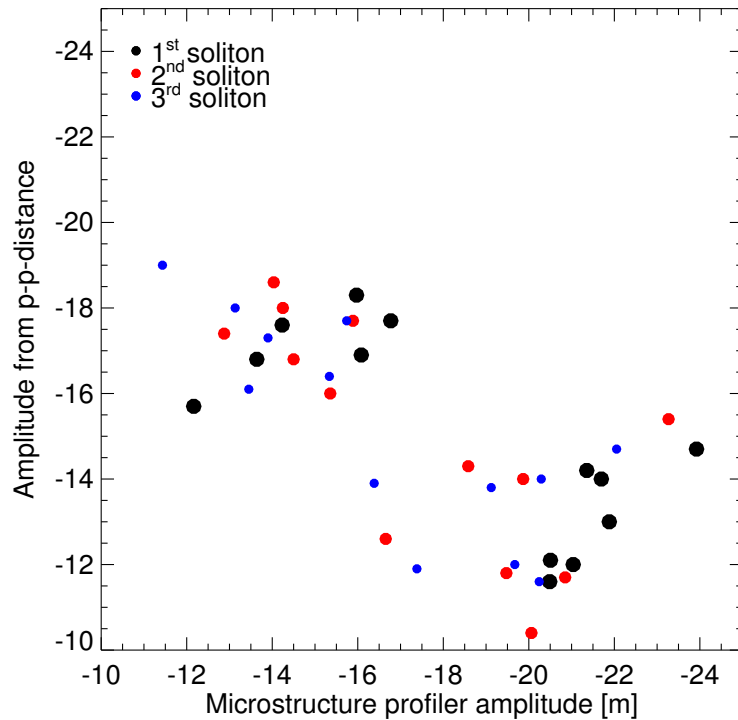


Figure 6.34: Scatter plot of measured and radar-derived amplitudes for leading three solitons for IW Rosey.

To conclude, the radar-based estimates that were obtained from the measured p-p-distances via an eKdV equation are of the same order of magnitude as the reference data. The radar-derived estimates are negatively affected by disturbances due to interacting IW groups, which the eKdV equation does not account for. A close inspection of the available marine radar and satellite data suggests that IW interactions represent a very common phenomenon in the Mid-Atlantic Bight. Further research is required to determine a method of correcting for the impact of IW interactions on p-p-distances. Alternatively, research by Xue et al. [133] suggests that the IW interaction patterns themselves can be used to retrieve IW amplitudes.

## 6.10 Discussion

This chapter summarizes results from the analysis of IW surface signatures in marine radar data recorded by *R/V Oceanus* during the NLIWI experiment off the coast of New Jersey. The focus lies on the particularly energetic IW Rosey, which was tracked over 11.5 hours starting August 17, 19:05 UTC. During this period, the wave traveled a distance of almost 40 km across the shelf.

Marine radar images of IW surface signatures can be used to determine some characteristics of the IW-induced dynamics of the interior ocean. In a first step, it was shown that hydrodynamic modulation is the dominant imaging mechanism of IWs by marine radar. Then, using a combination of localized Radon transform and cross-correlation techniques, estimates of IW packet direction and speed were derived. The changes both parameters exhibit over time are attributed to wave-bottom interactions and advection by the barotropic tide. Also, IW interactions could be responsible for some of the observed changes in the parameters. The background current-corrected IW speed, which initially increases and subsequently decreases, provides evidence of the wave's initial growth and subsequent decay.

Temporal averaging significantly enhances the IW signatures in marine radar data. Using techniques introduced by Lund et al. [70], the IW-induced surface current convergence and divergence zones were identified and mapped. This work helped visualize the evolution of the IW's surface manifestation and revealed the following: The solitons became better defined and their number as well as p-p-distances increased over time; the IW signatures have a significant amount of curvature and do not necessarily span across the whole image; they exhibit clear evidence of IW interactions.

The IW-induced enhancement of the radar backscatter intensity was found to be asymmetric. Contrary to what has been reported in the literature [23], the enhancement observed from behind is 19% smaller than that from ahead. Further research is needed to determine the origin of this asymmetry, its dependency on the environmental conditions, and to find a way of modeling it. It was found that both the IW amplitude and the surface velocity gradient correlate with the corresponding IW-induced modulation of the radar backscatter intensity. However, it is questionable whether these relationships can be used to reliably obtain radar-based estimates of IW characteristics. This is because wind influences the radar backscatter at the same order of magnitude as IWs, and it is difficult to separate the one from the other. However, if IW data covering a wide range of wind conditions are consulted, it may be possible to derive a wind-dependent empirical model function that relates the IW-induced backscatter modulation to the interior ocean dynamics. Future work is planned to derive a mo dependence on the wind conditions. The verification of this conjecture is left for future work.

An alternative approach makes use of an eKdV equation to derive IW amplitudes from the p-p-distances [132]. This approach has the great advantage that it is much less dependent on the prevailing environmental conditions. A reasonable agreement between radar-derived and reference IW amplitudes is found. The differences between the two are mainly attributed to IW interactions, which the eKdV equation does not account for.

In the future, we hope to further develop a model function that describes the marine radar backscatter dependency on the wind. In addition, the dependency of the IW-induced radar backscatter enhancement on the prevailing environmental conditions merits further research.

# Chapter 7

## Conclusions and Outlook

### 7.1 Summary of Conclusions

This work analyzes marine radar data from three ONR-sponsored research experiments. As part of ITOP 2010, data were collected from *R/V Roger Revelle* in the western Pacific Ocean. For Hi-Res 2010, *R/P Flip* and *R/V Sproul* were deployed to acquire data off California’s southern coast. Finally, during NLIWI/SW06, marine radar data were collected by *R/V Knorr* and *R/V Oceanus* in the Mid-Atlantic Bight. Here, both ITOP and Hi-Res data are used for wind retrieval purposes. The NLIWI/SW06 data is analyzed regarding IWs.

Marine radars offer the capability to sample the sea surface at high frequency, allowing them to monitor the evolution of both oceanic and atmospheric processes over short timescales. The high temporal resolution gives marine radar an edge over SAR satellite data. At the same time, radar’s capability to sample images represents an excellent complement to in situ “point” measurements.

The main conclusions of this dissertation can be summarized as follows:

1. Using measurements from two anemometers mounted at different locations on *R/V Roger Revelle*, it was demonstrated that the flow of air to the sensors is significantly distorted by ship structures, especially for winds coming from aft. Marine radars have

the advantage that they sample the surface roughness, which can then be related to the wind, over large areas that are most likely unaffected by such air flow distortions. Existing methods for the retrieval of wind directions from marine radar data focus on fixed platform data. This work proposes a new least-squares fit based approach with similarities to wind scatterometry. It makes use of the upwind peak in the radar backscatter strength and can be directly applied to ship data. Another advantage of this method is that it works even if a significant portion of the image is masked. A simple technique is suggested for the retrieval of wind speeds. It is based on a single backscatter strength value, obtained from the mean fit function that describes the backscatter's dependency on antenna look direction. This value is linked to the wind speed via an empirical model function. The obtained wind estimates agree well with the reference data: Standard deviations were found to be 0.78 m/s for the wind speed and 17.4° for the wind direction. It is hoped that this work can help establish marine radar-based wind estimates as a viable alternative to traditional ship-based measurements.

2. As an alternative to our upwind peak-based method for determining wind directions from marine radar data, one can use the so-called wind streaks, which are generally aligned with the wind. However, since they become visible only after averaging a series of radar images, moving platform radar data must first be geolocated to prevent the streaks from being obscured by the horizontal ship motion. This work proposes a new approach that geolocates the data before averaging, and then employs a localized Radon transform technique to determine the mean orientation of the streaks. To determine which of the two competing methods yields best results, we analyzed moving and fixed platform marine radar data from the Hi-Res experiment. The Hi-Res data are outstanding in that they offer a 360° view of the sea surface. While the wind streak-derived directions correlate well with the reference data, it was found that the upwind peak method yields better results, with a standard deviation of 6.0° (6.2°)

versus  $9.6^\circ$  ( $14.5^\circ$ ) for *R/P Flip* (*R/V Sprout*). The comparison between *R/P Flip* and *R/V Sprout* suggests that geolocating the data results in slightly deteriorated results. Here, since both radars enjoy an unobstructed view of the sea surface, the mean image intensity is used for estimating wind speeds. The resulting standard deviations are stunningly low: 0.42 m/s for *R/P Flip* and 0.62 m/s for *R/V Sprout*. These results indicate that marine radars yield highly reliable wind estimates for both moving and fixed platforms, in particular if the radars have an unobstructed field of view.

3. IWs create spatially varying surface current fields that interact with the cm-scale waves. Marine radars are capable of imaging the IW-induced surface roughness modulation. This work introduced a new tool to automatically retrieve IW surface signatures from marine radar data. The proposed methodology begins by determining the IW group direction through a localized Radon transform and the speed by applying cross-correlation techniques to image projections onto the IW propagation axis. It is demonstrated that temporal averaging significantly enhances the IW signal contained in marine radar data. The IW group characteristics are used to correct the georeferenced radar images for the IW motion, which enables us to extend the averaging period. The resulting IW-enhanced radar images show clear bands of enhanced and weakened backscatter strength that are due to the IW. In fact, this processing technique reveals faint IW surface signatures that would otherwise remain hidden. To retrieve IW soliton maps from a sequence of IW-enhanced images, local backscatter peaks and troughs are identified and clustered. The proposed algorithm then takes advantage of marine radar's high temporal resolution to isolate clusters that propagate at the IW group velocity, which effectively separates signal from noise. This new algorithm offers a unique view of the spatio-temporal evolution of IW surface signatures. It is hoped that this work demonstrates the promise of marine radar as an IW monitoring device. In addition, we hope that the proposed tool's fully automated character will encourage its future use during IW-centered research campaigns.

4. The tools developed for the retrieval of IW information from marine radar data were applied to an 11.5-hour long sequence of images collected during the tracking of IW Rosey, the most energetic wave observed during NLIWI/SW06. During this period the wave propagated just under 40 km across the continental shelf, through water depths ranging from above 80 m to just under 60 m. Using ship-mounted ADCP data, it was demonstrated that hydrodynamic modulation is the dominant backscatter mechanism: The peak backscatter strength is observed where the velocity gradient reaches a minimum, and a trough in the backscatter strength coincides with a maximum velocity gradient. The radar-derived time series of IW group speed and direction show significant changes, in particular for the speed. During the first half of tracking, the background current-corrected speed increases from around 0.8 m/s to 0.95 m/s, only to decrease back to the value it started from during the second half, which can be interpreted as evidence of the IWs growth and subsequent decay. The IW soliton maps obtained with the previously introduced methods illustrate how the number of solitons increases, and how they become better defined with time. In addition, the soliton's curvature and their phase shifts represent clear indicators of wave-wave interactions. The IW-enhanced radar images provide further evidence of interactions as they show the signal of several less-pronounced IW groups propagating in different directions. A study of IW-associated backscatter strengths revealed an asymmetry in the backscatter enhancement due to the IW: The enhancement observed from ahead the IW is 19% smaller than from behind, which suggests differing backscatter mechanisms, possibly due to IW-induced wave breaking. It was found that both the IW-associated enhancement and weakening of the backscatter strength correlate with the measured surface velocity gradients. The backscatter enhancement was also found to correlate with the measured IW amplitude. Since backscatter intensities strongly depend on the prevailing wind conditions, an alternative method is suggested. Here, the distance between neighboring positive and negative IW-induced

backscatter peaks, as obtained from our IW soliton maps, is used to derive IW amplitudes by means of an eKdV function. Results are promising, however, the observed wave-wave interactions appear to have a detrimental impact on the radar-estimated amplitudes.

5. Within this work, several new techniques and methods were developed that helped improve the marine radar wind and/or IW retrieval, but were not among this dissertation's main goals. Firstly, during the ITOP experiment, *R/V Roger Revelle* encountered several instances of heavy rain. Since rain enhances the backscatter strength, data collected during rain must be identified and sorted out. The percentage of radar image pixels with zero backscatter strength was identified as a suitable rain flag. Secondly, the presence of other X-band radars in the sampling area manifests itself in form of radar interference spikes in our data. A technique to identify and remove such spikes was developed in the wind retrieval context, and further improved for the IW signature retrieval. Thirdly, bright targets such as ships and buoys tend to overshadow the IW signal. This work suggests a simple technique to mask bright targets. Finally, the marine radar backscatter strength exhibits a strong dependency on range and antenna look direction. We require homogeneous images for both our wind and IW retrieval. Here, a new technique that fits empirical model functions to the observed backscatter dependencies is introduced. The resulting ramp models the decrease in the backscatter strength with range, the upwind peak, and the dependency of the upwind-downwind intensity difference on range.

## 7.2 Future Work

This work's goal was to derive and evaluate techniques for the retrieval of wind and IW information from marine radar data. These goals were accomplished, and it is hoped that

the newly developed techniques will help establish marine radar as a valuable tool for studying both sea surface winds and IWs.

As a general remark, it is safe to assume that the IW surface signature retrieval from our NLIWI/SW06 data could be much improved if greater care had been given to the marine radar data acquisition. At the time, the WaMoS software did not accurately log the image acquisition time and data gaps occurred regularly. (This issue has since been resolved.) In addition, the ship heading and positions were sampled only every 15 s. As a result, geolocating the radar images became highly laborious and error-prone, which limits our ability to enhance the IW surface signatures, in particular the signal of less-pronounced solitons. Furthermore, the system was programmed to sample only every fourth pulse, which is unfortunate, since the IW signal-to-noise ratio can be improved considerably by averaging, i.e. the azimuthal oversampling that would result from storing every pulse is highly desirable from an IW data quality point of view. For future IW experiments, it is recommended to sample every radar pulse and to ensure that ship heading and GPS data are available with an update rate that matches the radar's antenna repetition time.

During this dissertation, several new questions arose that merit further research. The following list summarizes future work recommendations:

- For both wind and IW retrieval, we need to remove the radar backscatter ramp, i.e. the backscatter's dependency on range and antenna look direction, from our measured return signal. It is assumed that the radar backscatter ramp depends most importantly on the prevailing wind conditions. It was found that a simple harmonic function can be used to model the radar backscatter dependency on the relative angle between wind and antenna look direction. To retrieve wind direction and speed, the harmonic function was fitted to the range-averaged backscatter strength. While an upwind peak can be observed for all ranges, the difference between up- and down-wind backscatter strength was found to change with range: The difference increases in the near range, levels out, and then declines towards a minimum in the far range.

So, we derived a function that mimics this behavior and used that in combination with yet another function that describes the backscatter dependency on range to construct the ramp, essentially using least-squares fit techniques. This approach has a flaw however: While the resulting ramp accurately models the mean backscatter strength, it cannot discriminate between the signal that is due to the wind and that of other phenomena, such as IWs. As a result, for marine radar images that show IW surface signatures, it is somewhat inaccurate to assume that the ramp-corrected radar return is representative of the IW-induced enhancement. As a long term goal, it would therefore be necessary to derive a two-dimensional transfer function that describes the dependency of the mean marine radar backscatter strength on the wind. If such a function existed, one could use measured wind data to construct a ramp that would then be independent of the radar backscatter modulation due to other phenomena. This would greatly facilitate interpreting the observed IW-induced backscatter enhancement. For example, it would add a level of confidence to the asymmetry of the IW backscatter strength enhancement that we found for the relative position between ship and IW. In addition, our marine radar-based wind estimates could probably be improved if we extended our model function to two dimensions. Finally, the standard deviation of the radar backscatter as a function of time is a function of both antenna look direction and range, and appears to also be controlled by the prevailing winds. To be able to normalize our data, i.e. divide it by the standard deviation after subtracting the ramp, we would in addition need to derive a model function that describes the radar backscatter's standard deviation as a function of wind. To conclude, while the suggested work poses several challenges, it offers the opportunity to improve not only the credibility of the measured IW-induced backscatter enhancement, but also the radar-based wind estimates. Finally, the proposed work might help broaden our knowledge about grazing incidence radar backscatter.

- For the ITOP experiment, this work compared *R/V Roger Revelle* marine radar-based wind estimates with shipborne measurements. It would be of interest to include our buoy data in the comparison. This is because the buoy wind sensors are much closer to the sea surface than the ship-mounted anemometers, and should therefore compare more favorably with our radar-based wind estimates. Buoy measurements have the additional advantage over shipborne in-situ data that they are less likely to be affected by platform-induced air flow distortions. Also, as part of the ITOP work, we proposed a rain flag that is based on the percentage of image pixels with zero backscatter strength. Wind retrieval results could be further improved if we applied this flag not to the image as a whole, but instead to image sections. In addition, since taking rain measurements on ships is very difficult due to the vessel motion and sea spray, attempting to estimate rain fall from marine radar data might be a worthwhile endeavor. Regarding marine radar wind direction retrieval, this work compared a wind streak-based approach with one that makes use of the upwind peak. To conclusively determine which approach yields best results, however, it would be necessary to analyze further data with a greater variability of wind conditions. In addition, yet another approach exists that is based on optical flow techniques. Basically, it analyzes the flow direction of patches of bright or dark backscatter which can be shown to correlate with the wind direction. For a complete discussion, this approach should be included in the comparison. Finally, it is feasible that, for data where a significant portion of the radar field of view is masked, the wind streak-based approach is preferable over the upwind peak one. The ultimate goal would be to find out which approach yields best results for moving and fixed platform data as well as for different image masking scenarios.
- Regarding marine radar wind retrieval in general, several research questions remain unanswered: What physical process is responsible for the wind streaks that become visible after averaging a sequence of radar images? Are these streaks an oceanic

or an atmospheric phenomenon? This question could be answered by studying the evolution of the wind streaks, e.g. using localized Radon transform techniques, and comparing the results with existing surface current measurements. If they can be shown to propagate in the direction of the current, one likely explanation for their existence would be Langmuir circulation. Above, it was mentioned that an optical flow analysis of marine radar data reveals patches of dark and bright backscatter that propagate in wind direction. It is currently not known what process induces these patches. They could be due to wind gusts, which would encourage further research since the wind gustiness represents an important parameter, e.g. from a maritime security or professional sailing perspective.

- The wind speed is linked to the radar backscatter intensity via an empirical model function. Since marine radars are not radiometrically calibrated, a model function needs to be derived for each system. While this can easily be accomplished with only a few days worth of data, it would be highly desirable to develop a technique that requires no calibration or further simplifies it. If it can be shown that the bright and dark radar backscatter patches that can be observed in averaged radar images are due to the wind, one possibility would be to relate the speed of the optical flow to the wind speed. However, this is not straight-forward and first results obtained by Horstmann et al. [52] show little correlation with the wind speed. To date, no technique has been proposed that is capable of determining the wind speed without a calibration step. Developing a technique that is calibration-free can therefore be viewed as the holy grail of marine radar wind speed retrieval.
- Regarding IWs, this work proposed new techniques to identify, enhance, and retrieve IW surface signatures from marine radar data. Providing high temporal resolution that is not possible to obtain with SAR data, marine radar offers great potential for IW studies. For studies that are designed to have a ship tracking IWs, marine radar

provides the unique opportunity of studying the spatio-temporal evolution of the IW surface signatures. The methodology proposed here allows the automatic retrieval of IW surface signatures. While first results were presented here, future work should further explore the relationship between the observed IW-induced radar backscatter enhancement (or weakening) and the dynamics of the interior ocean. Since the IW-associated modulation of the radar backscatter strength strongly depends on the prevailing wind conditions, this work evaluated an alternative and more promising approach proposed by Xue et al. [132]. This approach uses an eKdV equation to estimate the IW amplitude from the distance between neighboring positive and negative backscatter peaks. While some results were presented here, further research is required to establish the technique's reliability. In particular, IW interactions appear to have a detrimental impact on the IW amplitude estimates. Finally, our IW-enhanced radar images contain ample evidence of IW interactions. All necessary tools are in place to retrieve the surface signatures of multiple IW groups from our marine radar data. Future work will thus focus on studying the surface manifestations of IW interactions and their temporal evolution. First results by Xue et al. [133] suggest that the phase shifts, that may occur when two IW groups interact, can be used to derive the IW amplitude. To conclude, while it could be demonstrated that marine radar represents a powerful tool for the study of IW evolution, a wide array of questions remains to be answered before we can make reliable quantitative statements about the interior ocean dynamics from our marine radar data.

- Finally, marine radar technology currently undergoes a revolution [79]. It would be of great interest to study winds and IWs, but also surface waves and currents, using a new steady-state technology coherent marine X-band radar. In particular, the radial velocity of each scatterer gives rise to a Doppler shift, which, it is safe to assume, would provide additional valuable information about the physics of these phenomena. Also, the work presented here uses data from 8 foot antennas with radar scan-

ners that require a minimum pulse length of  $0.07 \mu\text{s}$ . Making use of a 14 foot radar antenna and a more powerful radar scanner, offering shorter pulse lengths, would improve the image resolution. This could in turn benefit our IW surface signature retrieval, but would also improve wave and surface current estimates. Finally, some research suggests that vertically polarized marine radars produce better wave retrieval results [28]. It would be of interest to study IW signatures within vertically polarized radar data and compare with horizontal polarization.

# Bibliography

- [1] M. H. Alford, R.-C. Lien, H. Simmons, J. Klymak, S. Ramp, Y. J. Yang, D. Tang, and M.-H. Chang. Speed and evolution of nonlinear internal waves transiting the South China Sea. *J. Phys. Oceanogr.*, 40(6):1338–1355, Jan. 2010.
- [2] W. R. Alpers. Theory of radar imaging of internal waves. *Nature*, 314(6008):245–247, 1985.
- [3] W. R. Alpers and K. Hasselmann. The two-frequency microwave technique for measuring ocean-wave spectra from an airplane or satellite. *Bound.-Lay. Meteorol.*, 13:215–230, 1978. 10.1007/BF00913873.
- [4] W. R. Alpers, D. B. Ross, and C. L. Rufenach. On the detectability of ocean surface waves by real and synthetic aperture radar. *J. Geophys. Res.*, 86(C7):6481–6498, 1981.
- [5] J. R. Apel, H. M. Byrne, J. R. Proni, and R. L. Charnell. Observations of oceanic internal and surface waves from the Earth Resources Technology Satellite. *J. Geophys. Res.*, 80(6):865–881, 1975.
- [6] V. Atanassov, L. Mladenov, R. Rangelov, and A. Savchenko. Observation of oil slicks on the sea surface by using marine navigation radar. In *Proc. Geoscience and Remote Sensing Symposium, IEEE International*, volume 3, pages 1323–1326, 1991.
- [7] V. Atanassov, W. Rosenthal, and F. Ziemer. Removal of ambiguity of two-dimensional power spectra obtained by processing ship radar images of ocean waves. *J. Geophys. Res.*, 90(C1):1061–1067, 1985.

- [8] D. E. Barrick. Near-grazing illumination and shadowing of rough surfaces. *Radio Sci.*, 30(3):563–580, 1995.
- [9] F. Bass, I. Fuks, A. Kalmykov, I. Ostrovsky, and A. Rosenberg. Very high frequency radiowave scattering by a disturbed sea surface Part II: Scattering from an actual sea surface. *IEEE Trans. Antennas Propag.*, 16(5):560–568, 1968.
- [10] P. S. Bell. Shallow water bathymetry derived from an analysis of X-band marine radar images of waves. *Coastal Eng.*, 37(3-4):513–527, 1999.
- [11] P. S. Bell and J. C. Osler. Mapping bathymetry using X-band marine radar data recorded from a moving vessel. *Ocean Dynam.*, 61(12):2141–2156, Dec. 2011.
- [12] P. Berens. CircStat: A MATLAB toolbox for circular statistics. *J. Stat. Softw.*, 31(10):1–21, 2009.
- [13] J. C. N. Borge. First experience with the use of marine radar to survey ocean waves close to the spanish coast. In *Proc. of the WMO/IOC Workshop on Operational Ocean Monitoring using Surface Based Radars*, number 32, pages 88–94, Geneva, Switzerland, 1995.
- [14] J. C. N. Borge, K. Reichert, and J. Dittmer. Use of nautical radar as a wave monitoring instrument. *Coastal Eng.*, 37(3-4):331–342, 1999.
- [15] J. C. N. Borge, G. Rodríguez Rodríguez, K. Hessner, and P. I. González. Inversion of marine radar images for surface wave analysis. *J. Atmos. Oceanic Technol.*, 21(8):1291–1300, 2004.
- [16] W. L. Bragg. The diffraction of short electromagnetic waves by a crystal. In *Proc. Cambridge Phil. Soc.*, volume 17, page 43, 1913.
- [17] P. Brandt, R. Romeiser, and A. Rubino. On the determination of characteristics of the interior ocean dynamics from radar signatures of internal solitary waves. *J. Geophys. Res.*, 104(C12):30039–30045, 1999.
- [18] G. S. Brown. *Surface Waves and Fluxes*, chapter Quasi-specular scattering from the air-sea interface, pages 1–39. Kluwer, 1990.

- [19] G. S. Brown. Guest editorial - Special issue on low-grazing-angle backscatter from rough surfaces. *IEEE Trans. Antennas Propag.*, 46(1):1–2, 1998.
- [20] J. R. Buckley, M. Allingham, and R. Michaud. On the use of marine radar imagery for estimation of properties of the directional spectrum of the sea surface. *Atmos.-Ocean*, 32(1):195–213, Mar. 1994.
- [21] S. Cai, S. Wang, and X. Long. A simple estimation of the force exerted by internal solitons on cylindrical piles. *Ocean Eng.*, 33(7):974–980, 2006.
- [22] P. A. Catalán, M. C. Haller, R. A. Holman, and W. J. Plant. Optical and microwave detection of wave breaking in the surf zone. *IEEE Trans. Geosci. Remote Sens.*, 49(6 Part 1):1879–1893, 2011.
- [23] M.-H. Chang, R.-C. Lien, Y. J. Yang, T. Y. Tang, and J. Wang. A composite view of surface signatures and interior properties of nonlinear internal waves: Observations and applications. *J. Atmos. Oceanic Technol.*, 25(7):1218–1227, 2008.
- [24] A. H. Chaudhry and R. K. Moore. Tower-based backscatter measurements of the sea. *IEEE J. Oceanic Eng.*, OE-9(5):309–316, 1984.
- [25] A. C. Copeland, G. Ravichandran, and M. M. Trivedi. Localized Radon transform-based detection of ship wakes in SAR images. *IEEE Trans. Geosci. Remote Sens.*, 33(1):35–45, 1995.
- [26] D. D. Crombie. Doppler spectrum of sea echo at 13.56 Mc./s. *Nature*, 175(4459):681–682, Apr. 1955.
- [27] J. Croney. Improved radar visibility of small targets in sea clutter. *Radio and Electronic Engineer*, 32(3):135–147, 1966.
- [28] L. Cui, Y. He, H. Shen, and H. Lu. Measurements of ocean wave and current field using dual polarized X-band radar. *Chin. J. Oceanol. Limnol.*, 28(5):1021–1028, 2010.
- [29] J. C. B. da Silva, S. A. Ermakov, I. S. Robinson, D. R. G. Jeans, and S. V. Kijashko. Role of surface films in ERS SAR signatures of internal waves on the shelf 1. Short-period internal waves. *J. Geophys. Res.*, 103(C4):8009–8031, 1998.

- [30] H. Dankert and J. Horstmann. A marine radar wind sensor. *J. Atmos. Oceanic Technol.*, 24(9):1629–1642, 2007.
- [31] H. Dankert, J. Horstmann, and W. Rosenthal. Ocean wind fields retrieved from radar-image sequences. *J. Geophys. Res. C: Oceans*, 108(11):3352–3363, 2003.
- [32] H. Dankert and W. Rosenthal. Ocean surface determination from X-band radar-image sequences. *J. Geophys. Res. C: Oceans*, 109(4):4016–4027, 2004.
- [33] J. Dittmer. Use of marine radars for real time wave field survey and speeding up transmission/processing. In *Proc. WMO/IOC Workshop on Operational Ocean Monitoring Using Surface Based Radars*, volume 32, pages 133–137, 1995.
- [34] P. G. Drazin and R. S. Johnson. *Solitons: an introduction*. Cambridge University Press, 1989.
- [35] S. A. Ermakov, J. C. B. da Silva, and I. S. Robinson. Role of surface films in ERS SAR signatures of internal waves on the shelf 2. Internal tidal waves. *J. Geophys. Res. C: Oceans*, 103(3334):8033–8043, 1998.
- [36] S. Flampouris, F. Ziemer, and J. Seemann. Accuracy of bathymetric assessment by locally analyzing radar ocean wave imagery (February 2008). *IEEE Trans. Geosci. Remote Sens.*, 46(10):2906–2913, 2008.
- [37] N. C. Freeman. Soliton interactions in two dimensions. In C.-S. Yih, editor, *Advances in Applied Mechanics*, volume Volume 20, pages 1–37. Elsevier, 1980.
- [38] L.-L. Fu and B. Holt. SEASAT views oceans and sea ice with synthetic aperture radar. *JPL Publ.*, 81-120, 1982.
- [39] Furuno Electrics Co., Ltd. *Furuno Operator's Manual, Marine Radar, FAR-2xx7 Series*, 2004.
- [40] R. Gangeskar. Ocean current estimated from X-band radar sea surface images. *IEEE Trans. Geosci. Remote Sens.*, 40(4):783 –792, apr 2002.

- [41] R. Gangeskar. Automatic oil-spill detection by marine X-band radars - New system based on capturing and processing digitized radar images: Ready for extensive tests in October. *Sea Technol.*, 45(8):40–45, Aug. 2004.
- [42] J. R. Garratt. *The atmospheric boundary layer*. Cambridge University Press, Cambridge; New York, 1992.
- [43] C. P. Gommenginger, N. P. Ward, G. J. Fisher, I. S. Robinson, and S. R. Boxall. Quantitative microwave backscatter measurements from the ocean surface using digital marine radar images. *J. Atmos. Oceanic Technol.*, 17(5):665–678, May 2000.
- [44] H. C. Graber, E. A. Terray, M. A. Donelan, W. M. Drennan, J. C. Van Leer, and D. B. Peters. ASIS - A new air-sea interaction spar buoy: Design and performance at sea. *J. Atmos. Oceanic Technol.*, 17(5):708–720, May 2000.
- [45] R. Grimshaw, E. Pelinovsky, T. Talipova, and A. Kurkin. Simulation of the transformation of internal solitary waves on oceanic shelves. *J. Phys. Oceanogr.*, 34(12):2774–2791, Dec. 2004.
- [46] O. Grønlie. Wave radars - a comparison of concepts and techniques. In *Hydro International*, 2004.
- [47] H. Hatten, J. Seemann, J. Horstmann, and F. Ziemer. Azimuthal dependence of the radar cross section and the spectral background noise of a nautical radar at grazing incidence. In *Proc. Geoscience and Remote Sensing Symposium, IEEE International*, volume 5, pages 2490–2492, 1998.
- [48] L. R. Haury, M. G. Briscoe, and M. H. Orr. Tidally generated internal wave packets in Massachusetts Bay. *Nature*, 278(5702):312–317, Mar. 1979.
- [49] K. R. Helfrich and W. K. Melville. Long nonlinear internal waves. *Annu. Rev. Fluid Mech.*, 38:395–425, 2006.
- [50] R. J. Hill. Motion compensation for shipborne radars and lidars. Technical report, NOAA Earth System Research Laboratory, 2005.

- [51] H. Hirakuchi and M. Ikeno. Wave direction measurement using marine x-band radar. In *Proc. 22d Int. Conf. on Coastal Engineering*, pages 703–715, Delft, Netherlands, 1990.
- [52] J. Horstmann, R. Carrasco, and L. C. Retrieval of ocean surface wind fields from marine radar image sequences. Unpublished work, 2012.
- [53] W. Huang and E. Gill. Surface current measurement under low sea state using dual polarized X-band nautical radar. *IEEE J. Sel. Topics Appl. Earth Observations Remote Sens.*, 6 pages, in press(99), 2012.
- [54] P. A. Hwang, M. A. Sletten, and J. V. Toporkov. Analysis of radar sea return for breaking wave investigation. *J. Geophys. Res.*, 113(C2):C02003, Feb. 2008.
- [55] P. A. Hwang, M. A. Sletten, and J. V. Toporkov. Breaking wave contribution to low grazing angle radar backscatter from the ocean surface. *J. Geophys. Res.*, 113(C9):C09017–, Sept. 2008.
- [56] P. A. Hwang, M. A. Sletten, and J. V. Toporkov. A note on Doppler processing of coherent radar backscatter from the water surface: With application to ocean surface wave measurements. *J. Geophys. Res.*, 115(C3):C03026, Mar. 2010.
- [57] T. Ijima, T. Takahashi, and H. Sasaki. Application of radars to wave observations. In *Proc. Conf. Coastal Eng. 11th*, volume 30, pages 10–22, 1964.
- [58] P. Izquierdo and C. G. Soares. Analysis of sea waves and wind from X-band radar. *IEEE J. Oceanic Eng.*, 32(11-12):1404–1419, 2005.
- [59] C. Jackson and J. Apel. An atlas of internal solitary-like waves and their properties, 2004.
- [60] M. N. Jha, J. Levy, and Y. Gao. Advances in remote sensing for oil spill disaster management: State-of-the-art sensors technology for oil spill surveillance. *Sensors*, 8(1):236–255, Jan. 2008.

- [61] J. T. Johnson, R. J. Burkholder, J. V. Toporkov, D. R. Lyzenga, and W. J. Plant. A numerical study of the retrieval of sea surface height profiles from low grazing angle radar data. *IEEE Transactions on Geoscience and Remote Sensing*, 47(6):1641–1650, 2009.
- [62] S. Kamminga. Personal communication, May 2012.
- [63] W. C. Keller, W. J. Plant, R. A. Petitt Jr, and E. A. Terray. Microwave backscatter from the sea: Modulation of received power and Doppler bandwidth by long waves. *J. Geophys. Res.*, 99(C5):9751–9766, 1994.
- [64] D. T. Lee and B. J. Schachter. Two algorithms for constructing a Delaunay triangulation. *Int. J. Parallel Program.*, 9:219–242, 1980.
- [65] P. H. Y. Lee, J. D. Barter, K. L. Beach, C. L. Hindman, B. M. Lake, H. Rungaldier, J. C. Shelton, A. B. Williams, R. Yee, and H. C. Yuen. X band microwave backscattering from ocean waves. *J. Geophys. Res.*, 100(C2):2591–2611, 1995.
- [66] P. H. Y. Lee, J. D. Barter, E. Caponi, M. Caponi, C. L. Hindman, B. M. Lake, and H. Rungaldier. Wind-speed dependence of small-grazing-angle microwave backscatter from sea surfaces. *IEEE Trans. Antennas Propag.*, 44(3):333–340, 1996.
- [67] A. K. Liu, Y. S. Chang, M.-K. Hsu, and N. K. Liang. Evolution of nonlinear internal waves in the East and South China Seas. *J. Geophys. Res.*, 103(C4):7995–8008, 1998.
- [68] B. Lund, H. C. Graber, J. Horstmann, and E. Terrill. Ocean surface wind retrieval from stationary and moving platform marine radar data. In *Proc. Geoscience and Remote Sensing Symposium, IEEE International*, pages 2790–2793, 2012.
- [69] B. Lund, H. C. Graber, and R. Romeiser. Wind retrieval from shipborne nautical X-band radar data. *IEEE Trans. Geosci. Remote Sens.*, 50(10):3800–3811, 2012.
- [70] B. Lund, H. C. Graber, J. Xue, and R. Romeiser. Analysis of internal wave signatures in marine radar data. Manuscript submitted for publication, 2012.
- [71] D. R. Lyzenga and J. R. Bennett. Full-spectrum modeling of synthetic aperture radar internal wave signatures. *J. Geophys. Res.*, 93(C10):12345–12354, 1988.

- [72] A. C. Magnusson. Operational use of marine radar information in wave forecasting - Status and future aspects. In *Proc. of the WMO/IOC Workshop on Operational Ocean Monitoring using Surface Based Radars*, number 32, pages 95–102, Geneva, Switzerland, 1995.
- [73] C. B. Markwardt. Non-linear least squares fitting in idl with mpfit. In D. Bohlender, P. Dowler, and D. Durand, editors, *Astronomical Data Analysis Software and Systems XVIII, Quebec, Canada, ASP Conference Series*, volume 411, pages 251–254, 2008.
- [74] M. G. Mattie and D. L. Harris. A system for using radar to record wave direction. *NASA STI/Recon Technical Report N*, 80:19342, Sept. 1979.
- [75] B. I. Moat, M. J. Yelland, R. W. Pascal, and A. F. Molland. The effect of ship shape and anemometer location on wind speed measurements obtained from ships. In *RINA, Marine Hydrodynamics, Papers*, pages 133–139, 2005.
- [76] J. N. Moum, M. C. Gregg, R. C. Lien, and M. E. Carr. Comparison of turbulence kinetic energy dissipation rate estimates from two ocean microstructure profilers. *J. Atmos. Oceanic Technol.*, 12(2):346–366, Apr. 1995.
- [77] J. N. Moum, J. M. Klymak, J. D. Nash, A. Perlin, and W. D. Smyth. Energy transport by nonlinear internal waves. *J. Phys. Oceanogr.*, 37(7):1968–1988, July 2007.
- [78] L. M. Murphy. Linear feature detection and enhancement in noisy images via the Radon transform. *Pattern Recognit. Lett.*, 4(4):279–284, 1986.
- [79] A. Norris. The fundamentals of NT radar. <http://www.kelvinhughes.com/marine/resources/articles/sharpeye/207-the-fundamentals-of-nt-radar>, Aug. 2012.
- [80] OceanWaveS GmbH. *WaMoS II, Wave Monitoring System, Operating Manual and Installation Guide*, 2006.
- [81] M. H. Orr and P. C. Mignerey. Nonlinear internal waves in the South China Sea: Observation of the conversion of depression internal waves to elevation internal waves. *J. Geophys. Res. C: Oceans*, 108(3):9–1, 2003.

- [82] H. M. Oudshoorn. The use of radar in hydrodynamic surveying. In *Proc. 7th Conf. on Coastal Eng.*, The Hague, Netherlands, 1960.
- [83] J. Pan and D. A. Jay. Dynamic characteristics and horizontal transports of internal solitons generated at the Columbia River plume front. *Cont. Shelf Res.*, 29(1):252–262, Jan. 2009.
- [84] J. Pineda. Circulation and larval distribution in internal tidal bore warm fronts. *Limnol. Oceanogr.*, 44(6):1400–1414, Sept. 1999.
- [85] W. Plant. *Surface Waves and Fluxes*, chapter Bragg scattering of electromagnetic waves from the air/sea interface, pages 41–108. Kluwer, 1990.
- [86] W. Plant. A model for microwave doppler sea return at high incidence angles: Bragg scattering from bound, tilted waves. *J. Geophys. Res.*, 102(C9):21131–21146, 1997. cited By (since 1996) 53.
- [87] W. J. Plant. A two-scale model of short wind-generated waves and scatterometry. *J. Geophys. Res.*, 91(C9):10735–10749, 1986.
- [88] W. J. Plant, W. C. Keller, and A. Cross. Parametric dependence of ocean wave-radar modulation transfer functions. *J. Geophys. Res.*, 88(C14):9747–9756, 1983.
- [89] W. J. Plant, W. C. Keller, K. Hayes, and G. Chatham. Normalized radar cross section of the sea for backscatter: 1. Mean levels. *J. Geophys. Res.*, 115(C9):C09032, Sept. 2010.
- [90] W. J. Plant, W. C. Keller, K. Hayes, and G. Chatham. Characteristics of internal waves in the South China Sea observed by a shipboard coherent radar. *IEEE J. Oceanic Eng.*, 36(3):441–446, 2011.
- [91] W. J. Plant, W. C. Keller, K. Hayes, G. Chatham, and N. Lederer. Normalized radar cross section of the sea for backscatter: 2. Modulation by internal waves. *J. Geophys. Res.*, 115(C9):C09033, Sept. 2010.
- [92] W. J. Plant and D. L. Schuler. Remote sensing of the sea surface using one- and two-frequency microwave techniques. *Radio Sci.*, 15(3):605–615, 1980.

- [93] S. Popinet, M. Smith, and C. Stevens. Experimental and numerical study of the turbulence characteristics of airflow around a research vessel. *J. Atmos. Oceanic Technol.*, 21(10):1575–1589, 2004.
- [94] J. Radon. Über die Bestimmung von Funktionen durch ihre Integralwerte längs gewisser Mannigfaltigkeiten. *Math. Phys. Klasse*, 69:262–277, 1917.
- [95] S. Rahmstorf. Improving the accuracy of wind speed observations from ships. *Deep Sea Res. Part A*, 36(8):1267–1276, 1989.
- [96] R. J. Ramos, B. Lund, and H. C. Gruber. Determination of internal wave properties from X-band radar observations. *Ocean Eng.*, 36(14):1039–1047, 2009.
- [97] K. Reichert, K. Hessner, J. C. N. Borge, and J. Dittmer. WaMoS II: A radar based wave and current monitoring system. In *Proc. ISOPE*, volume 3, 1999.
- [98] I. S. Robinson. *Measuring the Oceans from Space - The principles and methods of satellite oceanography*. Springer Berlin / Heidelberg / New York, 2004.
- [99] I. S. Robinson, N. P. Ward, C. P. Gommenginger, and M. A. Tenorio-Gonzales. Coastal oceanography applications of digital image data from marine radar. *J. Atmos. Oceanic Technol.*, 17(5):721–735, May 2000.
- [100] J. A. Rodenas and R. Garello. Internal wave detection and location in SAR images using wavelet transform. *IEEE Trans. Geosci. Remote Sens.*, 36(5):1494–1507, 1998.
- [101] R. Romeiser and W. R. Alpers. An improved composite surface model for the radar backscattering cross section of the ocean surface 2. Model response to surface roughness variations and the radar imaging of underwater bottom topography. *J. Geophys. Res.*, 102(C11):25251–25267, 1997.
- [102] R. Romeiser, W. R. Alpers, and V. Wismann. An improved composite surface model for the radar backscattering cross section of the ocean surface 1. Theory of the model and optimization/validation by scatterometer data. *J. Geophys. Res.*, 102(C11):25237–25250, 1997.

- [103] H. Sandstrom and J. A. Elliott. Internal tide and solitons on the Scotian Shelf: A nutrient pump at work. *J. Geophys. Res.*, 89(C4):6415–6426, 1984.
- [104] J. Seemann, F. Ziemer, and C. M. Senet. A method for computing calibrated ocean wave spectra from measurements with a nautical X-band radar. *Proc. Oceans, IEEE*, pages 1148–1154, 1997.
- [105] C. M. Senet, J. Seemann, S. Flampouris, and F. Ziemer. Determination of bathymetric and current maps by the method DiSC based on the analysis of nautical X-band radar image sequences of the sea surface (November 2007). *IEEE Trans. Geosci. Remote Sens.*, 46(8):2267–2279, 2008.
- [106] C. M. Senet, J. Seemann, and F. Ziemer. The near-surface current velocity determined from image sequences of the sea surface. *IEEE Trans. Geosci. Remote Sens.*, 39(3):492–505, 2001.
- [107] E. L. Shroyer, J. N. Moum, and J. D. Nash. Energy transformations and dissipation of nonlinear internal waves over New Jersey’s continental shelf. *Nonlinear Processes Geophys.*, 17(4):345–360, 2010.
- [108] E. L. Shroyer, J. N. Moum, and J. D. Nash. Vertical heat flux and lateral mass transport in nonlinear internal waves. *Geophys. Res. Lett.*, 37(8):L08601, Apr. 2010.
- [109] E. L. Shroyer, J. N. Moum, and J. D. Nash. Nonlinear internal waves over New Jersey’s continental shelf. *J. Geophys. Res.*, 116(C3):C03022, Mar. 2011.
- [110] B. Smith. Geometrical shadowing of a random rough surface. *IEEE Trans. Antennas Propag.*, 15(5):668–671, 1967.
- [111] S. D. Smith. Wind stress and heat flux over the ocean in gale force winds. *J. Geophys. Res.*, 10(5):709–726, 1980.
- [112] T. P. Stanton and L. A. Ostrovsky. Observations of highly nonlinear internal solitons over the continental shelf. *Geophys. Res. Lett.*, 25(14):2695–2698, 1998.
- [113] A. Stoffelen and D. Anderson. Scatterometer data interpretation: Estimation and validation of the transfer function CMOD4. *J. Geophys. Res. C: Oceans*, 102(C3):5767–5780, 1997.

- [114] D. Tang, J. N. Moum, J. F. Lynch, P. Abbot, R. Chapman, P. H. Dahl, T. F. Duda, G. Gawarkiewicz, S. Glenn, J. A. Goff, H. C. Graber, J. Kemp, A. Maffei, J. D. Nash, and A. Newhall. Shallow water '06: A joint acoustic propagation/nonlinear internal wave physics experiment. *Oceanogr.*, 20(4):156–167, Dec. 2007.
- [115] E. J. Tennyson. Shipboard navigational radar as an oil spill tracking tool - A preliminary assessment. In *Proc. Oceans, IEEE*, volume 3, pages 857–859, 1988.
- [116] J. Trask, M. Henschel, and B. Eid. Analysis of marine radar image spectra collected during the Grand Banks ERS-1 SAR wave experiment. *Atmos.-Ocean*, 32(1):215–236, Mar. 1994.
- [117] D. B. Trizna. Statistics of low grazing angle radar sea scatter for moderate and fully developed ocean waves. *IEEE Trans. Antennas Propag.*, 39(12):1681–1690, 1991.
- [118] D. B. Trizna. A model for Brewster angle damping and multipath effects on the microwave radar sea echo at low grazing angles. *IEEE Trans. Geosci. Remote Sens.*, 35(5):1232–1244, 1997.
- [119] D. B. Trizna. Errors in bathymetric retrievals using linear dispersion in 3-D FFT analysis of marine radar ocean wave imagery. *IEEE Trans. Geosci. Remote Sens.*, 39(11):2465–2469, 2001.
- [120] D. B. Trizna. Coherent microwave marine radars for deterministic wave profile mapping, decameter-scale coastal current mapping and ocean wave spectra measurements. In *Proc. Oceans, IEEE*, pages 1–5, 2009.
- [121] D. B. Trizna and D. J. Carlson. Studies of dual polarized low grazing angle radar sea scatter in nearshore regions. *IEEE Trans. Geosci. Remote Sens.*, 34(3):747–757, 1996.
- [122] D. B. Trizna, J. P. Hansen, P. Hwang, and J. Wu. Laboratory studies of radar sea spikes at low grazing angles. *J. Geophys. Res.*, 96(C7):12529–12537, 1991.
- [123] H. Tsuji and M. Oikawa. Oblique interaction of internal solitary waves in a two-layer fluid of infinite depth. *Fluid Dyn. Res.*, 29(4):251–267, Oct. 2001.

- [124] G. R. Valenzuela. Theories for the interaction of electromagnetic and oceanic waves - A review. *Bound.-Layer Meteor.*, 13:61–85, 1978. 10.1007/BF00913863.
- [125] A. van Dongeren, N. Plant, A. Cohen, D. Roelvink, M. C. Haller, and P. A. Catalán. Beach Wizard: Nearshore bathymetry estimation through assimilation of model computations and remote observations. *Coastal Eng.*, 55(12):1016–1027, Dec. 2008.
- [126] C. Wackerman, W. Pichel, and P. C. Colón. A projection method for automatic estimation of wind vectors with RADARSAT SAR imagery. *Eur. Space Agency Spec. Publ.*, SP-565:55–60, 2004.
- [127] C. C. Wackerman, P. Clemente-Colón, W. G. Pichel, and X. Li. A two-scale model to predict C-band VV and HH normalized radar cross section values over the ocean. *Can. J. Remote Sensing*, 28(3):367–384, June 2002.
- [128] G. Watson and I. S. Robinson. A study of internal wave propagation in the Strait of Gibraltar using shore-based marine radar images. *J. Phys. Oceanogr.*, 20(3):374–395, Mar. 1990.
- [129] L. B. Wetzel. *Surface Waves and Fluxes*, chapter Electromagnetic scattering from the sea at low grazing angles, pages 109–171. Kluwer, 1990.
- [130] J. Wright. Backscattering from capillary waves with application to sea clutter. *IEEE Trans. Antennas Propag.*, 14(6):749–754, 1966.
- [131] J. Wright. A new model for sea clutter. *IEEE Trans. Antennas Propag.*, 16(2):217–223, 1968.
- [132] J. Xue, H. C. Graber, B. Lund, and R. Romeiser. Amplitudes estimation of large internal solitary waves in the Mid-Atlantic Bight using synthetic aperture radar and marine X-band radar images. *IEEE Trans. Geosci. Remote Sens.*, accepted for publication, 2012.
- [133] J. Xue, B. Lund, H. C. Graber, and R. Romeiser. A case study of internal wave-wave interaction during the shallow water 2006 experiment. In *Proc. International Geoscience and Remote Sensing Symposium, IEEE International*, pages 2845–2848, 2012.

- [134] M. J. Yelland, B. I. Moat, R. W. Pascal, and D. I. Berry. CFD model estimates of the airflow distortion over research ships and the impact on momentum flux measurements. *J. Atmos. Oceanic Technol.*, 19(10):1477–1499, 2002.
- [135] I. Young. On the measurement of directional wave spectra. *Applied Ocean Research*, 16(5):283–294, 1994.
- [136] I. R. Young, W. Rosenthal, and F. Ziemer. A three-dimensional analysis of marine radar images for the determination of ocean wave directionality and surface currents. *J. Geophys. Res.*, 90(C1):1049–1059, 1985.
- [137] G. Zha, Y. He, T. Yu, Q. He, and H. Shen. The force exerted on a cylindrical pile by ocean internal waves derived from nautical X-band radar observations and in-situ buoyancy frequency data. *Ocean Eng.*, 41(0):13–20, Feb. 2012.
- [138] Q. Zheng, Y. Yuan, V. Klemas, and X.-H. Yan. Theoretical expression for an ocean internal soliton synthetic aperture radar image and determination of the soliton characteristic half width. *J. Geophys. Res.*, 106(C12):31415–31423, 2001.
- [139] F. Ziemer. An instrument for the survey of the directionality of the ocean wave field. In *Proc. WMO/IOC Workshop on Operational Ocean Monitoring Using Surface Based Radars*, volume 32, pages 81–87, 1995.
- [140] F. Ziemer and J. Dittmer. A system to monitor ocean wave fields. In *Proc. Oceans, IEEE*, volume 2, pages 28–31, 1994.
- [141] F. Ziemer and W. Rosenthal. Measurement of two-dimensional wave energy spectra during SAXON-FPN’90. In *Proc. Oceans, IEEE*, volume 2, pages II326–II331, 1993.
- [142] F. Ziemer, W. Rosenthal, and H. Carlson. Measurements of directional wave spectra by ship radar. In *IAPSO Symp., General Assembly, Int. Assoc. for Phys. Sci. of the Oceans*, Hamburg, Germany, 1983.

## Appendix A

### Marine Radar Backscatter Ramp Definition

The radar backscatter ramp describes the mean radar backscatter intensity as a function of range and antenna look direction. As part of the IW and wind streak retrieval techniques developed in this work, the backscatter ramp is removed from the marine radar data. This is necessary because the techniques require homogeneous radar images.

The mean radar image intensity decreases rapidly in the near range and more slowly in the mid to far range, which can be explained by the decay of received electromagnetic energy with distance. Furthermore, the backscatter intensity has a peak in upwind direction. The backscatter dependency on range is obtained by averaging all unobstructed radar pulses over antenna look direction. The backscatter dependency on antenna look direction is obtained by averaging all radar pulses over range. The empirical functions proposed to model these dependencies are repeated below for reference:

$$I_p = \frac{a_0}{a_1 + p^{a_2}}; \quad (\text{A.1})$$

$$I_\Theta = b_0 + b_1 \cos(0.5(\Theta - b_2))^2. \quad (\text{A.2})$$

The best-fit curve of Eq. A.2 has a peak in upwind direction, and its average intensity can be correlated with the wind speed. Therefore, it offers a means of estimating the wind speed and direction from marine radar data [69].

To construct the radar backscatter ramp we combine the previously determined backscatter dependency on range and antenna look direction as follows:

$$I_{\Theta,\rho} = I_\rho + A_\rho(\cos(0.5(\Theta - b_2))^2 - 0.5). \quad (\text{A.3})$$

Here, the amplitude  $A_\rho$ , which is a function of range, is obtained in several steps. Initially, the polar radar image is reduced in size by averaging eight range pixels (with the antenna look direction's dimension remaining unchanged) in order to increase computation speed. For each resulting range bin, we then fit Eq. A.2 to the corresponding measured backscatter dependency on antenna look direction. The goal of this operation is to determine the model function's amplitude,  $b_1(\rho)$ , which represents the only free regression parameter. The upwind-peak position, given by  $b_2$ , is assumed constant for all ranges, and the downwind intensity,  $b_0(\rho)$ , is tied to the unknown  $b_1(\rho)$  via  $b_0(\rho) = I_\rho - 0.5b_1(\rho)$ . Finally, the resulting amplitudes,  $b_1(\rho)$ , are smoothed by fitting a parabola to the near-range section and Eq. A.1 to the mid to far ranges. A smooth transition between the two functions is achieved using the hyperbolic tangent, yielding the fitted amplitudes needed for constructing the ramp:

$$A_\rho = \begin{cases} c_0(\rho - c_1)^2 + c_2 & \rho < \rho_{max}, \\ (c_0(\rho - c_1)^2 + c_2)(0.5 + 0.5 \tanh\left(\frac{\rho - d_0}{d_1}\right)) + \\ \frac{e_0}{e_1 + \rho^{e_2}}(0.5 - 0.5 \tanh\left(\frac{\rho - d_0}{d_1}\right)) & \rho_{max} \leq \rho < 2\rho_{max}, \\ \frac{e_0}{e_1 + \rho^{e_2}} & \rho \geq 2\rho_{max}. \end{cases} \quad (\text{A.4})$$

Here,  $\rho_{max}$  is the range at which  $b_1(\rho)$  reaches its maximum,  $c_0, c_1, c_2$  are the parabola's regression parameters (for the near range),  $e_0, e_1, e_2$  are regression parameters for the "mid-to far-range" function, and  $d_0, d_1$  control the transition between the two.

The amplitude varies significantly over range and, generally, it increases first before it rapidly decreases with range. Low amplitudes in the very near range can be explained by image saturation, which is not an issue at greater ranges.

A radar backscatter ramp is obtained by fitting Eqs. A.1-A.4 (with masked sections disregarded) to our marine radar data. The least-squares fitting is done using Markwardt's MPFIT package for IDL [73]. The ramp has the following characteristics: Its intensity has a peak in upwind direction; the difference between up- and downwind intensity first increases and then decreases; its mean intensity in range is controlled by the fitted backscatter dependency on range. As per definition, it resembles the raw data, however, it is much smoother, does not have a masked section, and shows no IW or wind streak signal.

By subtracting the ramp from a marine radar image, we obtain a ramp-corrected image with a mean intensity near 0. Alternatively, the ramp can be removed by dividing the image by the ramp, yielding an image that has an average intensity around 1.

Comparing ramp-corrected backscatter intensities over all ranges reveals that the variability is significantly enhanced in the near range. Generally, the radar backscatter intensity's standard deviation as a function of range has a similar shape as the amplitude. As for the amplitude, the low standard deviation in the very near range can be explained by image saturation. In order to obtain images with a similar dynamic range of backscatter intensity levels from the near to far range, we divide each pixel in range by its corresponding fitted standard deviation  $\sigma_\rho$ , which is obtained in the same way we derived  $A_\rho$ , using the right-hand side of Eq. A.4. The bulk of the resulting normalized image's intensities will range from -1 to 1, with occasional outliers that can be attributed to the masking by ship structures, the IW, surface waves, or bright targets such as ships or moorings.

Remaining image heterogeneities can be attributed to imperfections in the ramp model function and normalization approach. For example, it can be observed that the radar backscatter intensity's standard deviation changes depending on the relative angle between antenna look direction and wind direction. Our assumption of a standard deviation that varies only as a function of range but not antenna look direction is therefore inaccurate. Further research is required to derive a general rule from this observation.

# Appendix B

## SW '06 WaMoS Data Correction

### B.1 Introductory Remarks

During SW '06, the WaMoS on both *R/V Oceanus* and *Knorr* used OceanWaveS' newly developed single-image version. The WaMoS standard version collects radar data in sequences of 32 or 64 images, and then interrupts the image acquisition to do the wave processing. In contrast, the single-image version collects radar data continuously and performs the wave analysis in parallel. In 2006, it was still in the early stages of development and had not been fully tested. This appendix gives an overview of issues encountered with the WaMoS single-image version and how they are resolved. Here, the focus lies on *Oceanus* data. However, the same issues were encountered with the *Knorr* data, and similar solutions apply.

### B.2 Image Acquisition Time

In order to account for ship heading changes and horizontal motion, the image acquisition time must be known. WaMoS stores the raw radar backscatter information in polar coordinates in binary files with a .pol extension. WaMoS' single image version produces a POL file with every antenna rotation. In its latest release, the exact image acquisition time as well

as the antenna repetition time are written into each POL file's header section. The POL files produced by the beta version used during SW '06 lack this information. A rough estimate of the image acquisition time can be obtained from the time stamp in the file name, which has the format YYYYMMDDHHMISExxx.pol (e.g. a radar image collected from *Oceanus* on August 14, 2006, 06:00:00 UTC would have the name 20060814060000ocu.pol). However, this is only a rough estimate because the time stamp corresponds to the file creation time, which does not necessarily coincide with the image acquisition time. Furthermore, it is missing the fractional part of the second.

Fig. B.1a shows the creation time for 91 consecutive POL files collected on August 17, 2006, from 22:34 to 22:38 UTC. Fig. B.1b gives the creation time difference for each pair of consecutive files. The antenna repetition time as specified by Furuno is 2.5 s. During the WaMoS installation on *Oceanus*, an antenna repetition time of 2.55 s was measured. Here, we use the latter value as our best estimate of the true antenna repetition time. In practice, the antenna repetition time may vary slightly from image to image, but it should not change by more than a fraction of a second. As can be seen from the figure, the bulk of the file creation time differences is between 2 and 3 s, as could be expected from our best estimate for the antenna repetition time. However, on three occasions the file creation time difference reaches 5 s, and on five occasions it is only 1 s. These outliers indicate disruptions to the WaMoS data stream, since it is impossible for the antenna rotation speed to vary as drastically. The periodic character of these disruptions in turn suggests that they are due to the wave processing. This would explain why WaMoS, in its standard version, alternates between data collection and processing modes. An alternative explanation for these disruptions is provided in section B.6.

In a first attempt at estimating the image acquisition time, a straight line is least-squares fitted to the file creation times (see red dashed line in Fig. B.1a). Assuming a constant antenna repetition time, the best-fit line yields a first estimate of the antenna repetition

time. Fig. B.1c shows the difference between image acquisition time as estimated by the linear fit and file creation time.

There is one risk associated with this technique of estimating the image acquisition time: If there is a data gap between individual files, it will be smoothed out by the fit, which may lead to significant errors. Here, the antenna repetition time retrieved from the best-fit line's slope is with 2.67 s significantly longer than our best estimate for the true antenna repetition time. This apparent decrease in the antenna rotation rate suggests that the WaMoS data stream disruptions discussed above were accompanied by a data loss. Additional proof of data loss will be provided in the following section on bearing control, where it will furthermore be discussed how this issue can be mitigated.

### B.3 Bearing Control

Among the first 12 bits in every radar pulse recorded by WaMoS, a specific bit contains information on the antenna look direction. This works as follows: For the first half of any degree the bit is set to 0, while for the second half it is set to 1. In this way, every change from 1 to 0 indicates that the antenna has advanced to the next degree. Here, such a bit change will be referred to as a bearing pulse. It is used to assign the correct look direction to each pulse. This is necessary because the antenna rotation speed decreases slightly when the antenna is facing the wind and increases when the antenna is pointing into the wind. This antenna behavior leads to a varying number of pulses per degree. Since each POL file supposedly contains backscatter information for a full antenna rotation, each file should start with a “0-bit pulse” and end with a “1-bit pulse”. However, during our 4-min period, this is the case for only very few POL files. From this finding it can be concluded that the POL files do not generally begin with the first and end with the last radar pulse of their respective antenna rotations. In the following, evidence will be presented that a limited number of radar pulses tends to migrate between POL files.

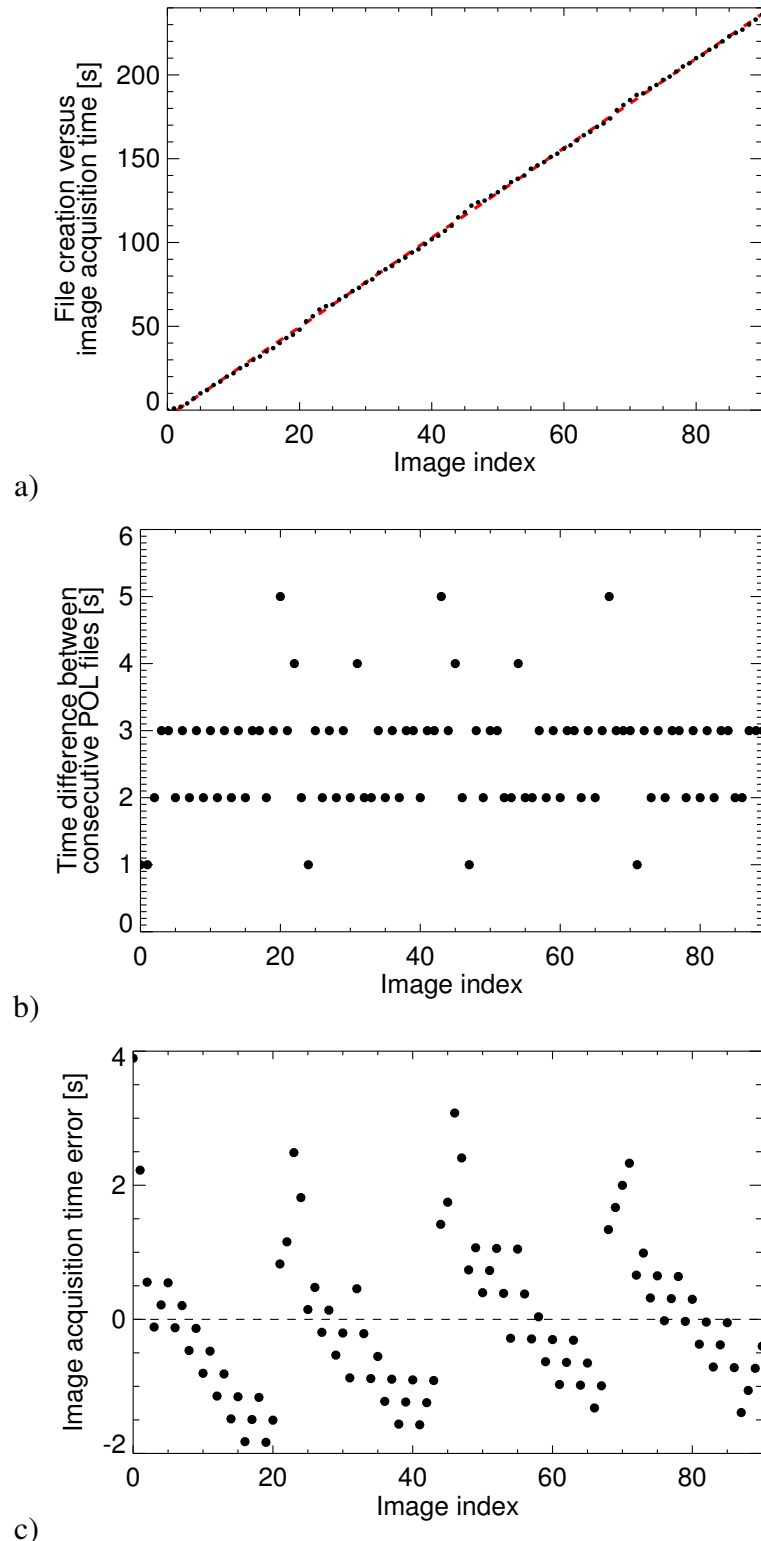


Figure B.1: File creation time in black and estimated image acquisition time marked by red dashed line (a). Creation time difference for consecutive files (b). Resulting temporal error if file creation time is mistaken for image acquisition time (c).

If for any given degree of rotation WaMoS misses all pulses with either a 0-bit or a 1-bit, a bearing pulse is lost. Our *Oceanus* data contain on average 5 radar pulses per degree. Therefore, a bearing pulse is generally lost if WaMoS misses 2 to 3 consecutive radar pulses with the same bit assignment. Here, we treat our marine radar data as a continuous data stream and assume that no bearing pulses were lost. Furthermore, we assume that our radar image sequence starts with data from the first degree of antenna rotation. Fig. B.2 illustrates the location difference between the first pulse of each new file and the one indicating the start of a new image. A value of zero means that the corresponding file begins with the first pulse of its antenna rotation, a value of one means that it begins one pulse late, etc. From the figure it becomes clear that POL files regularly contain pulses of the subsequent image. If the POL files were treated independently, this would result in missing pulses at the start and an excess of pulses at the end of each affected image. By treating the radar pulses within each individual POL file as a continuous stream of data, we can keep all radar pulses and correctly fill gaps that are due to this inter-file pulse migration. However, this procedure has a drawback: It assumes that WaMoS stores at least one radar pulse for every half-degree of antenna rotation. If this is not the case, the bearing control fails and the resulting error in the radar pulse placement propagates throughout the remaining sequence. In contrast, only a single image would be affected if POL files were handled individually.

An excess of bearing pulses represents yet another issue, providing clear evidence of a data stream disruption. Within a sequence of  $N$  POL files, we expect to find  $360N - 1$  bearing pulses. Our sequence of 91 POL files should therefore contain 32,759 bearing pulses. However, it contains 32,761 bearing pulses, i.e. we find an excess of radar pulses covering approximately  $2^\circ$ . This pulse excess value is too large to explain it by pulse migration. In this context, it helps to determine the number of bearing pulses within each individual file, which points us towards the following irregularity: The POL file from August 17, 22:37:09 UTC has 361 bearing pulses, indicating that it contains radar data covering more than  $360^\circ$ . Since in Fig. B.2 we treat our radar pulses as a continuous data stream, this causes the pulse

migration to advance by  $\sim 5$  pulses (compare figure at  $\sim 190$  s), which indicates that the subsequent files start with a  $1^\circ$  heading and not with a  $0^\circ$  heading, as would be expected. With the information at hand, it is difficult to determine what has actually happened. It does not help in this context that we do not know the exact image acquisition time (see section B.2). However, the following facts point towards a data gap:

- The suspicious file was created during a period that is characterized by irregularities in the file creation times, with the subsequent file being created only 1 s later;
- the number of files created during our 4-min period suggests that the antenna rotation rate is slightly lower than according to system specifications, indicating that data from one or more full antenna rotations were lost;
- periods during which the file creation times had a more regular character indicate an antenna repetition time that is in better agreement with the system specifications.

We therefore conclude that the radar data stream must have been disrupted and data from a full antenna rotation (or several rotations) have gotten lost.

This issue can be mitigated by attempting to identify data gaps and performing the bearing control individually for each complete period. Here, a data gap is assumed if the time difference in the creation of consecutive POL files is greater than 3 s or less than 2 s. Furthermore, we assume a data gap wherever there are POL files with less than 359 or more than 360 bearing pulses. This is unless these irregularities can be explained by pulse migration that is limited to the neighboring files. In the interest of completeness, data gaps may furthermore occur due to occasional input-output errors. However, this issue is not present during the 4-min period studied here.

By dividing our marine radar images into segments during which the data stream is presumably uninterrupted, we can furthermore improve our image acquisition time estimates. If for each segment of continuous data, we fit a straight line to the corresponding file creation dates, the resulting mean repetition time is 2.57 s. (Note that for segments with fewer

than three elements we assumed an antenna repetition time of 2.55 s.) This value is much closer to our best estimate for the true antenna repetition time than the one that has been determined by fitting a straight line to the full data set (compare section B.2). Finally, by limiting our segments to the ones containing a minimum of 10 POL files (during our 4-min period this includes 59 out of 91 files, divided into 4 segments), we can use the mean of the antenna repetition time estimates from two neighboring segments to determine the number of files that WaMoS should have recorded during the gap. This analysis suggests that WaMoS lost a total of 6 images during our 4-min period. For internal wave (IW) retrieval purposes, the data loss by itself would not be too bad. However, what causes serious complications is the fact that we do not know the exact image acquisition time, which constrains our correction of the insufficient ship heading and location data in the header section of the WaMoS POL files (see following section). Facing similar issues, Robinson et al. [99] use ground control points of known location to geolocate their marine radar pulses. Since no such option exists for data from the open sea, Bell and Osler [11] applied a 2D-FFT to their radar data, and used the surface wave signal within the resulting spectra to correctly orientate their radar images. While this solution could easily be applied to our IW data, the much simpler corrections described in the following have proven sufficient for our purposes. This is because our IW signal varies much slower than the surface waves studied by Bell and Osler, enabling us to use averaging techniques that smooth out inaccuracies due to erroneous image time stamps.

## B.4 Ship Heading and Location

WaMoS receives ship heading and location data from external sensors through the ship's NMEA stream. The software version used during SW '06 updated heading and location information in  $\sim 15$  s intervals only, which is much too infrequent since both *Knorr* and *Oceanus* changed course regularly. Furthermore, the ship heading information was stored

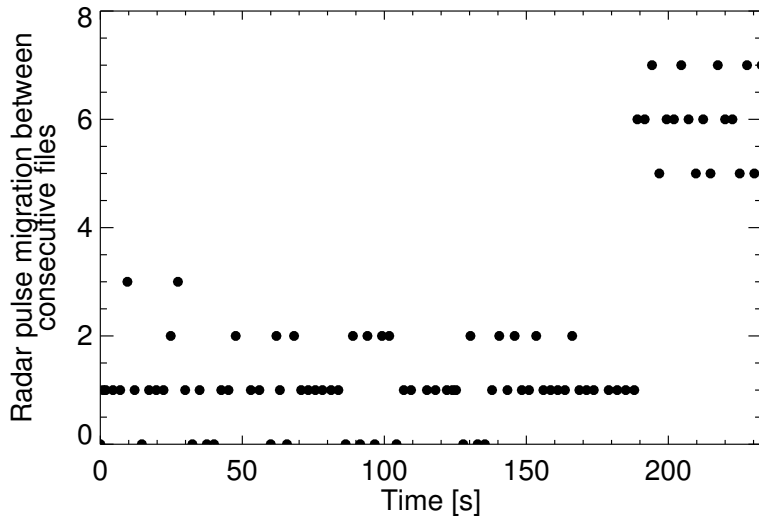


Figure B.2: Pulse migration between consecutive POL files.

with the fractional part of the degree missing. The current WaMoS version records both heading and location at the time of each image acquisition and the heading now includes the fractional part.

To correct the *Oceanus* heading and location, external gyro compass and GPS data acquired by Ashtech and Calliope are used. Ashtech provides heading and GPS data with high directional/spatial and temporal resolution ( $\sim 1$  s). Calliope data are equally well resolved in terms of direction and space but have a lower sampling rate of  $\sim 15$  s. When available, Ashtech data are used for corrections. During a 2-day period starting August 17, 20:21 UTC, Ashtech was unavailable and Calliope data had to be used. The Calliope data were linearly interpolated to a 1-s resolution.

Fig. B.3a shows the ship heading for each image as given by the WaMoS header (red) and from our external source (black). Fig. B.3b shows the resulting error if the WaMoS header gyro compass information is not corrected. The data shown here were acquired during our 4-min period starting August 17, 22:34 UTC. The WaMoS file acquisition time stamps were corrected to represent image acquisition times as discussed in sections B.2 and B.3. During this period the ship heading changed from an eastern to a northwestern orientation. During the course change, image heading errors reach values up to  $28^\circ$ .

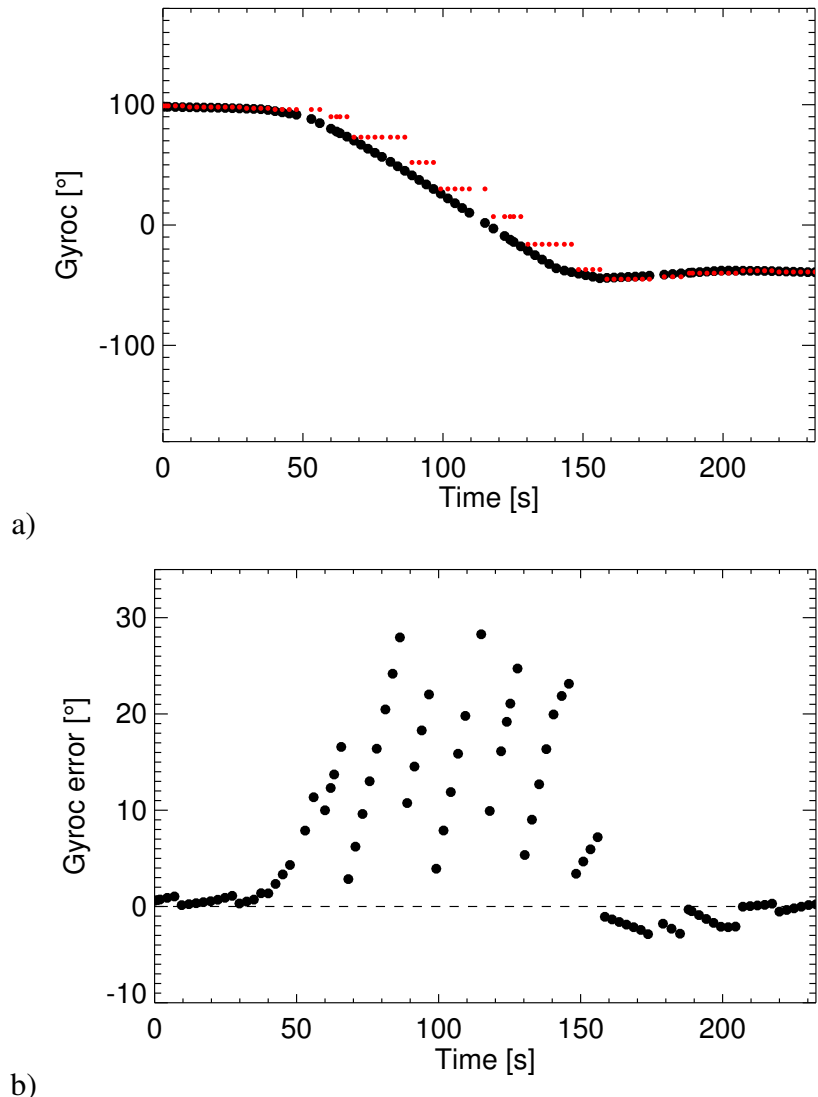


Figure B.3: Gyro compass measurements as recorded by WaMoS in red and from an external source in black (a). Gyro compass error without correction (b).

Fig. B.4a shows GPS measurements from the WaMoS header (red) and from the external source (black). Fig. B.4b shows the distance between the position logged in the WaMoS header and the true position. Especially during periods when the ship is moving fast, errors can be quite significant. With a range resolution of 7.5 m, the maximum error of 42 m would result in image data being misplaced by  $\sim 6$  resolution cells.

## B.5 Pre- vs Post-correction

Fig. B.5 shows 2-min averaged, geolocated, and IW-motion corrected marine radar images before and after the corrections discussed in the previous sections. The data were collected while the ship heading changed from an eastern to a northwestern orientation. Because of the rapidly changing course during this period, it is particularly important to know the exact image acquisition time and have highly accurate gyro compass information that is regularly updated. During times when the ship is moving fast, high quality GPS locations gain importance. As becomes clear from the figure, the IW signal is significantly enhanced by the corrections. In fact, the IW signatures within the pre-correction image are almost completely obscured by the averaging. In contrast, the image with the corrected parameters shows a clear IW signal. However, the IW signatures probably would be much better defined if we had reliable image acquisition times to match with our (external) high-resolution ship course data.

To summarize, our image acquisition times are estimated by least-squares fitting a line to the file creation dates associated with each gapless data segment. To address the issue of radar pulse migration, the bearing control is done by segments. The gyro compass and GPS data acquired by WaMoS have a too-low resolution and were corrected using external data sets.

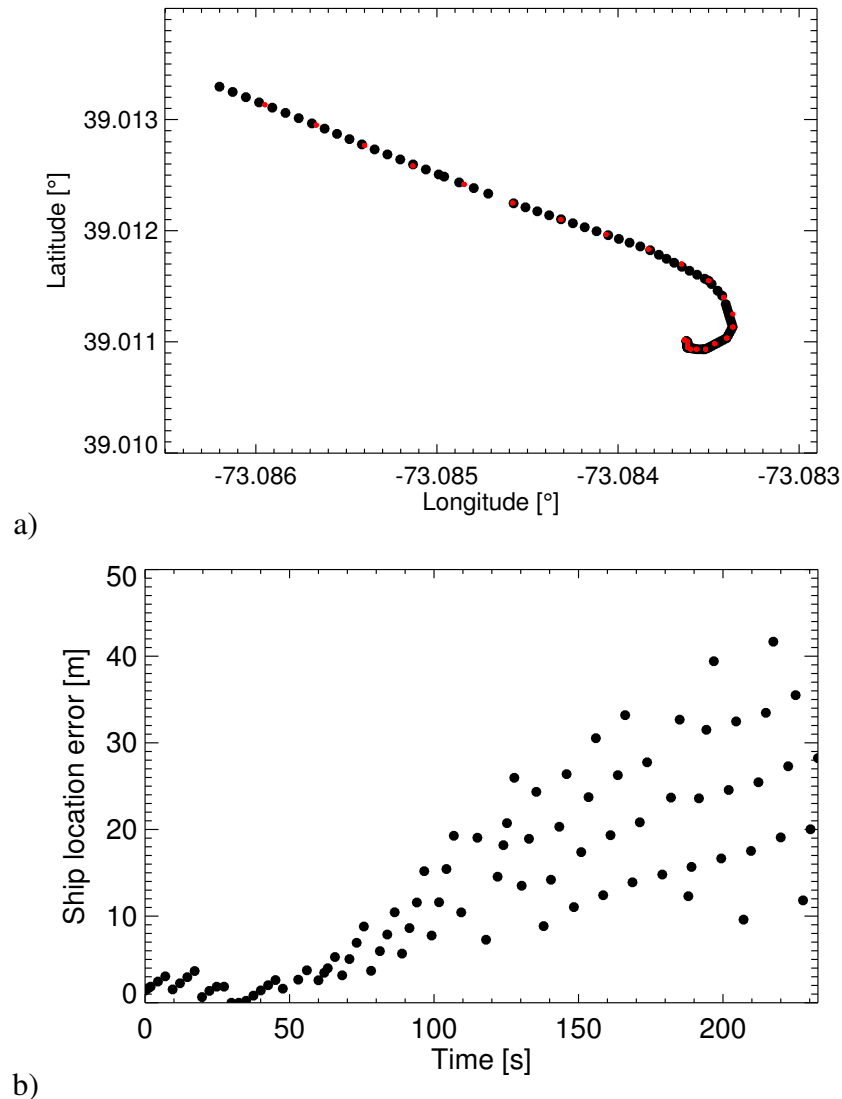


Figure B.4: GPS measurements as recorded by WaMoS in red and from an external source in black (a). Ship location error without correction (b).

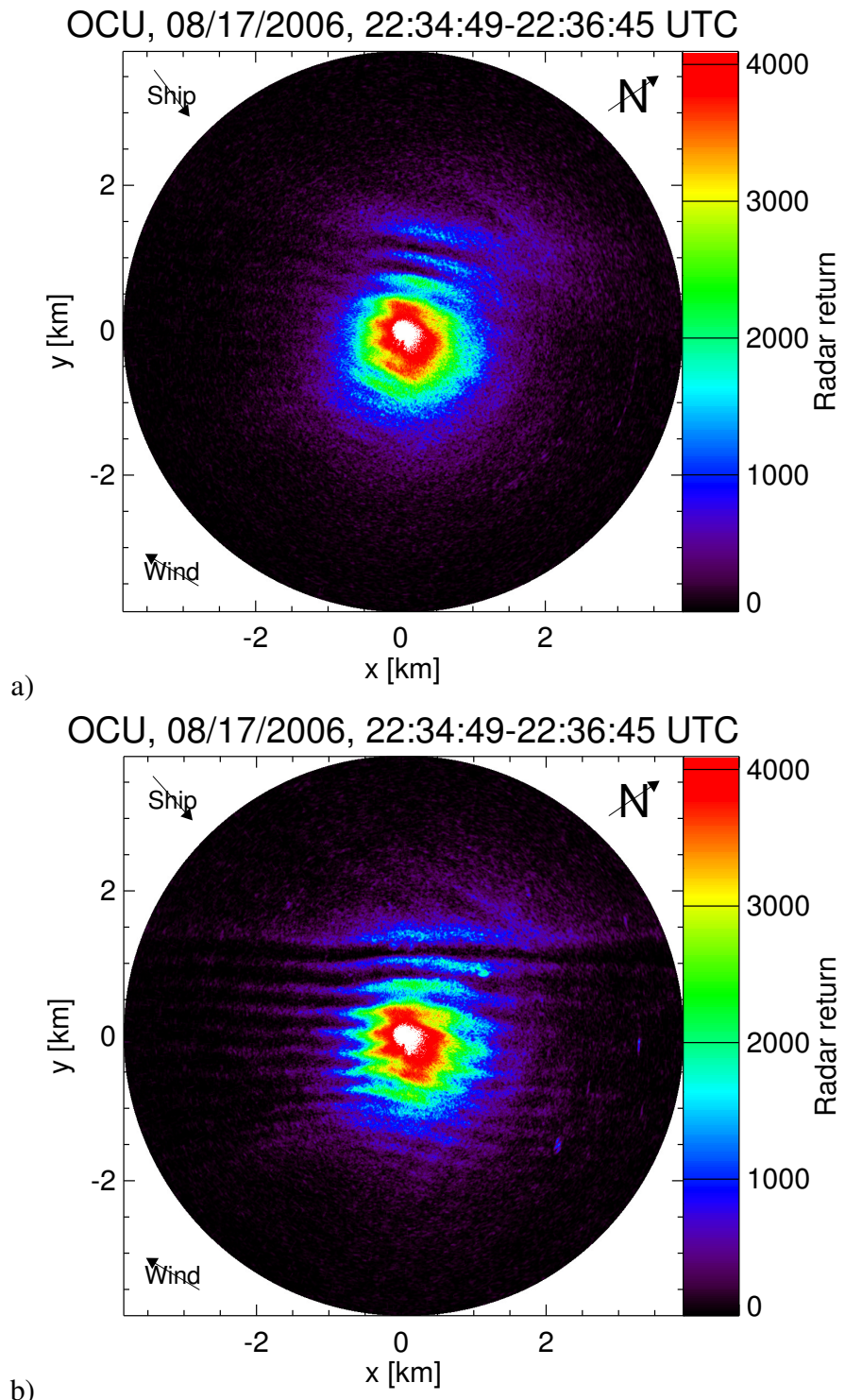


Figure B.5: Average of 2-min worth of geolocated and IW-motion corrected radar images before (a) and after correction of image acquisition time, ship heading, and location (b). The data were acquired from August 17, 22:34:49 to 22:36:47 UTC.

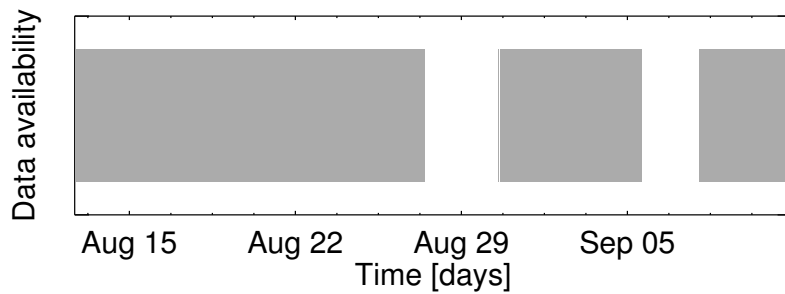


Figure B.6: Overview of WaMoS *Oceanus* data availability.

## B.6 WaMoS Radar Image Acquisition from *Oceanus*: An Overview

Fig. B.6 gives an overview of the availability of WaMoS POL files from *Oceanus* during SW '06. WaMoS data are available from August 12 to September 11, with two short gaps midway and towards the end of the experiment. In total, the available data amount to 826,106 POL files collected over 24.63 days. As mentioned above, we do not know the exact antenna repetition time. These numbers yield an average antenna repetition time of 2.58 s. However, due to the WaMoS data stream disruptions discussed in sections B.2 and B.3, this value must be treated cautiously.

Fig. B.7 shows the number of POL files collected per hour for a 1-week period starting August 13. While the majority of hours shows values around 1400 (an antenna rotation time of 2.55 s would produce 1412 files), the number of recorded POL files significantly decreases (by up to 10%) towards the end of all but the first day. It is safe to assume that such a decrease in the amount of recorded files cannot be explained by a changing antenna rotation speed. Instead, the decrease indicates a disruption of the WaMoS data stream, and the fact that it occurred regularly at roughly the same hour points us towards another likely cause of the disruption: During SW '06, the science team onboard *Oceanus* performed backups of the WaMoS POL data at roughly this time and at close to daily intervals. These

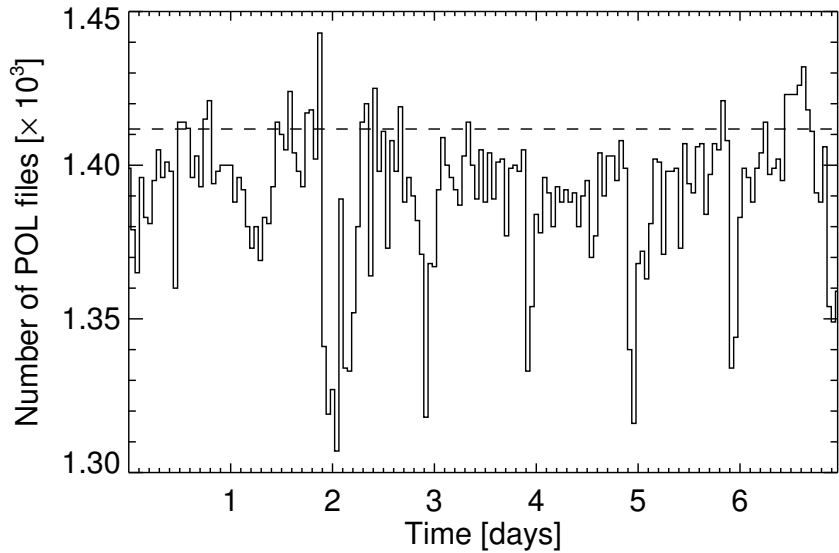


Figure B.7: Histogram detailing number of WaMoS *Oceanus* POL files available for each full hour during 1-week period starting August 13. The dashed line indicates the number of POL files expected for a 2.55 s antenna rotation time.

backups appear to have interfered with the data collection and/or the wave processing, resulting in the loss of radar data.

If we analyze the creation dates of all *Oceanus* POL files collected during SW '06 by searching for periods during which the file creation time differences range between 2 and 3 s, fit a straight line to the dates from each of these periods, and discard all other dates (which results in 56,397 of our 826,106 files being disregarded), we obtain a mean antenna repetition time of 2.55 s, which is in perfect agreement with the WaMoS measurement performed during the initial setup of the system.

# Appendix C

## Retrieval of Internal Wave Signatures from Marine Radar Data

### Summary

In this appendix we study the retrieval of internal wave (IW) signatures from marine radar data. In a first step, IW packet characteristics are determined, which are used to enhance the IW signal by temporal averaging. The IW-enhanced images are then channeled into our IW signature retrieval algorithm, where we employ localized Radon transform techniques to trace the signatures of each individual soliton. From the resulting IW soliton maps, one can easily extract parameters such as wavelength, velocity, and curvature for each soliton. During the Non-Linear Internal Wave Initiative 2006, *R/V Oceanus* was tracking IWs as they propagated across New Jersey's continental shelf. Our tool provides a first means of studying the spatio-temporal evolution of IW surface signatures as the underlying wave grows and subsequently decays.

### C.1 Introductory Remarks

This appendix studies the retrieval of internal wave (IW) signatures from marine radar data collected from *R/V Oceanus* during the ONR-funded Non-Linear Internal Wave Initiative

(NLIWI) off the New Jersey coast in 2006. The study of IWs is relevant for many disciplines within the scientific and engineering communities. IWs are ubiquitous features of coastal oceans and represent a significant mechanism for tidal energy transport. Their dissipation may induce intense vertical mixing that is important for multiple coastal processes [49]. Furthermore, IWs are responsible for modifying the patterns of acoustic propagation and can affect the navigation of vessels and underwater vehicles due to the strong currents and shears associated with them [21].

Marine radars operate by transmitting and receiving pulses of microwaves that interact with the rough sea surface. The radar echo from the sea surface is primarily dependent on small-scale ripple waves due to Bragg scattering. IWs are accompanied by a spatially and temporally varying surface current field. Marine radars show IWs as adjacent bands of weak and strong backscatter that propagate with the IW packet's velocity. As for synthetic aperture radar (SAR) images, such features can either result from hydrodynamic interactions between the short surface waves and the horizontal surface currents caused by IWs, or from surfactants that accumulate in IW flow convergence zones and dampen the short surface waves there [2].

SAR images have been used to demonstrate the existence of IWs in coastal oceans and derive IW parameters such as the propagation direction or the distance between solitons (e.g. [38]). More recently, methods to retrieve IW information from marine radar data have been introduced [23, 96]. In contrast to SAR, where an IW packet is generally imaged only once, and in-situ measurements that provide “point” observations, marine radars provide a more complete picture as they allow to study the IW evolution.

In this appendix we present a novel method to retrieve IW information from marine radar data. First, the images are divided by their respective radar backscatter ramps to produce near-homogeneous intensities. The ramp-corrected images are then used to retrieve IW packet speed and direction, employing a combination of Radon transform and cross-correlation techniques. In a next step, the images are georeferenced and corrected for the

IW packet motion. By averaging a 4 min sequence of such preprocessed radar images, we can now significantly enhance the IW signatures. The resulting IW-enhanced images are fed into our IW signature retrieval algorithm, where we use localized Radon transform techniques to trace the signatures of each individual soliton, yielding IW soliton maps. From such maps, one can easily extract parameters such as wavelength, velocity, and curvature for each IW soliton. Furthermore, they provide a unique view of the spatio-temporal evolution of IW surface expressions and can be used to study wave-wave interactions.

During the NLIWI project, *Oceanus* was tracking IWs as they grew and later decayed while propagating across the shelf. To illustrate our tool's capabilities, we use marine radar data that were collected during a particularly energetic IW event from August 17, 2006.

## C.2 Data Overview

The data used for the present work were collected by *R/V Oceanus* during the NLIWI experiment off the coast of New Jersey from August 12 to September 11, 2006. NLIWI's goal was to investigate the impact of non-linear IWs on acoustic propagation and scattering in shallow water. The experiment combined a great variety of instruments on different platforms including research vessels, moorings, aircraft, shore-based HF radar, air-sea interaction spar (ASIS) buoys, and satellite imagery.

Our marine radar data were acquired using a standard Furuno marine X-band radar operating at 9.4 GHz with HH-polarization and grazing incidence angle. The radar has an antenna repetition frequency of 24 rpm with a sampling frequency of 20 MHz. With this configuration, radar backscatter images were collected every 2.5 s, covering a range from 60 to 3,900 m with a range resolution of 7.5 m. The radar was connected to a Wave Monitoring System (WaMoS), which digitizes and stores the spatial and temporal radar backscatter information as a sequence of 12-bit images, i.e. digitized backscatter intensities

range from 0 to 4,095 [140]. Note that for standard marine radars the backscatter intensity is not radiometrically calibrated.

### C.3 Methodology

The IW signatures in marine radar images can be enhanced significantly by time-averaging a sequence of images. The following processing steps are required before averaging: Firstly, the decrease of the radar backscatter intensity with range and its dependency on wind direction must be removed by dividing each individual image by the sequence's radar backscatter ramp. Here, we determine the ramp by least-squares fitting empirical functions that model the backscatter intensity's dependency on range and antenna look direction to our radar data [69]. Alternatively, the backscatter ramp can be obtained by convolving an averaged image with a Gaussian smoothing kernel. The ramp correction is necessary because the subsequent linear feature detection works best with a homogeneous image. Secondly, each individual radar image must be georeferenced to correct for the horizontal ship motion. Thirdly, as IW packet speeds can be of the order of 1 m/s, averaging a several-minute-long sequence of radar images without correcting for the IW motion would risk blurring the signal. Therefore, we estimate an overall packet speed and direction (as well as wavelength) using methods that build on a technique introduced in [96], and shift the individual images to compensate for this motion. Here, we study marine radar IW signatures that were observed during a 10-min period starting August 17, 2006, 22:00 UTC. At this time, the IW packet is found to propagate at 0.85 m/s in a direction of 309°. The dominant wavelength is  $\sim 310$  m. Finally, the averaged image is rotated such that the IW propagates along the y-axis (from bottom to top) and subjected to a 9×3-pixel Gaussian smoothing kernel where the larger dimension is aligned with the IW crests.

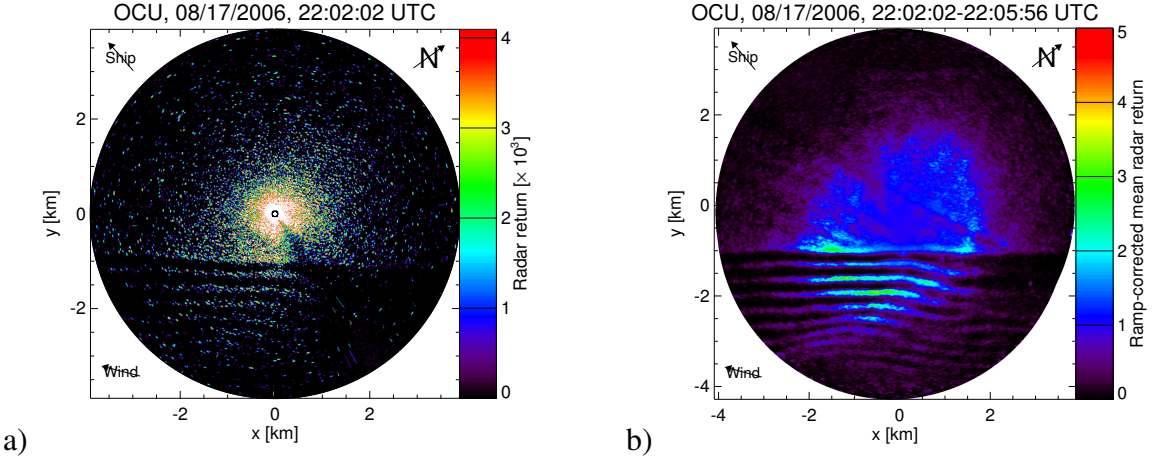


Figure C.1: Example of a single *Oceanus* radar image from August 17, 2006, 22:02:02 UTC (a) and the IW-enhanced version compiled from 86 consecutive images starting at the same time (b).

Fig. C.1 shows a single *Oceanus* radar image from August 17, 2006, 22:02:02 UTC (a) and the IW-enhanced version compiled from a sequence of 86 images (4 min) starting with the one shown at the top (b).

To retrieve the IW signatures from our IW-enhanced radar images, we use a localized Radon transform based method. The Radon transform maps the spatial domain of an image into the two-dimensional Euclidean space. It is defined as

$$f(\rho, \alpha) = \iint_D I(x, y) \delta(\rho - x \cos \alpha - y \sin \alpha) dx dy, \quad (\text{C.1})$$

where  $I$  represents the intensity level of the image at position  $(x, y)$ ,  $\delta$  denotes the Dirac delta function,  $\rho$  is the length of the normal from the origin to a straight line, and  $\alpha$  represents the angle between the normal and the x-axis. The Dirac delta function forces the integration of  $I(x, y)$  along the line  $\rho = x \cos \alpha + y \sin \alpha$ . Consequently, the Radon transform yields integrals across the image at varying orientations  $\alpha$  and offsets  $\rho$  relative to the image center. This operation facilitates the detection of linear features as it maps a straight line in the image space into a single point in the transform space. As the Radon transform essentially involves the integration of an image intensity function along a set

of lines, it is particularly well suited for application to marine radar images, which suffer from radar-inherent speckle noise. This is because the intensity fluctuations due to speckle tend to be canceled out by the process of integration. The main advantage of the Radon transform is therefore that it enables the detection of poorly defined linear features in noisy images since it significantly enhances their signal-to-noise ratio [78]. Finally, by localizing the Radon transform, features that are significantly shorter than the image dimensions or exhibit some curvature can be detected. Localized Radon transform techniques have been used previously to retrieve ship wake and IW information from SAR imagery [25, 100].

In a first step, we have to determine what section within our IW-enhanced radar image contains an IW signal. To this end, we define a set of overlapping circular boxes with a 256 pixel diameter covering the entire radar field of view. The backscatter intensities within each box are then transformed to Radon space, where each data point is divided by the number of image pixels along its projection line. This is to prevent the subsequent linear feature detection from being biased towards projection lines that are characterized by the greatest number of pixels. Furthermore, we limit the Radon transform to projection lines that cover a minimum of 192 pixels. To determine the dominant Radon direction, we compute the contrast (standard deviation divided by the mean intensity within the box) of Radon transform intensities as function of projection direction. For each transform box, we retain the projection direction with the greatest contrast as dominant direction. Boxes that contain IW signatures are then identified as follows: First, we assume all boxes that have dominant directions within  $10^\circ$  of our IW packet direction to contain IW signatures. To help eliminate the occasional outlying boxes, this approach is further refined by checking whether the neighboring boxes also contain IW signatures. For the IW signature retrieval, we keep only boxes where a minimum of 75% of the neighboring boxes were also determined to contain IW signatures. To retain as much IW information as possible, we furthermore keep boxes that do not themselves fulfill the 75% criterion, but have neighboring boxes that do fulfill it.

From the section of the IW-enhanced image where we have determined IW signatures to be present, we then extract a transect that crosses in the direction of the IW packet through the image origin (at a slight offset to avoid the radar dead range). Within the transect we identify IW peaks and troughs, making use of our knowledge of the dominant wavelength to discriminate between signal and noise. Fig. C.2a shows the image transect from the same IW-enhanced image shown in Fig. C.1b, with its IW peaks and troughs marked by black and red dashed lines, respectively. Finally, we use an iterative approach that is again based on localized Radon transform techniques to track each soliton, starting from the peaks found within the transect. A zoom into our IW-enhanced image with the retrieved IW signatures as well as the position of the transect are shown in Fig. C.2b.

Fig. C.3 shows a sequence of maps detailing IW signatures from 10-min worth of marine radar data starting August 17, 2006, 22:00 UTC. The IW-enhanced images used to compute these maps have 4-min averaging periods with a 2-min overlap. The maps, each showing the leading six solitons, clearly depict the IW propagation from bottom to top.

## C.4 Discussion

IWs are ubiquitous features of coastal oceans and play an important role for multiple ocean processes. We have developed a novel technique to retrieve IW information from marine radar images. This technique has been applied to *Oceanus* data from the 2006 NLIWI experiment. IW signatures are significantly enhanced by averaging over a sequence of preprocessed radar images. A localized Radon transform approach is used to extract IW signatures from such IW-enhanced images. In the future, we will apply these techniques to *Oceanus* data that were collected while the ship was following an IW packet over the course of several hours. This tool enables us to study the spatial and temporal evolution of individual solitons and investigate interactions between different IW packets. Furthermore, we hope to retrieve IW amplitudes from radar-based IW parameters using a higher-order

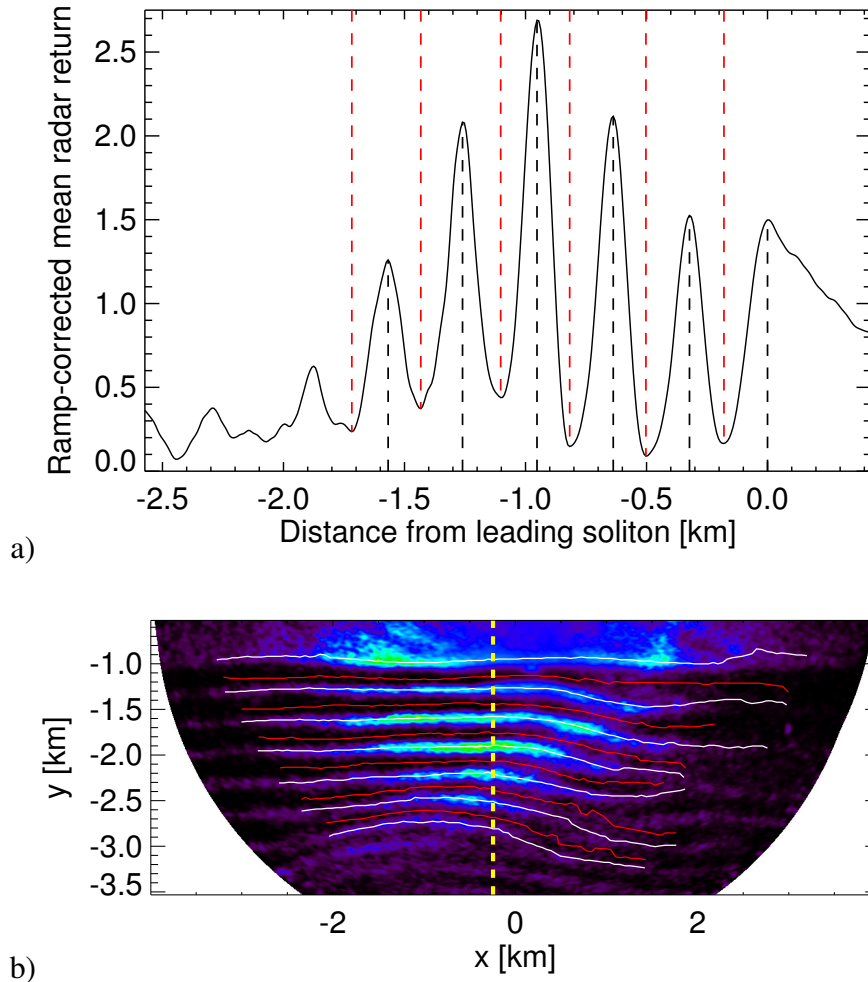


Figure C.2: Transect with IW peaks and troughs marked by dashed lines (a) and corresponding image with the transect position marked by a yellow dashed line and the detected IW signatures marked by white and red solid lines (b).

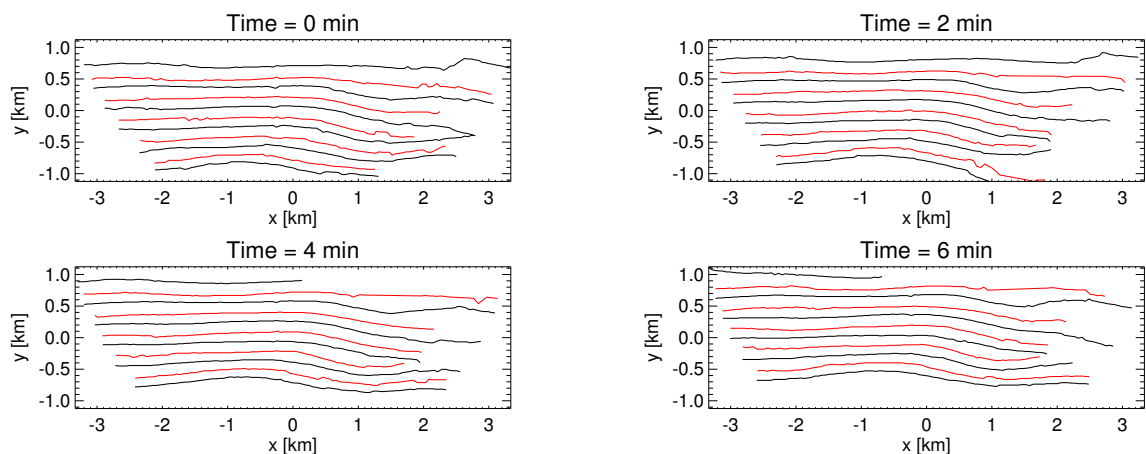


Figure C.3: Maps of IW signatures with peaks in black and troughs in red retrieved from 10-min worth of marine radar data starting August 17, 2006, 22:00 UTC.

Korteweg-de Vries equation. First results indicate that the soliton characteristic half width from SAR or marine radar images can be used to reliably retrieve IW amplitudes in shallow water [132]. The radar-retrieved amplitudes will be validated using ship acoustics.